

# High-resolution insights into the dynamics of Himalayan debris-covered glaciers

**Philip Kraaijenbrink**



# **High-resolution insights into the dynamics of Himalayan debris-covered glaciers**

**Gedetailleerde inzichten in de dynamiek van puingletsjers in de Himalaya**  
*(met een samenvatting in het Nederlands)*

## **P R O E F S C H R I F T**

ter verkrijging van de graad van doctor aan de Universiteit Utrecht  
op gezag van de rector magnificus, prof. dr. H.R.B.M. Kummeling,  
ingevolge het besluit van het college voor promoties in het openbaar  
te verdedigen op woensdag 19 september 2018 des middags te 4.15 uur

door

**Philip Derk Andreas Kraaijenbrink**

geboren op 24 december 1987 te Arnhem

**Promotor:**

Prof. dr. S.M. de Jong

**Copromotoren:**

Dr. W.W. Immerzeel

Dr. J.M. Shea

This research was funded by the Climate-KIC programme of the European Institute of Innovation & Technology.

PhD Thesis

**High-resolution insights into the dynamics  
of Himalayan debris-covered glaciers**

Philip Kraaijenbrink

Utrecht 2018

Faculty of Geosciences  
Utrecht University

**Promotor:**

Prof. dr. S.M. de Jong

**Copromotoren:**

Dr. W.W. Immerzeel

Dr. J.M. Shea

**Examination committee:**

Prof. dr. E. Berthier

*University of Toulouse, France*

Prof. dr. M.R. van den Broeke

*Utrecht University, The Netherlands*

Prof. dr. K. Fujita

*Nagoya University, Japan*

Prof. dr. A. Kääb

*University of Oslo, Norway*

Dr. F. Pellicciotti

*Swiss Federal Institute for Forest, Snow and Landscape Research*

ISBN: 978-90-6266-511-2

Published by the Faculty of Geosciences of Utrecht University in:  
Utrecht Studies in Earth Sciences (ISSN: 2211-4335)

Typeset using X<sub>Y</sub>L<sup>A</sup>T<sub>E</sub>X by Philip Kraaijenbrink.

Printed by Ipskamp Drukkers B.V., Enschede, The Netherlands.

Correspondence to Philip Kraaijenbrink ([p.d.a.kraaijenbrink@uu.nl](mailto:p.d.a.kraaijenbrink@uu.nl)).

On the cover: Composite image of different data products created from UAV imagery of Lirung Glacier. From left to right: optical orthomosaic, elevation model, thermal orthomosaic, slope map and object-based classification. The black lines on the three central images are elevation contours. Shape of the image masks resembles the top view of an eBee UAV.



© 2018 Philip Kraaijenbrink

This work is licensed under Creative Commons Attribution-NonCommercial-NoDerivatives 4.0 International License (<https://creativecommons.org/licenses/by-nc-nd/4.0>).

Chapters 3 to 7 and Appendix A are based on final author versions of published articles. More information and citation suggestions are provided at the beginning of these chapters.

No man ever steps in the same river twice,  
for it's not the same river, and he's not the same man.

*Heraclitus*



---

# Contents

<b>Samenvatting</b>	<b>1</b>
<b>Summary</b>	<b>5</b>
<b>1 Introduction</b>	<b>7</b>
1.1 Glaciers and their importance . . . . .	7
1.2 Climate, hydrology and glaciers in Asia . . . . .	8
1.2.1 Climate . . . . .	8
1.2.2 Hydrology . . . . .	10
1.2.3 Glaciers . . . . .	10
1.3 Debris-covered glaciers . . . . .	13
1.3.1 Occurrence and formation . . . . .	13
1.3.2 Consequences for ice melt . . . . .	13
1.3.3 Supraglacial ponds and ice cliffs . . . . .	16
1.3.4 Response to climate change . . . . .	16
1.4 Unmanned aerial vehicles . . . . .	17
1.4.1 Advances in UAVs . . . . .	17
1.4.2 Types and sensors . . . . .	18
1.4.3 Surveys and data processing . . . . .	19
1.4.4 Potential for glaciology . . . . .	20
1.5 Research aim and outline . . . . .	20
<b>2 Study area</b>	<b>23</b>
2.1 Langtang Valley . . . . .	23
2.2 Lirung Glacier . . . . .	26
2.3 Langtang Glacier . . . . .	27
<b>3 High-resolution thinning and velocity</b>	<b>33</b>
3.1 Introduction . . . . .	34
3.2 Data and methods . . . . .	36
3.2.1 Unmanned aerial vehicle . . . . .	36
3.2.2 Flight description . . . . .	37
3.2.3 Ground control points . . . . .	37
3.2.4 Digital elevation model and orthomosaic generation . . . . .	39
3.2.5 Surface velocity . . . . .	40
3.2.6 Accuracy assessment . . . . .	40

3.3	Results and discussion . . . . .	41
3.3.1	Accuracy and precision . . . . .	41
3.3.2	Downwasting patterns and estimated melt . . . . .	42
3.3.3	Surface velocity . . . . .	44
3.3.4	Role of ice cliffs and supra-glacial ponds . . . . .	45
3.4	Conclusions and recommendations . . . . .	49
	Author contributions . . . . .	50
<b>4</b>	<b>Seasonal surface velocities</b>	<b>51</b>
4.1	Introduction . . . . .	52
4.2	Data and methods . . . . .	53
4.2.1	UAV surveys . . . . .	53
4.2.2	UAV data processing . . . . .	55
4.2.3	Surface velocity determination . . . . .	56
4.2.4	Correlation accuracy . . . . .	58
4.3	Results and discussion . . . . .	58
4.3.1	UAV product accuracy . . . . .	58
4.3.2	Correlation assessment . . . . .	59
4.3.3	Seasonal surface velocities . . . . .	64
4.3.4	Value of UAV surveys . . . . .	66
4.4	Conclusions . . . . .	67
	Author contributions . . . . .	68
<b>5</b>	<b>Mapping surface temperatures</b>	<b>69</b>
5.1	Introduction . . . . .	70
5.2	Data and methods . . . . .	71
5.2.1	Temperature measurements . . . . .	71
5.2.2	Outline of methodology . . . . .	71
5.2.3	Meteorology . . . . .	72
5.2.4	UAV surface temperature . . . . .	73
5.2.5	In situ temperature measurements . . . . .	81
5.2.6	Ground-based thermal imaging . . . . .	82
5.2.7	Landsat 8 thermal infrared comparison . . . . .	83
5.2.8	Surface temperature and topography . . . . .	84
5.3	Results . . . . .	85
5.3.1	Tidbit correction and measurements . . . . .	85
5.3.2	Image registration accuracy . . . . .	86
5.3.3	Image classification and emissivity . . . . .	87
5.3.4	Thermal correction and imagery . . . . .	88
5.3.5	Surface temperature comparison . . . . .	89

5.3.6	Ground-based thermal imagery . . . . .	90
5.3.7	Landsat versus UAV . . . . .	91
5.3.8	Topography and surface temperature . . . . .	93
5.4	Discussion . . . . .	93
5.4.1	Applications of thermal UAV imagery . . . . .	93
5.4.2	Satellite-based surface temperatures . . . . .	96
5.4.3	Bias correction and errors . . . . .	97
5.4.4	Temperature measurement comparisons . . . . .	97
5.5	Conclusions . . . . .	98
	Author contributions . . . . .	99
<b>6</b>	<b>Automatic surface feature detection</b>	<b>101</b>
6.1	Introduction . . . . .	102
6.2	Data and methods . . . . .	106
6.2.1	UAV survey . . . . .	106
6.2.2	UAV data processing . . . . .	106
6.2.3	Object-based UAV imagery classification . . . . .	107
6.2.4	Analysis of feature characteristics . . . . .	112
6.2.5	Pond distribution over the entire tongue . . . . .	112
6.3	Results . . . . .	113
6.3.1	UAV data accuracy . . . . .	113
6.3.2	Image classification . . . . .	114
6.3.3	Surface feature distribution and characteristics . . . . .	114
6.3.4	Pond distribution over the whole tongue . . . . .	119
6.4	Discussion and recommendations . . . . .	120
6.4.1	Object-based classification and feature extraction . . . . .	120
6.4.2	Distribution and characteristics of ice cliffs . . . . .	124
6.4.3	Distribution and characteristics of supraglacial ponds . . . . .	125
6.5	Conclusions . . . . .	126
	Author contributions . . . . .	127
<b>7</b>	<b>The future of Asia's glaciers</b>	<b>129</b>
7.1	Future temperature rise . . . . .	130
7.2	Debris cover abundance . . . . .	130
7.3	Mass loss projections . . . . .	131
7.4	Regional differences . . . . .	135
7.5	Conclusions . . . . .	136
7.6	Methods . . . . .	136
7.6.1	Debris classification . . . . .	136
7.6.2	Ice thickness modelling . . . . .	138

7.6.3 Mass balance gradient and mass redistribution model . . . . .	138
Code and data availability . . . . .	144
Author contributions . . . . .	144
<b>8 Synthesis</b>	<b>145</b>
8.1 Spatially variable surface response . . . . .	146
8.2 Ice cliffs and supraglacial ponds . . . . .	147
8.3 Future of the glaciers . . . . .	148
8.4 Challenges, recommendations and research outlook . . . . .	148
<b>A Supplementary information to Chapter 7</b>	<b>153</b>
A.1 Supplementary figures . . . . .	153
A.2 Supplementary tables . . . . .	167
<b>Acknowledgements</b>	<b>189</b>
<b>About the author</b>	<b>191</b>
First author publications . . . . .	192
Co-authored publications . . . . .	192
Awards . . . . .	193

---

## Samenvatting

Gletsjers zijn kenmerkend voor het Aziatisch hooggebergte en vormen een belangrijke bron van water in het benedenstroomse dichtbevolkte gebied. Smeltwater van de gletsjers is met name van belang nabij de bergen en in gebieden met een relatief droog klimaat, waar het wordt gebruikt als drinkwater, voor geïrrigeerde landbouw en waterkrachtcentrales. Mogelijke veranderingen in gletsjers en de hoeveelheid smeltwater als gevolg van klimaatverandering kunnen daarom van groot belang zijn voor de voedsel en energievoorziening. Om dergelijke veranderingen goed te kunnen doorgronden en op te vangen, is het nodig om de gletsjerdynamiek in de regio te begrijpen op zowel kleine als grote schaal.

Een gedeelte van de gletsjers in Azië is bedekt met een laag puin bestaande uit rotsen, stenen en fijner materiaal. Dergelijke puingletsjers komen hier relatief veel voor, omdat in de jonge, spitse gebergten veel materiaal kan worden geërodeerd en op het gletsjeroppervlak kan worden afgezet. Aangezien puingletsjers veel voorkomen, speelt het smeltwater van dit type gletsjer een belangrijke rol in de rivierafvoeren, zowel nu als in de toekomst. Een puinlaag op een gletsjer zorgt voor een verandering van de smeltsnelheden van het onderliggende ijs en daarmee zorgt het tevens voor een andere dynamiek van de gletsjers. Over het algemeen zal een dunne laag puin zorgen voor een donkerder oppervlak, meer absorptie van zonnestraling en een verhoging van de smeltsnelheid. Een dikke laag puin daarentegen vormt een isolatielaag voor het gletsjerijs en zorgt voor een lagere smeltsnelheid. Ingewikkelde processen aan de oppervlakte van puingletsjer en verschillende terugkoppelingsmechanismen compliceren echter het ruimtelijke smeltpatroon. Deze processen zijn nog niet volledig bekend en er is meer onderzoek naar nodig.

Gletsjeronderzoek in deze regio is complex door de slechte toegankelijkheid van de gletsjers in de hooggelegen stroomgebieden. Bovendien zorgt de aanwezigheid van een puinlaag voor verdere complicatie van veldonderzoek. Satellietbeeldanalyses zijn daarom zeer waardevol gebleken voor de analyse van afgelegen gletsjers. Om kleinschalige smelt- en oppervlakteprocessen op puingletsjers te onderzoeken is de resolutie van de satellietbeelden echter over het algemeen niet hoog genoeg. Onbemande vliegtuigjes, of *unmanned aerial vehicles* (UAV's), kunnen worden gebruikt om beeldmateriaal en hoogtemodellen te produceren van hoge ruimtelijke en temporele resolutie. De ontwikkelingen van de laatste jaren op het gebied van UAV's zijn daarom veelbelovend voor puingletsjeronderzoek. In deze dissertatie worden nieuwe inzichten in dit type gletsjer verkregen door UAV's te gebruiken om puingletsjers in kaart te brengen.

In dit onderzoek is er voor het eerst een puingletsjer in de Himalaya onderzocht met een UAV. Hoge resolutie beeldmozaïeken en hoogtemodellen zijn geproduceerd van de ruwe UAV-gegevens door gebruik te maken van stereo beeldanalyse en het *structure-from-motion* algoritme. Deze data is vervolgens gebruikt om hoogteverschillen en oppervlaktestroming van de gletsjer zeer gedetailleerd in kaart te brengen. De studie toont aan dat er een zeer heterogene smelt is

op het oppervlak van de puingletsjer en dat het smelten van het ijs aanzienlijk wordt versterkt door ijskliffen en gletsjermeertjes.

De UAV-metingen zijn ook gebruikt voor het vergelijken van de stroomsnelheden in zomer en winter van de puingletsjer. Door de horizontale verplaatsing van het oppervlak te kwantificeren door kruiscorrelatie technieken toe te passen op UAV-beeldmozaïeken zijn oppervlaktesnelheden zijn in detail bepaald. De resultaten laten grote verschillen zien tussen de zomer en de winter. Over het algemeen is de stroomsnelheid van de gletsjer laag vergeleken met andere gletsjers, maar de snelheid in de zomer is veel hoger dan in de winter, wanneer de gletsjer vrijwel stagneert.

Een puinlaag veroorzaakt een verandering van de energiebalans van een gletsjeroppervlak. Meetgegevens van de oppervlaktetemperatuur kunnen daarom belangrijke informatie verschaffen die gebruikt kan worden in energiebalansberekeningen. Dit betreft onder andere de eigenschappen van het puin, de effecten hiervan op het onderliggende ijs, en de effecten op de atmosfeer nabij het oppervlak. In dit onderzoek is er een methode ontwikkeld om oppervlaktetemperatuur van een puingletsjer te meten met behulp van een thermische camera. Grote ruimtelijke en temporele verschillen in temperatuur zijn aanwezig op de gletsjer gevonden en deze zijn voornamelijk toe te schrijven aan lokale eigenschappen van de puinlaag.

Ijskliffen en gletsjermeertjes op puingletsjers zorgen voor een lokaal verhoogde smeltsnelheid. Om dit proces beter ruimtelijk te begrijpen, zijn de UAV-beeldmozaïeken verwerkt met behulp van een object-gebaseerde beeldanalysetechnieken. Deze methode maakt een geautomatiseerde detectie van kliffen en meertjes mogelijk alsmede een objectieve en gestructureerde analyse van hun eigenschappen.

UAV's zijn voornamelijk inzetbaar voor gebieden van beperkte omvang en leveren beelden van zeer hoge resolutie. Zij zijn daarom vooral waardevol voor de analyse van kleinschalige processen. Om de effecten van puin op de grote schaal te onderzoeken en dit te koppelen aan mogelijke veranderende temperaturen en neerslag bij toekomstige klimaatverandering zijn de kleinschalige UAV-bevindingen geïntegreerd in een grootschalig model dat gletsjersmelt in de 21e eeuw simuleert in het Aziatisch hooggebergte. De modelresultaten tonen aan dat zelfs bij optimistische klimaatscenario's zeker één derde van het gletsjerijs zal verdwijnen, maar dat realistischere scenario's zorgen voor een aanmerkelijk hoger verlies van de gletsjerijsmassa. De aanwezigheid van puinlagen zorgt over het algemeen voor een vertraging van het verlies van de ijsmassa door de isolerende werking van het puin.

Deze dissertatie toont aan dat kleinschalige oppervlakteprocessen van afgelegen puingletsjers op een unieke en vernieuwende manier kunnen worden onderzocht met behulp van UAV's. Toekomstig onderzoek van deze gletsjers zal toegespitst moeten zijn op het beter begrijpen van de ruimtelijke variatie in ijsmelt onder de puinlaag. Tevens is het belangrijk de precieze rol die ijskliffen en gletsjermeertjes spelen te ontrafelen, waarvoor met name meer onderzoek nodig is naar gletsjerstroming en ijsdynamiek van puingletsjers. Het innovatief combineren van UAV-,

satelliet- en grondmetingen van gletsjers op verschillende schaalniveaus en integratie van de metingen in grootschalige modellen zal leiden tot verdere inzichten in de regionale en lokale verschillen in gletsjersmelt als gevolg van klimaatverandering. Een multidisciplinaire aanpak waarin bevindingen vanuit de glaciologie, hydrologie en meteorologie worden geïntegreerd zal uiteindelijk zorgen voor een verdere ontrafeling van de water cyclus van berggebieden. Dit zal ons helpen de mogelijke effecten van klimaatverandering te begrijpen, zowel in de bergen als in de benedenstroomse gebieden.



---

## Summary

In the high mountains of Asia valley glaciers are pertinent features and an important water resource, both locally and downstream. In the vicinity of the mountains and in arid regions, their melt water can provide a sizeable contribution to stream flow and is of importance for cropland irrigation, drinking water and hydropower. Under future climate change, glacier melt water supply may change as glaciers will continue to lose mass because of rising temperatures. To better understand how this part of the future water balance will change, it is important to improve our knowledge of glacier dynamics from small to large scale.

A fraction of the glaciers is covered by a layer of debris that consists of dust, rocks and boulders. These debris-covered glaciers are relatively abundant in Asia, because the young and steep mountain ranges provide a large amount of erodible material. They are therefore important for the long-term glacier melt water supply to the rivers in the region. The glaciers have dynamics different than debris-free glaciers, because the debris layer alters surface melt rates. In general, thin debris layers enhance melt while thick layers insulate the ice and reduce melt, but the complex processes involved and their interplay are poorly understood and require further research.

The glaciers in the region are generally difficult to study due to their inaccessibility. Debris-covered glaciers have particularly been understudied, partly due to the complications the debris layer imposes on fieldwork. Satellite remote sensing enables analyses of remote debris-covered glaciers, but spatial resolution is generally too limited for detailed analysis of the small-scale effects of the debris layer on local ice melt. Recent advances in unmanned aerial vehicle (UAV) technology offer a promising complimentary observation method, since UAVs enable on demand acquisition of imagery and elevation data at very high spatial and temporal detail. In this thesis, our understanding of debris-covered glaciers and their surface processes is improved by exploring the value of UAVs in the research of these glaciers.

For the first time, a debris-covered glacier in the Himalaya is monitored by a UAV before and after the melt season. Based on stereo-imaging and the Structure-from-Motion algorithm, highly detailed orthomosaics and digital elevation models (DEMs) are derived and used to determine elevation changes and surface flow in unprecedented detail. It is shown that the surface of the glacier experiences highly heterogenous mass wasting and that ice melt is considerably higher near ice cliffs and supraglacial ponds.

Continued UAV surveys enable a comparison of summer and winter surface velocities of the debris-covered glacier. The seasonal surface velocities are derived by exploring the potential of frequency cross-correlation techniques for the high-resolution UAV imagery. Large differences are shown to exist between the two seasons, with limited flow during summer and practically

stagnant ice in winter.

Supraglacial debris significantly alters the surface energy balance of a glacier. Data on spatially distributed debris surface temperature can provide important information on the properties of the debris, its effects on the ice below and its influence on the near-surface boundary layer. Therefore, a methodology is presented to acquire corrected surface temperature maps of a debris-covered glacier from a UAV equipped with a thermal infrared camera.

Ice cliffs and supraglacial ponds on debris-covered glaciers were shown to cause highly heterogeneous surface melt. To improve understanding of these surface features an object-based image analysis procedure is presented that enables their automated delineation, which allows for objective analysis of ice cliff characteristics and spatial distribution.

UAV data primarily provides data on the small to moderate scale. To understand the effects of climate change and debris-covered glaciers on the large scale, the UAV findings are incorporated in a large-scale model that assesses transient glacier mass loss over the 21st century. It is shown that even if climate change is limited over one third of the current glacier mass will disappear by the end of the century, and that more severe mass losses are more likely. Supraglacial debris is shown to be able to provide considerable retention of glacier mass in Asia.

This thesis demonstrates that UAVs are a unique means to study small scale surface processes on remote debris-covered glaciers. Future research on debris-covered glaciers should focus on the causes of spatially variable surface melt by linking UAV data, ground-based measurements and process-based modelling. Moreover, to fully understand thinning of debris-covered glaciers and its relation with enhanced ablation at ice cliffs and supraglacial ponds more research is required of debris-covered glacier ice flow dynamics. Further improvement to our understanding of regional and local response of glaciers will be achieved by large-scale model approaches that combine UAV, ground-based and satellite data at multiple scales in innovative ways. Multidisciplinary studies that integrate findings over a broad spectrum, bringing together meteorology, glaciology and hydrology, will ultimately allow us to understand the entire mountain water cycle and current and future impacts of climate change.

---

## Introduction

### 1.1 Glaciers and their importance

Valley glaciers are distinct features that form in mountain regions where at high elevation snow accumulations do not melt completely and are compressed into ice. The balance between total annual snowfall and ablation determines whether a glacier gains ice mass, losses ice mass or is stable, i.e. the annual glacier mass balance. Given a stable temperature, an increase/decrease in precipitation will cause a glacier to gain/lose mass and grow/retreat. On the other hand, given stable precipitation, a increase/decrease in temperature will cause a glacier to lose/gain mass (Cuffey & Paterson, 2010; van der Veen, 2013).

Although the glacier mass balance varies from year to year with variations in atmospheric conditions, glaciers have resilience to short term variability in weather and climate, as their size and relatively slow dynamics provide a degree of inertia. On the other hand, small changes in the climate at longer time scales are clearly reflected by glaciers. Such changes disrupt the equilibrium between snow accumulation and ice ablation leading to advance and thickening or retreat and thinning of glacier tongues. Glaciers therefore provide an indication of the state of the climate and a way to monitor changes to our climate that is unobscured by interannual variability (Shrestha, 2011). Mountain glaciers exist on nearly every continent on the planet (Pfeffer et al., 2014). The response of glaciers in different regions can therefore also provide an indication of spatial variations in long-term climate change.

Precipitation stored as snow and ice is released during the summer melt season on a range of time scales. From long-term releases on the century scale to seasonal fluctuations or even singular releases such as outburst floods (Jansson et al., 2003). The melt water released can be of importance for a wide range of uses, such as cropland irrigation, drinking water production and hydroelectric power. It is also plays a role in mineral and sediment transport, and sea level changes (Benn & Evans, 2010; Larour et al., 2017). Since glaciers regulate the seasonal water availability and provide a source of melt water during dry seasons (Marzeion et al., 2014), climate perturbations that have an impact on glaciers can have considerable impacts on human livelihoods, for instance by affecting food and power security (Immerzeel et al., 2010).

Since the start of the industrial era, average global temperatures have increased by  $1.1 \pm 0.1$  °C

(WMO, 2018). In response, most of the glaciers on earth have been retreating and losing mass, as evidenced from field and satellite observations (e.g. Bhambri et al., 2011; Bolch et al., 2012; Cogley, 2016; Dyurgerov & Meier, 2005; Francou & Coudrain, 2005; Gardner et al., 2013; Haerberli et al., 1999; Kääb et al., 2012; Oerlemans, 1994; Singh et al., 2011; Zemp et al., 2009), and from glacier modelling studies (e.g. Huss & Hock, 2018; Marzeion et al., 2014; Radic et al., 2014). It has also been shown that  $69 \pm 24\%$  of the glacier mass loss between 1991–2010 had an anthropogenic cause (Marzeion et al., 2014). Enhanced climate warming is expected to occur over the 21st century and water demand will increase under the world's rising population (IPCC, 2014). Climate warming will cause accelerated glacier mass loss and possibly increased glacier melt water runoff in certain regions in the coming decades (Huss & Hock, 2018; Shea et al., 2015). Towards the end of the 21st century, however, the gradual reduction in glacier area and volume will result in decreased ice melt contributions to river discharge (Immerzeel et al., 2013).

## 1.2 Climate, hydrology and glaciers in Asia

High Mountain Asia (HMA) is a large, elevated region that includes numerous mountain ranges such as the Himalaya, Hindu Kush, Karakoram, Pamir and Tien Shan. It is the result of orogenesis caused by tectonic collision of the Indian Plate and the Eurasian Plate that started about 35–55 million years ago, and continues to date (Aitchison et al., 2008). The mountain ranges of HMA surround the Tibetan Plateau, which is the largest and highest plateau on earth with an average elevation that exceeds 4500 m (Figure 1.1).

### 1.2.1 Climate

Strong climatic contrasts exist in the region because of the large range in elevation and the presence of complex climatic systems (e.g. Dobrevá et al., 2017). During the Indian Monsoon (June–September), warm humid air that originates from the Indian Ocean is transported northwards and forced to rise because of the presence of the central and eastern Himalaya (Galewsky, 2009). This results in strong adiabatic cooling, i.e. reduction of temperature of an air parcel due to a decrease of atmospheric pressure, which forces the water to precipitate. Consequently, the southern slopes of the Himalaya and its foothills are generally moist. Its effect even results in the wettest location on earth, with locally over 11 000 mm of rainfall in Meghalaya, East India. On the northern, leeward side of the Himalayan range, the resulting rain shadow causes the Tibetan Plateau to be arid and bare, with only about 200 mm of precipitation (Maussion et al., 2014). North of the plateau the rain shadow effect is even more pronounced, where in the Taklamakan and Gobi deserts there is <50 mm precipitation annually (Bothe et al., 2012). To the west and south-west of HMA lands are arid as well (e.g. Afghanistan, Pakistan and west India), which is largely due to the absence of the monsoon. There, precipitation occurs throughout the year (Bookhagen & Burbank, 2010), although predominantly brought by Westerly disturbances

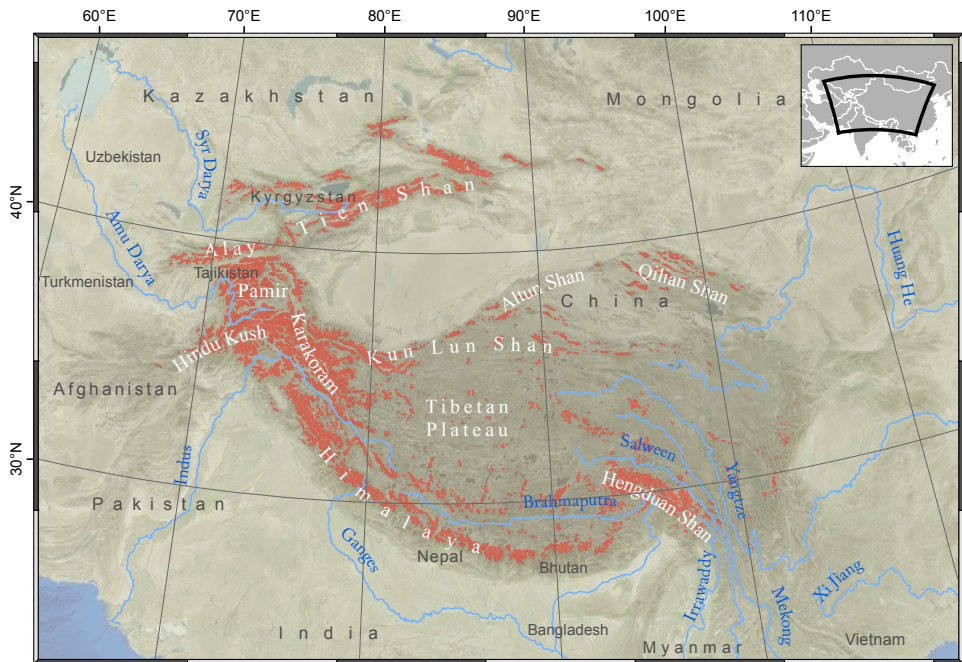


Figure 1.1: Overview map of High Mountain Asia with its major rivers, mountain ranges and glaciers (red) from the Randolph Glacier Inventory version 5.0 (Pfeffer et al., 2014).

during winter (Cannon et al., 2016; Lang & Barros, 2004).

### 1.2.2 Hydrology

HMA forms the headwaters of almost all major rivers in Asia, such as the Ganges, Brahmaputra and the Indus (Figure 1.1), and as such plays an important role in the water cycle in Asia. Approximately 60% of the world's population lives in Asia and a large fraction of it inhabits these river basins, and directly or indirectly uses the river water. The water in the rivers comes from precipitation, snow melt, glacier melt and groundwater, which are all released on different time scales. Moreover, a strong spatial and temporal variation in these stream flow components is found over the region, because of the strong climatic contrasts (Lutz et al., 2014). Liquid precipitation that is transported directly by the rivers is especially important in the central and eastern Himalaya, which is dominated by the monsoon. It can also infiltrate to become groundwater, which is released more gradually and provides an important base stream flow (Andermann et al., 2012). Solid precipitation can form seasonal snow packs that contribute to spring discharge in the western regions of HMA. At higher elevations, the solid precipitation can feed perennial snow masses or provide accumulation for glaciers. Similar to the melt of seasonal snow, glacier melt is especially important in the arid regions. Close to the mountains, where the contribution of rainfall to the stream flow is still limited, glacier melt water can be a considerable fraction of the stream flow (Lutz et al., 2014).

### 1.2.3 Glaciers

The extreme elevation in HMA results in the presence of  $9.8 \times 10^4$  km of glacierized area in its mountain ranges (Pfeffer et al., 2014) and a vast area of  $1.06 \times 10^6$  km with permafrost on the Tibetan Plateau (Zou et al., 2017), in spite of being located at subtropical latitudes. Besides the two poles, this region has the largest ice reserve in the world and is therefore often referred to as the 'Third Pole' (Yao et al., 2012b). Glaciers are predominantly present on the south-western, western, and north-western rim of the Tibetan Plateau in the Himalaya, Karakoram, Pamir and Tien Shan. A more limited glacier presence is found on the Tibetan Plateau itself and to its north and east (Figure 1.1).

Over the last decades glaciological research in HMA has increased. Field studies are scarce, however, largely caused by difficulties that are related with physical access to the glaciers in this region. Glaciers are often very remote and infrastructure is generally poorly developed in this region, requiring long expeditions to reach the glaciers that are secluded high in the mountains. Moreover, (geo)politics can complicate the field campaigns and the acquisition of research permits (Bolch et al., 2012). In the last decade, however, it has become increasingly evident that our understanding of the glaciers and their dynamics is important in order to understand future changes to the water cycle in this densely populated part of the world (IPCC, 2014). Hence, in recent years, research of the HMA cryosphere has increased. More and more glacier mass

balance studies have been performed at high-altitude remote study sites (Cogley, 2016). Furthermore, advances in satellite remote sensing over the last decade and ever increasing length of the satellite data record have enabled large-scale studies of the remote Asian glaciers (e.g. Bolch et al., 2012; Brun et al., 2017; Farinotti et al., 2015; Gardelle et al., 2013; Gardner et al., 2013; Kääb et al., 2012, 2015; Scherler et al., 2011).

The ground-based and satellite studies have revealed that, similar as to elsewhere in the world, glaciers in HMA are generally losing mass as a result of the largely anthropogenic climate change (Marzeion et al., 2014). In contrast, glaciers in the Karakoram range were found to be stable or slightly increasing in mass, a phenomenon that is called the 'Karakoram anomaly' (Hewitt, 2005). Recent satellite-based studies partly confirm this (Brun et al., 2017; Gardelle et al., 2013; Kääb et al., 2015) and expand the anomalous region to include the eastern Pamir and the Kunlun Shan. The recent study by Brun et al. (2017), who used thousands of images from the Advanced Spaceborne Thermal Emission and Reflection Radiometer (ASTER) to construct digital elevation models (DEMs) using photogrammetry, has shown that glaciers in the Karakoram and Pamir are largely stable with mass balances of  $-0.03 \pm 0.07$  and  $-0.08 \pm 0.07$  m w.e. a<sup>-1</sup> (m water equivalent per year), respectively (Figure 1.2). In Kunlun Shan, glaciers were found to be actually gaining mass with a mass balance of  $0.14 \pm 0.08$  m w.e. a<sup>-1</sup>. A clear explanation for the existence of the anomaly is yet absent. Although it was suggested that differences in mass-balance sensitivity of the glaciers have more explanatory power than regional differences in climate change (Sakai & Fujita, 2017), several climatic explanations for the anomalous behaviour of glaciers in these regions have been proposed. These include changes in the intensity of the westerly jet (Forsythe et al., 2017), distinctly different seasonal cycles (Kapnick et al., 2014), and the intensified irrigation in the Tarim basin (de Kok et al., 2018). The entire Himalaya, stretching from west to east, as well as the Tien Shan, exhibit considerable glacier mass losses of about  $-0.30$  m w.e. a<sup>-1</sup>. Most severe mass losses were found in Bhutan and in the Nyainqentanglha Range, both located in the far east of the Great Himalayan Range (Brun et al., 2017).

Besides the Karakoram anomaly, the spatial variability of glacier responses to past climate change in HMA is also poorly understood. The climate systems and extreme topography in HMA result in multiple complex regional and local effects and feedbacks. For example, climate warming in the mountains is a non-linear process as elevation dependent warming occurs through various processes, e.g. changes in condensation level, albedo and aerosols (Pepin et al., 2015). Also, precipitation can change non-linearly with changes in extreme events and shifts in seasonality of snow (Smith & Bookhagen, 2018). To gain more insights into future glacier response to climatic change, these effects in combination with specific glacier dynamics need to be better understood. It is therefore important to acquire more and new climate and glacier data, and incorporate these into novel models to predict future changes.

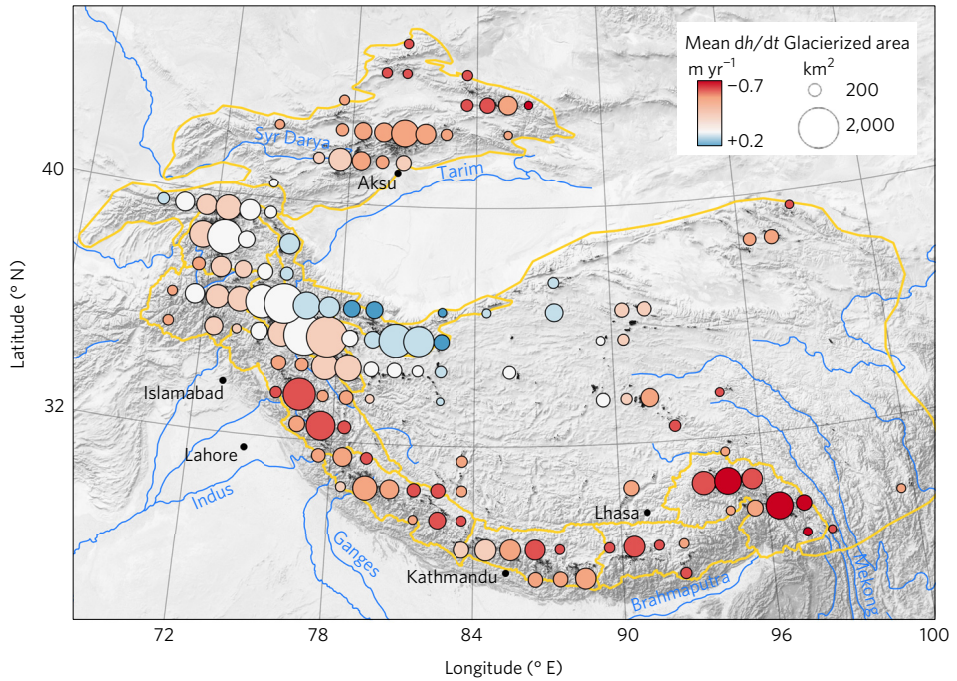


**Figure 1.2:** Glacier elevation changes in High Mountain Asia over the period 2001–2016 determined from ASTER satellite imagery (Brun et al., 2017).

## 1.3 Debris-covered glaciers

### 1.3.1 Occurrence and formation

Some valley glaciers have (parts of) their ablation area covered by a layer of rock debris (Figure 1.3), and are classified as debris-covered glaciers (Kirkbride, 2011). This type of glacier occurs in various mountain ranges around the world, for instance in the Alps, the Andes and the Caucasus. They are especially well-developed in HMA, as the exceptionally steep and young mountains provide ample material that can be deposited on the glaciers. It is estimated that approximately 10% of the total glacierized area in the region is affected by such a debris layer (Bolch et al., 2012), but variations in debris thickness complicate exact area estimations (Sasaki et al., 2016). The debris generally occurs only on the lower tongue, i.e. in the ablation zone, and thickens down-glacier with typical thicknesses of a few cm to about 3 m (Gibson et al., 2017; Rounce & McKinney, 2014). It is composed of a mixture of weathered material of different sizes, which can range from glacial silt to smaller rocks to boulders of 10 m (Hambrey et al., 2009).

The debris layer is formed by different erosion and deposition processes. Rockfall from glacier headwalls can be deposited on the ice, and transported englacially along the glacier flow lines to the ablation zone where it resurfaces as the ice emerges and melts (Figure 1.4) (Anderson & Anderson, 2016; Evatt et al., 2015; Stokes et al., 2007). Fine material may also be embedded in the ice by aeolian deposition. Through abrasion of bed material by the glacier itself, rocks can be entrained in the ice and reach the glacier surface further down. Thinning of debris-covered glaciers and the exposure of elevated, erodible lateral moraines (Benn et al., 2012) provide another source of supraglacial debris (Nakawo et al., 1986).

### 1.3.2 Consequences for ice melt

The presence of a debris layer on a glacier strongly alters its surface dynamics by modifying the energy exchange between the atmosphere and the ice. It decreases the surface albedo from approximately 0.20–0.50 to 0.05–0.15 (Brock et al., 2000; Nicholson & Benn, 2006), and thus increases absorption of solar radiation. Presence of a thin layer of debris can therefore enhance ice melt. A thick layer, on the other hand, can strongly reduce the melt rate despite the lower albedo, as the low rate of conductive heat transfer within the debris provides considerable insulation to sub-debris ice (Mattson et al., 1993; Nicholson & Benn, 2006; Østrem, 1959; Reznichenko et al., 2010). A number of measurements of glacier ablation at varying debris thickness are shown in Figure 1.5. The curves of ice ablation against debris thickness are referred to as the so called Østrem curves. Debris layers less than 3–5 cm thick enhance melt, while thicker layers insulate the ice below. At approximately 50 cm the transfer of solar radiation energy through the debris to the ice reaches a minimal level and a thicker debris layer will not offer much increased insulation (Nicholson & Benn, 2006).



**Figure 1.3:** Photograph of the debris-covered surface of Ngozumpa Glacier, Everest Region, Nepal. The picture shows an example of the hummocky surface of a debris-covered glacier and typical surface features such as ice cliffs and (frozen over) supraglacial ponds (© Petr Melssner, CC BY 2.0 license).

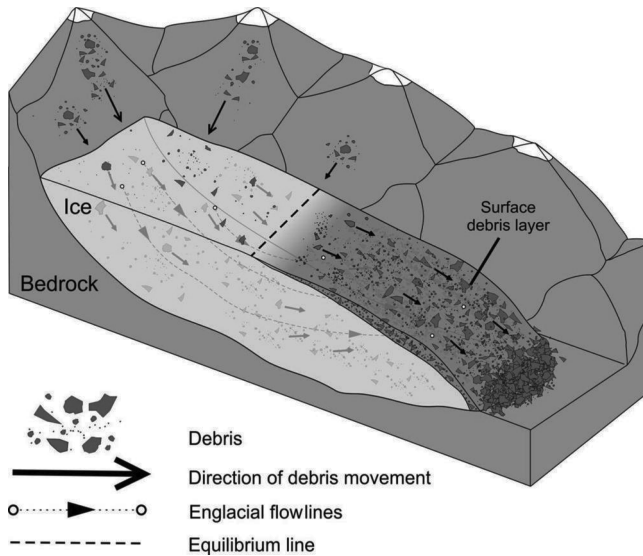


**Figure 1.4:** Schematic representation of a debris-covered glacier and the different sources of supraglacial debris: deposition from the headwalls, aeolian deposition, abrasion from the bed, and deposition from the lateral moraines (Evatt et al., 2015).

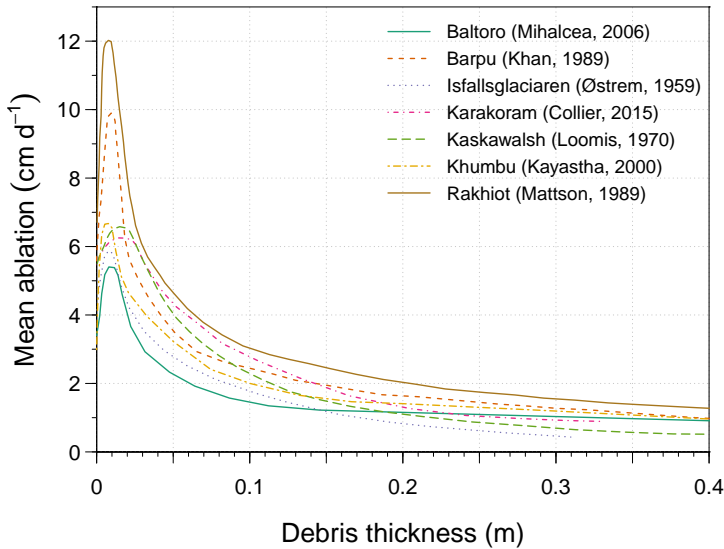


**Figure 1.5:** Influence of debris thickness on ice ablation rates below a supraglacial debris layer. The plot shows so called Østrem curves that were derived for a number of different glaciers. Data displayed here were taken from multiple sources (Collier et al., 2015; Kayastha et al., 2000; Mattson et al., 1993; Mihalcea et al., 2006).

The presence of debris also has a number of effects on the surface energy balance. For instance, debris (1) affects the longwave radiation budget (Steiner et al., 2015) and influences the temperature of the atmospheric boundary layer and surrounding debris; (2) affects the turbulent sensible and latent heat fluxes by changing the aerodynamic roughness of the surface (Miles et al., 2017b); (3) alters air temperature lapse rates over the glacier surface (Shaw et al., 2016; Steiner & Pellicciotti, 2016); (4) can contain moisture, which alters its physical properties and changes the heat conduction through the debris (Collier et al., 2014); and (5) can have a spatially variable pore space, which affects evaporation and the energy available for ice melt (Evatt et al., 2015). Although these processes have been identified, not all are fully understood and their interplay and feedbacks are complex.

Since supraglacial debris has a strong control on ice ablation, the spatial distribution of debris, its thickness and its properties are obviously important for the melt dynamics of debris-covered tongues. In contrast to debris-free glaciers, the surface of the ablation area of debris-covered glaciers is often typically hummocky, i.e. consisting of debris mounds, crests and depressions (Figure 1.3), as patches of thicker and thinner debris result in spatially variable melt rates (Benn & Owen, 2002). Because of the steep local elevation gradients that can develop in this process in combination with ice deformation through glacier flow, locally elevated (thick) debris moves down-slope in a continuous redistribution of the debris. As a result, local melt rates also change constantly over time.

As a result of the insulating properties of supraglacial debris, debris-covered glaciers gener-

ally have tongues that extend towards lower, warmer altitudes than debris-free glaciers. Consequently, they terminate in gentle-sloped valleys, are thicker (Cuffey & Paterson, 2010), and have different area-altitude distributions (hypsometries).

### 1.3.3 Supraglacial ponds and ice cliffs

Due to the hummocky surface of debris-covered glaciers, supraglacial ponding (Figure 1.3) can occur in depressions when supraglacial and/or englacial drainage is slow or absent. Ponds are partially fed by water from the local catchment by supraglacial flow, but also receive water through englacial conduits (Benn et al., 2012; Miles et al., 2016, 2017a). Especially at the start of the melt season ponding can be abundant, as englacial drainage channels are still frozen from winter while surface melt commences (Miles et al., 2017c; Watson et al., 2016b).

Supraglacial ponds enhance ice melt (Sakai et al., 2000). Incoming shortwave and longwave radiation is absorbed by the open water of supraglacial ponds, and transferred to the ice by various processes, such as by wind-driven thermo-erosion at the pond shore and by convection currents (Miles et al., 2016). As a result, one can often find ice cliffs near at the shores of larger supraglacial ponds (Kirkbride, 1993; Sakai et al., 2002). When ponds drain through the englacial conduits and cavities, their energy can also contribute to englacial melt and contribute to the formation of englacial voids (Miles et al., 2017a).

Ice cliffs are steep faces of exposed ice on a debris-covered glacier (Figure 1.3) and three major processes contribute to their formation. First, the wind-driven erosion at the shores of supraglacial ponds can result in ice calving and cliff formation. Second, the local surface slope on the glacier can become steep due to surface melt processes and ice deformation, resulting in slumping of the debris layer and exposure of the ice below. Third, collapses of englacial voids can occur and cause a sudden exposure of ice (Benn et al., 2012).

Ice cliffs are hotspots of ablation on debris-covered glaciers, since they are not insulated by the debris cover. Their surface is often covered by a thin layer of fine debris particles that decreases their albedo, resulting in absorption of much of the incoming direct and indirect solar radiation. Moreover, due to the steep slopes and near vertical orientation of the ice cliff faces, they are exposed to considerable amounts of long wave radiation emitted by the warm, surrounding debris (Sakai et al., 2002; Steiner et al., 2015). As such, ice cliffs on debris-covered glacier tongues contribute disproportionately to the overall melt of the glacier (Buri et al., 2016a; Buri & Pellicciotti, 2018; Pellicciotti et al., 2015; Sakai et al., 2002, 2000) with observed melt rates in the order of  $3\text{--}10\text{ cm d}^{-1}$  (Watson et al., 2016a).

### 1.3.4 Response to climate change

Glacier terminus retreat is a well-known indication of climate change for debris-free glaciers, and it is observed at many locations around the world (Roe et al., 2017). Debris-covered glaciers,

on the other hand, exhibit only very limited retreat (Scherler et al., 2011) and their response to past climate warming has mainly comprised thinning of the tongues (Gardelle et al., 2013). The presence of a supraglacial debris layer thus alters and complicates the response of a glacier to climate change. The difference in response is predominantly caused by the down-glacier thickening of the debris layer, which causes an increase in insulation with a decrease in altitude (i.e. decrease in temperature). As a result, in spite of the higher temperatures and melt potential at lower elevation, the ablation rates at the lower reaches of a debris-covered tongue are often equal to or less than those further up-glacier (Benn & Lehmkuhl, 2000; Hewitt, 2014; Nakawo et al., 1999). When a debris-covered glacier is forced into disequilibrium by climate warming, this effect can result in relatively equal thinning rates for the entire ablation zone of a glacier, or often even faster thinning at higher elevations. Various recent studies have shown the occurrence of this in detail using satellite-derived elevation models, for example for glaciers in the Central Himalaya (Ragettli et al., 2016a; Thompson et al., 2016; Watson & King, 2018), West Himalaya (Vijay & Braun, 2016), and on the South-East Tibetan Plateau (Neckel et al., 2017). Detailed data about the spatially variable debris and its exact down-glacier thinning are often lacking, and more research is required. Ultimately, the melt patterns on debris-covered glaciers could even result in a disconnection of the upper and lower parts of a glacier, such as has occurred for Lirung Glacier, Nepal (Chapter 2).

Thinning rates of debris-covered and debris-free glaciers at the same elevation were found to be largely in agreement (e.g. Gardelle et al., 2013; Kääh et al., 2012), which is unexpected due to the debris insulation. In recent years there has been debate in the glaciological community about these comparable thinning rates of debris-covered glaciers. Two major suggestions are presented about the cause of this 'debris-cover anomaly', i.e. (1) increased melt rates due to the presence of ice cliffs and supraglacial ponds (Pellicciotti et al., 2015; Thompson et al., 2016), and (2) lower and/or reducing ice emergence velocities for debris-covered glaciers (Brun et al., 2018; Vincent et al., 2016). The debate is complicated, however, by the variable thinning of (debris-covered) glaciers with similar climatological forcing, which may be caused by differences in specific local topography and morphology (Salerno et al., 2017), and the general lack of data for glaciers in the region.

## **1.4 Unmanned aerial vehicles**

### **1.4.1 Advances in UAVs**

Over the last decade, great advances have been made in Unmanned Aerial Vehicles (UAVs) (or Unmanned Aerial Survey Systems (UASS), Unmanned Aerial System (UAS), Remotely-Piloted Aerial Systems (RPAS), or simply 'drones') (Blockley et al., 2017). Although UAV technology is over 100 year old, it has now matured and has become much more affordable (Colomina & Molina, 2014). Consequently, there is a large-scale production and a widespread utilization of

UAVs at present, with over 2 million drones sold in 2016 (Garrett & Anderson, 2018). They are used extensively by hobbyists for recreation and by a wide range of professionals, ranging from videographers and real estate agents to rescue workers and engineers. UAVs have also become increasingly popular for use in scientific environmental monitoring.

When equipped with a camera, UAVs can acquire high-resolution overlapping imagery for remote sensing analyses. The imagery can be used to create high-resolution orthomosaics, i.e. geometrically corrected image mosaics, and to generate detailed three-dimensional (3D) models using a workflow called Structure-from-Motion-Multi-view Stereo (SfM-MVS) (Carrivick et al., 2016; Colomina & Molina, 2014; Nex & Remondino, 2014; Snavely, 2011; Snavely et al., 2008), generally referred to as SfM. The relative ease and cost-effectiveness of the UAV and SfM combination resulted in a new paradigm in aerial surveying of which numerous scientific applications benefit, e.g. crop health monitoring (Huang et al., 2013), forest fire monitoring (Rufino & Moccia, 2005), species counting (Koh & Wich, 2012), dune dynamics monitoring (Ruessink et al., 2018), landslide monitoring (Lucieer et al., 2013), and archaeological surveying (Rinaudo et al., 2012).

Compared to spaceborne remote sensing, UAVs offer a few distinct (dis)advantages. An important advantage is that UAVs can be used to acquire imagery and elevation data on demand at a high frequency, while satellites are bound to overpass and revisit times. This means that UAVs can easily be deployed additionally during ground or remote sensing surveys to provide complementary data. Atmospheric disturbances matter less for UAVs, since they are generally flown below clouds and the ground-sensor distance is relatively small. Moreover, because UAV flights are on-demand surveys, they can be performed during good atmospheric conditions by choice. They provide very high-resolution data in the order of a few cm per pixel, which is higher than all commercially available satellite products (Murillo-García et al., 2014). Since UAVs require the operator to physically go the survey area, they have the disadvantage of a bigger time investment. They also operate on battery power and have a limited survey area, which makes large scale surveys such as performed by satellites infeasible. Furthermore, satellite sensor technology is able to capture the large image scenes instantly or within very short time frame (Lillesand et al., 2015). Image acquisition by UAVs, on the other hand, is performed in a flight survey, which requires time. Highly dynamic environments or processes are therefore difficult to survey with a UAV.

#### **1.4.2 Types and sensors**

Two main categories of UAVs can be distinguished: fixed-wing and rotary . Fixed-wing UAVs consist of a rigid airfoil wing and are propelled by one or multiple propellers in order to create lift, similar to a conventional airplane. Rotary UAVs use a horizontally aligned rotor to generate lift, similar to a helicopter. Different from most helicopters, they often feature multiple rotors for stability, e.g. four (quadcopter) or eight (octocopter). Both categories have distinct advantages

and disadvantages. Fixed-wing UAVs generally have better endurance than rotary UAVs and can fly at higher altitude, but they can carry less payload. Take-off and landing of rotary UAVs is performed vertically, as compared to horizontally with fixed-wing UAVs, which is practical in confined spaces and on rough terrain (Colomina & Molina, 2014; Garrett & Anderson, 2018; Nex & Remondino, 2014; Toth & Józków, 2016).

At the advent of UAV technology not many sensors were available that complied with the dimension and weight requirements for UAV payload. However, with the rise of the UAV, sensor technology has also developed rapidly. Currently many options exist that can be mounted on UAV systems. Examples are sensors that capture (1) visual light, which can be used for detailed mapping and photogrammetry; (2) near infrared, which allows detailed vegetation analyses; (3) thermal infrared, which is useful in vegetation and moisture studies; (4) multi- and hyperspectral sensors (Mäkynen et al., 2012), which allows detailed analysis of light spectra; and (5) Light Detection and Ranging (LiDAR) systems (Sankey et al., 2018), which is used for altimetry. With the ongoing technological improvements, the possibilities of UAV monitoring continue to expand.

### 1.4.3 Surveys and data processing

A typical UAV survey consists of two major steps. First, before a UAV flight is performed, well-distributed markers are placed in the area that will be clearly visible on the UAV imagery. The geographic coordinates of these markers are then measured to provide ground control points (GCPs) that can be used during image processing. To georeference the high-resolution UAV data properly the coordinates have to be measured very accurately. Therefore, generally a differential Global Navigation Satellite System (dGNSS) is used, which has an accuracy of a few cm (Jin et al., 2014; Toth & Józków, 2016). When such a dGNSS is solely reliant on Global Positioning System (GPS) satellites, it is also referred to as dGPS. Second, the actual UAV survey is performed in which overlapping imagery is acquired, covering the entire survey area. Largely dependent on the type of UAV, the flight and image capture can be controlled fully manually using radio control or automatically using a predefined flight path, and an on-board GPS receiver and flight computer.

To process the imagery into a single image and generate a digital elevation model, the SfM-MVS workflow is implemented. It consists of several main sequential steps: feature detection and filtering, estimation of 3D geometry, scaling and georeferencing, and image matching (Carrivick et al., 2016; Smith et al., 2016). Several algorithms exist for feature detection on sets of images. All these methods detect so called keypoints for each image, i.e. points with clearly distinguishable mathematical descriptors. The most commonly used descriptor algorithm is the scale-invariant feature transform, which is robust to changes in viewpoint and scale (Lowe, 2004). Correspondences between keypoints of all images or sets of images are determined, points of strong correspondence are matched, and points of weak correspondence or weak geometric consistency are discarded. Using the matched points, a SfM bundle adjustment is performed that

reconstructs a sparse 3D scene structure, the camera positions and orientations, and the intrinsic camera parameters in an arbitrary coordinate system (Snavely et al., 2008; Szeliski, 2011). To georeference and refine the created structure, a scaling and georeferencing procedure is performed using the GCPs and/or image coordinates (if captured by the UAV). As a final step, the MVS algorithm is applied to construct a dense 3D point cloud. A widely used variant is the patch-based MVS (PMVS), which uses the sparse 3D structure together with the images in a three step iterative procedure of texture-based feature matching, patch expansion and filtering (Furukawa & Ponce, 2010).

#### **1.4.4 Potential for glaciology**

Since UAVs are able to provide high-resolution imagery from various sensors and can be used to produce high-resolution DEMs, they have large potential for the monitoring of glaciers. They may be of particular use for the research of debris-covered glaciers for two main reasons.

First, glacier melt is highly variable over small scales and important surface features are too small to be captured by most satellite remote sensing products. As such, the high-resolution data acquirable by a UAV may provide insights into the spatially variable melt and surface properties as well as the dynamics of ice cliff and supraglacial ponds.

Second, fieldwork on glaciers in HMA is difficult due to their inaccessibility. Debris-covered glaciers are particularly hard to measure in the field, because the unstable debris complicates fieldwork. As most ground-based measurements require (partly) removal of the debris they disturb the surface and the measurements. Moreover, they are generally only at point scale, while the surface is highly variable. UAVs offers a method to relatively easy acquire spatially continuous imagery and DEMs without surface disturbance.

### **1.5 Research aim and outline**

The preceding sections reveal that, although general dynamics are largely understood, many of the small scale surface processes that occur on debris-covered glaciers are complex and not well understood at present, and their interplay remains uncertain. This includes spatially variable properties of the debris and the dynamics of surface features such as ice cliffs and ponds. To be able to better predict future changes to water resources in High Mountain Asia (HMA) and to determine the state of the climate, they are important to unravel. In this thesis, the main objective therefore is:

**To increase understanding of small scale dynamics of debris-covered glaciers  
in order to improve projections of climate-induced glacier change**

Data on debris-covered glaciers are scarce, which is the reason for many of the unknowns and uncertainties around the dynamics of these glaciers. UAVs are a relatively new development that provide data that will advance research on the small scale dynamics of these glaciers. This thesis therefore has a strong focus on implementation of UAVs and SfM to reach the main objective. The thesis touches on five different topics that addresses the following specific research questions:

1. *What are the detailed spatial patterns in elevation change of a debris-covered glacier?*

To answer this question, the first multi-temporal UAV monitoring campaign on a debris-covered glacier is presented in Chapter 3. Two high-resolution image and elevation datasets are shown and elevation differences and surface velocities that were derived from these data are analysed.

2. *Are there spatio-temporal differences in debris-covered glacier surface velocity?*

Application of feature tracking techniques to three time steps of UAV imagery of a debris-covered glacier are presented in Chapter 4 to answer this research question. Optimal feature tracking inputs and settings are discussed, and surface velocities derived for summer (monsoon) and winter (dry season) are presented and interpreted.

3. *Can UAV thermal imaging provide new insights into debris surface properties?*

Surface temperatures of debris-covered glaciers may provide useful information on the surface properties of the debris and the surface energy balance. To determine to what extent UAVs can be used to obtain surface temperature data, a methodology to acquire, process and validate thermal infrared imagery of a debris-covered glacier with a UAV is presented in Chapter 5 to answer this research question.

4. *How can ice cliffs and supraglacial ponds be analysed systematically?*

This research question is answered in Chapter 6 by presenting object-based image classification techniques in combination with UAV surveying for semi-automatic detection of ice cliffs and supraglacial ponds on a debris-covered glacier. A characterization of the surface features is presented by analysis of properties such as aspect, slope and spatial distribution.

5. *What will be the response of HMA glaciers to future climate change and are there differences between debris-free and debris-covered glaciers?*

To answer this research question, I present a detailed region-wide debris-cover classification and a novel glacier model in Chapter 7, which incorporates specific insights about debris-cover glaciers that are gained in the preceding chapters. Using the model results, a comprehensive analysis of 21st century climate change impacts on HMA glaciers is presented and the effects of (debris-covered) glacier evolution on water resource availability is determined.

Additional to the chapters above, Chapter 2 presents the two study areas and its glaciers that were used for the unmanned aerial vehicle surveys. The global location of the study areas in the Himalaya is described, including background information on the local climatology and geomorphology. In Chapter 8, I synthesize the research presented in this thesis. I place it into a broader perspective, discuss its main findings with respect to the the literature, and provide recommendations and an outlook for future research.

---

## Study area

In this thesis, the main aim is to study debris-covered glaciers by examining the potential of UAVs in their research. In many regions in the high mountains of Asia, this type of glacier is relatively common (Chapter 1). The glaciers in the region are generally inaccessible, however, and as a consequence it is infeasible to study a large number of glaciers in detail using a UAV. Therefore, only two debris-covered glaciers were selected as the subject of UAV surveys in this thesis: Lirung Glacier and Langtang Glacier. The glaciers are both located in the Langtang Valley in Nepal. Glaciological research has been performed in the valley for multiple decades and, compared to most other locations in the high mountains of Asia, the valley and its glaciers are relatively accessible. Furthermore, the valley is the focus of a broader research program of Utrecht University's Department of Physical Geography. Selection of these two glaciers had the great advantage that fieldwork efforts were shared between multiple researchers and students, thereby reducing workload, improving continuation and frequency of measurements, and reducing costs. The remainder of this chapter provides more information and background on Langtang Valley and the two glaciers.

### 2.1 Langtang Valley

Langtang Valley is located in the Central Himalaya in Nepal and is located approximately 100 km north of Kathmandu, in between the well-known regions of the Annapurna Massif and Mt. Everest (Figure 2.1). The direction of the 584 km<sup>2</sup> valley is primarily east to west, although the final 25 km bends northwards. Elevation ranges from about 1500 m at the very start of the valley near the village of Syaphrubesi to the 7227 m Langtang Lirung, which is its highest peak. A range of other high peaks on the valley's northern rim mark the border with the Tibetan Autonomous Region of China, while lower peaks to the south seclude the valley from the highlands of Helambu. As a result of the large range in elevation, the valley is ecologically and geomorphologically varied. In the lower parts, a steep river-incised v-shaped valley is present with rich subtropical vegetation, while at higher elevation sparse- and non-vegetated lands in combination with rough alpine terrain is predominant. At approximately 2600 m the v-shaped valley opens up distinctly to a u-shaped valley, or glacial trough. This point is suggested to mark the extent of the 45 km long glacier that filled Langtang Valley during the last glacial maximum (Barnard et al., 2006).

At present, only the Upper Langtang Valley (>3850 masl, 453 km<sup>2</sup>, Figure 2.2) has glacier-

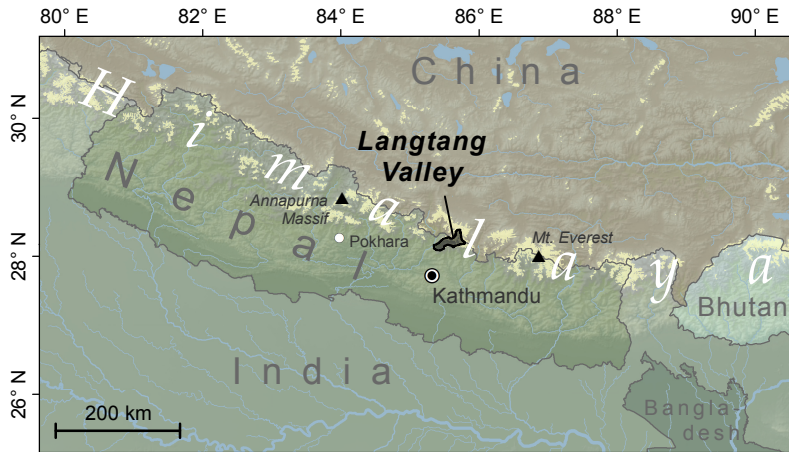


**Figure 2.1:** Location of Langtang Valley in the central Nepalese Himalaya, approximately 100 km north of Kathmandu. The bright yellow areas indicate glacierized regions (Pfeffer et al., 2014), and the blue lines the main drainage network (Lehner et al., 2008).

ized areas. It houses various small debris-free glaciers of which Kimshung Glacier and Yala Glacier are the most notable. Five debris-covered tongues exist in the valley: Lirung, Shalbachum, Ghanna, Langshisha and Langtang. Most of these tongues are relatively small with the exception of Langtang Glacier, which is a moderately-sized debris-covered glacier. Terminus elevations of the debris-covered tongues range from approximately 4050 to 4700 m. The lithological composition of the debris is likely to consist of mainly gneiss and quartzite, since these are the primary constituents of Langtang Valley bedrock (Kohn et al., 2005).

In the valley there are numerous small mountain streams that collect overland flow, groundwater and glacier melt water and transport it to the braided Langtang Khola, i.e. the main river in the valley and an important tributary of the Trishuli River. Discharge of the river measured at the runoff gauge at the outlet of the upper valley (Figure 2.2) ranges considerably. During the cold and dry winter months when there is limited precipitation and glacier melt is largely absent, discharge can be as low as  $2 \text{ m}^3 \text{ s}^{-1}$ . Peak flows during the wet monsoon, on the other hand, can reach  $30 \text{ m}^3 \text{ s}^{-1}$ .

The climate in the valley is monsoon-dominated and around 70% of the annual precipitation ( $800\text{--}1000 \text{ mm a}^{-1}$ ) falls during the monsoon from June to September (Figure 2.3). During the dry winter season from November to May, precipitation (mainly snow) is limited, as it is produced by the occasional passage of westerly troughs (Immerzeel et al., 2014b). In general, precipitation increases with altitude during both the monsoon and the dry season (Seko, 1987), although a reversed along-valley precipitation gradient exists during summer (Baral et al., 2014; Collier et al., 2015). As a result, the glaciers in the valley are characterized by synchronous accumulation and ablation during the monsoon season.

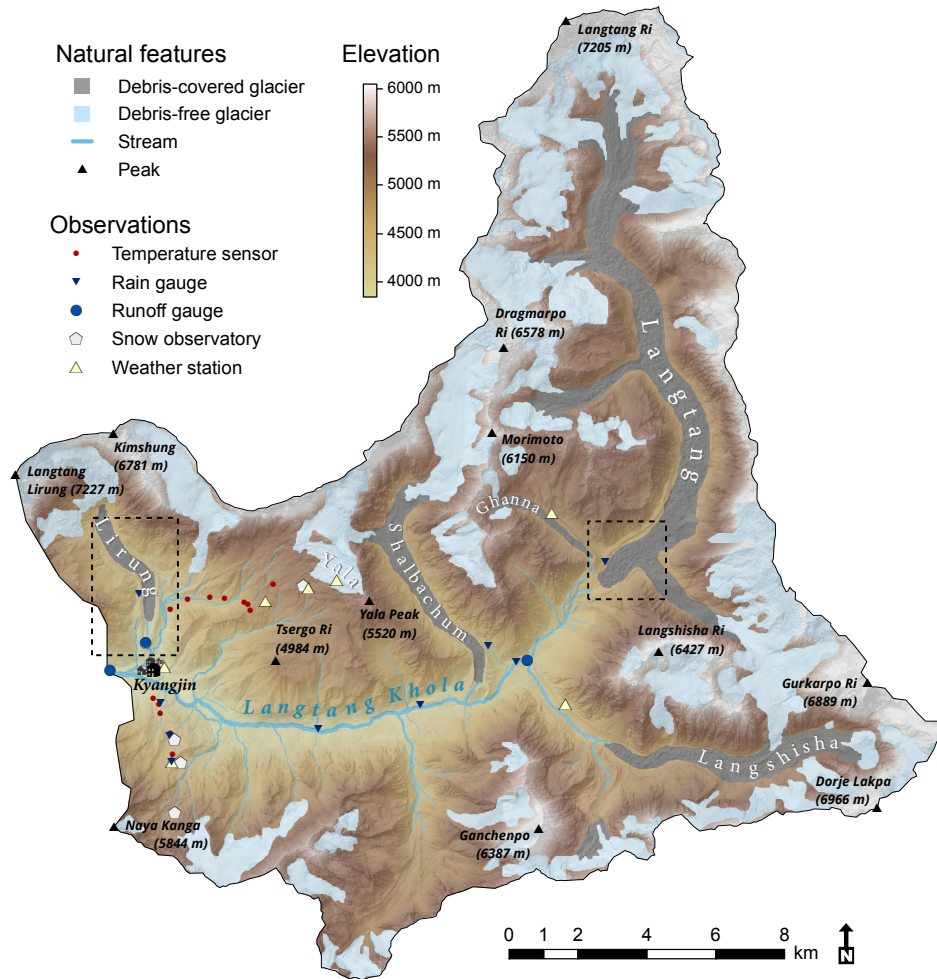


Figure 2.2: Overview map of the Upper Langtang Valley. The colour scale shows the elevation in the valley, with the gray and blue shading indicating debris-covered and debris-free glacierized area, respectively. The streams in the valley are shown by the blue lines, with line thickness denoting stream size. Additionally an overview of the observation network in the valley is shown. The dashed rectangles denote the extents of Figure 2.4 and Figure 2.7. The location of Langtang Valley is indicated in Figure 2.1.

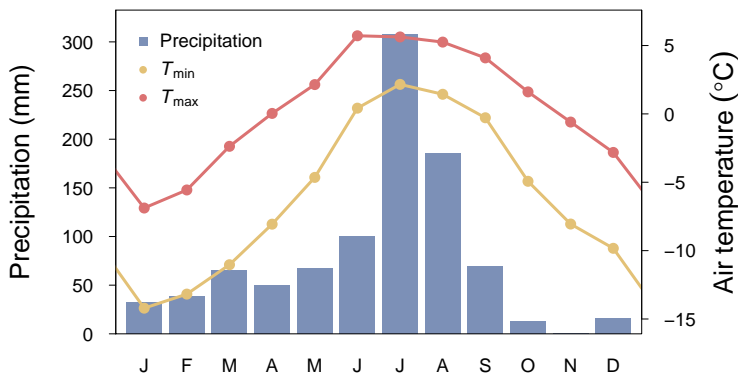


Figure 2.3: Monthly precipitation and air temperature measured at the Yala base camp weather station for the period 2012–2016. The station is located on a small plateau at 5090 m elevation, about 1 km west of Yala glacier Figure 2.1.

Since 2012, a wide range of measurements have been made in Langtang Valley by i.a. Utrecht University (UU), Swiss Federal Institute of Technology in Zurich (ETH Zurich), International Centre for Integrated Mountain Development (ICIMOD), Norwegian Water Resources and Energy Directorate (NVE), and Nepal's Department of Hydrology and Meteorology (DHM). Over the years, a comprehensive network has been built and maintained of weather stations, rain gauges, temperature loggers, snow observatories and runoff gauges (Figure 2.2). Additional to these semi-permanent stations, many temporary measurements and sampling campaigns have been undertaken over the years.

On the 25th of April, the Ghorka Earthquake with a magnitude of 7.8 on the Richter Scale struck central Nepal, tragically killing nearly 9000 people (Kargel et al., 2015). Langtang Valley was particularly hard-hit, as a large landslide obliterated Langtang Village, taking the life of over 200 local villagers, tourists and guides. The earthquake not only had devastating effects on the people in the valley, but also strong implications for the science, since a large part of the observation network was destroyed. Fieldwork campaigns to the region were cancelled that spring and following campaigns were largely dedicated to repairing and rebuilding stations and sensors.

## 2.2 Lirung Glacier

The Lirung Glacier (Figure 2.2; Figure 2.4;  $28^{\circ}14'2''N$ ,  $85^{\circ}33'43''E$ ) is the most accessible glacier in Langtang Valley, generally reachable with a three day walk from the start of the valley. It is located about 2.5 km north of Kyangjin, which is the last settlement in the valley (Figure 2.2). The glacier of  $6.5 \text{ km}^2$  has a debris-covered tongue with a length of 3.5 km and an average width of about 500 m. The remainder of the debris-covered part of the glacier reaches up to about 4350 masl. The debris covered surface is covered by a limited number of supraglacial ponds and

ice cliffs, as well as intermittent vegetation patches. The elevation of its current terminus, i.e. a south-facing exposed ice face that is rapidly melting and moving up-glacier, is approximately 4050 masl. In front of the terminus a network of drainage channels is present and a proglacial lake has formed of about 0.1 km<sup>2</sup>. The outlet of the glacier at the southern end of the lake at 3990 masl is monitored by a runoff gauge and reveals typical discharges of about 0.5 m<sup>3</sup> s<sup>-1</sup>. The glacier has a steep debris-free accumulation zone reaching close to the 7227 m summit of Langtang Lirung. Past mass wasting has disconnected the accumulation zone from the debris-covered glacier tongue (Figure 2.5) and consequently the tongue is fed only by avalanches from the steep slopes and occasional snow fall on the tongue itself.

The debris mantle of Lirung Glacier is generally thicker than the critical thickness (Chapter 1) and often even thicker than 0.5 m (McCarthy et al., 2017), which offers strong insulation to the ice below (Østrem, 1959; Scherler et al., 2011). It is also highly variable, as it ranges from 0.1 to 2.3 m thick on a spatial scale of 10 m (McCarthy et al., 2017), which is expected to result in spatially variable melt patterns. Despite the insulating effect of debris, the historical mass loss of Lirung Glacier has been considerable. Its lateral moraines are currently elevated above the debris-covered surface by ~90 m, providing an indication of the amount of mass wasting since the maximum glacier extent at the end of the Little Ice Age at 1823 ± 190 AD (Rowan, 2017). Over the period 1974–2006, determined by satellite-derived DEMs (Ragetti et al., 2016a), Lirung glacier has seen elevation losses of its debris-covered part of  $-1.03 \pm 0.05 \text{ m a}^{-1}$ , which have increased in recent years (2006–2015) with 62% to  $-1.67 \pm 0.59 \text{ m a}^{-1}$ . Comparable rates of elevation loss have been found by Nuimura et al. (2017). Surface velocities for the glacier are relatively low, since flow for 2009–2010 has been determined to be  $<5 \text{ m a}^{-1}$  using satellite imagery feature tracking (Ragetti et al., 2016a). This confirms older measurements from 1994–1996 that were performed using theodolites, which revealed surface velocities of approximately 2 m a<sup>-1</sup> for the lower part and 6 m a<sup>-1</sup> for the upper part of the debris-covered tongue (Naito et al., 1998).

### 2.3 Langtang Glacier

Langtang Glacier is located at the end of Langtang valley (Figure 2.2; 28° 14' 29" N, 85° 42' 17" E). The glacier has a debris-covered tongue approximately 15 km long and 800 m wide, and it is the largest glacier in the valley with 46.5 km<sup>2</sup>. The tongue ranges in elevation from approximately 4500 to 5200 masl, while its largely debris-free accumulation zone ascends steeply to Langtang Ri (7205 masl). The glacier has four confluences from smaller tributaries located at approximately 1.5, 8.0, 12.0 and 13.5 km from the terminus. Additionally, avalanches that originate from the steep slopes on each side of the tongue feed the glacier at numerous locations. Glacier melt runoff from the terminus of Langtang Glacier marks the start of Langtang Khola. On the debris-covered surface of Langtang Glacier ice cliffs and supraglacial ponds are abundant, and have higher spatial density than on Lirung Glacier. Ragetti et al. (2016a) found 10% of the 30 m grid

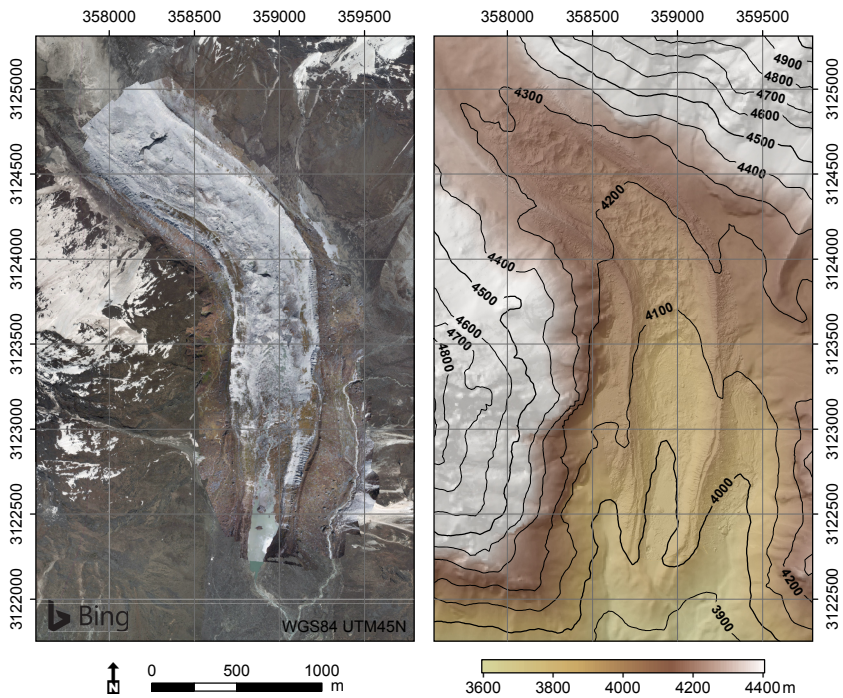


**Figure 2.4:** Satellite imagery with a UAV orthomosaic overlay for Lirung Glacier showing the study area for this debris covered tongue (left). Hillshaded elevation map of Lirung Glacier, generated using the High Mountain Asia DEM (Shean, 2017) and UAV DEM (right). Extent of the map is indicated in Figure 2.2.



**Figure 2.5:** Picture of upper part of the debris-covered tongue of Lirung Glacier with the steep slopes from Langtang Lirung in the background, taken from halfway up the eastern moraine. Note the disconnect between the debris-covered tongue and the debris-free ice on the slopes (© 2013 Philip Kraaijenbrink).



**Figure 2.6:** Photograph of Lirung Glacier and Langtang Lirung taken near the weather station (Figure 2.2) located 4 km east of the glacier (© 2013 Steven de Jong).

cells for Langtang Glacier to contain ice cliffs, while for Lirung Glacier this was 8%. Supraglacial pond presence on the glacier was shown to be variable over the year, with increasing pond area over the pre-monsoon season and peak pond area (~2% of the debris-covered area) at the onset of the monsoon (Miles et al., 2017c).

Over the past decade, mean surface lowering of  $-0.91 \pm 0.05 \text{ m a}^{-1}$  has occurred on the debris-covered portions of Langtang Glacier (Ragettli et al., 2016a). This rate is slightly lower than that is observed on other glaciers in the valley. Similar to Lirung Glacier, elevation loss rates have increased in the last decade, but only with 15%. Surface velocities on the lower reaches of the debris-covered tongue range from 0 to  $10 \text{ m a}^{-1}$ , with higher velocities (20 to  $30 \text{ m a}^{-1}$ ) in the upper parts (Pellicciotti et al., 2015; Ragettli et al., 2016a). These velocities are comparable to those observed for the other debris-covered glaciers in the Upper Langtang Valley in the same studies. Compared to Lirung Glacier, surface velocities observed at Langtang Glacier are considerably higher.

For Langtang Glacier, the main focus in this thesis lies at a 2.1 km long section of the snout of the glacier (Figure 2.7). Although this lower reach of the glacier has slower flow ( $<5 \text{ m a}^{-1}$ ) and consequently less abundance of ice cliffs than the upper reaches (Ragettli et al., 2016a), cliff presence is much higher than on Lirung Glacier. The area of interest includes the final tributary to Langtang Glacier at 1.5 km from the terminus, which is likely to increase the dynamics at the confluence of the two glaciers. Compared to the upper reaches of the glacier, this lower part has limited elevation loss (Ragettli et al., 2016a). The lateral moraines of the glacier are slightly less pronounced than those at Lirung Glacier with about 60 m difference with the glacier surface. There is no clear, exposed terminus present at the glacier such as is the case for Lirung Glacier, and terminus position has been nearly stable in recent years (Miles et al., 2017c).

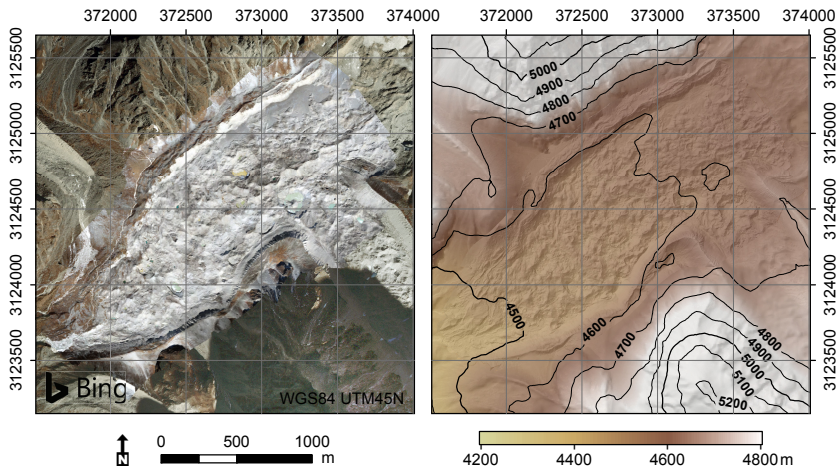


**Figure 2.7:** Satellite imagery with a UAV orthomosaic overlay for Langtang Glacier showing the study area near the terminus of this debris covered tongue (left). Hillshaded elevation map of Langtang Glacier, generated using the High Mountain Asia DEM (Shean, 2017) and UAV DEM (right). Extent of the map is indicated in Figure 2.2.



**Figure 2.8:** Picture of a part of the study area at Langtang Glacier. Photograph was taken from the northern moraine, looking in south east direction at the confluence with the small tributary glacier. Main tongue of the glacier flows from the top left of the photograph to the bottom right. On the foreground a marker used for ground control in the UAV surveys is visible (© 2017 Maxime Litt).

---

## High-resolution thinning and velocity

Himalayan glacier tongues are commonly debris covered and they are an important source of melt water. However, they remain relatively unstudied because of the inaccessibility of the terrain and the difficulties in field work caused by the thick debris layers. Observations of debris-covered glaciers are therefore scarce and airborne remote sensing may bridge the gap between scarce field observations and coarse resolution spaceborne remote sensing. In this study an Unmanned Aerial Vehicle (UAV) is deployed before and after the melt and monsoon season (May and October 2013) over the debris-covered tongue of the Lirung Glacier in Nepal. Based on stereo-imaging and the structure for motion algorithm highly detailed orthomosaics and digital elevation models (DEMs) are derived, which are geometrically corrected using differential GPS observations collected in the field. Based on DEM-differencing and manual feature tracking the mass loss and the surface velocity of the glacier are determined at a high spatial accuracy. On average, mass loss is limited and the surface velocity is very small. However, the spatial variability of melt rates is very high, and ice cliffs and supra-glacial ponds show mass losses that can be an order of magnitude higher than the average. Future research should focus on the interaction between supra-glacial ponds, ice cliffs and englacial hydrology to further understand the dynamics of debris-covered glaciers. Finally, it is concluded that UAV deployment has large potential in glaciology and it may revolutionize methods currently applied in studying glacier surface features.

Chapter based on:

Immerzeel, W. W., P. D. A. Kraaijenbrink, J. M. Shea, A. B. Shrestha, F. Pellicciotti, M. F. P. Bierkens, and S. M. de Jong (2014). **High-resolution monitoring of Himalayan glacier dynamics using unmanned aerial vehicles.** *Remote Sensing of Environment*, 150, 93-103.

### 3.1 Introduction

Glaciers are strong indicators of the prevailing and past climate as their dynamics are sensitive to small changes in precipitation and temperature. Glaciers can be valuable sources of water, and changes in glaciers may directly impact human livelihoods, food security and hydropower potential, particularly in the greater Himalaya (Immerzeel et al., 2013, 2010; Schaner et al., 2012). Monitoring of glacier extents, mass balances and surface velocity is therefore of key importance to understand how climate perturbations impact the status of glaciers (Paul et al., 2013). For both mass balance and surface velocity measurements, field and geodetic methods can be distinguished, each with its own advantages and shortcomings.

In field methods of mass balance estimation a distinction is made between the glaciological and the hydrological method (Hagg et al., 2004). The glaciological method uses ablation stake readings, accumulation pits and snow pillows in order to determine mass gain or loss from the glacier surface. Using measured or estimated snow and ice densities the local mass balance can then be calculated and interpolated over the glacier surface (Fischer, 2011). The hydrological method uses precipitation and outlet discharge measurements that are corrected for runoff and evaporation to estimate the mass balance (Hagg et al., 2004).

Field surface velocity measurements are performed by quantifying stake displacement using differential GPS (dGPS). Measurements using the field method generally yield high-resolution data on a small spatial extent and are therefore best used to examine local effects. A difficulty with field surface velocity measurements is that Himalayan glaciers are often located in inaccessible areas, which can render expeditions cumbersome, time consuming and expensive. In addition many Himalayan glacier tongues are characterized by a thick debris cover (Scherler et al., 2011) and the presence of the debris layer greatly complicates field measurement techniques.

The geodetic methods of glacier mass balance and surface velocity estimation use remotely sensed datasets, either spaceborne or airborne, obtained for at least two different points in time to determine velocities or surface elevation changes between acquisition dates. In recent years many studies have applied geodetic techniques as they provide a relatively easy and inexpensive method to obtain frequent data for large, possibly inaccessible areas (Paul et al., 2013). The sensors used for estimates of elevation changes can be divided into two main categories, active and passive. The active elevation measurements comprise altimetry techniques that use for example high-resolution airborne LiDAR techniques (Arnold et al., 2006), low resolution spaceborne laser altimeters such as ICESat's GLAS sensor (Bamber & Rivera, 2007; Kääb et al., 2012) or microwave ground-based and spaceborne techniques including InSAR (Strozzi et al., 2008; Sund et al., 2014). Passive elevation measurements use photogrammetry on spaceborne or airborne stereo imagery, e.g. Corona, ASTER or SPOT5, to generate elevation models (Berthier et al., 2007; Bolch, 2007; Bolch et al., 2011; Gardelle et al., 2013; Hubbard et al., 2000; Paul et al., 2013). The generated elevation data encompasses large areas, but at relatively coarse resolutions (approximately 30 to 90 m). The vertical error range of those products is generally in the order of

10–20 m (Fujita et al., 2008; Nuimura et al., 2012).

For geodetic measurements of glacier surface velocity, manual feature tracking or automated cross-correlation feature tracking is applied to satellite imagery. The imagery comprises optically sensed data such as ASTER, SPOT5 or Landsat Thematic Mapper (Copland et al., 2009; Kääh, 2005; Paul et al., 2013) or data sensed by synthetic aperture radar sensors such as ERS-2 or Envisat ASAR (Paul et al., 2013; Quincey et al., 2009a,b). The synthetic aperture radar data can also be used to determine the surface velocity by interferometry (Luckman et al., 2007; Quincey et al., 2009b). As with the geodetic measurements of glacier mass change, the spatial extent of the surface velocity products is large and the resolution is coarse. A difficulty with the geodetic approach is that artefacts such as shadows can considerably reduce the accuracy of the surface velocity or elevation change at specific locations.

Mass loss of Himalayan glaciers may for a large part be determined by surface features such as debris (Reid & Brock, 2010; Reid et al., 2012; Scherler et al., 2011), supra-glacial lakes (Sakai & Fujita, 2010; Sakai et al., 2004, 2009) and ice cliffs (Haidong et al., 2010; Reid & Brock, 2014; Sakai et al., 1998, 2002). However, there is presently no geodetic method available that allows for the systematic assessment of glacier surface features, their interrelationships and their changes over time at sufficiently high resolution.

The use of Unmanned Aerial Vehicles (UAVs) in glaciology is currently limited (Whitehead et al., 2013) and in the greater Himalayas non-existent. However, the application of UAVs to glaciological monitoring has the potential to overcome many of the difficulties related to present day field and geodetic methods. Highly detailed orthomosaics and DEMs obtained from overlapping multi-view photography allow for accurate assessments of glacier surface dynamics and surface height changes. UAV-acquired imagery may represent the missing link between the point observations of field methods and the relatively coarse resolution of geodetic approaches and as such it may improve our understanding of the spatio-temporal dynamics of Himalayan glaciers.

The objectives of this study are twofold:

- To apply, for the first time, a professional low-cost UAV on a debris-covered Himalayan glacier. Two field campaigns (May and October 2013) are combined with highly accurate dGPS measurements at Lirung Glacier in Langtang Valley, Nepal, to assess the magnitude of the downwasting of the glacier tongue and the average glacier movement over the monsoon season.
- To investigate the role and dynamics of ice cliffs and supra-glacial lakes by further detailed study of selected regions of the Lirung Glacier and discuss several controlling mechanisms for the strong surface change observed over one monsoon season.



Figure 3.1: The Swinglet UAV that is used for the surveys in this study.

## 3.2 Data and methods

### 3.2.1 Unmanned aerial vehicle

In this study the Swinglet CAM from SenseFly (Figure 3.1) is used as unmanned aerial vehicle (UAV). The Swinglet is a fixed-wing UAV that has a wingspan of 80 cm and a take-off capacity of 0.5 kg. It is capable of approximately 30-minute flights at cruise speeds of  $36 \text{ km h}^{-1}$  and can be flown either manually or using an autopilot. When using the autopilot the Swinglet follows the waypoints of a flight plan created using the included eMotion software. A constant radio link between the computer software and the Swinglet allows for inflight monitoring and control. The UAV is mounted with a GPS receiver, altimeter, wind meter and a Canon IXUS 125 HS digital compact camera that is electronically triggered by the autopilot system to acquire images at the correct positions.

The camera has a 16 megapixel sensor, i.e.  $4608 \times 3456$  pixels, and captures JPEG-format images in the visible light range. Its lens is capable of focal lengths between 4.3 and 21.5 mm. It is fixed at 4.3 mm, however, to minimize potential motion blur as well as to allow faster shutter speeds by maximizing the amount of sensed light. During surveys the camera is set to full-auto mode in which the device uses autofocus and automatically chooses the appropriate combination of aperture, ISO and shutter speed for the given light condition. In sufficiently light conditions the full-auto setting generally results in images captured with relatively large apertures, ISO values in the 125–250 range and shutter speeds of 1/320–1/1200 s.



Figure 3.2: The extent of the monitored area of Lirung Glacier and the off-glacier validation regions.

### 3.2.2 Flight description

To monitor the debris-covered surface of Lirung Glacier (Figure 3.2), image acquisitions were performed in ten separate flights (Figure 3.3, Table 3.1) during two separate expeditions to the site in May and October 2013. At the study site wind speeds generally increase over the course of the day and therefore the UAV flights were all performed in the morning to maximize flight stability and image quality. The launch location and the landing site were the same for all flights. The UAV was launched from a boulder on the ridge of the eastern moraine and was set to perform a circular auto-land on a nearby flat area. For all flights, the desired image overlap was set to be 60% in lateral and 70% in longitudinal directions with respect to the UAV flight path.

On the 18th and 19th of May five of the total of seven performed flights were successful and yielded imagery usable for DEM generation, i.e. flights 2, 3, 4, 5 and 6. The desired ground resolution that was set in the eMotion software, which is directly coupled to the flight altitude above the launch location, was varied over the flights to account for the glacier elevation gradient. The post-monsoon image acquisition of the glacier was performed in three flights on the 22nd of October. A lower ground resolution setting of 5 cm per pixel was used this time to increase the area covered per flight.

### 3.2.3 Ground control points

In October 2013, 19 ground control points (GCPs) along the eastern and western lateral moraines were collected using differential GPS (Topcon GB1000 antenna with a PG-A1 receiver). Two identical GPS devices were used simultaneously: a base station and a rover. A base station was

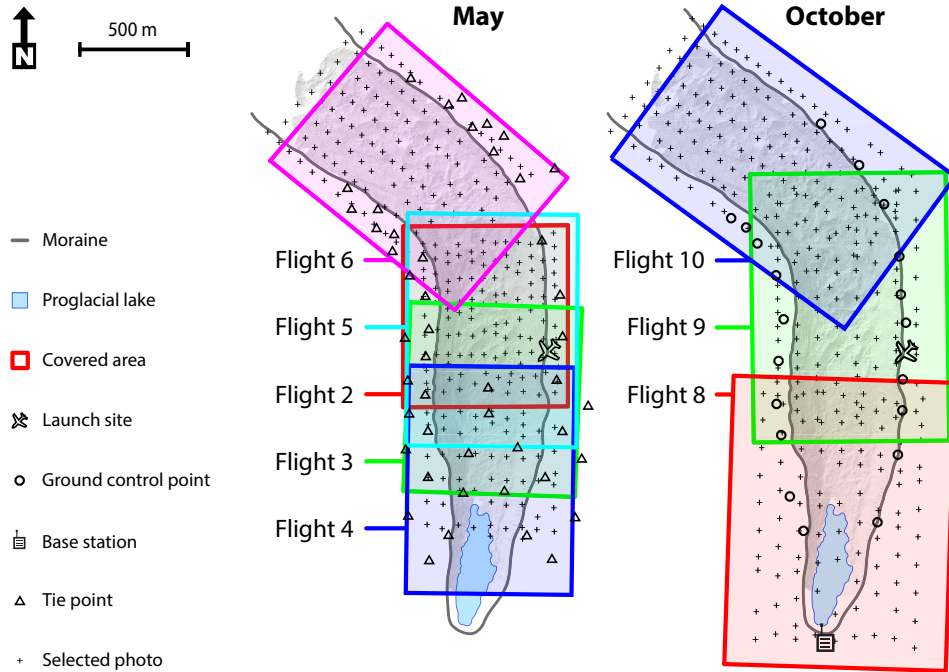


**Figure 3.3:** Overview of the study area, approximate coverages of the successful flights, positions of the selected images and locations of the ground control points (GCP) and tie points.

**Table 3.1:** Overview of all UAV flights performed in May and October 2013.

Flight	Date	Start time (hh:mm)	Duration (min)	Area (km <sup>2</sup> )	Altitude (m amsl)	Resolution (cm)	Photos taken	Photos used
1	18 May 2013	07:49	11	0.30	4304	3	72	0
2	18 May 2013	09:17	17	0.54	4308	3	139	96
3	18 May 2013	10:09	17	0.56	4312	3	132	14
4	19 May 2013	08:58	15	0.66	4353	4	117	63
5	19 May 2013	10:02	17	0.79	4360	4	132	0
6	19 May 2013	10:36	19	1.19	4410	5	132	111
7	19 May 2013	11:28	10	0.17	4258	2	52	0
8	22 Oct 2013	08:23	21	1.43	4396	5	166	89
9	22 Oct 2013	09:24	19	1.14	4392	5	130	88
10	22 Oct 2013	10:06	21	1.18	4393	5	160	130



**Figure 3.4:** Measuring marker locations on the lateral moraine of Lirung Glacier with a differential GPS rover to acquire ground control points for UAV imagery processing.

installed near the outlet of the Lirung Glacier (Figure 3.3) and was occupied for two consecutive days. The rover was used to measure the 19 GCPs. To ensure visibility a bright red fabric of  $1.0 \times 1.2$  m was used for the GCPs, the center point of which was measured using the dGPS rover (Figure 3.4). To avoid error due to changes in the antenna rod inclination, every second a measurement was taken during a 30-second interval. The base station and rover data were post-processed using Topcon tools software (Topcon Positioning Systems, 2009).

In May 2013 a total of 18 GCPs were collected that were marked using red spray paint. However, as this was the first experience of the team with UAV surveys in challenging terrain, the GCPs were not as evenly distributed over the lateral moraines as in the October campaign. The spray paint was difficult to find in the images as well, hence accurate georeferencing of the imagery turned out to be impossible. The May data were therefore georeferenced using 47 tie points (Figure 3.3) of which the x and y coordinates were sampled from the October orthomosaic and the z values from the October DEM at locations without changes in elevation or flow.

### 3.2.4 Digital elevation model and orthomosaic generation

The UAV-collected photos (Table 3.1) were processed into orthophotos and grid-based DEMs of the glacier, lateral moraines and direct surroundings using a Structure from Motion (SfM) workflow (Lucieer et al., 2013). The SfM process starts by selection of the photographs with sufficient overlap from multiple positions and/or angles and quality. Blurred photos are removed

where redundant. Next, an image feature recognition algorithm is used to automatically detect and match characteristic image objects between photographs, i.e. the scale invariant feature transform (SIFT) described by Lowe (2004). A bundle block adjustment is then performed on the matched features to identify the 3D position and orientation of the cameras, and the xyz-location of each feature in the photographs resulting in a sparse 3D point cloud (Fonstad et al., 2013; Plets et al., 2012; Snaveley et al., 2008; Triggs et al., 2007). A densification technique is applied to derive dense 3D models using multi-view stereopsis (MVS) or depth mapping techniques (Furukawa & Ponce, 2009). The use of ground control points (GCPs) and/or incorporation of camera GPS locations allows for the georeferencing of the 3D model in a coordinate system. Finally, the model is exported to a high-resolution grid-based DEM and orthophoto mosaics (orthomosaics) are derived based on the projected and blended photograph at a final resolution of 0.2 m and 0.1 m, respectively. In this study, the SfM workflow as implemented in the commercial software package Agisoft PhotoScan Professional version 0.9.1 (Agisoft LLC, 2013) was adopted. The specific algorithms implemented in PhotoScan are not detailed in the manual, but a description of the SfM procedure in PhotoScan and commonly used parameters are described in Verhoeven (2011).

### 3.2.5 Surface velocity

A manual feature tracking method was used to estimate the surface velocity of the glacier between May and October 2013. Approximately evenly spaced transects of clearly distinguishable surface features ( $n = 145$ ), i.e. primarily large boulders, were visually selected on the orthomosaics. The horizontal displacement between the two periods is precisely measured in a geographical information system. The resulting point data are interpolated into a continuous surface using ordinary kriging (Davis, 2002). To be able to make accurate comparisons of the DEMs between May and October 2013, the October 2013 DEM is geometrically transformed to exactly match the May 2013 DEM using the direction and magnitude of the surface velocity.

### 3.2.6 Accuracy assessment

To assess the geodetic accuracy of the SfM products, i.e. orthomosaic and DEM, two different types of errors are taken into account, i.e. input and output. The input errors comprise the deviations of the dGPS base station as well as the precision of each measurement performed by the dGPS rover. The input errors are given by the post-processing software of the dGPS system. The uncertainty introduced by the SfM processing technique is referred to as the output error, and is assessed using two methods. Firstly, the difference of the May and October DEMs is compared to ablation stake data (unpublished data) that were gathered during the same time period. The melt observed at the stakes is compared with the DEM difference integrated over the flow path between May and October 2013. To quantify the variability in the direct vicinity of the stakes, the zonal mean and standard deviation within a 5 m buffer around the stakes are

also computed. Secondly, the vertical output uncertainty is assessed by calculating the difference between the GCP elevation data and the generated DEMs. The horizontal uncertainty is determined manually by measuring the horizontal displacement between the original GCP (October) and tie point (May) coordinates and the apparent GCP locations on the orthomosaics.

### 3.3 Results and discussion

#### 3.3.1 Accuracy and precision

The dGPS system that was used during the surveys is reported to have an  $\sim 0.20$  m geodetic accuracy in x, y and z for the base station (Wagnon et al., 2013). The input precision reported by the dGPS device of all the separate measurements for the October GCPs has a mean of 6.6 mm and a standard deviation of 6.4 mm in the horizontal and a mean of 13.6 mm and a standard deviation of 14.0 mm in the vertical. These precision errors are very small compared to the geodetic accuracy of the base station hence they are negligible.

The distribution of the measured output errors for October (left panel Figure 3.5) shows that at the GCP locations the resulting DEM has a geodetic accuracy that is within 0.25 m for both the horizontal and vertical. For the May DEM and orthomosaic the errors are within 0.70 m (left panel Figure 3.5). However, the bulk of the measurements show deviations that are less than about 0.20 m. As the May data was georeferenced using the October data, only the deviations from the May tie points with the May orthomosaic and DEM are related to the uncertainty in the DEM difference. Because the locations of both the October GCPs and the reference GCPs are well distributed over the study area (Figure 3.3), it is assumed that the errors at locations away from the GCPs are not considerably higher than those at the GCPs. This assumption might not be valid for areas near the very edges of the orthomosaic and DEM due to edge effects that can be introduced by the SfM processing procedure such as a bowl effect and edge curling (Agisoft LLC, 2013). However, these effects do not affect the monitored area of the tongue.

The image processing, i.e. the stitching, orthorectification and DEM generation, also introduces an additional error. To evaluate this error, DEM differences between May and October area were computed for off-glacier terrain. The right panel of Figure 3.5 shows a histogram of elevation differences in the areas outlined in Figure 3.2 and the deviation is  $0.02 \pm 0.33$  m (mean  $\pm$  sd) based on an area of  $1.6 \text{ km}^2$ , which is an acceptable error.

Comparison of stake ablation data with the DEM differencing results (Table 3.2) shows that they are mostly in agreement considering the geodetic errors involved. Only the ablation at stake S3 is considerably different from the DEM difference at that location. The likely reason for this is that stake S3 is located in an area where the ice is forced upward by emergence velocity<sup>1</sup>, i.e.

---

<sup>1</sup>The importance of emergence velocity may have been underestimated in the original paper that this chapter is based on (Immerzeel et al., 2014a). Elevation losses at all stakes are affected by emergence velocity in varying (and unknown) degrees and a comparison of stake ablation and UAV-derived elevation change is not completely accurate without taking it into account.

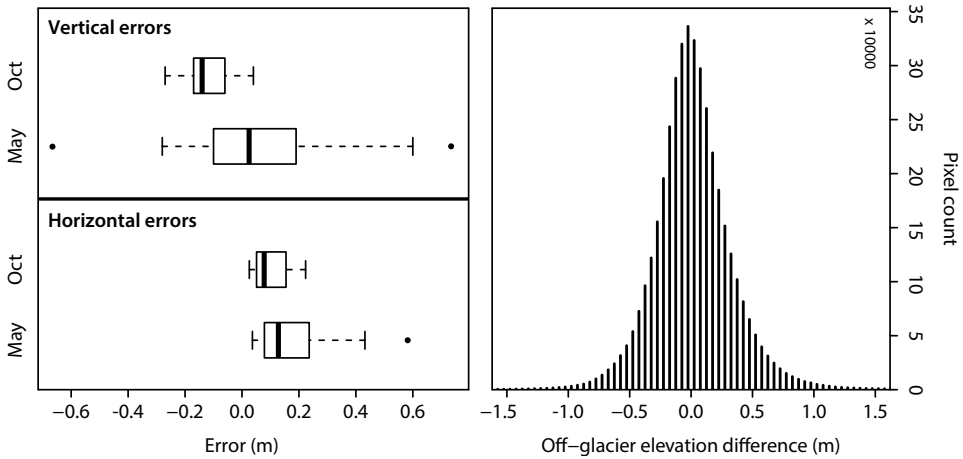


**Figure 3.5:** The left panels show boxplots of the errors that were measured between the ground control data and the generated DEM (vertical) and orthomosaics (horizontal) for both the May and October datasets. The boxes represent the interquartile ranges, the whiskers the quartile to extreme ranges and the thick lines the medians. The right panel shows a histogram of elevation differences between May and October 2013 in the off-glacier terrain outlined in Figure 3.2 (right panel).

**Table 3.2:** Stake ablation rates (m) for the May–Oct period (locations marked in Figure 3.6) and comparison with UAV-derived DEM differences (m). The DEM difference is integrated over the flowpath between May and October 2013. The zonal mean and standard deviation are based on a 5 m buffer around the stake.

Stake	Stake ablation	DEM difference	Difference	Zonal DEM mean	Zonal DEM sd
S1a	-1.77	-2.15	0.38	-2.17	0.32
S2_2	-2.05	-2.23	0.18	-2.22	0.29
S3	-2.13	-0.08	-2.05	-0.37	0.94
S4	-1.77	-1.90	0.13	-1.90	0.54

the vertical flow component of the glacier ice relative to the glacier surface that is related to ice dynamics (Cuffey & Paterson, 2010). Figure 3.6 shows that, just before the bend in the glacier, there is a small region where this occurs. These observations are confirmed by the flow direction and velocity. In addition the high standard deviation found within a 5 m radius shows that the area around this stake is quite variable in the rates of elevation change and that a horizontal measurement error can result in considerable changes in the point measurement.

### 3.3.2 Downwasting patterns and estimated melt

Our results show a strongly heterogeneous downwasting pattern on the tongue of the Lirung Glacier (middle panel Figure 3.6, Figure 3.7). Aggregated over the entire monitored area, the surface elevation change between May and October 2013 is  $-1.09$  m and the standard deviation computed over all pixels equals  $1.40$  m. The entire tongue shows a negative change in surface elevation, except for a small region before the bend in the glacier (middle panel Figure 3.6). Here

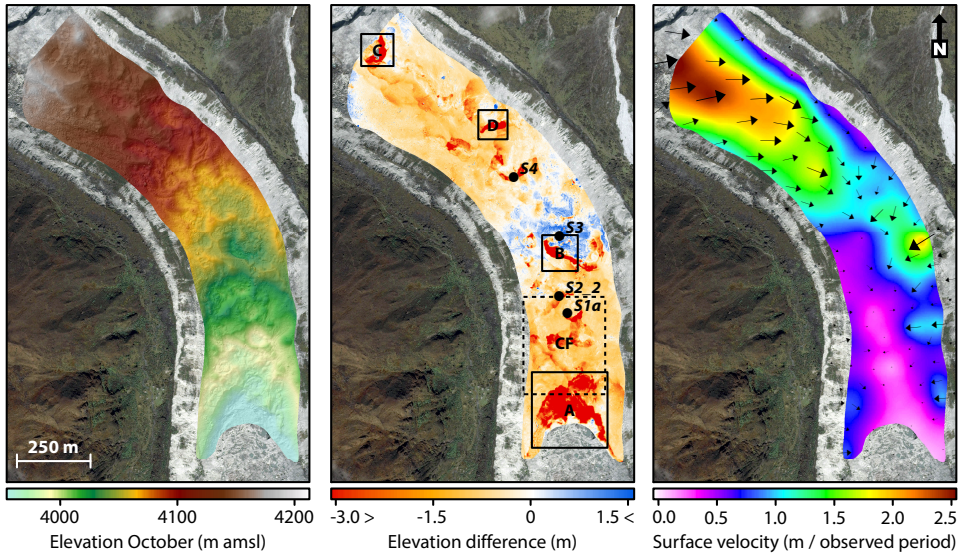
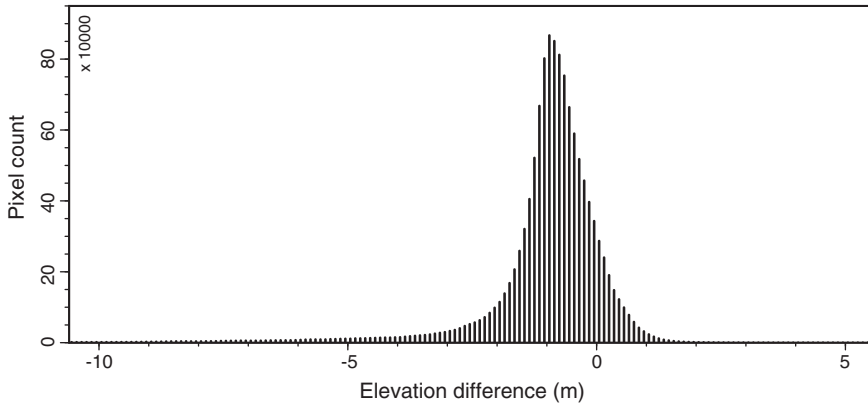


Figure 3.6: Digital elevation model in October 2013 (left panel), changes in elevation between May and October 2013 (middle panel), and the derived surface velocity and direction of flow (right panel). The middle panel shows the locations of the ablation stakes and the extents of the panels of Figure 3.8 (solid boxes) as well as the extent in Figure 3.9 (dashed box).

an uplift of around 0.50 m is observed as the vertical emergence velocity pushes the ice upward. It is interesting to note that the flow direction and velocity confirm this observation. The flow changes direction and magnitude in the bend and the ice is compressed and pushed upward as a result. As a result of emergence and compressive flow an error is made in the quantification of ice loss over the monitored area. Overall this error is likely to be limited as the flow velocity of the Lirung Glacier is small (right panel Figure 3.6). Based on 1994–1996 data, Naito et al. (1998) estimated that overall emergence velocity on the Lirung Glacier is  $0.18 \text{ m a}^{-1}$ . Presently the tongue of the glacier is completely separated from its accumulation zone and it is likely that the emergence velocity has further decreased since 1996.

Assuming an average ice density of  $900 \text{ kg m}^{-3}$ , the 1.09 m of downwasting corresponds to  $0.036 \text{ m}^3 \text{ s}^{-1}$  (or  $6.3 \text{ mm w.e. d}^{-1}$ ) of excess melt water over the total monitored area of  $0.49 \text{ km}^2$ . This excess water as a result of the loss in ice mass is only a small fraction of the average runoff generated for the Lirung catchment over the same period ( $2.09 \text{ m}^3 \text{ s}^{-1}$ , unpublished data) for several reasons: (i) the total amount of melt water will be larger than this amount of excess water; (ii) the period of observation covers the monsoon period when precipitation dominates the local hydrology; (iii) melt runoff occurs only during a limited period during the day when solar radiation is high; (iv) only 40% of the tongue is monitored, (v) emergence was not corrected for, and (vi) the thick debris cover limits the melt per unit area. To illustrate the latter a degree day factor (DDF) was computed based on the observed downwasting, air temperature data observed on the glacier, the DEM and a lapse rate of  $-0.006 \text{ }^\circ\text{C m}^{-1}$  (Pellicciotti et al., 2013). The aver-



**Figure 3.7:** Histogram of changes in elevation between May and October 2013 based on the 0.2 m resolution DEM difference.

age DDF for the entire monitored area is only  $0.74 \text{ mm } ^\circ\text{C}^{-1} \text{ d}^{-1}$  and this is in agreement with several other studies that relate debris thickness to melt rates (Hagg et al., 2008; Mihalcea et al., 2006; Nicholson & Benn, 2006). These studies confirmed also for the Himalaya that when the debris thickness is larger than 40 cm the melt rates are reduced dramatically (Østrem, 1959) to values that are in line with our findings on Lirung Glacier, where debris thickness is generally larger than 50 cm (Petersen & Schauwecker, 2013). Given that the runoff regime is a complex mixture of rain, melt and subsurface flow during the monsoon, it is difficult to provide a conclusive answer on the contribution of melt under the debris-covered tongue to the total runoff. Only a fully distributed and well calibrated glacio-hydrological model would be able to resolve the single components to runoff accurately.

Our findings indicate that glacier melt water generated under the debris cover plays only a marginal role in the total amount of water that is generated in the Lirung catchment. The zero degree isotherm during the monsoon is on average located at 5400 m elevation and it is therefore possible that, in addition to rain runoff, significant amounts of melt water are generated just above the upper part of the tongue (4400 m) in the transition zone towards the steep accumulation area where debris cover is thin or non-existent and ice is exposed. This is also confirmed by recent estimates of an equilibrium line altitude of 5260 m elevation of the Yala glacier in the same valley (Fujita & Nuimura, 2011).

### 3.3.3 Surface velocity

The surface velocity (right panel Figure 3.6) varies from 2.5 m between May and October in the upper part of the monitored area to completely stagnant near the terminus. Naito et al. (1998) report surface velocities between 2.8 and 7.5 m between June and October in the period 1994–1996 for the middle part of the glacier and between 1.9 and 2.5 m for the lower part of the

glacier. Although surface velocity is in the same order of magnitude, it shows that the glacier has further slowed down relative to 1994–1996. The direction of flow is also strikingly similar. The measured flow direction at the upstream part is eastward, which may be due to the possibility that most of the avalanches that feed the glacier tongue occur on the north western part of the tongue. The slight elevation gain of around 0.5 m in the outer curve of the glacier is likely the result of a vertical emergence velocity as a result of ice compression in the bend of the glacier (Figure 3.6, middle panel).

The thick debris layer, the low melt rate and the slow flow are indicative that the Lirung Glacier is in a final stage. The accumulation zone is separated from the tongue, the tongue has slowed down almost completely and is losing mass. The present state of the Lirung Glacier, with its relatively low altitude tongue, may be a preview of the fate of other debris-covered tongues in the Himalaya, and our observations match with what is projected for debris-covered glaciers at higher altitude in the Everest region of Nepal (Naito et al., 2000; Shea et al., 2015).

### 3.3.4 Role of ice cliffs and supra-glacial ponds

The spatial variation in elevation changes and DDFs is striking and the largest changes are found in the vicinity of supra-glacial ponds and adjacent ice cliffs, which have been manually digitized on the basis of the orthomosaic. Several studies have stressed the accelerating role these ponds and cliffs have in the overall melt of debris-covered tongues of Himalayan glaciers (Benn et al., 2012; Haidong et al., 2010; Reid & Brock, 2014; Sakai et al., 2009).

Supra-glacial ponds have been observed on glaciers with a low inclination and strong down-wasting since the end of the Little Ice Age (Sakai & Fujita, 2010) and both of these conditions are met on the Lirung Glacier. These ponds are generally above the hydrological base, i.e. the glacier outlet, and they can drain episodically when connected to the glacial drainage system. The water in the ponds warms in response to solar radiation inputs, and surveys in the Everest region revealed large englacial voids created by the drainage of warm water from the ponds (Benn et al., 2012). In that study it is hypothesized that the "roof" of such voids may collapse and this would generate a new depression that could lead to the formation of a new lake. Ice cliffs are generally found near the lakes and their melt rates are much higher on the exposed cliffs compared to ice covered by a thick debris mantle. A previous study suggests that on the Lirung Glacier 69% of the total melt originates from ice cliffs while they only cover 2% of the total area (Sakai et al., 1998). Heat fluxes of the cliffs measured in a more recent study, however, indicate that it is likely less pronounced (Sakai et al., 2000). Similar conclusions are drawn for the Koxkar glacier in China (Haidong et al., 2010; Juen et al., 2014) and the Miage glacier in Italy (Reid & Brock, 2014). In our case and for this season a total area of 0.04 km<sup>2</sup> (8% of the total monitored area) of supra-glacial ponds and associated ice cliffs is observed and this 8% in area generates 24% of the total melt and can largely be explained by the backwasting of the ice cliffs (Reid & Brock, 2014; Sakai et al., 1998). This is a first order estimate and in the future our

findings must be validated with a full energy balance model of the glacier including ice cliffs and lakes. The upper portion of the debris-covered tongue, which was not covered in the surveys, has a greater density of lakes and ice cliffs.

The interplay between englacial conduits and voids, ice cliffs and glacial lakes is likely a key factor controlling mass loss on debris-covered glaciers rather than melt at the surface. To investigate this in detail, I focus on four specific areas marked in Figure 3.6 in the middle panel. Figure 3.8 shows the orthomosaic of May 2013 (left column), October 2013 (middle column) and the DEM difference (right column) for the four selected areas. As shown in the figure, the ice cliffs present on the glacier can have different aspects. This is consistent with the theory that incoming shortwave radiation is not the dominant process in the formation of ice cliffs and that other processes such as debris slope slumping, ice cliff calving and collapsing englacial conduits play an important role (Benn et al., 2012).

Panel A shows the terminus, where strong mass wasting is observed over a large area. The dotted line shows the estimated position of the ice and substantial changes have occurred. New ponds have formed in the proglacial valley and cliffs with exposed ice have emerged between May and October to the right and left of the dotted line in the October image. The cliffs have a DDF between  $5$  and  $7 \text{ mm } ^\circ\text{C}^{-1} \text{ d}^{-1}$ , which is roughly a factor 10 higher than the glacier average. These observations are interpreted as indications that the terminus area is undergoing rapid change, which exposes ice cliffs and results in accelerated mass loss.

Panel B shows a typical supra-glacial pond with an adjacent ice cliff. In May the pond is about 60 m wide while in October the pond has almost completely drained. This process is observed all over the glacier. It is hypothesized that the englacial conduits that drain surface water are frozen in May and that the inputs of warmed lake water and precipitation during the monsoon season open the conduits and allow drainage to occur. Figure 3.8b also shows that large parts of the ice cliffs in the north west corner have been covered by debris and that the DDF on the main cliff reached values up to  $12 \text{ mm } ^\circ\text{C}^{-1} \text{ d}^{-1}$ , indicating that the debris cover is thin. The translocation of a boulder between May and October can also be clearly seen in this image, north of the melt pond.

Panel C illustrates extreme changes observed around a supra-glacial pond. The pond has slightly drained and shifted toward the southeast. Mass wastage related to ice calving (Benn et al., 2012) clearly occurs here. A steep scarp of  $\sim 80^\circ$  developed between May and October on the east side of the lake, visible as the darker shaded area in the October image. Furthermore, a steep part of the cliff part has collapsed at the northeast side of the pond. The calving is likely related to the lack of drainage during the monsoon season of the pond.

Other cliff-forming processes that occur in the vicinity of this pond appear to confirm those described by (Benn et al., 2012), e.g. slumping of the debris slope seems to have formed the large cliff at the area north of the pond while the southern part of the cliff is possibly caused by a roof collapse. This may be the cause of a conduit blockage that resulted in the lack of pond drainage.

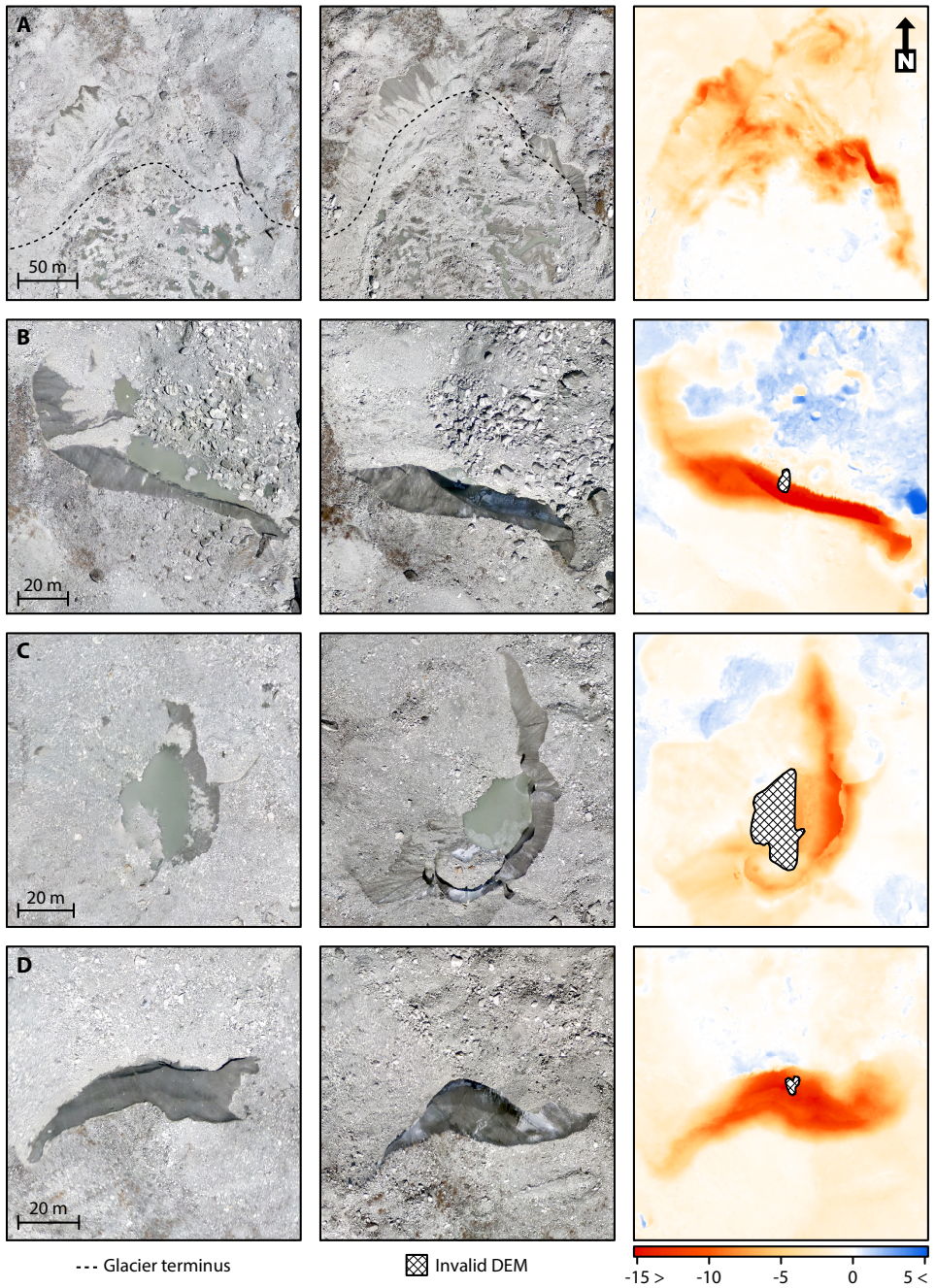


**Figure 3.8:** Changes in surface features around selected locations. The left column shows the orthomosaic of May 2013, the middle column of October 2013 and the right column the DEM difference.

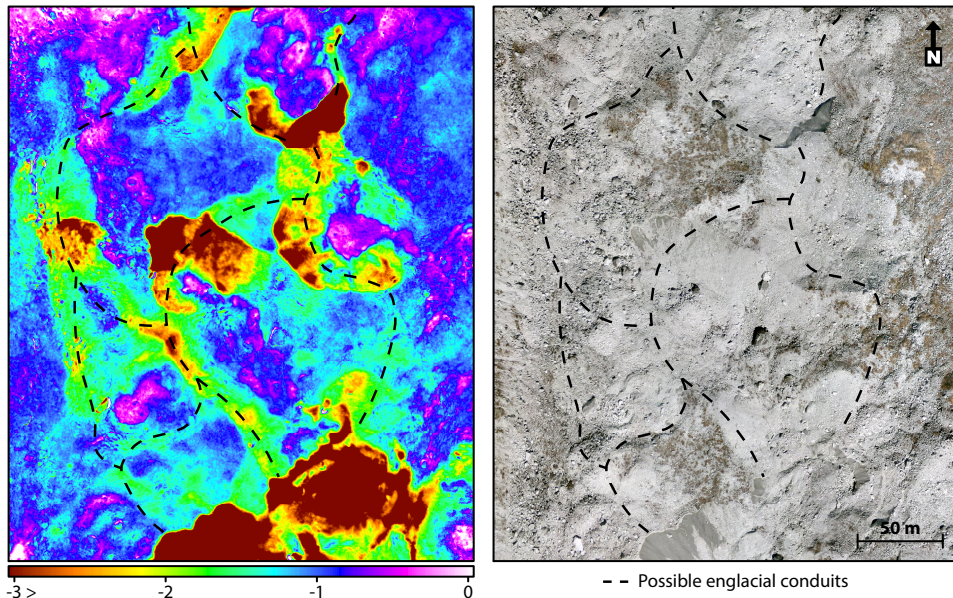


**Figure 3.9:** Possible locations of englacial conduits superimposed on DEM difference (left) and orthomosaic (right).

Finally, Panel D shows the migration of a north-facing ice cliff without the presence of a pond. The horizontal movement is substantial (7–11 m) and the cliff is more pronounced in October. The DDF for this cliff is between 6 and 10  $\text{mm } ^\circ\text{C}^{-1} \text{d}^{-1}$ , compared with the average DDF of 0.7  $\text{mm } ^\circ\text{C}^{-1} \text{d}^{-1}$  that was computed for the entire monitored region. Generally north-facing ice cliffs melt at lower rates as the amount of incoming radiation is limited compared to south-facing cliffs (Benn et al., 2012; Sakai et al., 2002). In this case, the absence of an adjacent pond results in a relatively shallow slope of  $\sim 35^\circ$ , which allows for more incoming shortwave radiation and a relatively high DDF.

Near the terminus of the glacier there is a large area with a high density of ice cliffs and high melt, and it is hypothesized that these areas are connected by a network of englacial conduits (Figure 3.9). The conduit locations were visually estimated from the subsidence patterns present in the DEM difference that were assumed to be caused by thawing and deformation of the conduits. These conduits could play an important role, not only in draining water, but also in the dynamics of surface deformation. Therefore, to develop a better understanding of the dynamics of debris-covered glaciers, it is key to study the conduits in more detail using, for example, ground penetrating radar techniques (Bernard et al., 2014; Sakai & Fujita, 2010; Shea et al., 2015; Wagnon et al., 2013) and repeated UAV surveys.

### 3.4 Conclusions and recommendations

In this study a UAV is deployed over a debris-covered Himalayan glacier for the first time. The imagery is used to derive high-resolution orthomosaics and digital elevation models. Results from May and October 2013 campaigns are compared to quantify mass loss and surface velocity and the following conclusions are drawn.

The potential of using UAVs in glaciology is high and it may revolutionize classical field based methods. Traditionally stakes are drilled into the glacier, but this is challenging on glaciers with a thick debris cover and only results in an aggregated amount of melt at a few point locations with inaccuracies that can be high. Given the large variation in melt rates, it is almost impossible to drill stakes with a sufficiently high density such that this heterogeneity in melt rates is captured. Furthermore, while stake drilling is a labor-intensive and time consuming process, the UAV data acquisition in May and October was carried out in just two half days. Our results show that high-resolution DEM differencing based on UAV imagery provides the equivalent of millions of stakes at a sufficiently high accuracy.

Some important caveats are warranted here, which in fact pertain to all studies where stake readings are compared with a geodetic approach. Geodetic approaches quantify surface elevation changes and the measured signal is a combination of ablation (or accumulation) and surface submergence/emergence. Stakes quantify relative changes in ice thickness from the surface and therefore only ablation (or accumulation is measured). Averaged over the entire glacier the error made in mass balance estimates using the geodetic approach is negligible, but locally it could be significant, in particular for dynamic and fast flowing glaciers. For future applications on dynamic glaciers it would be recommendable to quantify the emergence velocity based on estimates of ice thickness (e.g. derived from ground penetrating radar measurements) and flow velocity and direction.

Our results also show that UAV imagery provides results at a resolution and accuracy that cannot currently be met by satellite derived products. Geodetic methods based on satellite imagery generally cover decadal-scale intervals to be able to distinguish noise from the signal of surface height change. Satellite imagery also does not allow detailed analysis of glacier surface velocity and image availability depends on the satellite overpass compared to the on-demand deployment of the UAV system. For the future, annual campaigns with UAVs on benchmark glaciers could be an important contribution to understanding the impacts of climate change on Himalayan debris-covered glaciers, something which is still very uncertain (Cogley, 2011).

The results show that the average mass loss over the part of the debris-covered tongue that was monitored is limited, mostly due to the thick debris cover that insulates the ice. In addition, the low surface velocity and the separation of the tongue from the accumulation area show that the Lirung Glacier is in a decaying condition. The tongue of the Lirung Glacier is at a low elevation compared to other Himalayan glaciers and it is therefore very sensitive to temperature

increases. It may also serve as an example of the future fate of many debris-covered Himalayan glaciers if global warming persists at the projected rates.

As the ablation of debris-covered glaciers results in increases in debris thickness, the melt rate per unit area will decrease with time. In response, the altitude at which maximum melt occurs will shift upward to the transition zone between tongues and accumulation zones, where debris-free ice is exposed. Future research should focus on this shift and assess the climate sensitivity of glaciers as a function of projected temperature increase, glacier hypsometry and the presence and thickness of debris cover.

With a  $-1.09$  m DEM difference, the overall melt of the monitored area is low, but our results show that there is a high spatial variability in melt and surface dynamics. Areas around ice cliffs and supra-glacial ponds show melt rates which can be up to an order of magnitude higher than the average. Areas of higher melt rates may be connected or created by englacial conduits and voids, which may play an essential role in melt of glaciers characterized by a thick debris cover. To understand the true dynamics of such glaciers UAV data should be combined with energy balance measurements on the lakes and cliffs and ground penetrating radar systems to identify subsurface voids and conduits.

### **Author contributions**

WI, SJ and PK designed the study. WI, PK, JS, MB and SJ performed the UAV surveys. PK processed the UAV imagery and performed the analyses with suggestions by WI and SJ. WI and PK wrote the manuscript with input by JS, AS, FP, MB and SJ.

---

## Seasonal surface velocities

Debris-covered glaciers play an important role in the high-altitude water cycle in the Himalaya, yet their dynamics are poorly understood, which is partly because of the difficult fieldwork conditions. In this study I therefore deploy an unmanned aerial vehicle (UAV) three times (May 2013, October 2013 and May 2014) over the debris-covered Lirung Glacier in Nepal. The acquired data are processed into orthomosaics and elevation models by a structure from motion workflow and seasonal surface velocity is derived using frequency cross-correlation. In order to obtain optimal surface velocity products the effects of different input data and correlator configurations are evaluated, which reveals that the orthomosaic as input paired with moderate correlator settings provides best results. The glacier has considerable spatial and seasonal differences in surface velocity as maximum summer and winter velocities are  $6.0$  and  $2.5 \text{ m a}^{-1}$  respectively at the upper part of the tongue while the lower part is nearly stagnant. It is hypothesized that the higher velocities during summer are caused by basal sliding due to increased lubrication of the bed. I conclude that UAVs have great potential to quantify seasonal and annual variations in flow and can help to further our understanding of debris-covered glaciers.

Chapter based on:

Kraaijenbrink, P. D. A., S. W. Meijer, J. M. Shea, F. Pellicciotti, S. M. D. E. Jong, and W. W. Immerzeel (2016). Seasonal surface velocities of a Himalayan glacier derived by automated correlation of unmanned aerial vehicle imagery. *Annals of Glaciology*, 57(71), 103-113.

## 4.1 Introduction

Himalayan glaciers play a varying, but generally important role in the water supply of many regions in Asia (Immerzeel et al., 2010; Kaser et al., 2010; Lutz et al., 2014). Most glaciers in high mountain Asia are losing mass at rates similar to other regions in the world, except for the Karakoram mountain range where there are indications of positive mass balances (Bolch et al., 2012; Gardelle et al., 2012). In the central Himalaya, for example, negative mass balances of  $-0.26 \pm 0.13$  m w.e.  $a^{-1}$  for the Everest region and of  $-0.32 \pm 0.13$  m w.e.  $a^{-1}$  for West Nepal are reported for the period 1999 to 2011 (Gardelle et al., 2013), whereas for the Langtang catchment in central Nepal a mass balance of  $-0.33 \pm 0.18$  m w.e.  $a^{-1}$  is reported (Pellicciotti et al., 2015). These negative mass balances temporarily result in a higher water availability until the glaciers have receded so far that absolute melt water yield starts to decline (Immerzeel et al., 2013).

Around 10% of Himalayan glacierized area is debris covered (Bolch et al., 2012) and the debris-covered tongues are generally located at the lowest elevation. Most debris-covered tongues exhibit slower rates of retreat than debris-free glaciers, but they thin at substantial rates (Scherler et al., 2011). Theoretically, the debris, when thicker than a few centimetres, should insulate the ice from melt (Østrem, 1959). However, recent work suggests that the debris-covered tongues lose mass at the same rates as debris-free glaciers (Gardelle et al., 2013; Kääb et al., 2012; Pellicciotti et al., 2015). The underlying reason may be the presence of supra-glacial lakes and ice cliffs that accelerate melt significantly (Chapter 3; Benn et al., 2012; Sakai et al., 1998). Little is known, however, about the behaviour and response of debris-covered glaciers as they are generally inaccessible and the spatial and temporal resolution of satellite remote sensing products limits our ability to understand the governing thinning processes.

The flow velocity and the associated mass turnover determine to a large extent the sensitivity of a glacier to climate change. Recent work showed that many of the mountain glaciers are slowing down considerably. Glaciers in the Pamir, for example, decreased their velocity by 43% between 2000 and 2010 (Heid & Kääb, 2012). For the Yala Glacier in the Langtang catchment in Nepal a 70% reduction in flow velocity was reported between 1982 and 2009 (Sugiyama et al., 2013). In contrast, Karakoram glaciers again exhibit anomalous behavior as glaciers there generally have accelerated (Heid & Kääb, 2012). Recent work in the central Himalaya shows great variation in surface velocities. To the north side of the Himalayan arc near Bhutan on the Tibetan plateau flow velocities of  $100\text{--}200$   $ma^{-1}$  are reported, whereas on the south side maximum flow velocities of a few tens of metres are reported (Kääb, 2005). This is confirmed for the south side of the Everest region where flow velocities for debris-covered tongues vary between 0 to  $37$   $ma^{-1}$  (Quincey et al., 2009b). Most of the glacier velocity studies in the Himalaya are based on optical, spaceborne satellite remote sensing and feature tracking. The first automated approach applied to glaciers was published more than two decades ago (Scambos et al., 1992) and over the years the approach has proved very powerful and relatively accurate (Copland et al.,

2009; Quincey et al., 2009a,b; Scherler et al., 2008).

Unmanned aerial vehicles (UAVs) have a large potential in glaciology in particular for debris-covered glaciers as was shown in a recent study for the Lirung Glacier in central Nepal (Chapter 3). The study revealed a highly heterogeneous pattern of mass loss on the debris-covered tongue over a single monsoon season, with a possibly important catalytic role for supra-glacial lakes and ice cliffs. Additionally, the study showed that it is possible to determine the glacier's surface velocity and its general spatial pattern by a manual digitization and interpolation of the displacements found between UAV image pairs. Such a digitization method, however, does not optimally use the full information content present in the UAV data, is subject to human error and is time consuming. To overcome these issues, an automated feature tracking approach can also be applied to the high-resolution UAV imagery. This would result in surface velocity products with a better accuracy and spatial resolution that may achieve a level of detail that is currently unobtainable with spaceborne remote sensing.

In this study I derive surface velocities of Lirung Glacier (Figure 2.4) for both the summer monsoon and the dry winter season by applying frequency cross-correlation algorithms (Leprieux et al., 2007) on UAV-acquired imagery of May 2013, October 2013 and May 2014. Our objectives are two-fold. First I evaluate the effect of two high-resolution image products on the correlation output, i.e. digital elevation models (DEMs) and orthomosaics, and different settings for the cross-correlation algorithm. Based on the best performing configuration I then assess differences between monsoon and winter velocities, and discuss implications for debris-covered glacier dynamics. The two 2013 datasets were already presented by (Chapter 3), but are reanalyzed in this study using the frequency cross-correlation technique to improve the detail of the surface velocity product and to increase its comparability with the 2014 data.

## 4.2 Data and methods

### 4.2.1 UAV surveys

Lirung Glacier was surveyed by UAV three times on 18 May 2013, 22 October 2013 and 01 May 2014. For the first two dates a Swinglet CAM UAV from the company senseFly was used (SenseFly, 2015). In May 2014 an eBee from the same company was used. These particular months were chosen as ideal survey and fieldwork conditions usually prevail, i.e. calm winds, moderate temperatures and little to no precipitation. Also, they are right before and after the monsoon, which is the most dynamic season when synchronous accumulation (at high altitudes) and ablation (on the tongue) processes prevail (Immerzeel et al., 2013). These months in particular are therefore optimal to understand the difference in behaviour of the glacier between the monsoon and the remainder of the year, which is generally colder and drier. The monsoon and dry season covered by the three datasets are from here on referred to as respectively summer (May 2013 – Oct 2013; 157 days) and winter (Oct 2013 – May 2014; 191 days).

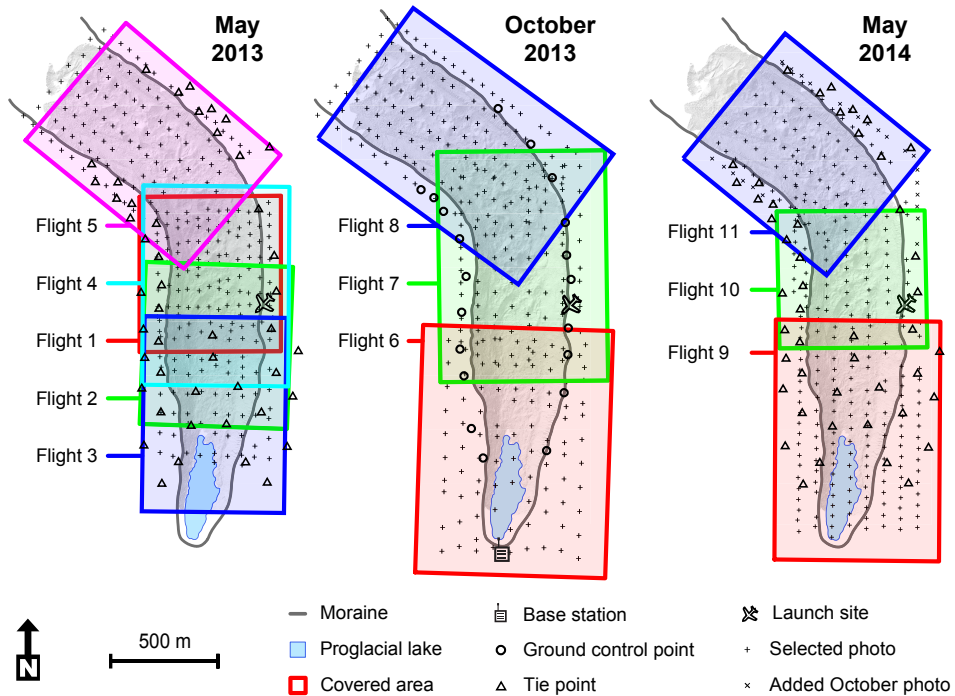


**Figure 4.1:** Overview of the 11 UAV flights among the three survey periods, their approximate ground coverages, positions of the gathered images selected for processing, locations of the ground control points (GCP) and locations of the tie points.

To obtain the required imagery the UAV was deployed over the glacier in 11 separate flights (Figure 4.1) over the course of the three survey dates. A total of 284, 307 and 314 usable JPEG images, respectively, with ground resolutions of 4 to 7 cm and sufficient overlap of about 60% were acquired with a 16 megapixel consumer grade digital camera using a fixed focal length. Images that were either redundant, had too much motion blur or strong rolling shutter distortions were removed from the image set. Although the lossy compression associated with the JPEG format is not ideal for data analysis and consistent results, it is currently a limitation of the UAV system in use.

During the October 2013 field campaign a total of 19 ground control points (GCPs) were collected on Lirung's lateral moraines using differential GPS to georeference the imagery. During the other two campaigns no GCPs were collected of sufficient quality. It was therefore chosen to tie the data together geodetically by sampling 47 tie points from the October 2013 data, which were used as GCPs in the processing of the May 2013 and 2014 datasets similar to the approach taken by (Chapter 3).

#### 4.2.2 UAV data processing

The UAV-acquired images of the three dates were processed using a Structure from Motion (SfM) workflow (Chapter 3; Lucieer et al., 2013; Westoby et al., 2012). In the workflow, feature recognition and matching algorithms together with multi-view stereo techniques (Szeliski, 2011; Westoby et al., 2012) are applied to the overlapping input images to obtain per-image depth maps and camera orientations. This information is used to construct 3D point clouds that can be triangulated and interpolated into gridded digital elevation models (DEMs) and to stitch the input imagery into geometrically corrected image mosaics, so called orthomosaics. By marking the measured GCPs and/or tie points on the input images during the SfM workflow xyz-georeferencing of the output is obtained. In this study I use the SfM workflow as implemented in the software package Agisoft Photoscan Professional version 0.9.1 (Agisoft LLC, 2013).

To obtain optimal results from the SfM workflow in Agisoft each processing step was performed using high quality settings. The 3D point clouds were cleaned in a three-step iterative process by using the point reprojection error. High reprojection errors indicate poor localization accuracy of the corresponding point projections at the point matching step and are also typical for false matches (Agisoft LLC, 2013). Points with a reprojection error larger than 1.5 pixels, i.e.  $\sim 10$  cm for most input images, were therefore removed at each iteration. After removal the point coordinates and camera calibrations were optimized each time by minimizing the sum of the reprojection error (Agisoft LLC, 2013). If camera calibration estimates are inaccurate, the SfM matching algorithms can introduce a doming or bowl effect in the output 3D model. This was counteracted by using the spatially well-distributed GCPs and tie points during the optimizations. The output orthomosaics and DEMs, which have 0.1 m and 0.15 to 0.2 m resolutions respectively, were all resampled to a 0.2 m resolution to reduce the effects of any remaining motion blur as well as JPEG artefacts for further processing.

During the May 2014 field campaign the UAV had difficulty acquiring GPS fixes causing the UAV to skip a number of image captures. Consequently, a handful of tie points could not be placed during the SfM workflow and the quality of the output was reduced considerably. As a solution some off-glacier images of static areas from the October 2013 set (Figure 4.1) were added to the May 2014 image set during processing, which allowed placement of all but two of the tie points.

An indication of the horizontal accuracy of the DEMs and the orthomosaics is obtained by measuring the difference between the GCP or tie point coordinates and their positions on the output orthomosaics. The vertical accuracy is determined by calculating the differences between the GCP or tie point elevations and the output DEMs while correcting for the horizontal error. The number of GCPs collected in October 2013 was limited because of the inaccessible terrain and all points were required for the SfM processing. This led to the absence of redundant GCPs that could be used for independent accuracy checks.

### 4.2.3 Surface velocity determination

#### Cross-correlation feature tracking

COSI-Corr (Co-registration of Optically Sensed Images and Correlation) is a software tool developed to co-register pairs of satellite images, perform orthorectification and also sub-pixel automated image correlation (Ayoub et al., 2009; Leprince et al., 2007). Its correlation algorithms are used for the determination of surface velocity of glaciers, but until now they have only been applied to comparatively much coarser resolution satellite imagery (Herman et al., 2011; Leprince et al., 2008; Scherler et al., 2008). Here, I apply the COSI-Corr's correlation algorithms to the high-resolution UAV data.

The software provides two ways to correlate images, either statistical or frequential. Both act on a moving window level. It is advised to use the frequential correlation method when performing feature tracking on optical images that are relatively noise free and the statistical method when images have considerable amounts of noise or when image pairs have different content, such as when correlating an orthomosaic with an elevation model (Ayoub et al., 2009). As I have relatively noise free data frequency correlation is used. The correlator obtains image-to-image displacements by determining phase differences between Fourier transforms of the moving window of both images. It does this in a two-fold process, first roughly on pixel-level and subsequently on sub-pixel level (Leprince et al., 2007).

#### Multi-scale windows

Lirung Glacier, besides its general ice flow, has considerable temporal surface variations that are unrelated to the flow of the ice but are clearly noticeable on the high-resolution UAV data. Examples are the melt of ice cliffs, tumbling of boulders and the collapse of debris slopes. Ideally these features are not detected by the correlation algorithm as the aim is to extract surface velocities only. It was therefore chosen to use COSI-Corr frequency correlator's multi-scale mode (Ayoub et al., 2009), as it has the potential to filter out these unwanted disturbances.

In the multi-scale mode windows of decreasing sizes are correlated iteratively using a pre-configured initial and final window size. The dominant displacement is first detected by correlation at the initial window scale. Increasingly smaller windows are then used while accounting for the dominant signals that were found. If a correlation at a current iteration deviates too much from the previous one, the iteration is stopped and the previous window's results are used.

The multi-scale mode decreases the amount of irregularly distributed noise in the output (Ayoub et al., 2009), i.e. small displacements present in the images that are unrelated to the dominant signal. The use of larger initial window sizes allows for the reduction of more noise. However, it is a tradeoff as too large initial window sizes may result in loss of detail that is actually relevant. Some of this detail can be retained by using a smaller final window size, but the use of smaller final windows introduces more uniformly distributed noise (Ayoub et al., 2009). A right

balance of the settings with respect to the input data is therefore of key importance to obtain the best results.

### Input and setting assessment

Most studies use optical imagery as input data for automated feature tracking (Copland et al., 2009; Kääh, 2005; Scherler et al., 2008). However, a correlation algorithm has been applied successfully to a UAV-derived hillshade (Lucieer et al., 2013). In order to achieve optimal results I therefore first assess the use of three different input data types: the orthomosaic, a hillshade and the DEM processed by the Sobel edge detection operator (Szeliski, 2011). COSI-Corr requires a single band raster as input and it was chosen to use the orthomosaic's red band as its longer wavelength experiences less influence from atmospheric scattering (Lillesand et al., 2003). The hillshade was created using a solar azimuth of  $120^\circ$  and a zenith angle of  $45^\circ$ . The edge detected DEM is added as it accentuates the outlines of the boulders that are abundantly present on the glacier. It presents a strong contrast that may be picked up by the correlation algorithm. All assessments are performed using the summer dataset only as the expected larger flow velocities in this season will allow for a better evaluation of possible differences in the correlation output. Initial and final window size settings are held equal for each input data type. Their optimal settings are determined by trial and error, keeping in mind the suggestion to work with window sizes that are at least 5 times the expected displacement (Leprince et al., 2007), which is about 3 m (15 pixels) in this case (Chapter 3).

To assess the effects of varying window sizes the frequency correlator is applied to the input dataset with the most satisfying correlation results by testing various combinations of initial and final window size. The start window sizes are varied so that they yield increasing levels of irregularly distributed noise reduction and detail retention with respect to the input data resolution. The final window sizes are always chosen to have a good balance, visually determined, between detail and noise. After the evaluation of the effects of different input data and correlation settings the single optimal configuration found for the summer period is applied to the winter data as well. To be able to compare the surface velocities measured over the summer and winter the values are scaled to year equivalent values ( $\text{m a}^{-1}$ ) throughout this paper.

COSI-Corr analyzes the input data using a moving window that has the preconfigured initial window size. The moving window samples the input data at a configurable spatial interval, called the step size. This step size can be set to be both smaller and larger than the size of the moving window itself. Note that the chosen setting for the step size also predetermines the output pixel size of the velocity field, i.e. input resolution times the step size. For consistency, this parameter is held constant at a value that provides a good output resolution while limiting noise in the output and the processing time required.

## Post-correlation noise reduction

The use of optimal correlator settings will result in a good balance between noise and detail but to a certain extent noise will persist after the cross-correlation procedure. This comprises both Gaussian noise and some remaining non-normally distributed noise. To further improve the final surface velocity products for summer and winter two separate noise reduction methods are applied to the velocity fields. First Gaussian noise is targeted using non-local means filtering (Buades & Coll, 2005) as implemented in COSI-Corr (Ayoub et al., 2009). The algorithm is applied using moderate noise reduction settings that are able to reduce most noise without having too much of a smoothing effect, determined by visual inspection of the output. Patches of irregular noise are subsequently targeted by removing velocity values above a threshold if the focal standard deviation is high. The threshold values for the velocity and the focal standard deviation are determined by trial and error. The noise is replaced by values that are calculated by an ordinary kriging approach (Davis, 2002) applied to the values on the perimeter of the patches.

### 4.2.4 Correlation accuracy

A proper assessment of the accuracy of the frequency cross-correlation algorithms is difficult as there is no quality reference data available. To estimate accuracy I assess whether the algorithm can reproduce surface velocities that are derived by a manual digitization. A comprehensive manual image matching for the summer period is performed by digitizing flow vectors on the image pair visually in a geographical information system. Only surface features are selected for matching that encounter no displacements that are unrelated to the flow of the ice as determined by expert opinion. The differences between the two methods are assessed by plotting the digitized data against the correlation output value for each window setting, which is sampled from COSI-Corr's gridded velocity field output at the coordinates of the digitized vectors' origin. Linear regression models are fitted to the data to quantify the velocity differences.

To get another measure of the possible errors involved horizontal displacements found by the correlator for a static off-glacier area of  $0.18 \text{ km}^2$  are evaluated and compared with the errors of the SfM output. Signal-to-noise ratios (SNRs) that are provided by COSI-Corr (Leprince et al., 2007) are evaluated for the three different window settings as another indicator of the quality of the frequency cross-correlation.

## 4.3 Results and discussion

### 4.3.1 UAV product accuracy

The horizontal errors of the UAV products obtained by SfM processing are shown in panel A of Figure 4.2. It shows the differences that are found between the GCP or tie point coordinates and

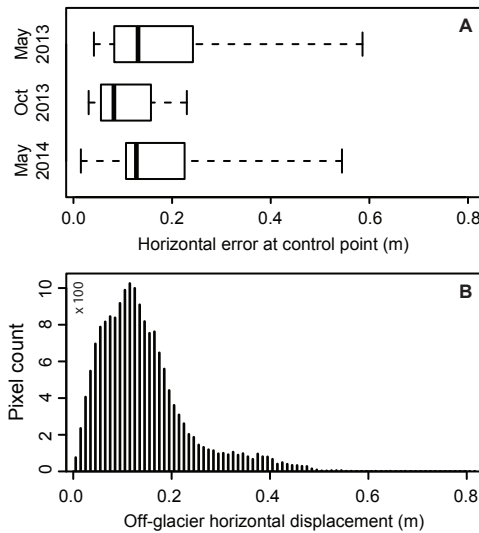


**Figure 4.2:** Boxplots of the horizontal errors between GCP (October 2013) and tie point (May 2013 and 2014) coordinates and their positions on the orthomosaics (panel A). Histogram of displacements at static off-glacier areas ( $0.18 \text{ km}^2$ ) as calculated by frequency cross-correlation using W256 F64 (panel B).

their positions on the output orthomosaics for the three periods. Only the errors found for the May datasets are reflected in the accuracy of the derived surface velocities as they are directly georeferenced to the October 2013 dataset using the tie points. The accuracy of the surface velocity products is not affected by the true geodetic accuracy of the data, which is indicated by the GCP errors for October 2013. The errors found for both May datasets have a similar distribution and range. About 75% of the tie points are located on the orthomosaic within 0.2 m of their original position with only few outliers that go up to 0.6 m. Errors found further away from the tie points on the off-glacier moraine area and on the glacier surface itself are assumed to be similar due to the high density of tie points used. The bulk of the vertical errors at the tie points is within 0.5 m and 75% is even within  $\sim 0.25$  m. The vertical errors, however, do not contribute considerably to the accuracy of the surface velocity product determined by feature tracking as they have little to no influence on the orthomosaic, hillshade and edge detected DEM.

#### 4.3.2 Correlation assessment

##### Optical vs DEM derivatives

COSI-Corr's frequency correlator is applied to the UAV-derived orthomosaic, hillshade and edge detected DEM using an initial window size of 128 pixels (px) and a final window size of 64 px (coded as W128 F64). It was found that a step size of 16 px provides a good balance between output detail, noise and processing times while working with the 0.2 m resampled

input data. Note that the output resolution of COSI-Corr's velocity field is consequently 3.2 m. The resulting surface velocities are shown in Figure 4.3. The vectors plotted on the map denote the detected flow direction. Vectors that have a magnitude of less than the maximum horizontal error of  $\sim 0.6$  m (Figure 4.2), i.e.  $0.5 \text{ m a}^{-1}$ , are left out.

The general pattern of flow velocity and direction that is detected by the correlation algorithm is similar for each type of input data. A noticeable difference, on the other hand, is that irregularly distributed noise is very abundant in the correlated hillshade and edge detected DEM while the orthomosaic reveals this type of noise almost exclusively at and around the ice cliffs. This higher noise abundance is possibly because the hillshade and edge detected data both contain similar recurring patterns of crests and edges that result in mismatches of the correlator. The edge detected DEM, while showing slightly less irregular noise than the hillshade, does experience more erratic variation in flow directions. This is likely because the edge detection filter also enhances the pattern of tiny edges that results from triangulation of the point cloud, which spatially varies independently from image to image. Also, the very strong contrast and lack of clear gradients may play a role.

The noise near the ice cliffs in the correlated orthomosaic arises because the cliffs on Lirung Glacier are generally larger (Chapter 3) than the initial window size of 128 px, which equates to 25.6 m in case of the 0.2 m resampled input data. As a result, the melt of the ice cliff will be the local dominant signal picked up by the moving window. In terms of noise filtering the opposite of the desired filter effect now occurs, as the cliff-unrelated displacement is filtered locally, e.g. the flow. Additionally, other mismatches might be introduced near the ice cliffs as they are not merely displaced features, but represent an actual change in their appearance and shape due to melt (Chapter 3). Most other displacements that are unrelated to flow have been filtered out at W128 F64, except some slope anomalies on the lateral moraine walls.

### Window size assessment

The results show that use of the orthomosaic as input to the frequency correlator yields the best, noise free output to be used for determination of the surface velocities. I therefore assess the effects of varying the window sizes by using this input data type.

As ice cliff related noise persists at a window size setting of W128 F64, it is chosen to assess changes in noise level and detail retention by using two larger initial windows, i.e. W256 F64 and W512 F128 (Figure 4.4). To limit the amount of uniformly distributed noise in the output a final window size of 128 px was chosen for the correlation with the initial window size of 512 px.

The pixel values for the surface velocity are very similar between the three settings. Excluding noise and outliers that are larger than  $6 \text{ m a}^{-1}$ , the averages found over the entire area for the different window settings (small to large) are 1.62, 1.59 and  $1.57 \text{ m a}^{-1}$ . Furthermore, 90% of the pixel-by-pixel differences between W512 F128 and W128 F64 are within  $-0.56$  and  $0.29 \text{ m a}^{-1}$

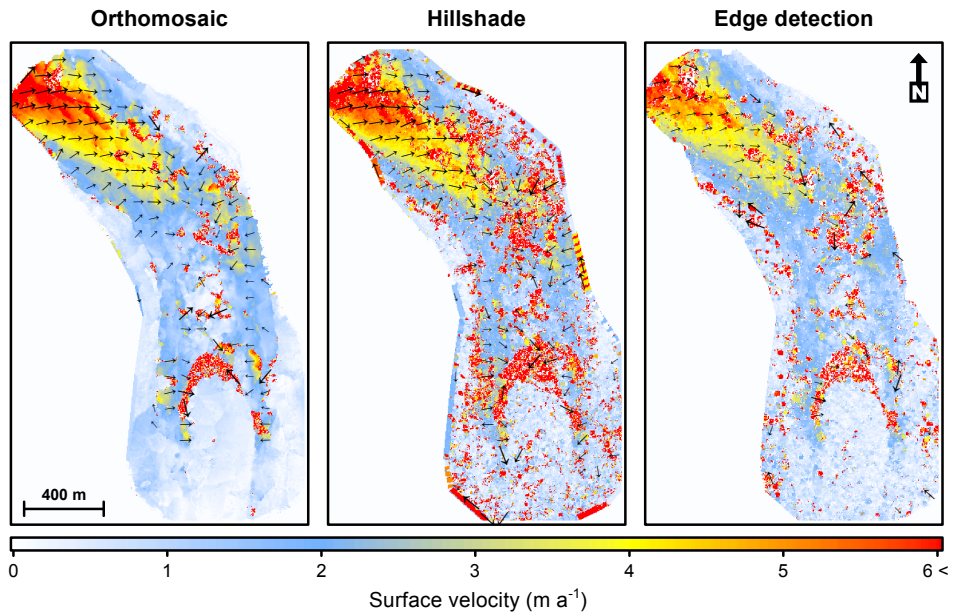


**Figure 4.3:** Surface velocity results obtained by frequency cross-correlation of three different input data types for the summer period: the orthomosaic, hillshade and edged-detected DEM. Every input image product consisted of a 0.2 m resampled raster and was processed using an initial window size of 128 px and a final window size of 64 px. Note that the vectors are not linearly scaled and that vectors with a magnitude of less than  $1.4 \text{ m a}^{-1}$  are not displayed.

and 75% are even within  $-8.78 \times 10^{-2} \text{ ma}^{-1}$  and  $6.59 \times 10^{-3} \text{ ma}^{-1}$ . In terms of SNR, larger window sizes yield more pixels that are reported to have little to no correlation. The percentage of pixels reported to have a SNR of less than 0.75, i.e. little correlation quality, are 7.09, 11.15 and 13.80% (small to large windows).

As shown, larger initial window sizes are capable of reducing most cliff-related noise present in the output. On the other hand, they introduce sharper, unrealistic boundaries between areas with contrasting velocities. Additionally, much of the finer spatial variability that is present in the W128 F64 results is lost at W512 F128. To balance noise levels, artefact presence and measured correlation performance the results from W256 F64 are chosen as optimal configuration.

To further improve the W256 F64 output moderate non-local means filtering is effective regarding Gaussian noise. Almost all noise is removed while the detail is largely retained. Replacement of correlated velocities with interpolated values proves to be effective in removing any remaining patches of irregular noise near the ice cliffs and terminus (Figure 4.6). For the summer dataset, the use of a threshold of  $7.5 \text{ ma}^{-1}$  on the velocity values if the focal standard deviation of a  $9 \times 9 \text{ px}$  window is larger than the 95<sup>th</sup> percentile of all focal standard deviations shows good results. A threshold of  $5.0 \text{ ma}^{-1}$  while using the same settings for the focal standard deviation suffices for the winter velocity product.

Panel B in Figure 4.2 shows a histogram of the displacements over a static off-glacier area of  $0.18 \text{ km}^2$  as calculated by COSI-Corr using W256 F64. The off-glacier displacements have a mean of 0.14 m and 95% of the values is below 0.34 m, which are acceptable errors. Note that the errors of the SfM output (panel A) are, besides the cross-correlation error, also reflected by these displacements and that the actual frequency cross-correlation output errors thus are likely smaller than the values shown in the histogram.

### Digitized vs correlated flow

To evaluate and compare the results of the summer correlation output a visual interpretation and manual digitization were performed on the summer image pair by manually digitizing 459 vectors in a geographical information system. Note that this was performed on the original orthomosaic of 0.1 m resolution. A higher sampling density at areas with higher surface velocities was used to obtain more detail there, but generally the measurements are well distributed over the glacier's surface. Figure 4.5 shows a scatter plot of the correlation output for the three different windows sizes against the manually digitized flow as well as the spatial distribution of the point measurements. Extreme and unrealistic outliers that are due to noise in the correlation output are removed from the scatter plot, i.e. values above  $8 \text{ ma}^{-1}$  ( $n = 6$ ). The results of linear regression models that were fitted to the filtered results are shown in the inset table.

Reproduction of the manually digitized flow by the frequency correlator is very good and the overall flow pattern found is similar. Points scatter close to the 1:1 line with  $R^2$  values of 0.83 to 0.90 and with relatively small root mean square errors of  $\sim 0.6 \text{ ma}^{-1}$  over the observed

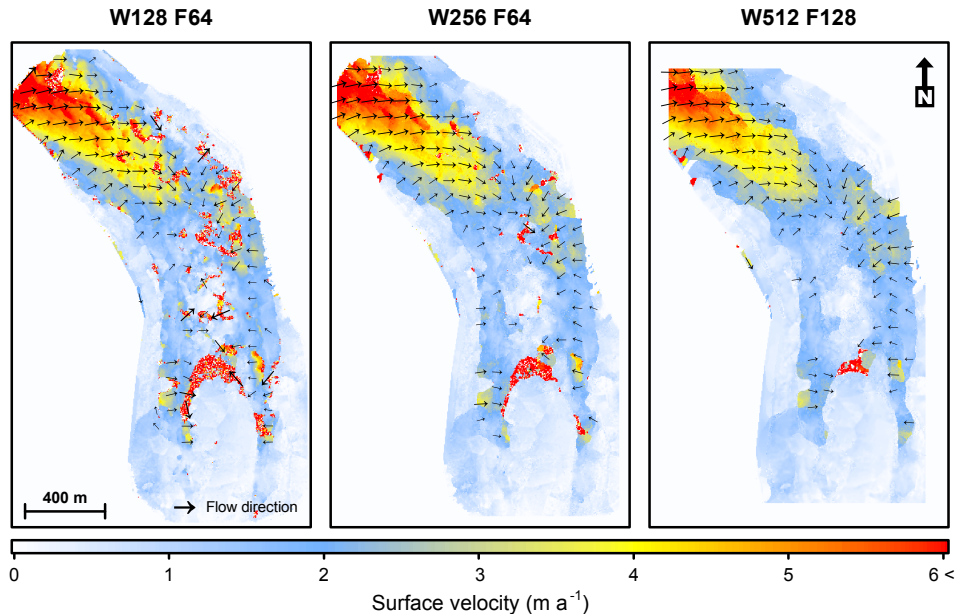


**Figure 4.4:** Summer period frequency cross-correlation results for three different window sizes settings applied to the 0.2 m resampled orthomosaic. The initial and final window sizes that were used in each case are denoted by W and F respectively. Note that the vectors are not linearly scaled and that vectors with a magnitude of less than  $1.4 \text{ m a}^{-1}$  are not displayed.

period. Mean velocity errors between the two methods are in the order of 0.10 to 0.15 m. The slopes of the fitted model indicate a slight underestimation of surface velocity by the correlator as compared to the manual digitization. The cause for this is unclear and it is so far not possible to attribute this specifically to one of the methods.

The flow directions that follow from correlation and digitization have, similarly to the velocities, the same overall trend and only slight differences between the two methods are found locally. Compared to W256 F64, half of the digitized vectors have differences in bearing of less than  $8.0^\circ$  and 75% are within  $19.6^\circ$ .

Note that small differences in velocity and direction are expected here for two main reasons. Firstly, the digitized surface velocities at a point scale are compared with those that are measured for blocks of 16 px by a correlator that bases itself on windows of 128, 256 and 512 px. Secondly, manual digitization is not always completely accurate. Differences in lighting conditions can cause the small surface features on the glacier used for digitization to appear quite differently from image to image. It is estimated that the visual pixel matching errors may be as large as 2–4 px on the 0.1 m resolution orthomosaic. This equals to about 0.2–0.4 m over the summer period, i.e.  $0.46\text{--}0.93 \text{ m a}^{-1}$ .

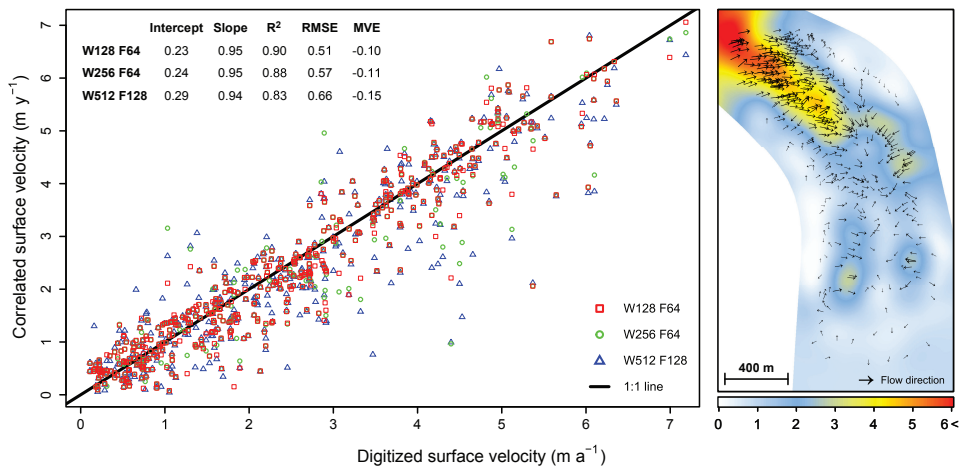


**Figure 4.5:** Manually digitized surface velocity measurements ( $n = 453$ ) plotted against the three different frequency cross-correlation outputs for the summer period (left) and the locations of the measurements plotted over an interpolated surface obtained by ordinary kriging (right). The results of fitted linear models and mean velocity errors (MVE) are shown in the inset table.

### 4.3.3 Seasonal surface velocities

Our finding of different flow velocities in summer and winter is notable, as velocity measurements on debris-covered glaciers are rare (Quincey et al., 2009a). While it is possible that short-term and unmeasured variations in velocity may contribute to the overall differences, the seasonal patterns point towards differences in flow regimes. During the summer period surface velocities of Lirung Glacier range from completely stagnant at the lower (southern) sections of the terminus to  $\sim 6 \text{ m a}^{-1}$  at the upper (northernmost) surveyed area (Figure 4.6). Surface velocities decrease gradually down-glacier to about  $2 \text{ m a}^{-1}$  at the junction between south-eastward and southward flow vectors. Due to this velocity gradient, longitudinal ice compression and a related emergence velocity are expected to occur here, which coincides with the reported elevation gain of  $+0.5 \text{ m}$  over the summer (Chapter 3). Although the south-eastward flow in summer in the upper regions of the surveyed area is also reported by Naito et al. (1998), it is slightly unexpected given the direction of the glacier and the differences with winter flow direction in the same area. It may partly be caused by small horizontal deformations of the photogrammetric model and/or a disturbance of the signal by moving moraine material. I find summer velocities for the Lirung Glacier that are considerably lower than those reported by Naito et al. (1998). They state the glacier had moved between 2.8 and 7.5 m ( $\approx 6.5$  and  $18.0 \text{ m a}^{-1}$ ) in the middle part and between 1.9 and 2.5 m ( $\approx 4.5$  and  $6.0 \text{ m a}^{-1}$ ) in the lower area over the period June–October in the years 1994–1996. In two decades the glacier thus seems to have reduced its flow velocity by about a factor of two, though short-term velocity variations could contribute to this difference.

As opposed to the summer, the winter period shows a considerably different picture. Here, the

high velocities for the upper area are absent and have reduced to about 2 to 3  $\text{m a}^{-1}$ . Velocities on the lower (southward-flowing) portion of the terminus are similar to those found in the summer period. Combining and rescaling the summer and winter velocities, respectively valid for 157 and 191 days, to full year values the upper portion of the surveyed area has velocities of approximately 3.5  $\text{m a}^{-1}$  and velocities at the transition zone between upper and lower regions are approximately 1.5  $\text{m a}^{-1}$ .

The distinct contrasts between (a) the surface velocities for the upper and lower portions of the terminus in the summer and (b) summer and winter velocity fields indicate the presence of two different dominant flow regimes (Copland et al., 2009). I hypothesize that the faster flow in summer is caused by basal sliding dominated processes while the lower velocities found in winter and at the lower portions are mainly due to deformation. The large amounts of monsoon precipitation and the opening of sub- and englacial conduits due to rising temperatures (Benn et al., 2012) are likely to lubricate the base of the ice and introduce a basal sliding component to the flow in the summer season. In areas where basal sliding dominates, the ice is expected to move in a block-like motion with relatively high and constant velocities in the center and sharp lateral velocity gradients (Copland et al., 2009). Transverse velocity profiles over the glacier (Figure 4.6) show that there indeed is a difference between the summer and winter flow in terms of lateral gradients. Especially near the northeastern ice boundary, the summer velocity profile is reduced by 3  $\text{m a}^{-1}$  over a few tens of metres (profile A and B). The lateral winter velocity variation generally shows a more parabolic pattern, as does the summer velocity at profile C. This is usually associated with more deformation-dominated flow (Copland et al., 2009). Why the basal sliding occurs only at the upstream area is not entirely clear, but it likely results from increased driving stresses caused by thicker ice that is due to the regular avalanches and rockfall from the steep slopes of the Langtang Lirung Peak to the northwest. This difference in ice thickness may also play a role in the contrasting velocities found laterally, i.e. fast flow at the western ice boundary and limited flow on the other side of the tongue.

Glacier ice flow is a complex process and is governed by a wide range of processes and forces (van der Veen, 2013). Nevertheless, an improved understanding of the ice thickness of Lirung Glacier and the local bedrock configuration underneath the ice will greatly contribute to a better understanding of the flow patterns found in this study. Furthermore, it would provide the ability to estimate mass turnover rates that are related to the flow velocities found. Ice thickness measurements of the glacier were performed one and a half decade ago using radio echo-sounding techniques (Gades et al., 2000), but the quality, resolution, specific locations and time period of the measurements make them not particularly usable in this case. A new survey of Lirung Glacier using ground penetrating radar would help to fill some of the gaps raised by this study.

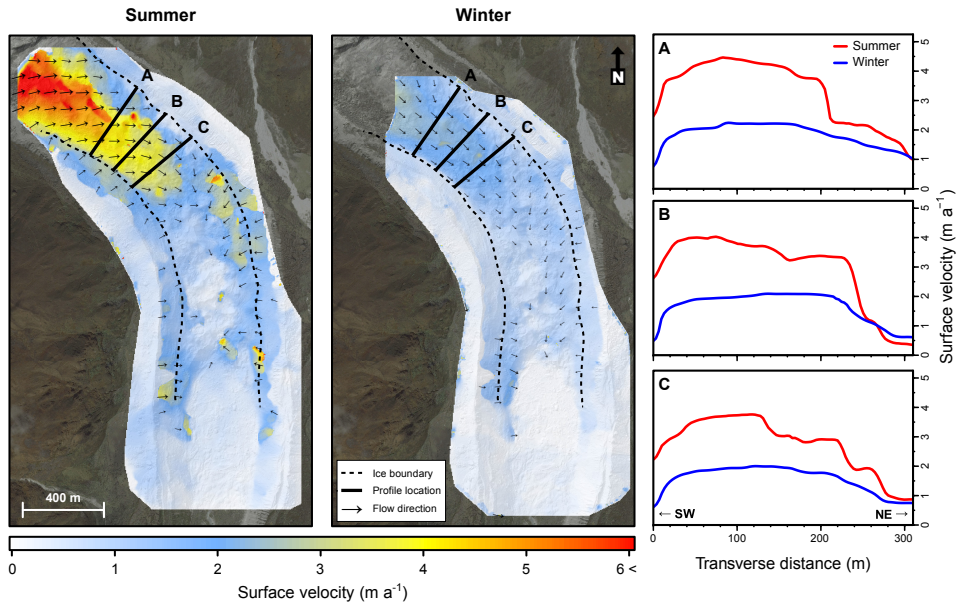


**Figure 4.6:** Surface velocity and flow direction obtained by noise-filtered frequency cross-correlation (W256 F64) for the summer (left) and winter (middle) period. The plots on the right show transverse surface velocity profiles for both seasons taken at the three indicated locations.

#### 4.3.4 Value of UAV surveys

As the typical pixel size of spaceborne imagery that is suitable for glacier velocity monitoring is often considerably larger than the seasonal or even annual displacements of Himalayan debris-covered glaciers, data that span multiple years are generally required to extract meaningful velocity signals (Herman et al., 2011; Käab, 2005; Scherler et al., 2008). This renders the quantification of seasonal variations in surface height change and velocities very difficult. Of course, this is even more so an issue when flow velocities are relatively low, such as for many debris-covered glaciers in the Himalaya (Quincey et al., 2009b). Although a high temporal resolution can be achieved using in situ methods, they are unfeasible for high spatial resolution surveys of large glacier surfaces as fieldwork on debris-covered glaciers is often difficult and time consuming.

The use of UAVs allows high-resolution continuous surfaces of the surface velocities of a single season to be obtained. The techniques used here would also allow for large scale determination of interannual flow. This will improve our understanding of the relations with local precipitation and temperature perturbations, which will eventually lead to the ability to provide better predictions of possible future changes in glacier volume under climate change scenarios. A deepened knowledge of the smaller scale variations in flow, both spatially and temporally, also helps to unravel the bigger picture of heterogeneous mass wasting and distribution of surface features found on debris-covered glaciers (Chapter 3).

## 4.4 Conclusions

In this study UAVs are used to acquire images of the debris-covered Lirung Glacier for May and October 2013, and May 2014. The imagery is processed into orthomosaics and digital elevation models using a structure from motion workflow and georeferenced using GCPs and tie points. Displacements of the glacier surface are derived for both summer and winter using an automated frequency cross-correlation algorithm, which is tested for sensitivity to input datasets and parameters. From the study I draw the following conclusions.

Summer and winter surface velocities for Lirung Glacier are in the order of respectively 6.0 and  $2.5 \text{ m a}^{-1}$  at the upstream part of the tongue. In the bend and at the lower areas of the tongue both seasons show comparable slow flows of about  $1.5$  to  $2.0 \text{ m a}^{-1}$  and stagnancy. The differences in surface velocity and flow direction between the two seasons leads to the hypothesis that the fast flow in summer is caused by basal sliding dominated processes while the lower velocities found in winter are mainly due to plastic deformation. Transverse velocity profiles over the glacier seem to confirm this hypothesis. For an improved understanding of the spatial surface velocity differences and flow patterns of Lirung Glacier found in this study it is important learn more about its ice thickness and bedrock configuration.

The use of frequency cross-correlation techniques applied to high-resolution UAV imagery is suitable to determine surface velocities of a debris-covered glacier. Displacements unrelated to ice flow can largely be filtered out by the correlation method and any remaining noise can be removed using post-correlation noise reduction techniques. In comparison to a manual digitization technique both methods have similar accuracies taking into account the associated errors. The continuous surface output that the correlator yields provides more detail, however, and the method is less time-consuming.

It is found that using an orthomosaic as input for the correlation outperforms the use of a hillshade or an edge detected DEM in terms of irregularly distributed output noise. The use of different settings for the correlation algorithm does not alter surface velocities and flow directions significantly. There are, however, subtle differences present and small window sizes give better performance in terms of SNR, the retention of detail and the overall results in comparison with manual digitization. However, displacements such as the melt of ice cliffs are not filtered out; this requires the use of larger correlator windows which can result in loss of fine-scale detail. Optimal settings for the input resolution are found to be an initial window size of 256 px with a final window size of 64 px.

The use of UAV imagery and feature tracking algorithms allows determination of high-resolution seasonal surface velocities, something not possible with most spaceborne remote sensing techniques. Our approach yields insights into the smaller scale temporal and spatial variations in glacier flow, and improves our understanding of heterogeneous mass wasting and surface features found on debris-covered glaciers.

**Author contributions**

PK, WI, and SJ designed the study. PK, WI, JS and SJ performed the data collection. SM performed the feature tracking analysis. PK processed UAV imagery, refined the feature tracking analysis and performed the other analyses. PK wrote the manuscript with suggestions by JS, FP, SJ and WI.

---

## Mapping surface temperatures

A layer of debris often accumulates across the surface of glaciers in active mountain ranges with exceptionally steep terrain, such as the Andes, Himalaya and New Zealand Alps. Such a supraglacial debris layer has a major influence on a glacier's surface energy budget, enhancing radiation absorption and melt when the layer is thin, but insulating the ice when thicker than a few cm. Information on spatially distributed debris surface temperature has the potential to provide insight into the properties of the debris, its effects on the ice below and its influence on the near-surface boundary layer. Here, we deploy an unmanned aerial vehicle (UAV) equipped with a thermal infrared sensor on three separate missions over one day to map changing surface temperatures across the debris-covered Lirung Glacier in the Central Himalaya. We present a methodology to georeference and process the acquired thermal imagery, and correct for emissivity and sensor bias. Derived UAV surface temperatures are compared with distributed simultaneous *in situ* temperature measurements as well as with Landsat 8 thermal satellite imagery. Results show that the UAV-derived surface temperatures vary greatly both spatially and temporally, with  $-1.4 \pm 1.8$ ,  $11.0 \pm 5.2$  and  $15.3 \pm 4.7^\circ\text{C}$  for the three flights (mean  $\pm$  sd), respectively. The range in surface temperatures over the glacier during the morning is very large with almost  $50^\circ\text{C}$ . Ground-based measurements are generally in agreement with the UAV imagery, but considerable deviations are present that are likely due to differences in measurement technique and approach, and validation is difficult as a result. The difference in spatial and temporal variability captured by the UAV as compared with much coarser satellite imagery is striking and it shows that satellite derived temperature maps should be interpreted with care. We conclude that UAVs provide a suitable means to acquire surface temperature maps of debris-covered glacier surfaces at high spatial and temporal resolution, but that there are caveats with regard to absolute temperature measurement.

Chapter based on:

Kraaijenbrink, P. D. A., J. M. Shea, M. Litt, J. F. Steiner, D. Treichler, I. Koch, and W. W. Immerzeel (2018). **Mapping surface temperatures on a debris-covered glacier with an unmanned aerial vehicle.** *Frontiers in Earth Science*, 6(64), 1-19.

## 5.1 Introduction

Around 10% of the total glacierized area in High Mountain Asia (Gardelle et al., 2013; Scherler et al., 2011) is covered by a debris layer, but in terms of mass, a substantially larger amount of ice is affected by debris. Especially in regions with many large debris-covered glacier tongues, such as the Karakoram and Himalaya, the proportion of glacier ice mass that is covered by debris in the ablation zone reaches ~40%. Consequently, future changes in water resources for heavily glacierized catchments in the region partly depend on the long-term melt rates of debris-covered glaciers (Chapter 7).

Ice melt rate beneath a layer of supraglacial debris is a function of debris thickness (Mattson et al., 1993; Nicholson & Benn, 2006; Østrem, 1959), with melt enhancement under thin ( $\lesssim 5$  cm) debris layers, and melt reduction under thicker layers ( $\gtrsim 5$  cm). Debris is generally thin at higher elevations and thickens down-glacier due to various processes, e.g. rockfall, (re)surfacing of englacial debris and erosion of lateral moraine material (Evatt et al., 2015). In practice, however, debris thickness and ice melt rates can be quite variable on small scales (Rounce & McKinney, 2014), resulting in heterogeneous thinning and the hummocky surface that is often observed on debris-covered glaciers. Supraglacial ponds and ice cliffs, which are typical surface features for this type of glacier, as well as supra- and englacial drainage also contribute to (spatially variable) surface lowering (Chapter 3; Buri et al., 2016b; Miles et al., 2016; Sakai et al., 2000).

Surface temperatures derived from satellite-based thermal infrared (TIR) measurements have been previously used to infer debris thickness by temperature inversion methods (Chapter 7; Foster et al., 2012; Mihalcea et al., 2008b; Rounce & McKinney, 2014; Schauwecker et al., 2015). Higher surface temperatures are assumed to correspond to thicker debris layers, as the insulating effect of the debris shields the debris surface from the cold ice. However, the accuracy of satellite-based surface temperature measurements has not been examined in detail for high-altitude glacierized regions. Furthermore, the use of a single thermal image to constrain debris thicknesses may result in significant errors as surface temperatures can evolve rapidly under changing solar radiation, solar azimuth angle, and weather conditions.

Unmanned aerial vehicles (UAVs) offer the opportunity to measure surfaces of debris-covered glaciers in high spatial and temporal resolution and this has been explored in recent years (e.g. Chapter 3; Chapter 4; Chapter 6; Westoby et al., 2012). Ground-based thermal infrared mapping of debris-covered glaciers has already been demonstrated (Aubry-Wake et al., 2015, 2017), but the recent advances in UAV-mounted thermal cameras have not yet been explored for this type of glacier.

The primary objectives of this research are to demonstrate UAV thermal mapping techniques for the debris-covered glacier surfaces, and to pave the way for applied studies on the surface properties and processes of debris-covered glaciers. Using Lirung Glacier (Figure 2.4) as case study area, I outline a methodology to generate surface temperature maps using optical and

thermal imagery, compare UAV measured temperatures against bias-corrected *in situ* surface temperature measurements, and quantify spatial and temporal variability in observed surface temperatures from both UAV and satellite-based thermal imagery.

## 5.2 Data and methods

### 5.2.1 Temperature measurements

Two main definitions of the temperature of a body can be distinguished (Becker & Li, 1995), which are both measured differently. First, there is the thermodynamic temperature of a body in thermal equilibrium, which can be measured by a thermometer for a given position in space. Second, there is radiometric temperature, which corresponds to the radiance emitted by a surface and is also referred to as skin temperature. It can be measured by a radiometer from a distance given that the emissivity of the body is known. In the case of homogeneous, isothermal bodies, the two temperatures agree. However, the situation is more complex for land surfaces with small-scale roughness and a composition of various materials, such as moist gravel, or sparse grass cover with exposed soil (Minnis & Khaiyer, 2000). This is particularly true under incoming solar radiation during daytime, which heats up the surface (skin) of a body and creates temperature gradients both within the body and at the body-air interface.

A temperature sensor placed on a surface will measure the micro climate surrounding the sensor, whereas a radiometer will measure the temperature emitted by the skin of the body (radiant temperature). Consequently, the two temperature measurements correspond best for shaded surfaces or liquids with a submersed thermometer. Measurements may differ for thermometers placed on sunlit surfaces or within a body with inhomogeneous temperatures (e.g. sand during day time), and for radiometric temperatures if the atmosphere between the radiometer and the radiance-emitting surface has a different temperature than the surface.

### 5.2.2 Outline of methodology

To produce and evaluate the UAV-derived surface temperature maps of the debris-covered Lirung Glacier five main steps were performed:

1. On 30 April 2016, a UAV survey of the glacier was performed in which I collected optical imagery. On 1 May 2016, thermal data was collected on three separate UAV surveys over the course of the morning. The acquired imagery of both sensors were processed into orthomosaics.
2. A correction for emissivity was applied to orthomosaics of radiant temperature to obtain actual skin temperatures of the debris. For this, a spatially distributed emissivity map was produced using object-based image classification of the optical data.

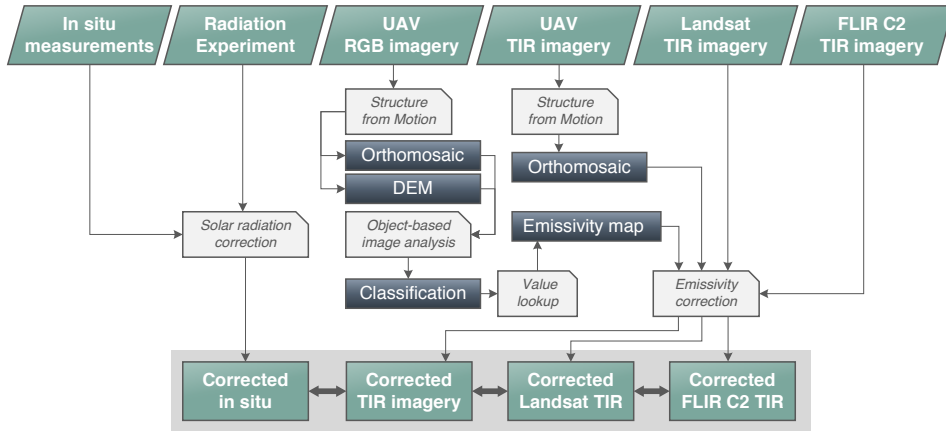


**Figure 5.1:** Flowchart that shows the steps used to process the spaceborne, airborne and ground-based data into corrected output products.

3. UAV-measured skin temperatures were evaluated against (1) *in situ* temperature measurements taken at the time of the survey using a set of distributed temperature sensors (Tidbit T-loggers), and (2) skin temperatures obtained with a hand-held thermal camera for a single location on the glacier. Biases in the Tidbit T-logger measurements caused by the micro climate from direct shortwave radiation on the sensors were determined in an experimental setup and corrected.
4. The UAV temperature product and emissivity-corrected Landsat 8 data from comparable conditions were compared to determine differences between UAV and satellite approaches for obtaining surface temperature.
5. A statistical analysis was performed to assess the influence of solar insolation and local topography on the warming of the glacier surface, and to determine which part of the variability in the surface warming rate can be explained by other debris properties and surface processes.

In the following sections the details of each step are given. A flowchart that outlines our methodology is provided in Figure 5.1.

### 5.2.3 Meteorology

Meteorological data from the Kyangjin automatic weather station (AWS), which is located 2.5 km south of Lirung Glacier at 3862 m.a.s.l (meter above sea level)(Figure 5.2), shows typical conditions for the time of the year for each of the surveys (Figure 5.3). Air temperature ranges from close to freezing at night to about 10 °C in the afternoon. After sunrise, temperatures rise very quickly because of the high incoming solar radiation found at this high elevation and sub-tropical latitude. The radiation data shows there were no clouds in the morning and

that winds picked up around noon (Figure 5.3), which are both characteristic for the site. For the entire survey period there was no precipitation observed.

#### 5.2.4 UAV surface temperature

##### Optical survey

On 30 April 2016 an approximately 2 km<sup>2</sup> portion of the tongue of Lirung Glacier (Figure 5.2) was surveyed using a fixed-wing eBee from UAV manufacturer SenseFly. The UAV was launched from a point along the eastern moraine and was set to land in a meadow below. The eBee was equipped with a Sony WX RGB (i.e. red-green-blue) compact camera with an 18.2 megapixel sensor. The camera's shutter was electronically triggered by the UAV autopilot along a predefined flightpath. Zoom, exposure and other camera settings were all controlled by the flight management software provided with the eBee, i.e. eMotion2 (SenseFly, 2017a). Two separate flights during clear skies and light winds were required to cover the entire survey area (Table 5.1). The UAV was set to adapt its flight altitude to the (general) topography and capture 6 cm resolution imagery, which roughly equates to a flight altitude of 210 m above the surface. Image overlap was set to 60% laterally and 70% longitudinally with respect to the flight direction. A total of 237 RGB images were captured by the camera. Flight paths and image locations of the two flights are provided as supplementary data.

##### Thermal infrared survey

A ~0.4 km<sup>2</sup> portion of the debris-covered tongue of Lirung Glacier (Figure 5.2) was monitored using the eBee mounted with a thermoMAP thermal infrared camera (SenseFly, 2017b). The uncooled microbolometer sensor of the thermoMAP has a relatively high resolution of 640×512 pixels and can measure surface temperatures between -40 and 160 °C. Temperature resolution of the sensor is 0.1 °C and it performs automatic temperature calibration in flight based on the sensor's internal temperature. The thermoMAP assumes an emissivity of the surveyed surface of 1, and thus captures images of radiant temperatures only. The peak spectral response of the sensor lies at 10 μm, with a full width half maximum of approximately 5 μm (8.5–13.5 μm) (SenseFly, 2017b). The camera stores its imagery in uncompressed TIFF. I surveyed a considerably smaller area than for the optical flights because the higher energy consumption of the sensor. Moreover, on the contrary to optical UAV surveys, multi-flight surveys of the glacier are infeasible with a thermal camera due to rapidly changing surface temperature conditions between flights. Off- and on-glacier terrain could not be surveyed synchronously because of the low flight altitude that is required for proper functioning of the thermoMAP (<120 m from the surface) and the high lateral moraines of the glacier (up to 100 m).

The UAV was deployed over the survey area four times over the course of the morning on 1 May 2016 (Table 5.1) to acquire a spatio-temporal signature of the surface temperature. A first

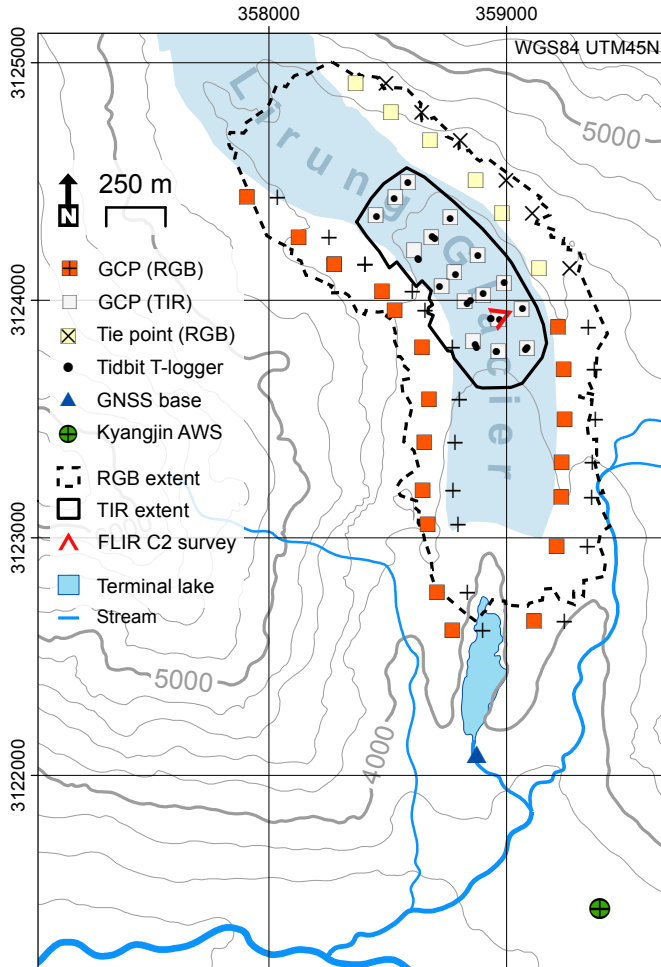


**Figure 5.2:** Map of Lirung Glacier with the locations of all ground control points (GCPs), tie points, Tidbit temperature loggers, the automatic weather station (AWS), the FLIR C2 survey, and the coverage of both the optical (RGB) and thermal infrared (TIR) surveys.

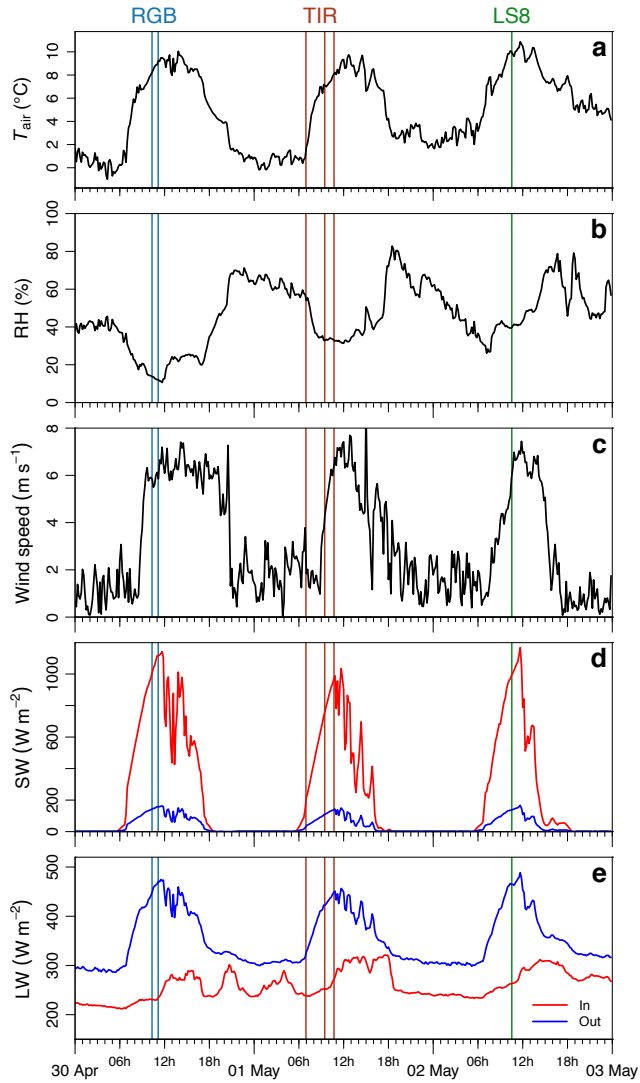


**Figure 5.3:** Meteorological data from the Kyangjin automatic weather station (Figure 5.2) for 30 April to 2 May 2016. Panels a-e show the air temperature, relative humidity, wind speed, shortwave radiation and longwave radiation, respectively. The vertical lines indicate the times of the RGB and TIR surveys performed with the UAV, and the time of the Landsat 8 overpass (Table 5.1).

**Table 5.1:** Details of the optical and thermal UAV surveys, as well as the Landsat 8 thermal scene.

Date and time	Weather	Sensor	Duration	Altitude (m)	Images	Resolution
30-04-2016 10:10	Clear, light winds	Sony WX RGB	00:18	210	134	0.06 m
30-04-2016 11:00	Clear, light winds	Sony WX RGB	00:17	210	103	0.06 m
01-05-2016 06:15	Slight haze, calm winds	thermoMAP	00:08	95	Failed flight	-
01-05-2016 06:45	Slight haze, calm winds	thermoMAP	00:23	95	2127	0.18 m
01-05-2016 09:20	Slight haze, light winds	thermoMAP	00:15	95	2009	0.18 m
01-05-2016 10:35	Shade, slight haze, medium winds	thermoMAP	00:15	95	2040	0.18 m
02-05-2016 10:32	Moderate haze, calm winds	Landsat 8 TIRS	-	-	-	100 m

flight was performed early morning before sunrise at 6:15, but the UAV lost radio contact and returned without usable imagery. Subsequent successful flights of approximately 15 minutes each were performed at 6:45, 9:20 and 10:35, which together collected 6176 highly-overlapping thermal images. These flights will be referred to as Flight 1–3 hereafter. During Flight 1 there was little to no incoming shortwave radiation (Figure 5.3), and most of the surveyed surface was still in the shade, except for the western moraine. Flight 2 was performed during fully sunlit conditions and an incoming shortwave radiation of approximately  $600 \text{ W m}^{-2}$ . By Flight 3, air temperatures and incoming shortwave radiation had increased to  $8 \text{ }^\circ\text{C}$  and  $900 \text{ W m}^{-2}$ , respectively (Figure 5.3). However, during the third flight there was intermittent blockage of the sun by thin, local clouds. Flight paths and image locations of Flight 1–3 are provided as supplementary data.

### Ground control survey and processing

The eBee records coordinates for every image it takes using its GPS module with an accuracy of about 5 m. However, to georeference and co-register the high-resolution surveys performed with the UAV, ground control surveys are required. Accurate measurement of the coordinates of markers that will be visible on the captured imagery (e.g. Lucieer et al., 2013; Westoby et al., 2012) yields ground control points (GCPs) that can be utilized in the image processing.

In this study I have deployed two different types of markers near or on Lirung Glacier. Prior to the optical survey on 30 April a total of 20 rectangular pieces red fabric of approximately  $1.0 \times 1.2 \text{ m}$  were distributed over the lateral moraines of Lirung Glacier (Figure 5.2). The planned ground control survey on the eastern moraine of the glacier was not fully completed due to time constraints imposed by changing weather conditions. For the parts of the moraine where the survey could not be completed six virtual ground control points, or tie points (Figure 5.2), were determined using georeferenced UAV imagery that was acquired in October 2015, using

techniques similar to those described in Chapter 3.

For the survey with the thermal camera markers of different material were required, since the striking contrast in visible light between the red fabric and the surrounding terrain is not captured in the thermal infrared part of the spectrum. Markers are required with sufficient contrast in the radiant temperature that is captured by the thermoMAP sensor. The relation between radiant temperature and surface temperature is controlled by emissivity and incoming longwave radiation (Li et al., 2013; Lillesand et al., 2015), and is given by Stefan-Boltzmann's law :

$$T_s = \sqrt[4]{\frac{\sigma T_{\text{rad}}^4 - (1 - \epsilon)LW_{\downarrow}}{\epsilon \sigma}} \quad (5.1)$$

where  $T_s$  is surface temperature (K),  $T_{\text{rad}}$  the radiant temperature (K),  $\epsilon$  the emissivity,  $\sigma$  the Stefan-Boltzmann constant ( $5.67 \times 10^{-8}$ ), and  $LW_{\downarrow}$  the incoming longwave radiation ( $\text{W m}^{-2}$ ). To obtain clear contrast on thermal imagery, it is therefore possible to use markers with considerably different emissivity than the surrounding natural surfaces on the glacier ( $\sim 0.87$ – $0.98$ ). This was achieved by using  $1.0 \times 1.0$  m corrugated plastic squares wrapped in aluminium foil. Aluminium has an emissivity of  $0.03$ – $0.07$  (Lillesand et al., 2015) and will exhibit a low radiant temperature relative to surrounding natural surfaces.

The center position of each marker (latitude, longitude, and elevation) was measured with a Global Navigation Satellite System (GNSS); a base station and a rover that both consist of a Topcon GB1000 antenna with a PG-A1 receiver. The base station was set up at a fixed position near the outlet of the glacier (Figure 5.2) and was in operation during the entire ground control survey, which was performed on 29 and 30 April 2016. I used the system in post-processed kinematic mode and measured each marker for about 30 seconds. This particular system has a reported geodetic accuracy of about  $\sim 0.2$  m in x, y and z (Wagnon et al., 2013). The measured points were post-processed in Topcon Tools (Topcon Positioning Systems, 2009) and placed accurately in a real-world coordinate system through a precise point positioning procedure (Zumberge et al., 1997) to acquire the final GCP positions.

### Optical imagery processing

Imagery acquired in the optical UAV survey was processed into image mosaics using the Structure from Motion with Multi-view Stereo (SfM-MVS) algorithm (Chapter 3; Carrivick et al., 2016; Lucieer et al., 2013; Snavely et al., 2008; Szeliski, 2011; Triggs et al., 2007) implemented in Agisoft Photoscan Professional 1.2.6 (Agisoft LLC, 2016). In this procedure, feature recognition and matching algorithms (Szeliski, 2011) are applied to the overlapping imagery to generate high-resolution 3D point clouds of the glacier, which are accurately georeferenced using the GCP coordinate information. The 3D-information from the point clouds was used to stitch the imagery and apply orthorectification, i.e. correction of image distortion and parallax caused by topographical variations and varying viewing angles of the UAV, and create an orthomosaic.

The SfM-MVS procedure followed here is similar to as described in Chapter 6. The optical orthomosaic was exported at 0.1 m resolution and the point cloud was gridded into a 0.2 m resolution DEM.

The aluminium thermal markers were clearly identifiable both in the thermal imagery (squares consistently below  $-10^{\circ}\text{C}$ ) and optical imagery (distinctly bright squares). To improve spatial co-registration of the optical image products with the thermal data, the GCPs designed for the thermal surveys were also used to process the optical imagery. The use of thermal GCPs, which are focused in the thermal survey area, ensures a high horizontal accuracy in the area where it is required.

### Thermal imagery processing

To process each of the three successful thermal surveys I used Postflight Terra 3D (version 4.0.104), which is SfM-MVS processing software provided by senseFly with the eBee (SenseFly, 2017a). It is a licensed derivative of the commercial SfM-MVS software suite Pix4D Mapper Pro (Pix4D SA, 2017). Although Photoscan is the most commonly used SfM-MVS software in geoscience applications (e.g. Chapter 3; Chapter 4; Chapter 6; Lucieer et al., 2013; Mallalieu et al., 2017; Ryan et al., 2017, 2015; Turner et al., 2014; Watson et al., 2017), and it has also been proven to work with thermal imagery (Turner et al., 2014), I chose to use Postflight because of its seamless integration with the thermoMAP camera (SenseFly, 2017a).

For each of the flights, all available images were used as input in a photo alignment procedure in Postflight. This procedure generates an initial point cloud and determines the orientation of the camera for each photo. Equal to SfM-MVS processing of optical imagery, feature recognition algorithms were applied to match similar points on multiple images. Visual pre-selection of images based on quality was not performed because the quality of the raw thermal imagery is difficult to judge and because of the large number of images per flight. To achieve optimal output, I ran the alignment procedure on the full resolution images and used a high image tie point limit. Nevertheless, many of the images were discarded by the software in this first processing step for all three flights, because insufficient tie points were found on certain image pairs. This is most likely due to the relatively low contrast of the thermal imagery for the debris-covered glacier surface. For Flight 1–3 a total of 800, 769 and 759 images (out of 2127, 2007 and 2038) were maintained by Postflight for further processing, respectively.

Georeferencing of the thermal imagery was achieved by matching all available thermal GCPs (Figure 5.2) visually on all the aligned images they appeared on. The markers were pinpointed visually in Postflight's raycloud editor. The number of images to which a single GCP was matched ranged from 14 to 96. After the GCP matching, a point cloud densification was performed on highest accuracy settings to create a thermal 3D model of the glacier surface. The model was then gridded into an orthomosaic raster with a resolution of 0.3 m.

## Image co-registration

Usage of the thermal GCPs in the SfM-MVS processing of both the optical and thermal UAV imagery provides good geodetic accuracy of the datasets. However, small spatial displacements on the order of a few decimeters between all four orthomosaics remain. To reduce those, the data were shifted horizontally using the mean displacement of the imagery at the thermal markers with the GNSS-measured coordinates, which was determined visually in a geographical information system. This provides a spatial match between the optical and thermal UAV products that is sufficiently accurate for emissivity correction of the thermal data. Implementation of co-registration algorithms for multi-sensor imagery layers (Turner et al., 2014) can potentially provide a better match and improved multi-band image analysis capabilities, but this is beyond the scope of and requirements for this study. The accuracy of the eventual co-registration was determined separately for each pair of orthomosaics from the displacements between the images at the thermal markers, and error statistics were derived from this data.

## Object-based emissivity correction

To obtain surface temperature maps from the radiant temperature orthomosaics an emissivity correction must be applied (Li et al., 2013) using Equation 5.1. The debris-covered surface of Lirung Glacier is spatially heterogeneous and within the thermal survey area there are large boulders, gravel, sand, patches with dry shrubs, supraglacial ponds and ice cliffs. The geology and consequently the supraglacial debris in this part of the valley largely consists of gneiss and quartzite (Kohn et al., 2005). Since all these surfaces have different emissivities, spatially distributed emissivity data is required to derive an accurate surface temperature. Such data could be acquired using *in situ* measurements of emissivity, generally performed with the box method (Sobrino & Caselles, 1993) or variants thereof (Rubio et al., 1997). However, such measurements are time and energy consuming, and as a result not feasible during the field campaigns in our remote study area. Therefore, I chose to estimate spatially distributed emissivity through image classification of the optical orthomosaic with object-based image analysis (OBIA) and the use of emissivity values (debris: 0.94, dry vegetation: 0.87, rough ice: 0.97, water: 0.98) reported in literature (Lillesand et al., 2015; Salisbury & D'Aria, 1992).

OBIA is a classification method that is preferred over traditional pixel-based image analysis methods when the objects of interest are multiple pixels in size (Blaschke et al., 2014). The OBIA procedure consists of two main steps. First, imagery is segmented into objects, i.e. groups of pixels that are spectrally homogeneous or that are part of a shape (Trimble, 2017). Second, the generated objects are classified based on specific object features. These can be spectral statistics of the pixels of which the object consists, but also object neighbour relations and object shape (Blaschke et al., 2014).

Our OBIA procedure is performed entirely in eCognition Developer 9.3 (Trimble, 2017). In-

put for the procedure are the optical orthomosaic and the DEM-derived slope. Both products were resampled to 0.2 m to match resolution. A single segmentation procedure was performed generating a single object level, purely based on the three-band optical orthomosaic. To accurately capture small patches of vegetation, small supraglacial ponds and exposed ice cliffs, the scale of the output objects was chosen to be moderately small with respect to the image resolution, i.e. an eCognition scale parameter setting of 25 (Trimble, 2017). For the actual classification of the objects a two-step approach was implemented. First, I chose to classify water and ice cliff objects visually, since accurate classification of these surface features requires sufficient training data (Chapter 6) and there are only two relatively small ice cliffs with adjacent ponds in the thermal survey area. Second, to distinguish between vegetation and debris a nearest neighbour classifier was implemented in eCognition (Chapter 6; Trimble, 2017). For each class, a training set of 15 samples was selected randomly. The classifier was subsequently applied using the five object characteristics that provided the largest class separability within the training set: blue band mean, red band standard deviation, green band standard deviation, brightness range, and mean slope. By evaluating the classification visually at 100 random points for each class, the classification's producer accuracy, user accuracy and kappa coefficient (Lillesand et al., 2015) were found to be 91.3%, 94.0% and 0.85, respectively.

To correct for emissivity through Equation 5.1, *in situ* observations of  $LW_{\downarrow}$  were used. During the surveys I measured  $LW_{\downarrow}$  only at the Kyangjin AWS. However, meteorological data from previous years (Buri et al., 2016b; Steiner & Pellicciotti, 2016; Steiner et al., 2015) and from recent field campaigns reveal that it is higher over the debris-covered surface of Lirung Glacier than at Kyangjin AWS due to longwave radiation emitted and reflected by surrounding steep headwalls, lateral moraine slopes, and debris mounds. Comparison of on- and off-glacier  $LW_{\downarrow}$  data from multiple field campaigns reveals an approximate additional  $20 \text{ W m}^{-2}$ , which I used to offset the Kyangjin AWS  $LW_{\downarrow}$  data.

To estimate the effect of uncertainty in emissivity on the derived surface temperatures I have applied a Monte Carlo sensitivity analysis. An ensemble of 1000 random emissivity samples per surface type was drawn from a truncated normal distribution ( $0 \leq \epsilon \leq 1$ ) using a different mean and standard deviation for each surface type (debris:  $0.94 \pm 0.015$ , dry vegetation:  $0.87 \pm 0.062$ , rough ice:  $0.97 \pm 0.012$ , water:  $0.98 \pm 0.005$ , (mean $\pm$ sd)). These were derived from sets of emissivities for metamorphic rock, vegetation, rough ice and sediment-laden water (Salisbury & D'Aria, 1992). For each ensemble member surface temperatures were calculated for each of the three thermal flights and ensemble statistics were derived.

### ThermoMAP bias correction

Surface temperatures derived from the thermoMAP sensor have a remaining dark current bias that is due to the internal mechanics and calculations of the camera. The thermal response measured by an uncooled microbolometer sensor, such as from the thermoMAP, must be corrected

with the internal sensor temperature (Ribeiro-Gomes et al., 2017), and this is performed automatically in flight. The temperature is estimated at the beginning of each flight leg (for each of the flights  $n = 24$ ) by measuring the camera's shutter with the sensor, and comparing this with an internal thermometer (SenseFly, 2017b). However, if the internal temperature differs greatly from 20 °C large deviations can start to occur, especially on long flight legs (pers. comm. senseFly representative M. Montecchchio). Such a sensor bias is likely to be the case for our study (relatively short flight legs, but air temperatures of 0–8 °C at Kyangjin AWS). In our case, the potential biasing influence of the atmospheric column between the sensor and the ground on the measured temperature (Li et al., 2013; Torres-Rua, 2017) is likely limited due to the dry conditions, thin air and low flight height.

To remove the sensor bias it is required to know the skin temperature and emissivity of an object that was captured in the imagery at the time of the survey. Due to the lack of dedicated markers in our case, I assume that exposed clean ice is at the melting point of snow and ice (0 °C) during Flights 2 and 3, and use the mean difference between the emissivity-corrected surface temperatures of a vertical clean ice band of one of the ice cliffs to calculate the sensor bias. The resulting sensor bias has subsequently been removed from all three thermal orthomosaics to obtain the final thermal imagery product. Note that this approach assumes that the bias is constant over the range of measured temperature values, which is most likely not the case. The required data to estimate the non-linearity of the bias is however unavailable.

## 5.2.5 In situ temperature measurements

### Sensor placement

A total of 25 HOBO Tidbit v2 temperature loggers with an accuracy of  $\pm 0.2$  °C (hereafter referred to as Tidbits) were distributed on the surface of Lirung Glacier to validate surface temperature estimates from the thermal UAV survey. The sensors were placed in a semi-regular grid (Figure 5.2) on different surface types (Figure 5.4). Two Tidbits were submerged 5 cm in the water of a supraglacial pond underneath a float of semi-rigid foam. Most sensors received direct solar radiation for almost the entire day, but three Tidbits were placed into the shade to shield them from solar radiation. All sensors were operational during the aerial surveys and set to record temperature at a 5-minute interval.

### Correction for solar radiation

Tidbit temperatures are overestimated when exposed to direct solar radiation due to the micro climate generated. To correct for this, I ran reference experiments at two AWS sites, one in Kathmandu and one in Langtang Valley. The Tidbit temperature measurements ( $T_{\text{tid}}$ ) were compared with surface temperature ( $T_s$ ) as derived from incoming and outgoing longwave radiation ( $LW_{\downarrow}$  and  $LW_{\uparrow}$ ) that was measured with radiometers (Apogee SI-111 and Kipp & Zonen

CNR4), and using:

$$T_s = \sqrt[4]{\frac{LW_{\uparrow} - (1 - \epsilon)LW_{\downarrow}}{\epsilon\sigma}} \quad (5.2)$$

Two types of surfaces were examined below the AWSs. Debris was artificially set up in the experiment that was run in Kathmandu, while naturally occurring dry vegetation was monitored at the Kyangjin AWS in Langtang Valley (Figure 5.2). The artificial debris layer comprised of a mixture of irregularly shaped concrete blocks, natural rocks and mud, which had a size distribution representative for supraglacial debris and comparable emissivity, as concrete has an emissivity of 0.92–0.94 (Lillesand et al., 2015). For practical reasons, the thickness of the layer was shallower (5–10 cm) than what is usually found on Lirung Glacier, but it was thick enough to completely cover the concrete substrate. For each surface type,  $\epsilon$  was first set as the value minimizing the difference between  $T_s$  and  $T_{\text{tid}}$  ( $\Delta T$ ), using night-time data only. As  $\Delta T$  increases with incoming shortwave radiation ( $SW_{\downarrow}$ ), separate regressions for each surface type were calculated using daytime observations where  $SW_{\downarrow} > 20 \text{ W m}^{-2}$

$$T_{\text{cor}} = T_{\text{tid}} - aSW_{\downarrow} \quad (5.3)$$

where  $T_{\text{cor}}$  is the corrected Tidbit temperature and  $a$  the correction factor ( $\text{K m}^2 \text{ W}^{-1}$ ). It is assumed that with little or no direct shortwave radiation, i.e. at night,  $T_s$  and  $T_{\text{tid}}$  are equal, and so the regression was forced through the origin. Additionally, since all our thermal UAV flights performed between 6:45 and 10:50, Equation 5.3 only considers experimental observations collected before noon, which limits the influence of temperature hysteresis caused by Tidbit lag. Correction factors for the most suitable surface type were applied to the *in situ* temperature measurements for the Lirung thermal surveys. Corrections were not applied to Tidbits that were put in the shade or submerged in water, since these were not subjected to direct shortwave radiation.

$SW_{\downarrow}$  varies considerably spatially over the hummocky debris-covered surface of Lirung Glacier because of varying aspects and shading effects that result from the small-scale surface topography. To account for this in the correction, I modelled distributed  $SW_{\downarrow}$  using the hemispherical viewshed algorithm of Fu & Rich (1999) and a 30 cm resolution resampled DEM derived from the optical UAV data. In the model, I used an effective atmospheric transmissivity of 0.42, which was determined by minimization of modelled and measured  $SW_{\downarrow}$  at the Kyangjin AWS (Figure 5.3). Any residual variability captured by the AWS as compared to the idealized modelled  $SW_{\downarrow}$  was superimposed on the modelled data.

### 5.2.6 Ground-based thermal imaging

To compare the UAV surface temperature measurements with independent radiometric measurement, I have used a FLIR C2 (hereafter C2) compact hand-held thermal camera during the UAV flights. The camera has a  $80 \times 60$  pixel uncooled microbolometer TIR sensor and a  $640 \times 480$  pixel optical sensor that take aligned images synchronously. The TIR sensor senses

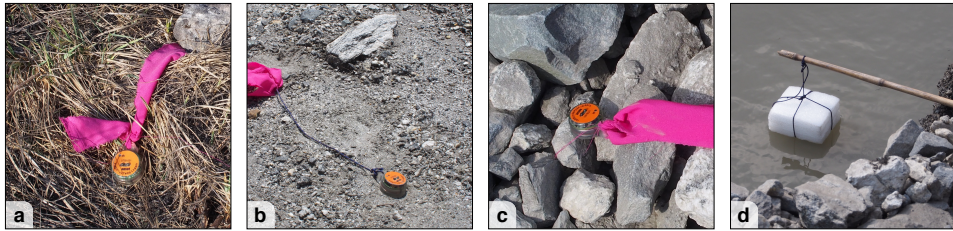


**Figure 5.4:** Different types of surfaces on Lirung Glacier the temperature loggers were placed on or in: vegetation (a), fine debris (b), coarse debris (c), and water (d). The pink ribbons were attached to the Tidbits to improve their discoverability.

objects of  $-10$  to  $150$  °C in the in the  $7.5\text{--}14$   $\mu\text{m}$  range, with a thermal sensitivity of  $0.1$  °C. The accuracy of the sensor is  $\pm 2$  °C at an outside temperature of  $25$  °C (FLIR Systems, 2017).

The C2 survey was performed at a single location during the entire survey (Figure 5.2). The camera was mounted on a monopod that was fixed between debris, facing in west-southwest direction at the largest largest ice cliff within the survey area. In the field of view of the camera most of the ice cliff was visible, as well as parts of the adjacent supraglacial pond and the surrounding debris. The shutter of the C2 was manually triggered at a semi-regular interval of 10 minutes between 06:40 and 11:09.

Radiometric thermal data and the optical images taken by the camera's sensors were retrieved using FLIR's ResearchIR software. As a result of the relatively unstable monopod setup and the manual triggering of the shutter, the captured imagery for the different time steps was not perfectly coregistered. To coregister the data accurately, manual tie points were identified on the optical imagery in a geographical information system, which were subsequently applied to both the optical and thermal image sets. From the optical imagery, zones of different surface classes were identified visually corresponding to those of the classified UAV data, but with an extra distinction between clean and dirty ice. For each zone an emissivity correction was applied using Equation 5.1 and the values reported in Section 5.2.4. For comparison of the data with UAV-derived  $T_s$ , zones that correspond spatially to those defined on the C2 imagery were identified visually on the UAV-derived orthomosaic.

### 5.2.7 Landsat 8 thermal infrared comparison

Medium resolution thermal infrared satellite imagery (e.g. Landsat 7 (60 m) (Rounce & McKinney, 2014), ASTER (90 m) (Foster et al., 2012; Mihalcea et al., 2008a,b) and Landsat 8 (100 m) (Chapter 7)) has been previously used to infer debris thickness using temperature inversion methods. To get an impression of the accuracy and spatial detail of such spaceborne thermal infrared imagery for analyses of the debris layer, I compared satellite and UAV-derived surface temperatures.

For the comparison, surface temperatures of Lirung Glacier's debris cover were esti-

mated from Landsat 8 Thermal Infrared Sensor (TIRS) data. I used a Landsat 8 scene (LC81410402016123LGN00) that was acquired on 2 May 2016 at 10:32 local time (Table 5.1), one day after the thermal UAV survey. Although the original sensor resolution of the TIRS instrument is 100 m, the only data that is made available by the United States Geological Survey comprises thermal imagery that is coregistered, geometrically corrected and resampled using irreversible cubic convolution to match the 30 m resolution of the satellite's optical data (USGS, 2016). Uncertain weather conditions prevented us from performing the UAV and *in situ* measurements the same day as the Landsat 8 overpass, but atmospheric and meteorological conditions during the morning of both acquisition days were generally comparable (Figure 5.3). Nevertheless, comparison of absolute temperature values of the two different products is inaccurate because of three reasons: (1) a small amount of cloud cover was present during the final UAV flight, which was not the case at the time of the satellite acquisition; (2) I observed slightly more atmospheric haze on 2 May 2016, but I did not quantify changes in atmospheric transmissivity; (3) Landsat 8 TIRS is affected by stray light, which can result in considerable overestimations of the recorded radiance that are hard to correct (USGS, 2016). Comparison of spatial variability, on the other hand, is still meaningful.

Surface temperatures were determined from the satellite's band 10 by first calculating the top of atmosphere brightness temperature from the Level 1 satellite product using the standard procedure described by USGS (2016). A subsequent correction for emissivity was applied using Equation 5.1 and the UAV-derived emissivity map, resampled to the satellite product resolution. Comparison with the UAV-derived surface temperatures was performed by evaluating pixel statistics of the UAV thermal data for each Landsat pixel.

### 5.2.8 Surface temperature and topography

To evaluate the influence of the small scale hummocky topography of Lirung Glacier on debris surface temperatures, I have compared the mean warming rate over the entire morning ( $\text{K h}^{-1}$ ) with the modelled  $\text{SW}_{\downarrow}$  and four DEM derivatives: aspect, slope, flow accumulation and high pass filtered DEM (see next paragraph). For the analysis, I have fitted a random forest regression model with the warming rate as dependent variable and the five topography indicators as independent variables. A random forest is a statistical machine learning algorithm that can fit non-linear relations, is insensitive to overfitting, has no requirements on the statistical distribution of variables, and is largely insensitive to multicollinearity (Breiman, 2001). It is therefore particularly suitable for this analysis. The algorithm can also provide a natural measure of variable importance in model prediction as well as measures of total explained variance (Breiman, 2001; Louppe et al., 2013). These were used to determine to what extent solar insolation in combination with topography is causing temperature change, and how much is unexplained by different processes. The entire analysis was performed only for the actual glacier surface (Figure 5.6a), and using data resampled to 3 m ( $n = 33999$ ) to reduce the required processing time

for the random forest algorithm and to remove noise in both the surface temperature maps and the DEM.

Aspect is closely linked to  $SW_{\downarrow}$ , since the amount of insolation at a point is directly related to the solar azimuth and the local aspect. However, on the contrary to  $SW_{\downarrow}$  it is not affected by the viewshed at a point. It can easily be calculated from a DEM and does not require data on surrounding topography, and is therefore of interest as a predictor of the warming rate. Slopes (facing toward the sun) are exposed more directly to the sun than flat areas and may be dryer, since water is expected to run off to lower areas. As a result, it could be that areas of relatively high slope have an increased warming rate due to increased radiation, decreased debris heat capacity, and less evaporative cooling. A flow accumulation map, or upstream area map, indicates the size of the catchment upstream of a pixel. The larger the upstream area, the higher the debris moisture content may be due to supraglacial runoff and the lower the warming rate. Note that supraglacial melt water runoff also depends strongly on the configuration of the englacial drainage network. A high-pass filtered DEM, here created for a large circular focal window of 25 m, provides information on relative local elevation. That is, whether a point is relatively high or low in comparison with its surroundings. Local depressions can be expected to be more humid and cooler, whereas mounds and crests may be dryer and warmer.

## 5.3 Results

### 5.3.1 Tidbit correction and measurements

Radiometer-derived  $T_s$  (Equation 5.2) and  $T_{tid}$  showed considerable deviations for both reference experiments (Figure 5.5). Temperature differences between the two methods ( $\Delta T$ ) were as high as 10 °C over the course of the morning. The debris experiment performed in Kathmandu revealed a more linear relation between  $\Delta T$  and  $SW_{\downarrow}$  than the vegetation experiment performed near the study area at the Kyangjin AWS. There is more hysteresis for the latter, which is most likely caused by evaporation of moisture from the vegetation and the top soil layers. The range of  $SW_{\downarrow}$  for the two experiments is considerably different because of the difference in altitude (~1400 m and ~4000 m) and atmospheric pollution at the two reference sites. The regression analysis of  $\Delta T$  against  $SW_{\downarrow}$  (Equation 5.3) resulted in correction factors  $a$  of  $13.3 \times 10^{-3}$  and  $11.4 \times 10^{-3} \text{ K m}^2 \text{ W}^{-1}$  for debris and vegetation, respectively.

The  $T_{cor}$  values for the morning of 1 May 2016 reveal a large range in temperatures between flights and between different surfaces (Table 5.2). During thermal Flight 1 (06:45), measured *in situ* temperatures were generally just below freezing point with little variability between different Tidbits. This is similar to air temperature observations at the Kyangjin AWS, which are just above freezing point but measured 250 m lower (Figure 5.3). As incoming radiation and temperature increase over the course of the morning,  $T_{cor}$  increases considerably with mean values up to 28 °C for vegetated surfaces. Water temperatures only changed slightly throughout the

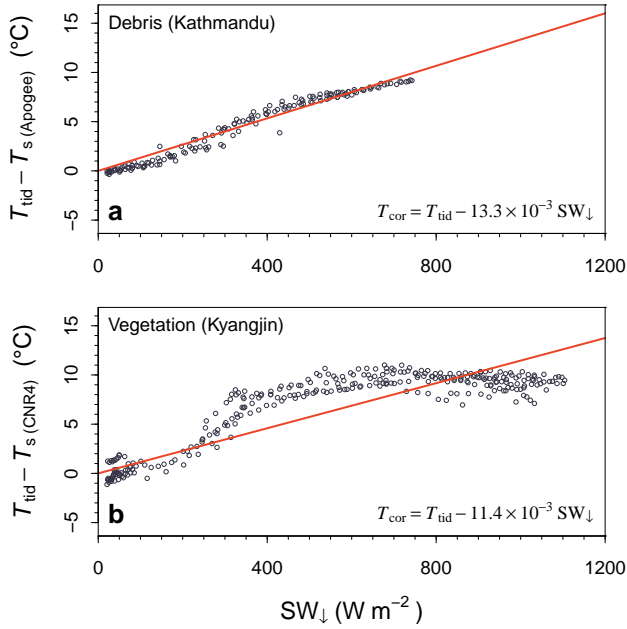


**Figure 5.5:** Difference between radiometer-derived and Tidbit-derived surface temperatures versus incoming shortwave radiation for daytime measurements before 12 am. The two panels show the biases for an experimental debris layer in Kathmandu (a) and natural vegetation present at below the Kyangjin AWS (b). The red lines show the linear regressions that were used for bias correction of the Tidbits.

**Table 5.2:** Statistics of  $T_{\text{cor}}$  at the time of the thermal UAV flights for the four different surface types (mean  $\pm$  sd).

	Flight 1	Flight 2	Flight 3
Vegetation ( $n = 4$ )	$-0.5 \pm 2.4$	$27.8 \pm 5.5$	$27.0 \pm 9.4$
Debris ( $n = 16$ )	$-1.2 \pm 1.9$	$15.0 \pm 6.5$	$16.0 \pm 6.1$
Shade ( $n = 3$ )	$-0.1 \pm 0.7$	$8.9 \pm 5.3$	$16.4 \pm 9.4$
Water ( $n = 2$ )	$0.4 \pm 0.2$	$1.6 \pm 0.1$	$1.8 \pm 0.1$

morning and shaded tidbits warm considerably slower than those in direct sunlight.

### 5.3.2 Image registration accuracy

After SfM-MVS processing of the optical and thermal UAV surveys I co-registered the imagery by applying shift factors ( $x$ ,  $y$ ) for the optical survey (0.05 m, 0.03 m), thermal Flight 1 (0.18 m, -0.15 m), thermal Flight 2 (0.14 m, -0.16 m) and thermal Flight 3 (0.13 m, -0.15 m) to optimally match all orthomosaics with the GNSS-measured thermal GCPs. The root mean square errors (RMSE) at the thermal markers show a considerable improvement after application of the shift (Table 5.3). Before shifting, the thermal orthomosaics were already reasonably well registered with each other, despite completely independent processing of the three flights in Post-

**Table 5.3:** Root mean square errors (m) of orthomosaic co-registration at the thermal markers locations ( $n = 17$ ). Errors are shown between the imagery and the GNSS-measured ground control points, and for every orthomosaic pair. The errors between the orthomosaics before applying the horizontal shift are shown in parentheses.

	GCPs	Optical	TIR F1	TIR F2
Optical	0.09 (0.11)	-		
TIR F1	0.19 (0.31)	0.18 (0.29)	-	
TIR F2	0.19 (0.29)	0.19 (0.29)	0.17 (0.18)	-
TIR F3	0.19 (0.28)	0.18 (0.27)	0.17 (0.18)	0.03 (0.03)

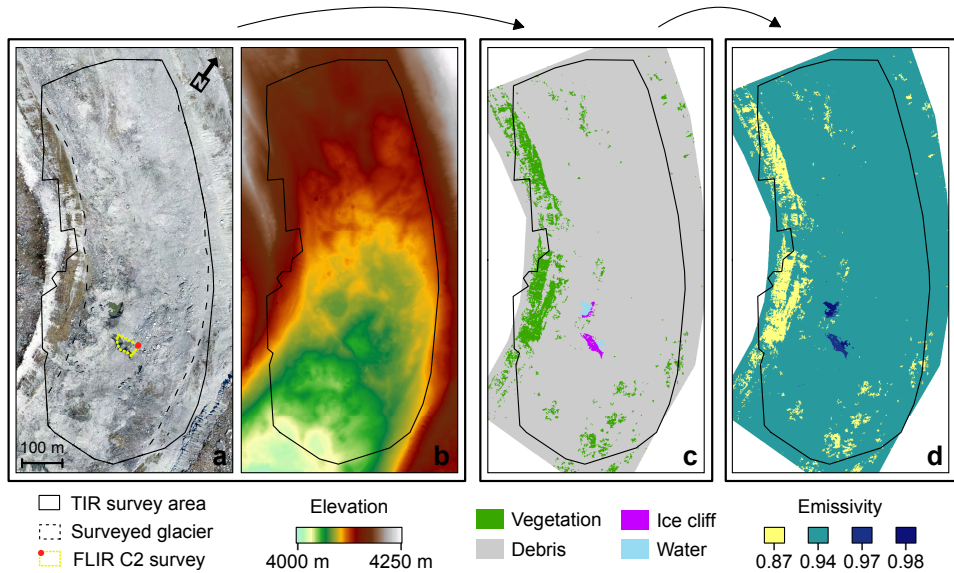


**Figure 5.6:** The input data used and the output data created in the emissivity estimation procedure: (a) the orthomosaic and (b) digital elevation model that follow from SfM-MVS processing of the optical UAV data; (c) the object-based image classification and (d) the final emissivity map used to calculate surface temperatures.

flight. The horizontal shift between the optical and thermal orthomosaics may thus be caused largely by differences in processing and optimization algorithms between Photoscan (optical data) and Postflight (thermal data).

### 5.3.3 Image classification and emissivity

The result of the object-based image classification is shown in panel C of Figure 5.6. The most abundant surface type in the study area is debris with 92.3%, followed by vegetation (7.2%), ice cliff (0.3%) and water (0.2%). Vegetation is mainly present on the western lateral moraine, and not so much on the glacier surface itself. Using the classification and emissivity values reported in Section 5.2.4, the emissivity map with mean emissivity of 0.93 was derived (Figure 5.6d).

### 5.3.4 Thermal correction and imagery

The three final thermal orthomosaics that were corrected for emissivity and sensor bias are shown in Figure 5.7. Due to the non-linear nature of Stefan–Boltzmann’s law and the spatial distribution of emissivity, the emissivity correction is both spatially and temporally variable. Mean corrections that were applied to the imagery of Flights 1–3 were in the order of  $0.5 \pm 1.3$  °C,  $0.8 \pm 1.9$  °C and  $0.7 \pm 1.9$  °C (mean  $\pm$  sd), respectively. The magnitude of mean sensor bias was determined to be 7.5 °C (7.6 °C for Flight 2 and 7.4 °C for Flight 3) from the ice cliff surface at melting point. The bias for the same ice cliff pixels for early morning Flight 1 is indeed less, i.e. 4.6 °C, indicating that the ice surface was not yet at melting point at that time. For the bias correction the mean bias based on flight 2 and 3 was subtracted for all three flights.

Similar to the *in situ* measurements of  $T_{\text{cor}}$ , the magnitude of UAV-derived  $T_s$  varies greatly over the morning, with temperatures for thermal Flights 1–3 (°C) of  $-1.4 \pm 1.8$ ,  $11.0 \pm 5.2$  and  $15.3 \pm 4.7$  (mean  $\pm$  sd), 95th percentile ranges of  $-3.4$  to  $3.6$ ,  $4.0$  to  $25.7$  and  $8.6$  to  $27.5$ , and maxima of  $9.1$ ,  $43.0$  and  $49.7$ , respectively (Table 5.4). It is clear that in the early morning the mostly shaded glacier surface has not yet warmed and surface temperatures have low spatial variability. Flight 2 shows a much warmer surface with high spatial variability. On the hummocky debris-covered surface of the glacier there are warm areas that received greater insolation, e.g. crests and slopes that face towards the azimuth of the rising sun, and colder parts in local depressions and north-facing slopes (Figure 5.7b). The last flight, with the debris exposed to greater and more evenly spatially distributed insolation under higher solar elevation angles, has overall high values of  $T_s$  that are less spatially variable (Figure 5.7c). For all three flights there is a distinct lateral trend in  $T_s$  that is directly related to the duration of insolation, with the western parts of the glacier being exposed to the sun first. With respect to the different surface classes, debris and vegetation are warmer than ice and water for all three flights, as expected. Remarkably, vegetation is consistently warmer than debris for all flights. This is likely due to its higher abundance on the western moraine slope. Also worth noting is that ice is generally warmer than water, which could be due to the dark debris film on large parts of the ice cliffs.

The sensitivity of  $T_s$  for variations in emissivity of the surface classes is limited (Table 5.4). The standard deviations of raster average  $T_s$  for each Monte Carlo member in the ensemble ( $n = 1000$ ) for F1–F3 are only 0.33, 0.43 and 0.43 °C, respectively. The uncertainty in the surface temperature for vegetation only is considerably larger, as the emissivity of dry vegetation is more uncertain (Section 5.2.4), emissivity is lower, and vegetation has the highest surface temperatures. Ice and water, on the other hand, have relatively certain and high emissivities as well as generally low temperatures, and consequently have low ensemble uncertainty.

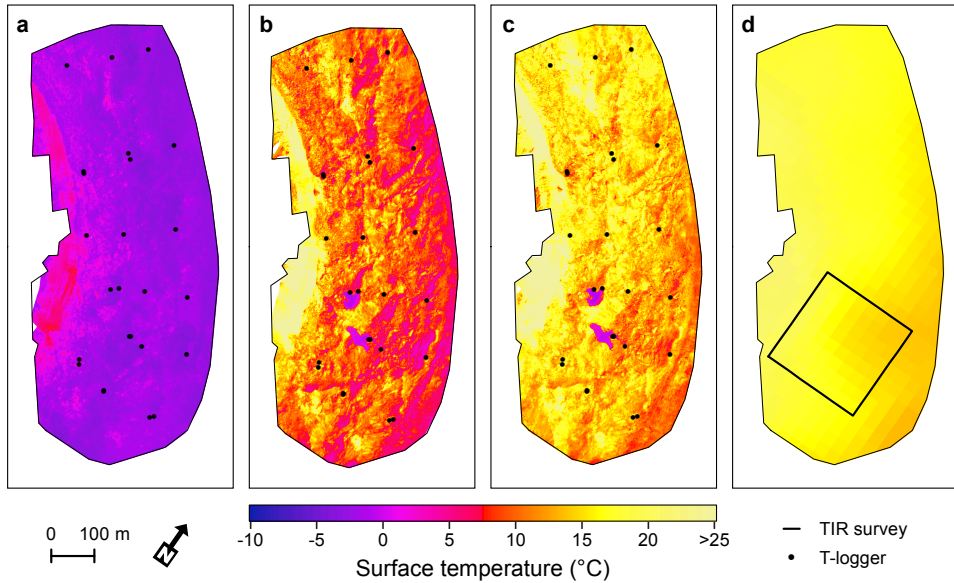


**Figure 5.7:** Emissivity and bias-corrected surface temperature orthomosaics of the three UAV flights on 1 May 2016 (a-c; 06:45, 09:20 and 10:35) and the brightness temperature of the Landsat 8 band 10 on 2 May 2016 at 10:32 (d). The black rectangle in panel d indicates the extent of Figure 5.10.

### 5.3.5 Surface temperature comparison

Comparison of surface temperature derived from the Tidbits ( $T_{\text{cor}}$ ) and from the UAV imagery ( $T_s$ ) for each of the three thermal surveys and for all Tidbits showed that the recorded temperatures were largely in agreement (Figure 5.8a). The data scatter mainly around the 1:1 line and are generally the same order of magnitude ( $r = 0.93$ ). The data of Flight 1 show the best agreement with a mean  $T_{\text{cor}}^{\text{F1}}$  and  $T_s^{\text{F1}}$  of  $-0.9$  and  $-1.6$  °C, respectively, and a RMSE of  $0.9$  °C. Note that of the three thermal flights, the Tidbit correction that was applied for this flight was minimal because of low  $\text{SW}_{\downarrow}$  in the early morning, and that the applied thermal sensor bias correction was independent of  $T_s^{\text{F1}}$ . The agreement between  $T_{\text{cor}}$  and  $T_s$  for Flight 2 is less, as there were considerable overestimations of surface temperature by  $T_{\text{cor}}^{\text{F2}}$  of over  $10$  °C for some of the Tidbits. The RMSE for this flight was also considerably higher with  $7.0$  °C. The last flight of the morning shows again better agreement with an RMSE of  $5.1$  °C. Tidbits that were put on vegetation still have a considerable bias in this case, but especially those on debris show relatively good agreement with RMSE values of  $7.8$  and  $3.7$  °C, respectively.

Time series of a selection of the Tidbits (Figure 5.8b-e) for each surface type that have a good match between  $T_{\text{cor}}$  and  $T_s$  show the variability in Tidbit temperature over the course of the morning. Tidbits in direct sunlight clearly had fluctuating temperature profiles, while measurements in the shade or in water are relatively stable and smooth over time. The temperature of Tidbits directly exposed to the sun deviate considerably from  $T_s$ , but temperature measurements

**Table 5.4:** Mean, standard deviation, 2.5 and 97.5 percentiles of  $T_s$  for the three UAV flights for the survey area and for each class. The right column shows the ensemble standard deviation of the Monte Carlo emissivity sensitivity analysis.

Flight	Class	Mean	SD	P <sub>2.5</sub>	P <sub>97.5</sub>	Ensemble SD
1	All	-1.4	1.8	-3.4	3.6	0.33
	Debris	-1.7	1.3	-3.4	1.5	0.33
	Vegetation	2.8	1.9	-1.1	6.7	1.47
	Water	-2.9	0.3	-3.1	-2.3	0.20
	Ice	-2.8	0.4	-3.5	-1.9	0.01
2	All	11.0	5.2	4.0	25.7	0.43
	Debris	10.2	3.9	4.2	19.8	0.43
	Vegetation	22.2	5.7	8.3	31.8	2.28
	Water	0.0	1.2	-0.9	3.7	0.20
	Ice	1.4	2.0	-0.1	7.6	0.02
3	All	15.3	4.7	8.6	27.5	0.43
	Debris	14.6	3.5	8.8	22.5	0.43
	Vegetation	25.0	5.1	13.9	34.8	2.21
	Water	0.3	1.6	-0.9	5.1	0.19
	Ice	1.7	2.3	-0.2	9.1	0.02

in the shade and in water agree well. Therefore it is likely that the deviations between  $T_{\text{cor}}$  and  $T_s$  can be largely explained by errors in the Tidbit measurements.

### 5.3.6 Ground-based thermal imagery

Time series with statistics for four zones of different surface type (Figure 5.9a) of the surface temperatures derived from the C2 imagery ( $T_s^{\text{C2}}$ ) are shown in Figure 5.9e. Similar to  $T_{\text{cor}}$  and UAV-derived  $T_s$ , surface temperatures measured by the C2 are low in early morning at the start of the time series ( $-7.4 \pm 0.7$  °C) and quickly rise as radiation increases.  $T_s^{\text{C2}}$  for debris continues to rise steadily until 10:00 when it reaches  $19.9 \pm 3.7$  °C, while for ice it stabilizes relatively quickly to a temperature just below 0 °C, i.e. around the melting point of ice. Since the imagery thus has very low sensor bias, no bias correction was required. Only a slight difference between clean and dirty ice patches is present, as after 08:00 dirty ice has a mean temperature that is on average 0.2 °C above that of clean ice. On the C2 imagery, the temperature for the supraglacial pond ( $5.1 \pm 3.8$  °C) rises to levels considerably above those of the ice, but remain well below that of debris. After 10:00 all zones exhibit a decrease in surface temperature of  $\sim 2.5$  °C, which coincides with the thin local clouds that were observed during the last flight.

Figure 5.9f shows boxplots of  $T_s^{\text{F1}}$ ,  $T_s^{\text{F2}}$  (Figure 5.9c) and  $T_s^{\text{F3}}$  for the zones corresponding to Figure 5.9a and b. Compared to early morning  $T_s^{\text{C2}}$ ,  $T_s^{\text{F1}}$  appears to be considerably higher with temperatures of  $-2.7 \pm 0.4$  °C. Note, however, that over the course of Flight 1  $T_s^{\text{C2}}$  rapidly changes with a warming of about 5 °C, and that the C2-measured temperature right after the flight at 07:10 is more comparable ( $-3.5 \pm 1.7$  °C). Contrastingly, temperature is 8 °C lower than  $T_s^{\text{C2}}$  in the late morning, with a  $T_s^{\text{F3}}$  of  $11.9 \pm 1.8$  °C for debris. Pond temperatures measured by the UAV and by the Tidbits (Figure 5.8e) are consistently near freezing and lower than  $T_s^{\text{C2}}$ .

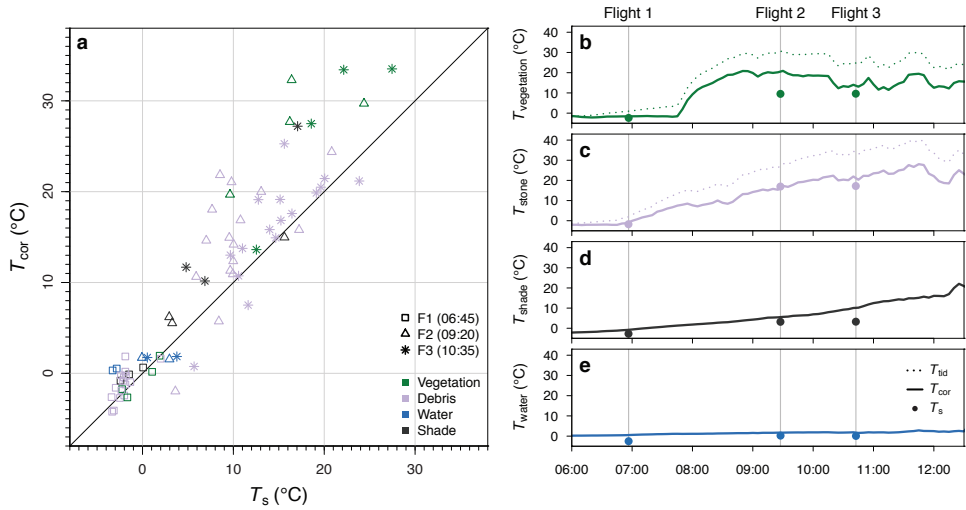


**Figure 5.8:** Corrected Tidbit temperature measurements ( $T_{cor}$ ) against corrected surface temperatures from the three UAV flights ( $T_s$ ) (panel a). Point shape denotes the UAV flight, point color the surface class, and the black line a 1:1 relation. Panels b–e show time series for selected Tidbits of the surface classes vegetation, debris, shade, and water, respectively. For vegetation and debris both the uncorrected ( $T_{tid}$ ) and corrected temperatures ( $T_{cor}$ ) are plotted. The points on panels b–e indicate  $T_s$  at the Tidbit location.

### 5.3.7 Landsat versus UAV

The Landsat 8 (L8) thermal imagery of 2 May 2016 that was processed into a surface temperature map ( $T_s^{L8}$ ) shows that the satellite image failed to capture any substantial spatial variation over the area of interest (Figure 5.7). The pixel size of 30 m of the Landsat 8 thermal data, which is created by cubic convolution of the 100 m raw product (USGS, 2016), results in substantial smoothing and loss of detail as compared to the data obtained from the UAV. The raw data product is unavailable unfortunately. While  $T_s^{F3}$  had a total range of about 50 °C, a mean of 15.3 and standard deviation of 4.7,  $T_s^{L8}$  only ranges between 18.2 °C and 27.3 °C, with a mean of 22.0 °C and a standard deviation of 2.1 °C. The overall spatial pattern of  $T_s^{L8}$ , however, appears to match the pattern of  $T_s^{F3}$ , with generally higher temperatures on the western side of the glacier.

A more detailed view on both the UAV and Landsat data is presented in Figure 5.10, where the same spatial subset of 240 × 240 m is shown for both datasets. Here it is further evidenced that the satellite image cannot capture the heterogeneity of  $T_s$  over a debris-covered glacier, and that moderate scale features with distinctly low temperatures such as ice cliffs and supraglacial ponds appear to have little to no effect on the temperature recorded by the satellite. Figure 5.10c shows a scatter plot of  $T_s^{L8}$  against  $T_s^{F3}$  for each Landsat pixel over thermal survey area. Although there is a significant correlation between the two products ( $r = 0.79$ ),  $T_s$  found by the two different sensors is considerably different, with a mean overestimation of  $T_s^{L8}$  of 6.9 °C. This may partly

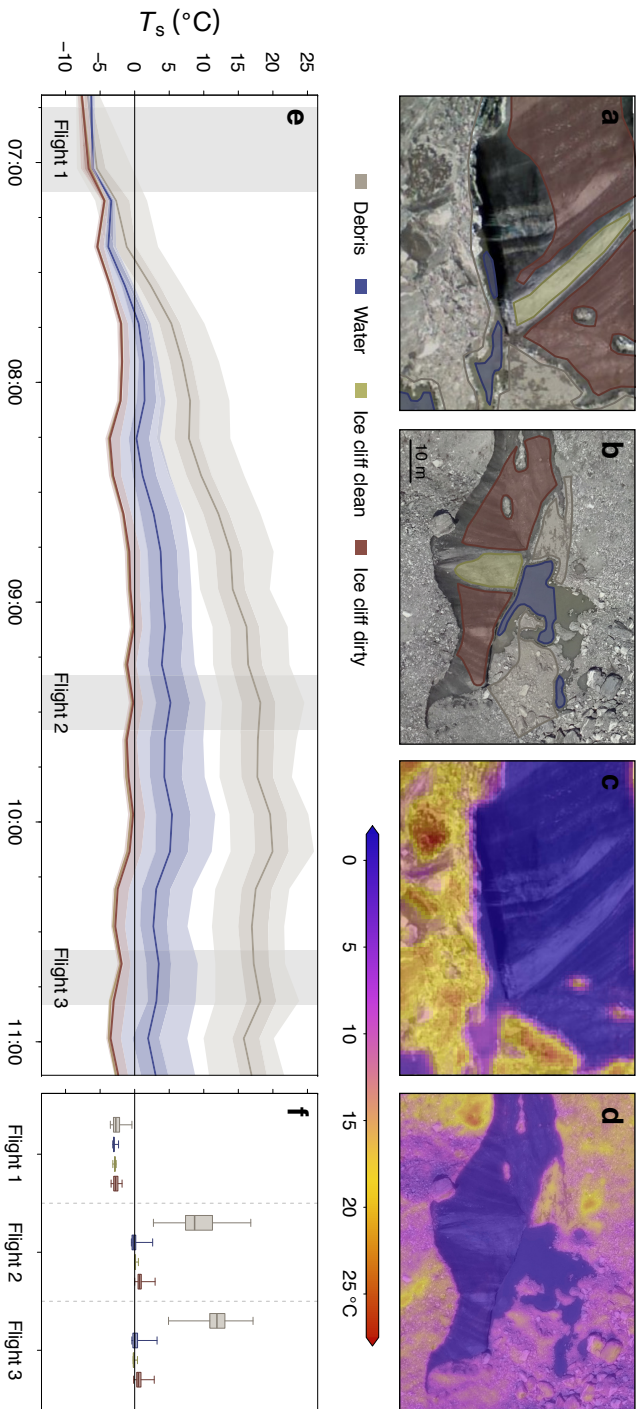


**Figure 5.9:** Ground-based FLIR C2 optical (a) and thermal infrared (c) imagery (09:28 example) of a selected ice cliff supraglacial pond, and the surrounding debris location indicated in Figure 5.6a. UAV optical (b) and thermal infrared nadir orthomosaics (d) of the same location (Flight 2, 09:20–09:35). Image regions used for comparison of the two datasets are indicated by the polygons (a,b). Time series with region statistics (mean, interquartile range and 95th percentile range) of  $T_s^{C2}$ ,  $T_s^{E1}$ ,  $T_s^{E2}$  and  $T_s^{E3}$  for the corresponding regions on the UAV imagery in panel f.

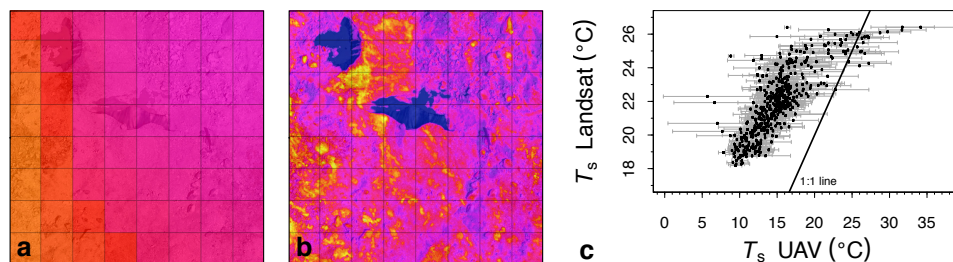


**Figure 5.10:** Comparison of a subset (extent denoted in Figure 5.7d) of  $T_s$  derived from Landsat 8 TIRS band 10 (2 May 2016 10:32; panel a) and from the thermal UAV survey (Flight 3, 1 May 2016 10:35; panel b). The grid overlay denotes the 30 m grid in which the Landsat data is provided. Panel c shows, for the entire extent of the UAV survey, a plot of Landsat pixel values against mean UAV surface temperatures within those pixels. The whiskers denote  $\pm 1$  sd of the UAV surface temperatures.

be attributed to actual differences in surface temperature between the two days of acquisition, since there were differences in  $T_{\text{air}}$  and  $SW_{\downarrow}$  (Figure 5.3), and to differences in atmospheric transmissivity. The overestimation of radiance at the sensor caused by stray light is also likely to play a role, as it may result in biases of up to  $5^{\circ}\text{C}$  for band 10 (USGS, 2016). Standard deviations of  $T_s^{\text{F3}}$  within each Landsat pixel (Figure 5.10c) show there is a very large variation in the relatively small 30 m plots of debris-covered glacier surface.

### 5.3.8 Topography and surface temperature

The results of the random forest analysis that was used to evaluate the relation between topography and surface warming rate are presented in Figure 5.11. Of the five DEM derivatives that were analysed there were only two that showed a clear relation: aspect and  $SW_{\downarrow}$ . Pixels with an east-facing aspect ( $45^{\circ}$ – $135^{\circ}$ ) warm significantly more ( $+1.0\text{Kh}^{-1}$ ) than west-facing pixels ( $225^{\circ}$ – $315^{\circ}$ ) (Figure 5.11g), a logical result as morning flights are analysed. North-facing ( $315^{\circ}$ – $45^{\circ}$ ) and south-facing ( $135^{\circ}$ – $225^{\circ}$ ) pixels do show a difference in warming rate, but only very moderately with  $0.1\text{Kh}^{-1}$ . A more distinct effect on surface warming is caused by  $SW_{\downarrow}$ , although the variable also exhibits considerable residual variability (Figure 5.11k). Linear regression revealed that  $SW_{\downarrow}$  alone explains 29.4% of the variance in the warming rate. The slope, upstream area and local relative elevation are all shown to have very limited influence on the warming rate (Figure 5.11l). In total, the combination of all independent variables can account for 38.8% of the variance.

## 5.4 Discussion

### 5.4.1 Applications of thermal UAV imagery

The methods employed in this study reveal the possibility of capturing spatially distributed  $T_s$  on a debris-covered glacier with unprecedented detail using a UAV equipped with a thermal

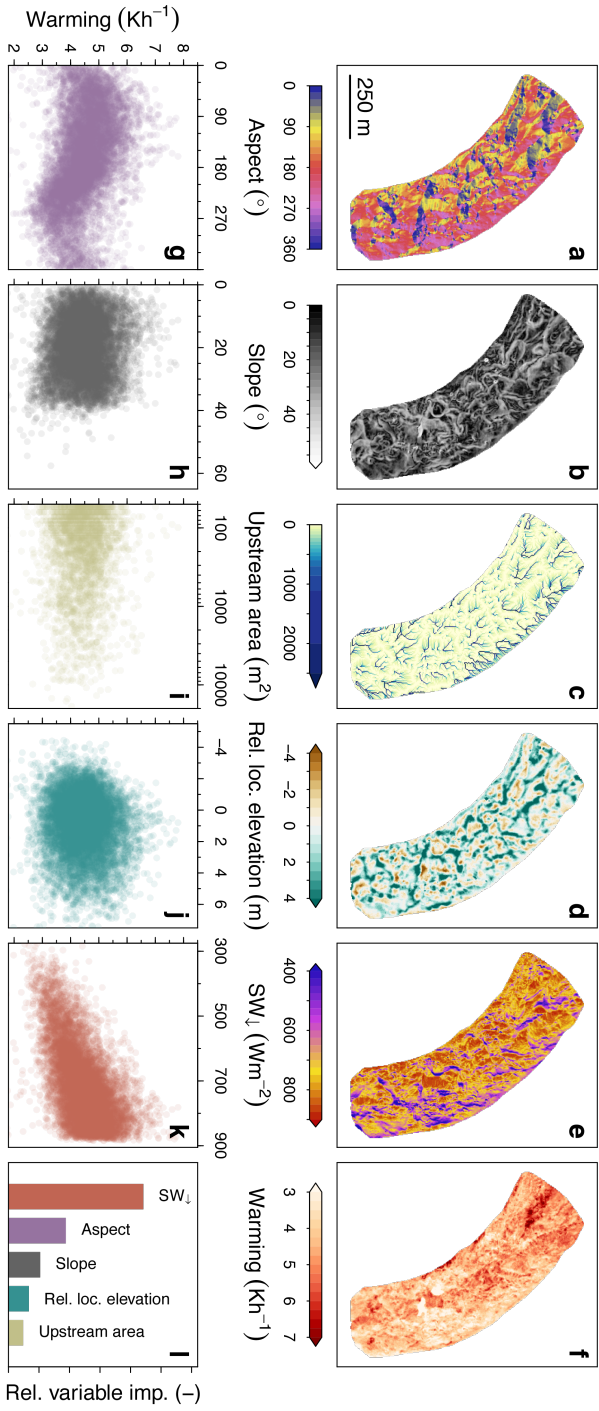


Figure 5.11: Comparison of the average warming rate (f) over the surveyed glacier surface area (Figure 5.6a) with five different DEM derivatives: aspect (a, g), slope (b, h), upstream area (c, i), relative local elevation (d, j), and mean incoming shortwave radiation (e, k). The relative importance of each variable as a predictor in a random forest regression is shown in panel l.

infrared sensor. There are distinct spatial patterns in the output maps of  $T_s$  and the temporal variability of temperature is captured well in the three flights that were performed. The spatial variability in temperatures is partly explained by the complex local topography, as sunlit slopes and big boulders will warm more than shaded slopes and local depressions, and by differences in ground cover. The random forest analysis performed in this study shows that, of topography-related variables, incoming shortwave radiation has the largest effect on the warming rate of the glacier surface. In general, however, surface topography is unable to account for the majority of the warming rate signal, as 61.2% of the variance remains unexplained. Consequently, spatial variations in the glacier's surface properties and processes seemingly play a large role in controlling debris surface temperatures. The high-resolution thermal imagery therefore has various potential applications in the research of the debris-covered glaciers.

An obvious application of high-resolution thermal imagery is to inversely estimate debris-cover thickness (Chapter 7; Foster et al., 2012; Gibson et al., 2017; Mihalcea et al., 2008b; Rounce & McKinney, 2014; Schauwecker et al., 2015), since thickness is an important variable in the surface energy balance of debris-covered glaciers (e.g. Collier et al., 2015; Nicholson & Benn, 2006, 2013; Ragetli et al., 2016b). As I show in this study, the UAV is able to capture spatial patterns and heterogeneity in  $T_s$  (Figure 5.7, Figure 5.10). This would allow for detailed estimations of debris thickness, which in turn may lead an improved understanding of small-scale glacio-hydrological surface processes on debris-covered glaciers. The temporal information on  $T_s$  provided by the repeat UAV surveys might be particularly valuable. Analysis of spatially variable warming rates of the debris (such as presented in Figure 5.11), for example, may provide more detail on actual debris thickness than a single image. Performing more flights over the course of the day and increasing the temporal resolution would therefore be worthwhile.

Secondly, surface temperature imagery at such high resolution may reveal important insights in the energy balance of a debris-covered glacier. The energy balance drives the melt of the debris-covered tongues and several studies point towards a yet unexplained faster surface lowering of the tongues of these glaciers than what can be expected based on the melt suppression by thick debris (Azam et al., 2018; Gardelle et al., 2013; Käab et al., 2012; Pellicciotti et al., 2015). It is unclear whether this behaviour can be attributed to turbulent fluxes, supra-glacial features such as cliffs and ponds, a reduced emergence velocity or other processes (Azam et al., 2018; Vincent et al., 2016). Highly detailed information about the surface temperature provides  $LW_{\uparrow}$ , a term often assumed to be spatially constant and only measured point-scale at a weather station (Reid et al., 2012; Steiner & Pellicciotti, 2016). Our results show it is highly variable and will therefore also explain a large part of the variability in net energy available for melt. In addition, the surface temperature controls the sensible heat flux, which plays an important role in the energy balance of debris-covered glaciers and ice cliffs (Buri et al., 2016a,b; Steiner & Pellicciotti, 2016; Steiner et al., 2015). A comparison of thermal imagery collected before and after precipitation events might also help identify the role of moisture in the debris layer and its effect on latent heat fluxes, and lead to an overall improvement in turbulent flux parameterizations (e.g. Radić et al., 2017).

Thirdly, thermal UAV imagery could be applied in understanding the surface and subsurface hydrology. Englacial hydrology likely plays a key role in the drainage and transport of melt water through the glacier to the outlet (Miles et al., 2017a), but the drainage paths are complex and difficult to measure. With a combination of thermal imagery, optical imagery, and the high-resolution DEM, it may be possible to infer supraglacial (sub-debris) and englacial drainage patterns.

#### 5.4.2 Satellite-based surface temperatures

Spaceborne thermal infrared imagery has the advantage that, if atmospheric conditions permit,  $T_s$  can be acquired relatively accurately for large spatial extents and remote areas (Li et al., 2013). Currently, this is a limitation of UAVs, since it is infeasible to deploy them over large inaccessible areas on a regular basis. However, in the study of supraglacial debris, the distinct advantages of thermal satellite imagery are largely counteracted by the inability of its moderate resolution to resolve the spatial heterogeneity in  $T_s$  found over debris-covered glaciers (Figure 5.10). Although the imagery can be used for coarse maps of debris thickness (e.g. Chapter 7; Mihalcea et al., 2008b), surface melt varies considerably over smaller spatial scales, as indicated by the hummocky surface of most debris-covered glaciers. The heterogeneity of surface elevation changes (Chapter 3) and the thermal UAV data presented in this study further supports a high variability of melt rates and possibly debris thickness. To better understand the local surface energy balance and the processes involved, thermal imagery with a sufficiently high resolution, i.e. a resolution finer than the spatial scale of the melt patterns, is required. An additional advantage of the UAV is the possibility to deploy it synchronously with other *in situ* measurements to acquire complementary data.

In addition to the limitations imposed by sensor resolution, spaceborne thermal imagery is unable to capture sub-daily temporal variations in surface temperature (with the exception of very coarse-resolution geostationary meteorological satellites). The temporal variation observed in  $T_s$  over the three UAV flights, shows us that the use of a single satellite image in the assessment of the debris-layer could be an issue. Surface temperatures on debris-covered glaciers will vary significantly with day of year, time of day, and cloud conditions prior to acquisition, and the variability that occurs on short time scales (Figure 5.8b-e) will affect satellite-based analyses of the debris layer.

However, further implementation of the method I present in this study in the research of debris-covered glaciers does not only have the potential to improve our knowledge of small scale debris-covered glacier surface processes. Together with more process-oriented studies, more elaborate comparison of satellite and UAV data has the potential to improve the moderate resolution spaceborne thermal products, spatially and temporally. Namely, development of optical- or DEM-based downscaling of spaceborne thermal data using the UAV products could provide a way to upscale our knowledge on small scale surface processes to the glacier or catch-

ment scale, which will enable better assessments of the impacts future changes in debris-covered glacier dynamics may have. Moreover, UAV data could prove valuable in the validation of thermal satellite imagery of debris-covered glaciers.

### 5.4.3 Bias correction and errors

The presence of the sensor bias of  $6.9^{\circ}\text{C}$  reveals difficulties in the determination of absolute debris temperatures with the thermoMAP. The sensor bias correction I have applied is based on the assumption that clean ice cliff surfaces will be at melting point and thus  $0^{\circ}\text{C}$  during Flight 2 and 3. This is a reasonable assumption, but admittedly there are uncertainties regarding its usability. For instance, atmospheric variability, such as air temperature and water vapor content, may affect the bias over time (Torres-Rua, 2017). It was not taken into account because of a lack of accurate data of the atmospheric column over the glacier that is required for such a correction (e.g. Li et al., 2013; Perry & Moran, 1994; Torres-Rua, 2017). The potential effect on the measurements is likely limited, however, due to the relatively shallow column of about 90 m and the generally dry air (Figure 5.3). The Tidbit measurements and the independently corrected Flight 1 thermal data are in relatively good agreement (Figure 5.8a), and the FLIR C2 data reveals stabilization of ice cliff temperatures at the melting point (Figure 5.9). I therefore have confidence that the magnitude of the applied bias correction is correct, but it is impossible to determine this with high accuracy. Future efforts in determining the bias may be improved by deploying additional markers on the glacier with known emissivity and known temperature, measured by a well-calibrated hand-held thermal infrared sensor. Preferably these would be distributed over a range of different surface temperature to evaluate non-linearity of the bias.

### 5.4.4 Temperature measurement comparisons

The experiments performed to determine Tidbit temperature overestimation under incoming solar radiation revealed a clear and distinct relation of  $\Delta T$  with  $\text{SW}_{\downarrow}$  for both reference surfaces. Comparison of  $T_{\text{cor}}$  with UAV-derived  $T_s$  on the other hand, shows deviations between both datasets, especially under higher temperatures (Figure 5.8a). One of the probable causes is insufficient Tidbit bias correction, indicated by much better performance of Tidbit measurements in the shade and water. Also, the correction of near-surface temperature measurements uses only two correction slopes that will not work equally accurate for all surfaces on which the Tidbits were placed, because of slight variations in surface type, moisture content, shading, and indirect radiation among others.

Probably most important in this case, however, is that the thermodynamic temperature measured by the Tidbits is different from the skin temperature measured radiometrically by the UAV (Section 5.2.1), and a direct comparison of the two temperatures is not entirely fair. The Tidbit measurements are greatly affected by a micro climate that develops within the plastic casing of the Tidbit sensor, which will heat up differently than the skin of the underlying surface that

is measured by the UAV. This mismatch is expected to be of different magnitude for different surface types. Ground-based radiometric measurements with a hand-held TIR sensor are better suited to validate the UAV-derived  $T_s$  (e.g. Turner et al., 2014). This is not trivial, however, since for proper validation measurements would have to be performed at the time of the survey at multiple locations within a UAV survey area, which is practically infeasible on a debris-covered glacier. Furthermore, such comparisons are also subject to uncertainties (Ribeiro-Gomes et al., 2017), as is also shown by the skin temperatures measurements made using the FLIR C2.

$T_s^{C2}$  is considerably lower than UAV-derived  $T_s$  in early morning, which may partly be attributed to the uncertainties in exact timing of the UAV images. That is, the UAV imagery is captured over a ~15 minute timespan in which  $T_s$  can rapidly change. Unfortunately, the flight pattern of the UAV (supplementary data) in combination with the SfM-MVS orthomosaicking makes it impossible to know the exact measurement time of each pixel in our setup. Improving the timing of UAV to ground-based data is advisable. It could possibly be improved by capturing ground-based thermal video instead of images, as this would ease syncing. While lower at the beginning of the survey in early morning,  $T_s^{C2}$  for debris is considerably higher than  $T_s^{F2}$  and  $T_s^{F3}$ . This is likely explained by the difference in camera angle, i.e. forward looking (C2) in comparison with nadir (UAV). The C2 imagery was taken in west-southwest direction and consequently the east faces of boulders, which heat up first, were in view. The UAV captures the entire surface including the colder west faces, leading to a lower average  $T_s$ . The viewing angle of a thermal camera has a considerable effect on the emissivity of an object. For instance, viewing angles of  $70^\circ$  for water lower the emissivity to about 0.89 (Sobrino & Cuenca, 1999) and thereby increase reflectivity, since these are inversely related. This is likely the cause of the higher temperature readings of the C2 for supraglacial pond class, since the angle between the sensor and the pond normal was very large. Primarily the part of the pond located center right on the image (Figure 5.9c) has an increased temperature, which could originate from reflected thermal infrared signal of the debris face behind.

## 5.5 Conclusions

In this study I present a method to map the surface temperatures of a high-elevation debris-covered glacier using a thermal infrared sensor mounted on a UAV. From our study and method development I draw the following main conclusions:

- Thermal surveys from UAV platforms provide an easy and reasonably quick method to acquire high-resolution and multi-temporal temperature maps of the surface of debris-covered glaciers.
- Obtaining absolute temperatures of the glacier surface using UAV-based thermal imaging is difficult, and it is important to have accurate ground control with reference temperatures and emissivity to improve accuracy of the results.

- The temperature of the debris layer on Lirung Glacier is temporally highly variable, with temperatures ranging from near-freezing to about 50 °C over the course of four hours. Spatially, surface temperatures are highly heterogeneous.
- Much of the spatial heterogeneity in surface temperature is not captured in Landsat 8 thermal imagery, and satellite revisit times prohibit the acquisition of diurnal temperature variations. Satellite image analyses of small to moderate scale debris thickness and surface energy balance should therefore be performed thoughtfully and may benefit greatly from statistical downscaling using UAV data.
- High-resolution, multi-temporal thermal mapping of debris cover has the potential to improve analyses of debris thickness, surface hydrology, and turbulent fluxes, thereby improving the understanding of the surface energy balance of the debris layer and the glacier surface.

### Author contributions

PK, WI, and JMS designed the study. DT and IK performed the *in situ* surveys. WI, JMS, and PK performed the UAV surveys and JFS lead UAV test flights. ML and JMS designed and performed the temperature experiments and correction scheme. PK processed the UAV data and performed the analyses. PK wrote the manuscript with suggestions and input by JMS, ML, JFS, DT, IK, and WI.



---

## Automatic surface feature detection

Debris-covered glaciers in the Himalaya may have spatially-averaged rates of surface height change that are similar to those observed on bare-ice glaciers, despite the insulating effects of thick debris. Spatially heterogeneous melt patterns caused by the development and evolution of ice cliffs and supraglacial pond systems result in substantial mass losses over time. However, mechanisms controlling the formation and survival of cliffs and ponds remain largely unknown. To study the distribution and characteristics of these surface features I deploy an unmanned aerial vehicle (UAV) over a stretch of the debris-covered Langtang Glacier, Nepal. Acquired images are processed into high-resolution orthomosaics and elevation models with the Structure from Motion (SfM) photogrammetry algorithm. Ice cliffs and ponds are classified using object-based image analysis (OBIA) and their morphology and spatial distribution are analysed and evaluated using object, pixel and point cloud approaches. Results show that ice cliffs are predominantly north-facing, and larger ice cliffs are generally coupled with supraglacial ponds, which may affect their evolution considerably. The spatial distribution of ice cliffs indicates that they are more likely to form in areas where high strain rates are expected. The spatial configuration of ponds over the entire tongue reveals high pond density near confluences, possibly due to closure of conduits via transverse compression. I conclude that the combination of OBIA and UAV imagery is a valuable tool in the semi-automatic and objective analysis of surface features on debris-covered glaciers. The technique may also have potential for upscaling to the use of spaceborne imagery, and the use of UAV-derived point clouds to analyse ice cliff undercuts is promising.

Chapter based on:

Kraaijenbrink, P. D. A., J. M. Shea, F. Pellicciotti, S. M. De Jong, and W. W. Immerzeel (2016). **Object-based analysis of unmanned aerial vehicle imagery to map and characterise surface features on a debris-covered glacier.** *Remote Sensing of Environment*, 186, 581-595.

## 6.1 Introduction

Glaciers are an important component of the rivers in High Mountain Asia (HMA) that provide a large number of people with water for irrigation, electricity production, sanitation, and religious practices (Immerzeel et al., 2010). With the exception of the Karakoram, glaciers in HMA have experienced negative glacier mass balances over the past decades (Bolch et al., 2012; Gardelle et al., 2012; Kääb et al., 2012, 2015). Sustained negative mass balances have resulted in a decreased volume of ice stored in these mountain ranges. Under current climate projections, accelerated glacier mass loss and increased glacier melt water runoff are expected in the coming decades (Shea et al., 2015). Towards the end of this century, however, the reduction in glacier area and volume will result in decreased ice melt contributions to streamflow (Immerzeel et al., 2013).

To increase our ability to predict and adapt to these future changes induced by climatic change, it is key to more about the melt processes of glaciers in this region. Debris-covered glaciers in particular, which account for about 10% of the glaciers in HMA (Bolch et al., 2012), are relatively understudied because of difficulties in both accessibility and the collection of in situ measurements. Very thin layers of supraglacial debris will enhance ice melt, but buried ice is insulated from melt once a critical debris thickness of a few centimetres is reached (Mattson et al., 1993; Østrem, 1959; Reznichenko et al., 2010). Spatial variability of debris thickness (Nicholson & Benn, 2013) and properties such as albedo, roughness, porosity and moisture content, further complicate the effects of debris cover on local glacier melt (Evatt et al., 2015). The lower elevations of debris-covered glaciers, i.e. the areas where melt rates are typically greatest for bare-ice glaciers, generally have thick debris which thins upglacier (e.g. Anderson & Anderson, 2016; Nicholson & Benn, 2013; Rounce et al., 2015). Supraglacial debris should consequently have an overall melt-reducing effect. However, several studies report that debris-covered glaciers in the Himalaya have elevation change rates similar in magnitude to uninsulated, bare-ice glaciers in the same region and at the same altitude (Gardelle et al., 2013; Kääb et al., 2012).

This debris-cover anomaly (Pellicciotti et al., 2015) may be linked to ice cliffs that form on debris-covered glaciers (Figure 6.1) and provide a mechanism for high melt rates because of their low albedo and surface exposure (Sakai et al., 1998). Recent studies confirm that the ice cliffs accelerate melt locally (Chapter 3; Buri et al., 2016b; Miles et al., 2016; Reid & Brock, 2014; Steiner et al., 2015). However, their exact effects on and interplay with larger scale glacier melt dynamics are still largely unknown.

Ice cliffs on debris-covered glaciers are thought to form in three different ways: slumping of debris from steep slopes, calving into supraglacial ponds or by the collapse of englacial voids (Benn et al., 2012). Once ice becomes exposed, a positive surface energy budget will result in ice melt and backwasting of the cliff. The main components of ice cliff energy budget include both direct and diffuse solar radiation as well as longwave radiation from the atmosphere and surrounding debris (Sakai et al., 2002). South-facing ice cliffs (in the northern hemisphere) generally disappear quite quickly after their formation (Buri et al., 2016b; Steiner et al., 2015). It

is hypothesized that bases of such ice cliffs receive less incoming solar radiation than the tops of the cliffs and experience less ice melt. This causes slope relaxation and eventually burial by debris when the slope becomes less than about  $30^\circ$  (Sakai et al., 2002). In contrast, north-facing cliffs do not experience direct solar radiation because of shading by the cliff itself. The surface energy budget is thus composed mainly of diffuse shortwave radiation and longwave radiation from the surrounding debris and the atmosphere. Because the debris-view factor (Reid & Brock, 2014) is larger at the base, north-facing cliffs experience more incoming longwave radiation there which tends to steepen and sustain the cliffs (Buri et al., 2016b; Reid & Brock, 2014; Steiner et al., 2015).



**Figure 6.1:** Photograph of an ice cliff on Langtang Glacier with an adjacent, partly-drained supraglacial pond typically found on debris-covered glaciers in the Himalaya (Photo: Joseph Shea).

Some ice cliffs have adjacent supraglacial ponds, i.e. water bodies of a similar scale as the ice cliffs that touch the base of the exposed ice (Figure 6.1). Observations show that these ponds fill and drain over time (e.g. Chapter 3; Benn et al., 2000; Gardelle et al., 2011; Roehl & Röhl, 2008; Wessels et al., 2002). Ponds may be filled by surface runoff, englacial conduits, or cliff melt, and drainage occurs via conduits (Benn et al., 2012; Gulley & Benn, 2007). Total pond area on debris-covered glaciers is largest at the onset of the melt season, because of snow and ice melt. As the melt season progresses, and water is transported through the englacial hydraulic system, the drainage efficiency increases (Miles et al., 2017c). Energy stored in the water is transferred

to the surrounding ice, conduits are enlarged, and englacial conduit collapse could lead to the formation of ice cliffs (Miles et al., 2016). Changes in the hydrological regime from a slow distributed drainage to fast channelised drainage also has consequences for glacier velocity and deformation (Bjornsson, 1998; Hewitt, 2011; Mair et al., 2010) and may therefore also contribute to the difference in pond outflux between the seasons.

When water is in contact with an exposed ice cliff, energy is transferred from the water to the cliff face through two processes. Firstly, the density/temperature relation of water causes pond circulation and promotes melt along the ice-water interface through this free convection. Secondly, wind fetch may force currents that drive thermal erosion of the exposed subaqueous ice surface (Miles et al., 2016; Sakai et al., 2009). These processes result in thermal undercutting, notch development, and ice cliff calving (Röhl, 2006).

In recent years there have been many developments in the use of unmanned aerial vehicles (UAVs) for environmental monitoring. As the technology has advanced, their use has become a viable option for scientists to perform detailed remote sensing surveys. At present, UAVs are being used in an increasing number of fields of natural sciences (Colomina & Molina, 2014), and have been proven to be exceptionally useful and a promising tool in glaciology (Chapter 3; Chapter 4; Bhardwaj et al., 2016; Ryan et al., 2015; Westoby et al., 2012, 2016; Whitehead et al., 2013). For debris-covered glaciers, UAVs offer a valuable addition to traditional measurements. Although capable of measuring the true glaciological mass balance, glaciological mass balance measurements on debris-covered glaciers (e.g. Vincent et al., 2016) require the installation of ablation stakes through a debris layer, which disturbs the surface. The spatial and temporal resolution of spaceborne remote sensing imagery is typically too coarse to study glaciers in detail. Satellite revisit periods can be considerable and atmospheric disturbances and clouds can render image scenes useless (Lillesand et al., 2015). UAV imagery fits a gap here as it allows the acquisition of on-demand, high spatial and temporal resolution imagery for continuous surfaces on a medium spatial scale of up to several square kilometres. Overlapping images acquired by UAVs can be used to create highly-accurate 3D-models and orthorectified image mosaics using Structure from Motion (SfM) photogrammetry (Snavely, 2008, 2011; Szeliski, 2011). UAV data are therefore valuable for debris-covered glacier studies, including surface feature morphology (Brun et al., 2016) and energy balance modelling (Buri et al., 2016b).

Traditionally, remote sensing image classification and image entity extraction is done using pixel-based image analysis (PBIA). Every pixel is evaluated and grouped together on the image level by means of statistical clustering of pixel values, with or without the use of training samples in the clustering process (Lillesand et al., 2015). When pixel sizes are similar in size or coarser than the entities of interest PBIA is the preferred technique. On the other hand, when dealing with high spatial resolutions the analysis of objects that are constructed by multiple pixels is preferred (Blaschke, 2010; Blaschke et al., 2014). This object-based image analysis (OBIA) requires the segmentation of an image into near-homogeneous groups of pixels, i.e. objects (Baatz & Schäpe, 2000). This is performed by growing objects, starting from a pixel-scale, and itera-

tively merging them with neighbours. The merges are directed by relative object heterogeneity and internal homogeneity criteria that are based on weighted spectral and shape characteristics (Trimble, 2015). OBIA techniques thus have important advantages compared to traditional pixel-based methods, and are much closer to how we as humans observe the world around us.

The set of objects that result from OBIA segmentation provide great advantages compared to the pixel clusters available in PBIA. Namely, polygonal objects can be analysed to provide more than just spectral information. Spatial, contextual, hierarchical and textual attributes of the objects allow for highly complex image analyses and classifications that can improve classification accuracy (Blaschke et al., 2014; Liu & Xia, 2010; Robson et al., 2015). As the objects consist of groups of pixels, statistical properties of each of the objects' pixel population are also available for analysis. Moreover, multiple sources of pixel data can be used simultaneously in OBIA in both the segmentation and analysis stage, e.g. optical and elevation data. Actual classification of objects is performed via two main strategies or a combination of them: (i) by statistical classifiers such as nearest neighbour or a random forest, or (ii) by rule-based classification (Lillesand et al., 2015). A difficulty with OBIA is the selection of object scale in the segmentation procedure (Addink et al., 2007; Gao et al., 2011). There is the possibility of over- and under-segmentation, i.e. either too small or too large objects with respect to the features of interest, which can result in reduced classification accuracy (Liu & Xia, 2010). Methods have been developed to mitigate the effects and provide more objectivity to the segmentation (Drgu et al., 2014), which is especially valuable for the classification of large scale areas with different entities of different sizes.

In glaciology, there have been relatively few studies that utilize OBIA. The technique has so far been used to map glacier extents (Ardelean et al., 2011; Bajracharya et al., 2015; Karimi et al., 2015; Nie et al., 2010; Nijhawan et al., 2016; Rastner et al., 2014; Robson et al., 2016, 2015), glacial lakes (Nie et al., 2013; Qiao et al., 2015), icebergs (Foga et al., 2014) and glacial landforms (Eisank et al., 2011) from satellite imagery using mostly rule-based classification strategies. Most studies combine different types of data, e.g. optical, thermal, radar and elevation, and show that such a strategy improves the classification. Rastner et al. (2014) noted that glacier outlines mapped using OBIA have an overall higher quality than those obtained by PBIA. In particular, they find that contextual OBIA resulted in a 12% improvement in accuracy.

For the delineation of surface features on the almost exclusively gray-shaded surfaces of debris-covered glaciers OBIA may be preferable to PBIA. Spectral contrast between different surface elements is low and thus analysis of shape is key. Considering high-resolution UAV data this is particularly true, as its pixel size of a few centimetres is considerably smaller than the features of interest that are usually in the order of tens of meters. A study by Watson et al. (2016a) suggests that this idea is valid as they successfully mapped supraglacial ponds on a debris-covered glacier using OBIA of high-resolution satellite imagery.

In this study I analyse the spatial distribution of ice cliffs and supraglacial ponds on the lower part of the debris-covered Langtang Glacier in Nepal (Figure 2.7). The features are delineated

by OBIA of UAV-acquired data of May 2014. I then systematically analyse the features based on their geometric characteristics and spatial configuration. Additionally, I use a satellite image to perform an analysis of pond presence on the entire debris-covered tongue of the glacier (Figure 2.2). Our study has two main objectives:

- To test whether quantitative data on ice cliffs and supraglacial ponds can be extracted from high-resolution imagery using a semi-automatic object-based classification approach.
- To examine the distribution and morphology of these features on Langtang Glacier and discuss their formation, dynamics and relation to the overall glacier dynamics.

## 6.2 Data and methods

### 6.2.1 UAV survey

A 3 km long section of the snout of Langtang Glacier was surveyed by UAV on 7 May 2015 during clear conditions and relatively soft winds. To cover a glacier surface area of 2.7 km<sup>2</sup> (Figure 6.2), two 25-minute flights were performed with the eBee (SenseFly, 2015), a fixed-wing UAV produced by the Swiss company SenseFly. The UAV was launched from the western moraine and was programmed to land in a nearby field.

In flight, the UAV followed waypoints of a predefined flight plan at an altitude of approximately 200 m above the take-off elevation (4580 m) using its built-in GPS. The flight plan allowed for lateral and longitudinal overlaps of ~60% and 75% respectively, and a ground resolution of ~6 cm per pixel (px). The camera mounted for the survey was a Canon IXUS 127 HS compact camera carrying a 16 megapixel sensor. The focal length of the camera's zoom lens was set to its widest setting of 4.3 mm to increase image overlap and reduce the number of required photos and flight time. The camera's uncalibrated RGB images are stored in the JPEG format. In total the UAV acquired 286 separate images of which seven were discarded after visual inspection because of poor image quality, i.e. exposure or motion blur issues.

In order to improve the geodetic accuracy of the output product during processing, 16 ground control points (GCPs) in the form of 1.0 × 1.2 m pieces of red fabric were distributed on the lateral moraines beforehand (Figure 6.2a). The coordinates of the centre of the markers were measured using a differential global positioning system (dGPS), i.e. a Topcon GB1000 antenna with a PG-A1 receiver. This particular system has a reported base station accuracy of ~0.2 m in x, y and z (Chapter 3; Chapter 4; Wagnon et al., 2013).

### 6.2.2 UAV data processing

Images from the UAV survey ( $n = 279$ ) were processed using SfM as implemented in the software package Agisoft Photoscan Professional version 1.1.6 (Agisoft LLC, 2014). In the workflow (e.g. Chapter 3; Chapter 4; Lucieer et al., 2013; Westoby et al., 2012), feature recognition and

matching algorithms are applied to the input set of overlapping images to generate a sparse point cloud via bundle adjustment (Szeliski, 2011). Camera positions and orientations, initialised by GPS coordinates recorded by the UAV for every image, are also solved in these calculations using the very high image overlap.

The sparse point cloud was cleaned from poorly localised points and false matches by thresholding the point reprojection error, i.e. the distance in pixels between a projected point and a measured one (Agisoft LLC, 2014). All points that were localised with an error larger than 0.6 px were removed from the cloud. Accurate georeferencing of the output product in an absolute coordinate system is achieved by introducing the dGPS-measured GCPs and adjusting the sparse point cloud accordingly. In contrast to traditional photogrammetry, this is done after the bundle adjustment in SfM (Fonstad et al., 2013).

Using the optimised camera positions and the image data itself, multi-view stereo techniques (Westoby et al., 2012) were applied to produce depth information per image and a dense 3D point cloud of the glacier surface. The dense point cloud was used to construct a gridded DEM (Figure 6.2c) with a resolution of 0.2 m by averaging the points within a pixel. Additionally, the elevation information was used to create an orthomosaic with a resolution of 0.1 m (Figure 6.2b). All processing steps in Agisoft Photoscan, i.e. feature matching, bundle adjustment and densification, were performed with the quality settings set to high to achieve an optimal balance between required processing time and output accuracy.

The geodetic accuracy of the DEM and the orthomosaic was estimated by measuring the difference between the GCP coordinates and their positions on the output orthomosaic ( $x,y$ ) and DEM ( $z$ ) in a geographical information system (GIS). Unfortunately, because of the inaccessible terrain it was not feasible within the weather window to place additional independent GCPs that could be used for accuracy checks, as all the control points were required for processing. However, as no geodetic comparison is made here between datasets from different acquisition times, this has no effect on the analyses and results presented in this study.

### 6.2.3 Object-based UAV imagery classification

#### Classification preprocessing

Before classification, UAV data were cropped to a manually digitised outline of the area where ice was assumed to be present under the debris. This pre-processing step aims to minimise the possible negative influences of non-glacier areas on the classification procedure. Six different UAV data derivatives were chosen as input to the classification: (1) blue band of the orthomosaic, (2) green band of the orthomosaic, (3) red band of the orthomosaic, (4) brightness, i.e. the mean signal of the three bands, (5) DEM and the (6) DEM-derived slope.

All three visible bands were included to utilise the limited spectral information that the UAV system provides. Elevation and slope were included because cliffs and ponds both have a specific

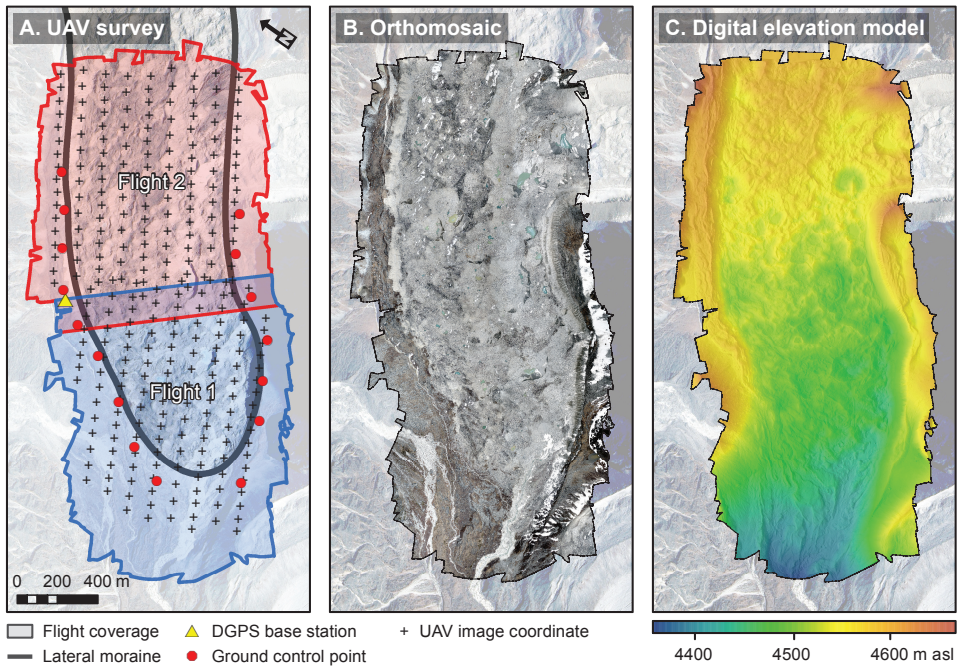


**Figure 6.2:** The coverage of the two UAV flights performed on the 7th of May 2014, and the positions of the ground control markers and the DGPS base station (a); The orthomosaic obtained by SfM image processing (b); Digital elevation model obtained by SfM image processing (c).

elevation signature, i.e. relatively uniformly sloped and completely flat, respectively. However, because of the high resolution of the UAV data the local variation of the slope map is relatively large. Small scale variation in morphology of ice cliffs could negatively influence the classification of these much larger features of interest. A  $3 \times 3$  px averaging filter was therefore applied to spatially smooth the slope map.

Ice cliffs generally consist of a relatively homogeneous, dark grey surface with a few lighter patches and occasionally banding patterns. Debris has a spectrally more uniform distribution because of the small boulders and the shadows they cast (Figure 6.1). To make better use of this contrast between cliff and debris in the classification, the 0.1 m resolution brightness raster was processed into two different products: (1) a local brightness variation map made by applying a  $5 \times 5$  px standard deviation filter, and (2) a smoothed brightness map produced using a  $3 \times 3$  px averaging filter. Finally, to reduce the influence of noise in the UAV-data and to increase the potential use of the classification procedure on similarly high-resolution satellite imagery in the future, all input data were resampled to 0.5 m.

## Image segmentation

To create objects a multi-resolution segmentation algorithm (Batz & Schäpe, 2000) was applied to the input layers in the OBIA software eCognition Developer 9.1.2 (Trimble, 2015). Most entities on a debris-covered glacier, except for supraglacial ponds, exhibit considerable variation in elevation and slope. As finding homogeneous regions drives the segmentation, elevation and slope data were thus excluded from the segmentation procedure. The object-to-object heterogeneity is determined using both spectral and shape characteristics (Benz et al., 2004), which can be weighted by the user. Ice cliffs and ponds have a distinct shape compared to the surrounding debris and therefore a relatively high weight of 0.4 was given to the shape parameter. The segmentation is also influenced by a compactness setting, which is defined by the ratio of the object circumference and the number of pixels forming an object (Benz et al., 2004). As ice cliffs are usually elongated and ponds are compact a moderate compactness setting of 0.5 was used.

The surfaces of most ice cliffs are not solely bare ice, and there are often patches of debris or snow (Figure 6.1). A similar situation exists for supraglacial ponds that can contain debris mounds or floating ice. The scale of the output objects in the segmentation procedure was therefore not set to the scale of the cliffs or ponds, but the scale of these subfeatures. Because of the limited amount of features and feature scales in the study area, the optimal scale was not determined automatically (Drgu et al., 2014). Instead, the scale parameter in the multiresolution segmentation was determined by expert judgement, and set to 500. This provided the least (visually determined) over- and under-segmentation of the region of interest.

## Object-based training, classification and accuracy

On the glacier surface four distinct main classes are present: ice cliffs, ponds, debris and snow (snow patches on debris or snow frozen to ice cliffs). For classification I first evaluated the use of a rule-based approach that used thresholds on slope, brightness and homogeneity of the objects as well as contextual rules. The rule-based approach was found to be difficult to implement as many rules would have been required to accurately classify the few objects present in the study area. Therefore, I chose to continue with a statistical classifier approach (Figure 6.3) that utilised many object characteristics for classification. Classifier statistics were obtained by gathering a number of training samples randomly for each of the four classes: 20 for ice cliffs, 20 for water, 20 for snow and 50 for debris. The vast majority of the glacier's surface consists of different types and appearances of debris, ranging from lighter to darker coloured patches. In order to obtain a representative sample population a larger number of samples were taken for this class.

To separate the classes, I use object characteristics given by the internal pixel statistics. The shapes of the cliffs, ponds and snow patches and their relations to neighbouring objects are not consistent from one feature to the next, hence shape and neighbour relations cannot be used to distinguish between classes. Debris and ice cliff objects are difficult to distinguish spectrally. On an object level, however, the two classes exhibit different textures. To describe these differences in object texture, four parameters based on the gray-level co-occurrence matrix (GLCM) were determined using the red band of the orthomosaic: contrast, homogeneity, dissimilarity and entropy (Haralick et al., 1973; Trimble, 2015). The final object attributes selected as input for the classification procedure are the mean pixel value per object for all input data layers, the pixel standard deviation per object for all input data layers, and the four GLCM texture parameters.

A fuzzy nearest neighbour (NN) object classification procedure (Blaschke et al., 2008; Trimble, 2015) as implemented in eCognition Developer was applied to classify the object set obtained from image segmentation. I chose the NN procedure because it provided better classification results than other evaluated algorithms, such as random forests (Breiman, 2001; Genuer et al., 2010) or Bayesian classifiers (Lillesand et al., 2015; Trimble, 2015). The NN classifier predicts an objects' class by determining a normalised difference between the average attribute value of the training set and the attribute of an unclassified object. The distances for all input training attributes are combined into a multidimensional vector and used to construct a membership function for all classes. The class with the highest membership value is assigned to the object (Trimble, 2015).

To finalise the classification a rule-based alteration was applied. Objects that were completely enclosed by cliff or pond objects were classified as cliff and pond respectively. Also, to classify the snow patches frozen to ice cliffs as cliff, all objects classified as snow that were within one object distance to an cliff object and on a slope larger than  $30^\circ$  were assigned the class cliff.

For the analysis of ice cliffs and ponds it is important to have a classification that is as accurate as possible, especially considering a study area with such a limited number of features of interest

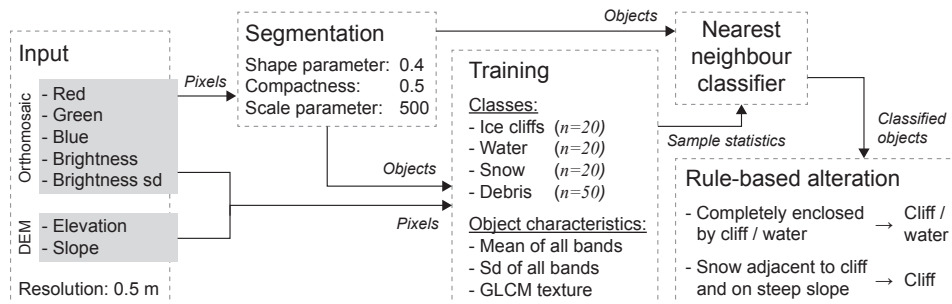


Figure 6.3: Flowchart of the steps and settings used in OBIA procedure used to classify the cliffs and ponds.

present. To maximize the accuracy the NN classification was altered through a multi-pass visual inspection. Misclassified objects were manually reclassified in this procedure based on expert and field knowledge. The resulting reference object set was used to create error matrices (Lillesand et al., 2015) to estimate classification accuracy. The NN classification was performed multiple times using different sets of object attributes. The estimated accuracy was then used to determine the set that provided the best classification.

To finalise the cliff and pond delineation, individual neighbouring objects of snow and debris classes were fused into single objects. The exposed ice faces of cliffs are often partially buried by debris and ponds are sometimes at a low water level that separates them into a few unconnected smaller ponds. These objects were assigned to a specific cliff or pond group by visual inspection. Finally, ponds that are assumed to be adjacent to ice cliffs for at least some time during the year were identified and jointly classified as dynamic cliff-pond systems.

### Pixel-based classification

To evaluate the difference in classification accuracy of OBIA and PBIA, a pixel-based supervised classification procedure (Lillesand et al., 2015) was performed on the preprocessed UAV data using a maximum likelihood classifier. The red band, green band, blue band and slope data were taken as input and the classifier was trained using representative samples for the classes water, cliff, snow and debris. As the small pixel size of the UAV data and the limited spectral contrast between the classes results in high-frequency classification patterns, the output was smoothed using a  $3 \times 3$  px majority filter.

The accuracies of the OBIA and PBIA were determined using error matrices constructed from random samples. Debris is much more abundant than the other three classes and that may impact the accuracy assessment. A stratified random sampling approach was therefore used to sample 250 random points for each of the four classes, according to the created reference object set. All 1000 points were subsequently checked visually on the orthomosaic for the actual class present at each point's location.

### 6.2.4 Analysis of feature characteristics

Ice cliff slope and aspect as well as supraglacial pond presence are thought to be important factors in the existence and survival of ice cliffs (Buri et al., 2016b; Miles et al., 2016; Steiner et al., 2015). To assess these characteristics quantitatively, UAV-derived slope and aspect were extracted for each cliff using the classified objects. Mean and standard deviation of cliff slope and aspect were calculated and compared with exposed ice surface area, which was determined trigonometrically.

Ponds classified on the UAV imagery were analysed by their mean elevation, their area, and their relation to adjacent cliffs. The ponds appear to have highly variable concentrations of suspended sediments as their colour varies considerably from pond to pond (Takeuchi & Kohshima, 2000; Wessels et al., 2002). Pond colours range from dark blue (low sediment concentrations) to light brown/orange (high sediment concentrations). To test if the suspended sediment concentrations are dependent on pond size or the presence of an ice cliff nearby, a blue index (BI) of the ponds was calculated as:

$$BI = \frac{\text{Blue}}{\text{Red} + \text{Green}} \quad (6.1)$$

where the colours stand for the different image bands of the UAV-derived orthomosaic. A BI smaller than 0.5 indicates more orange ponds with high sediment concentrations, and a BI greater than 0.5 indicates more blue ponds with low sediment concentrations.

To investigate the value of the UAV point cloud data for ice cliff morphology analysis, a 100 m long cross section of the UAV-derived 3D point cloud was extracted for a cliff with a large undercut using the open source software CloudCompare (Girardeau-Montaut, 2015). From the cross section, cliff face slopes were determined using linear regression and undercut size was estimated geometrically.

### 6.2.5 Pond distribution over the entire tongue

To examine possible causes for supraglacial pond formation their spatial distribution was determined for the entire tongue of Langtang Glacier through OBIA of a 5 m resolution RapidEye satellite image from 4 March 2010. The imagery was subset using a manually digitised glacier outline, as both the recent GAMDAM (Nuimura et al., 2015) and Randolph v5 glacier inventories (Pfeffer et al., 2014) were too inaccurate for the glaciers in the study area. Previous attempts have been made to classify supraglacial ponds and lakes using ASTER and Landsat data (Chen et al., 2013; Gardelle et al., 2011; Miles et al., 2017c; Wessels et al., 2002). Classification proved difficult without using elevation data. Moreover, shadows of mountains as well as clouds caused problems for classification and require masking, which can yield difficulties for a proper classification of a single image. However, on the RapidEye imagery used here there are no shadows or atmospheric disturbances present.

For the classification, an image segmentation was performed on a small scale, i.e. the smallest objects representing ponds of about 3 px in size. Subsequently, 20 training samples were randomly selected for each of the classes: pond, dark debris, light debris and snow/ice. For classification of the objects a nearest neighbour algorithm was applied using each of RapidEye's five bands for training as well as a normalised difference water index (NDWI), defined as:

$$\text{NDWI} = \frac{\text{Blue} - \text{NIR}}{\text{Blue} + \text{NIR}} \quad (6.2)$$

where Blue and NIR are the blue and near-infrared bands of the RapidEye satellite image, respectively.

In order to determine whether pond presence is dependent on ice dynamics, surface velocity for Langtang Glacier was determined using a pair of ASTER images for the period October 2010 to October 2012. The two L1A ASTER scenes were orthorectified using 1-arc-second elevation data from the Shuttle Topography Radar Mission (SRTM) and co-registered in ENVI (Exelis, 2014). Surface displacement was determined between the preprocessed image pair using frequency cross-correlation as implemented in COSI-Corr (Ayoub et al., 2009; Leprince et al., 2007). Noise in the output velocity fields was removed by moderate non-local means filtering (Buades & Coll, 2005) from within the software.

Stresses within the ice and the resulting deformation are likely larger in areas with high curvature. To examine if this affects pond formation, the curvature of the glacier was determined by analysis of the glacier centreline. The classified ponds were finally analysed by binning them in 1 km longitudinal sections and comparing pond density to the SRTM elevation, ASTER-derived velocity and centreline curvature. These were all sampled at the glacier centreline averaged over 100 m intervals and subsequently low pass filtered to reduce noise and reveal overall trends.

## 6.3 Results

### 6.3.1 UAV data accuracy

The horizontal error of the UAV output products, estimated by comparison of the 16 DGPS-measured GCPs and the marker positions on the orthomosaic and DEM, was found to be 0.05 m on average with a standard deviation of 0.04 m and a root mean square error (RMSE) of 0.07 m. The vertical error at the marker positions has a mean of 0.08 m, with a standard deviation of 0.06 m and a RMSE of 0.11 m. Errors estimated using 10 independent GCPs in a recent study by Vincent et al. (2016) that uses the exact same UAV workflow are on average 0.04 m and 0.10 m in the horizontal and vertical, respectively. Compared to the cliff and pond scale these errors are small and negligible for the uni-temporal analysis performed in this study.

### 6.3.2 Image classification

The spatial subset of the UAV raster data used as input for the segmentation and classification comprised an area of 1.33 km<sup>2</sup> (Figure 6.4). Segmentation of this subset resulted in a total of 5557 objects with a mean area of 240 m<sup>2</sup>. I found that inclusion of the object means and standard deviations of all input layers except the DEM resulted in the highest classification accuracy. Inclusion of any of the GLCM texture parameters caused a decrease in accuracy, especially with regard to cliff delineation. Slope data, on the other hand, proved to be key as accuracy drops considerably when it is omitted. Comparison of all objects of the final NN classification with the reference object set (Table 6.1) shows a producer's accuracy (Lillesand et al., 2015) of 87.4% and 96.7% for ice cliffs and ponds, respectively, when considering object counts. Taking into account object area the accuracy rises to 93.1% and 98.0%, respectively, indicating that misclassification occurs mainly for smaller objects. User's accuracies are even higher, especially for object area. Kappa coefficients for the error matrix, which are a better indication for overall accuracy when having unequal class sizes (Lillesand et al., 2015), indicate good agreement between classification and reference set with a value of 0.93.

The final object set to be used for cliff and pond analysis comprised 73 separate cliffs and 77 ponds. Cliff objects were part of 22 separate cliff systems (Figure 6.4). Most ponds were independent, but a few belonged to a group resulting in a total of 69 pond objects. From the set of cliffs and ponds 14 cliff-pond systems were identified. The final set of classified objects shows that 1.80% and 1.66% of the total area of this section of Langtang Glacier consists of ice cliff and pond, respectively.

Estimates of the difference in accuracy between PBIA and OBIA show that PBIA performs considerably worse on a debris-covered glacier than OBIA (Table 6.2 & Table 6.3). Kappa coefficients for the classification methods are 0.463 and 0.897, respectively. PBIA has difficulty distinguishing debris from the other classes, which is especially true for the cliff class which has a producer's accuracy of only 33.7%.

### 6.3.3 Surface feature distribution and characteristics

#### Ice cliffs

Classification of ice cliffs shows that there is an uneven distribution of these features over the UAV-surveyed area (Figure 6.4). Upstream of the tributary confluence there are no cliffs present, while at the confluence there is a high density of large cliffs. Most of these are part of larger cliff-pond systems. Overall, the majority of cliffs (14 out of 22) are present on the south-eastern lateral half of the glacier. These cliffs comprise the bulk of the exposed ice surface area (79%). On the northern half of the glacier only a group of medium sized cliffs (cliff 9–11 and 14–16) is present. Cliff shape varies from cliff to cliff. Some are straight and elongated, e.g. cliff 7 and 11, while others are much more curved. Near the tributary few completely circular cliff systems

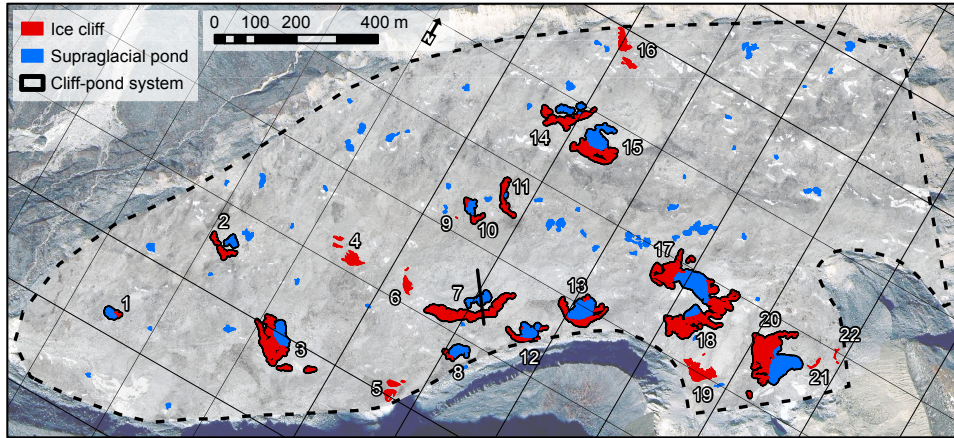


**Figure 6.4:** Ice cliffs and supraglacial ponds on Langtang Glacier as classified on the May 2014 UAV imagery by OBIA. Annotation shows the numbered, grouped cliff objects that belong to the same cliff system. Additionally, cliff-pond systems are outlined with black. The extent of the imagery and elevation subset used as classification input is delineated by the dashed line. The black line at cliff 7 denotes the location of the profile shown in Figure 6.7.

**Table 6.1:** Error matrix for the nearest neighbour classification and the reference classification. Matrices and confusion statistics are shown for both the object counts (top) as the objects' total area (bottom).

<b>Object counts</b> <i>Classification</i>	<i>Reference</i>				
	Cliff	Other	Snow	Snow on cliff	Water
Cliff	160	19	0	1	0
Other	23	4498	33	8	7
Snow	0	13	550	0	0
Snow on cliff	0	3	7	23	0
Water	0	6	1	0	205
Producer's accuracy	0.874	0.991	0.931	0.719	0.967
User's accuracy	0.996	0.930	0.997	0.998	0.999
Overall accuracy	0.978				
Kappa coefficient	0.931				

<b>Object area (m<sup>2</sup>)</b> <i>Classification</i>	<i>Reference</i>				
	Cliff	Other	Snow	Snow on cliff	Water
Cliff	19904	574	0	29	0
Other	1486	1252667	2701	8	440
Snow	0	2807	25729	1283	0
Snow on cliff	0	59	773	1404	0
Water	0	68	6	0	22068
Producer's accuracy	0.931	0.997	0.881	0.516	0.980
User's accuracy	1.000	0.937	0.997	0.999	1.000
Overall accuracy	0.988				
Kappa coefficient	0.929				

**Table 6.2:** Error matrix for the pixel-based classification of the UAV data, constructed from stratified random sampling using a 1000 points.

<b>Pixel-based</b> <i>Classification</i>	<i>Reference</i>			
	Pond	Cliff	Snow	Debris
Pond	161	0	0	0
Cliff	1	81	0	8
Snow	0	0	102	2
Debris	85	159	142	259
Producer's accuracy	0.651	0.337	0.418	0.963
User's accuracy	1.000	0.900	0.981	0.402
Global accuracy	0.603			
Kappa coefficient	0.463			

**Table 6.3:** Error matrix for the OBIA of the UAV data, constructed from stratified random sampling using a 1000 points.

<b>Object-based</b> <i>Classification</i>	<i>Reference</i>			
	Pond	Cliff	Snow	Debris
Pond	240	0	0	4
Cliff	2	223	2	6
Snow	0	1	207	6
Debris	5	16	35	253
Producer's accuracy	0.971	0.929	0.848	0.941
User's accuracy	0.984	0.957	0.967	0.819
Global accuracy	0.923			
Kappa coefficient	0.897			

that form the perimeter of a large supraglacial pond are present, (cliff 13, and 17–18).

Ice cliff slopes are generally between  $25^\circ$  and  $60^\circ$  (Figure 6.5). For the cliff-pond systems there is a small peak above  $80^\circ$ , which is absent for the independent cliffs, and likely related to undercuts at the pond-ice interface. More precisely, 95% of the exposed ice has a slope between  $35.2^\circ$  and  $77.2^\circ$ , and 50% of the ice area is between  $35.2^\circ$  and  $41.7^\circ$ . The mean slope for all ice cliffs is  $44.6^\circ$  and the standard deviation  $15.0^\circ$ . There are slight differences in slope distribution between cliffs that belong to a cliff-pond system and those that are independent. The mean slope of cliff-pond systems is almost equal, but their standard deviation and the tail of the distribution indicate the presence of few steeper slopes.

In terms of individual cliff slope statistics (Figure 6.6), cliff-pond systems do not clearly exhibit the steepest slopes. In fact, among the 8 cliffs with the shallowest slopes, 7 are part of cliff-pond systems. Many of these are large systems with rather consistent slopes with small standard deviations. Only three cliff-pond systems have a relatively steep slope on average: cliff 7, 12 and 11. Of those ice cliffs only cliff 7 can be considered large, with an exposed ice area of  $4760 \text{ m}^2$ .

The aspect of cliffs-pond systems on the surveyed part of lower Langtang Glacier shows a bimodal distribution with peaks at  $-20^\circ$  (NNW) and  $+80^\circ$  (ENE) (Figure 6.5). Independent cliffs do not show this bimodal pattern but have a peak in aspect around  $0^\circ$  with a large right-hand tail, i.e. eastward in the polar coordinate system. Overall 19.4% of the ice cliff area faces

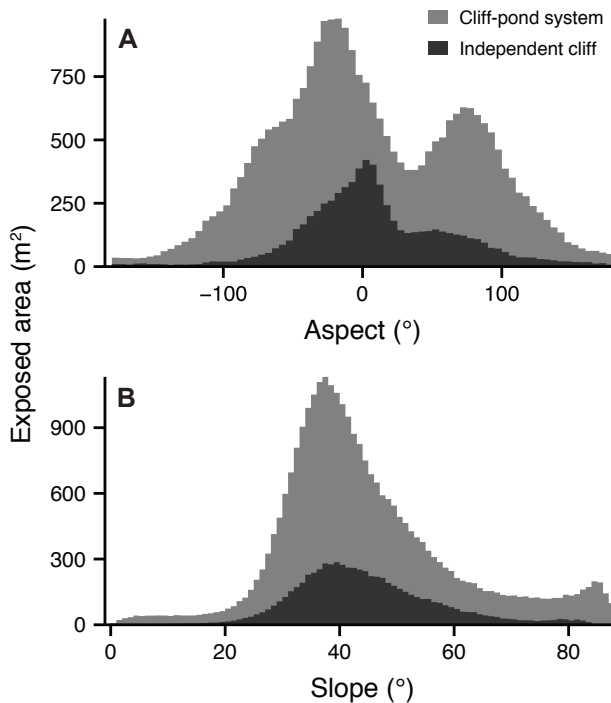


**Figure 6.5:** Histograms of aspect (a) and slope (b) for all classified ice cliffs that either belong to a cliff-pond system or are independent.

south. For the independent cliffs and those that belong to cliff-pond systems this is 7.5% and 15.9%, respectively.

Considering the mean and circular variance of aspect (Davis, 2002) on a per cliff basis (Figure 6.6), it is clear that most cliffs have relatively little variation in their aspect. Four of the largest cliff-lake systems (7, 17, 18 and 20) are not north-facing, but either west or east with a low variance. The small cliff-pond system located near the glacier terminus (cliff 1 in Figure 6.4), is the only cliff that is south-facing on average. It also has the shallowest average slope. In general though, as indicated by the scatter of Figure 6.6a, there is no distinct relation between slope and aspect. The per cliff variation of the parameters (Figure 6.6b) does have a slight correlation ( $R^2 = 0.46$ ).

### Ice cliff cross-section

The cross-section constructed from the extracted point cloud of ice cliff 7 (Figure 6.7) presents the morphology of a part of the cliff. The cliff face of 18 m in height consists of large undercut for about half of that. The low flight altitude of the UAV in combination with the wide-angle lens and oblique photos caused by UAV instability allow for the reconstruction of such overhanging

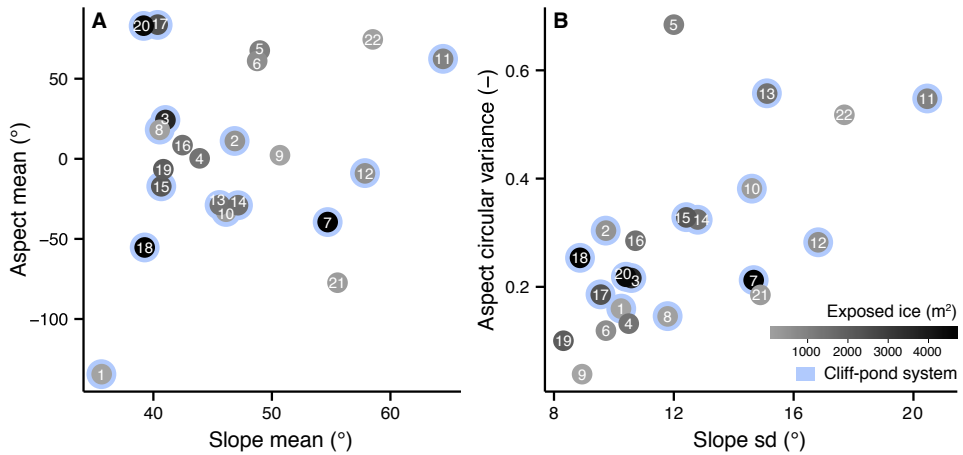


**Figure 6.6:** Scatter plots that show the means (a) and variability (b) of both aspect and slope for all the cliffs classified on the UAV data using OBIA. Additionally, exposed ice area and cliff-pond systems are indicated in the plot.

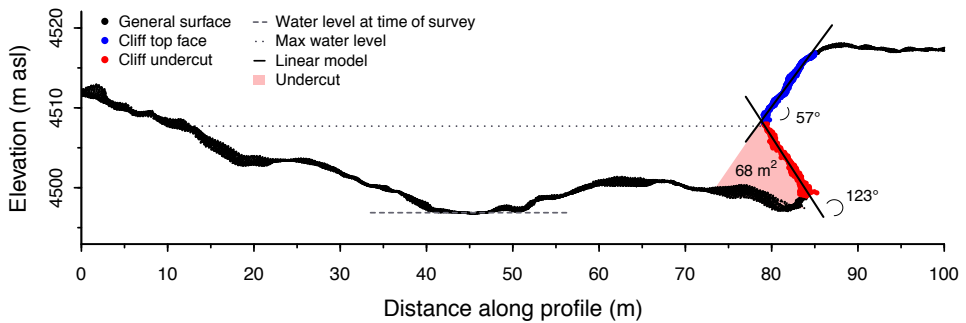


**Figure 6.7:** Cross section of the UAV-derived point cloud of cliff 7 and its vicinity. Points were extracted from the cloud for a 2 m by 100 m rectangular extent (Figure 6.4).

parts. The maximum water depth of the pond is estimated to be ~9 m, i.e. the difference between the bed and the top of the undercut. The water level in the adjacent pond at the time of the survey is very low, it only comprises the flat area between 40 and 50 m along the profile (Figure 6.4; Figure 6.7). Compared to the horizontal plane, the slope of the cliff top face is 57° and the overhanging part is 123°. The size of the undercut at this cross-section is a considerable 68 m<sup>2</sup>.

### Supraglacial ponds

Near the terminus of Langtang Glacier the abundance of ponds is relatively low, with most ponds located further up the glacier (Figure 6.4). Pond density is especially high in the triangle formed by cliffs 8, 14 and 18, as various pond clusters are present in that area. This area also houses the largest ponds. The most upstream part of the surveyed area of the main tongue, where there is

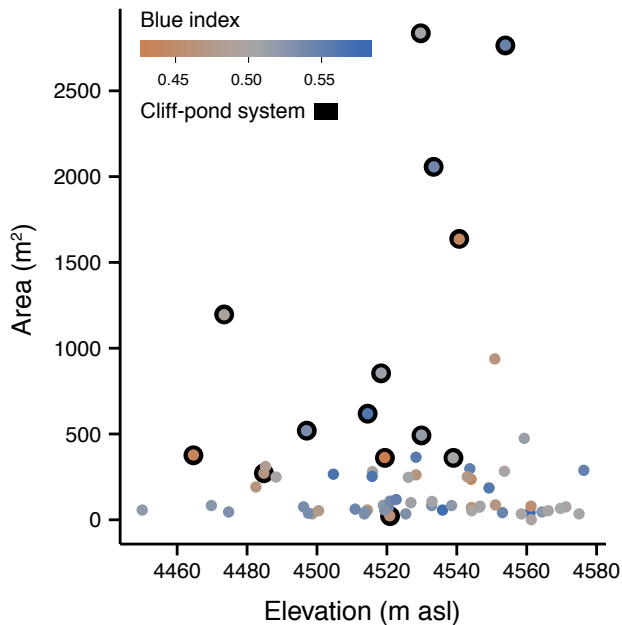


**Figure 6.8:** The elevation, surface area and blue index of all the ponds classified on the UAV imagery by OBIA. Ponds that belong to a cliff-pond system are circled in black.

an absence of ice cliffs, has again a relatively low abundance of ponds.

The distribution of area, elevation and blue index of each of the 69 ponds shows there are no clear patterns between any of these characteristics (Figure 6.8). The majority of the ponds are smaller than  $400 \text{ m}^2$  ( $n = 59$ ). The few larger ponds that are present are for the most part related to a cliff-pond system. The suspended sediment concentration of ponds does not seem to be related to cliff presence, size or position on the glacier. Ponds that have high sediment concentration, i.e. low BIs, are uncommon. Only 5 ponds have a BI of less than 0.45 and two third has a BI that is higher than 0.50. Cliff-pond systems ( $n = 14$ ) have a slightly lower mean BI of 0.49 than the mean of 0.52 of the independent ponds ( $n = 56$ ).

### 6.3.4 Pond distribution over the whole tongue

The longitudinal distribution of ponds ( $n = 267$ ) over the debris-covered tongue of Langtang Glacier, determined using OBIA of RapidEye imagery (Figure 6.9), is non-uniform. The number of ponds that are present in a 1 km bin decreases towards the terminus. The upper area (12–15 km from the terminus) has a high number of small ponds, and peak pond count and coverage occurs at 11–12 km from the terminus. Most ponds in this section are present on the western lateral half of the glacier (Figure 6.10), the same side as the tributary. A small peak in pond size is also present at 6–8 km from the terminus.

The ASTER-derived surface velocity of the glacier (Figure 6.10) shows velocities of about  $20 \text{ m a}^{-1}$  at the most upstream part of the debris-covered tongue of Langtang Glacier. At approximately 12 km from the terminus velocities decrease over a distance of 1 km to about  $10 \text{ m a}^{-1}$ . This reduction in velocity occurs at the location of the tributary and coincides with the peak in pond presence (Figure 6.9). Between 10 and 8 km from the terminus, velocities decrease again to  $5 \text{ m a}^{-1}$  at a confluence and right before the peak in pond presence. The remainder of the tongue, i.e. about half of the total, experiences slow velocities in the range  $0\text{--}5 \text{ m a}^{-1}$ . Surface velocities found in this study are comparable to those found using Landsat TM imagery in recent studies (Miles et al., 2017c; Pellicciotti et al., 2015; Ragetti et al., 2016a). Changes in curvature of Langtang Glacier and the related stresses within the ice do not appear to influence pond presence, other than the decreased pond cover observed in the relatively straight part between 3 and 6 km from the terminus.

The ponds delineated on the RapidEye imagery for the first 2 km from the terminus show similarities and differences with the ponds classified on the 2014 UAV imagery. All RapidEye ponds appear to have been classified on the UAV imagery, except the large pond near the 1 km line, i.e. the pond adjacent to cliff 7. Pond locations shifted over the four year period between the two datasets, as a result of ice flow and ice cliff backwasting. The main dissimilarity is that a considerably larger number of ponds are classified on the UAV imagery than on the RapidEye imagery (Figure 6.10), i.e. 69 versus 19. The mean pond area for UAV and RapidEye classifications is also very different, with  $252 \text{ m}^2$  and  $1137 \text{ m}^2$ , respectively.

## 6.4 Discussion and recommendations

### 6.4.1 Object-based classification and feature extraction

For the spectrally uniform debris-covered surface of Langtang Glacier the semi-automatic OBIA procedure presented in this study is an accurate method to delineate ice cliffs and supraglacial ponds on UAV imagery. Especially when compared to PBIA, the value of the object-based approach is clear. As with most classifications 100% accuracy is impossible to achieve. The requirement of a modest manual alteration of the classifier's output in order to achieve a better dataset for further analysis show that a fully automated procedure is not feasible, yet OBIA is a great advancement over the labour-intensive subjective manual approach. Additional analyses could utilise the cliff and pond database established here to improve the sample statistics and to develop improved rule-based classification alterations or even a completely rule-based classification scheme. The use of UAV-mounted sensors capable of sensing in other wavelengths, such as infrared or thermal, would likely help improve delineation results.

Spaceborne imagery can be considered for larger scale classification and analysis using similar techniques as presented in this study. At present, imagery from satellites such as Pléiades, the Worldview family, and GeoEye, have spatial resolutions similar to those of the resampled UAV

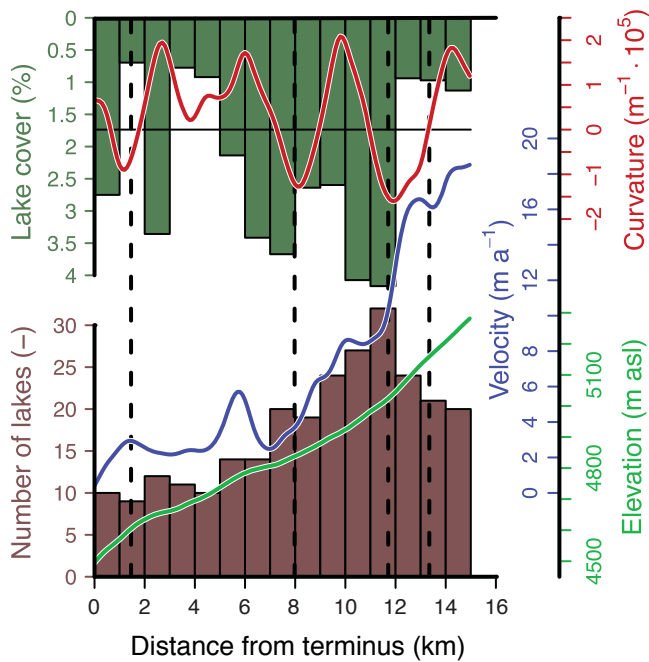


**Figure 6.9:** Pond count and relative cover for one km bins along the glacier (Figure 6.10) as determined from classification of the RapidEye 2010 image. The three profiles show ASTER-derived velocity, local glacier curvature and SRTM elevation at the centreline of the glacier. The vertical dashed lines denote the location of the confluences.

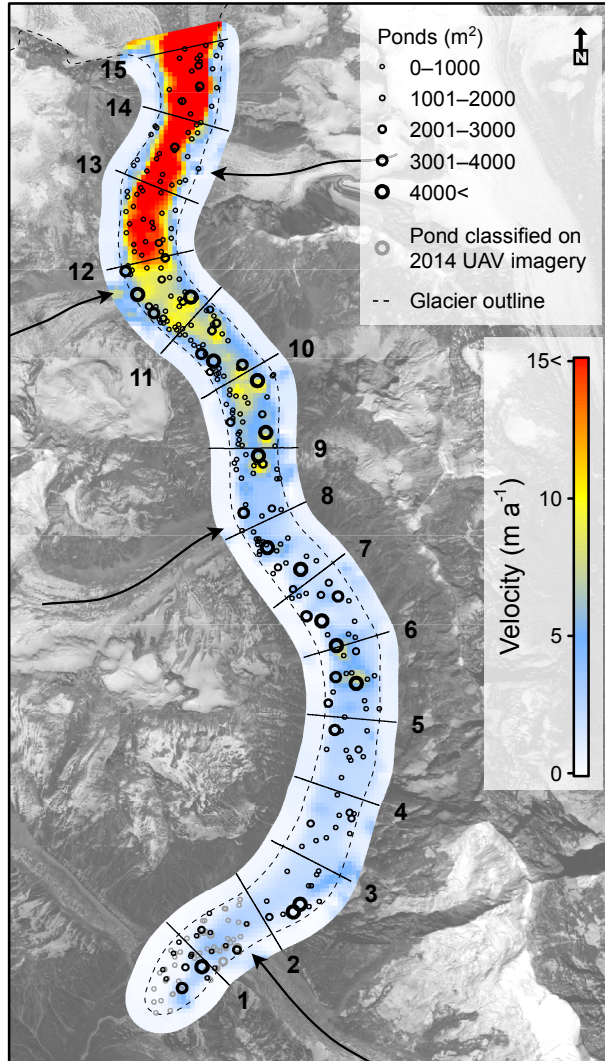


**Figure 6.10:** Ponds obtained by OBIA of the RapidEye 2010 image plotted over ASTER-derived surface velocity for 2010–2012. The arrows indicate locations of confluences and the transverse lines denote the distance from the terminus in km. The ponds classified on the 2014 UAV imagery are plotted in light gray.

data (Murillo-García et al., 2014). Access to high-resolution slope data, however, is an important prerequisite to achieve good accuracy in the object-based delineation. Elevation data from the stereo pairs or triplets thus is required. It is questionable if analysis of cliff morphology will lead to results of similar detail. The 0.2 m resolution used in this study is finer than those currently available from satellites and at steep areas such as near ice cliff undercuts, large pixels degrade the slope data, i.e. larger pixels result in shallower slopes. Moreover, having only stereo pairs may also introduce some errors in the DEM on locations where the view is obstructed by steep areas, e.g. at the face of ice cliffs. The transferability of the NN classifier to larger scale satellite analyses is uncertain. Sample statistics determined in this study cannot be transferred directly, so new samples have to be collected for individual satellite scenes and possibly individual glaciers also. Fortunately, the random sample selection procedure is performed reasonably quickly. Differences in spectral contents, resolution and analysis over larger, more varied areas might also result in inaccurate results for the NN classifier. Other statistical classifiers or advanced rule-based classification might prove to be more suited.

Upscaling findings from in situ measurements and OBIA of UAV imagery using medium-resolution imagery such as from Landsat 8 OLI or Sentinel-2 MSI could be an important step forward in the systematic analysis of ice cliffs over large regions. Such an approach may use advanced sub-pixel classification methods, e.g. super resolution mapping (Atkinson, 2013), that are driven by the characteristics derived at the smaller scale. More accurate large scale data will mean better parameterisation of hydroglaciological models, which will improve estimates on future changes to glacier volume and river discharge.

Compared to the other methods that were used to delineate ice cliffs in the past, OBIA has distinct advantages. For example, Reid & Brock (2014) used a simple threshold of  $40^\circ$  on the slope and removed connected pixel groups of less than  $10 \text{ m}^2$ . I show, however, that substantial parts of the cliffs on lower Langtang Glacier have slopes shallower than  $40^\circ$ . Furthermore, 68% of the areas steeper than  $40^\circ$  and larger than  $10 \text{ m}^2$  do not belong to the cliff class. A simple threshold method thus has considerable limitations and overestimates cliff area, while missing shallow cliffs. Other studies delineated ice cliffs on high-resolution remote sensing imagery and elevation models by digitisation (Brun et al., 2016; Buri et al., 2016b; Ragetti et al., 2016a). OBIA has disadvantages and advantages compared to such a manual digitisation of cliff outlines. Manual digitisation is aided by expert knowledge about cliffs and may include parts of the surface that are currently obscured from view by a thin layer of debris or snow in order to achieve better delineation and analysis results. But this process is highly subjective. As a result, it is subject to inconsistency and not favourable for larger scale analyses. Different opinions and approaches to cliff digitisation also reduce comparability between datasets when performed by different analysts. A semi-automatic OBIA is completely objective and results are comparable and consistent, given the same type of input data. Additionally, an automated procedure makes the analysis of much larger extents and many datasets feasible.

The cliff analysis presented in this study uses a gridded DEM in which undercuts cannot be

expressed. The edge of pixels that lie at the boundary between the top face and the undercut will maximally obtain slope values close to  $90^\circ$ . Calculations of the differences in slope between independent cliffs and cliff-pond systems are affected by this limitation and the method used in this study consequently limits the accuracy of the results. However, multiple studies have shown that for cliff-pond systems the undercuts may contribute significantly to the backwasting of ice cliffs (Brun et al., 2016; Buri et al., 2016b; Miles et al., 2016; Steiner et al., 2015). The UAV captures images from many different angles and, as shown, can also be used to identify and measure undercuts. To improve the analysis on the importance and effect of supraglacial ponds on ice cliff characteristics, a systematic multi-temporal analysis of a point cloud could be used to estimate volume losses and relative contribution of pond-induced erosion to total ice cliff backwasting. By performing such analyses on multi-temporal datasets important validation and calibration data on volume losses can be obtained for the use in distributed energy balance modelling of ice cliffs and supraglacial ponds (Buri et al., 2016b; Miles et al., 2016). UAVs provide accurate data at high spatial resolution, and they can also be used to gather data at high temporal resolution (Chapter 3; Chapter 4). Consequently, intra-seasonal changes in cliff morphology and the causes thereof can be evaluated.

A point cloud approach may also be used in the classification stages to overcome some issues and improve accuracy. As cliffs can have very steep slopes, they can be difficult to delineate from the orthogonal perspective that orthorectified UAV and satellite imagery provide. Very steep cliffs that consist primarily of an undercut may not even be detected, although this has not been encountered in this study. By developing classification methods applicable to the full 3D point cloud representation of a debris-covered glacier, such steep areas could be delineated better. This is probably also true for more gently sloping cliffs, thereby improving the analysis of cliff morphology. Full 3D representations are computationally intensive, however, which may pose difficulties for medium to large scale analyses.

#### **6.4.2 Distribution and characteristics of ice cliffs**

The distribution of ice cliffs and supraglacial ponds over the UAV surveyed area shows that abundance of these surface features is higher at the confluence, especially for larger cliff-pond systems. Strain on the glacier at that location is expected to be higher because the ice will experience both transverse and longitudinal compression (Gudmundsson, 1997). This supports previous suggestions that the cliff-forming processes of debris slumping and void or conduit collapses occur more frequently at high strain areas (Benn et al., 2012), caused by fracturing and hydrologically driven conduit formation (Benn et al., 2009; Gulley, 2009). Manual delineations of ice cliffs on Langtang Glacier presented in a figure in Ragettli et al. (2016a) support this, as in the two main areas of deceleration there is a higher cliff density, i.e. upglacier of the confluences at 8 and 12 km from the terminus. Immediately at the confluences, however, only a few ice cliffs are present. As for the UAV-surveyed confluence, some large cliffs are already present

just upstream of the confluence on the tributary itself. Consequently, longitudinal compression caused by deceleration of the tributary may be the more likely cause of their formation rather than the strain directly at the confluence itself. Also, no cliffs are present on the high-strain medial line of the confluence, although their absence here might be due to the addition of debris from the eastern moraine of the tributary glacier, causing a relatively thicker debris layer.

The existing hypothesis on ice cliff survival as a result of its aspect and pond presence is largely validated by our cliff analysis. Few south-facing cliffs are present, and more than 80% of the cliff surfaces face northwards. However, ice cliffs that belong to cliff-pond systems appear to deviate slightly from the expected pattern with the bimodal aspect distribution. This seems to be mainly caused by the two large southeast-facing cliff-pond systems at the tributary, cliff 17 and 20. They have a consistent low mean slope of  $40^\circ$  and do not appear to have large undercuts present. These cliffs might survive as rapid melt on exposed south-facing ice is balanced by the subaqueous melt. Such cliffs could play an important role in the mass loss of debris-covered glaciers, as they will melt comparatively faster than others. In contrast to cliff 17 and 20, cliff 11 also faces almost completely east, yet it has the steepest mean slope of all cliffs on the surveyed area caused by the presence of a large undercut. This is most likely because the debris view angle (Reid & Brock, 2014; Steiner et al., 2015) at the base of this cliff ( $109^\circ$ ) is greater than the angle at cliff 17 ( $49^\circ$ ), resulting in more incoming longwave radiation. Additional UAV datasets of Lantang Glacier would provide more detail on the relative backwasting rates of these cliffs compared to the other cliffs on the glacier by enabling multi-temporal analyses of UAV-derived elevation models. This could further validate the hypothesis.

### 6.4.3 Distribution and characteristics of supraglacial ponds

The RapidEye imagery reveals the presence of ponds over the entire tongue, but they seem especially dense near the decelerated areas of the main tongue at the two western tributaries. This agrees with suggestions by others that areas of low velocity and low gradient cause large scale pond development. Drainage in this areas is likely reduced due to low hydrological gradients and the lack of reorganisation of englacial conduits (e.g. Miles et al., 2017c; Quincey et al., 2007; Salerno et al., 2012). However, I observe many small ponds in the upper part of Langtang Glacier as well, which is a faster flowing and higher gradient area. Also, contrary to our expectations, large ponds are absent in the region of low velocities and low curvature between 3 to 6 km from the terminus, although the slight change in gradient there might be of influence. Nevertheless, a distinct spatial pattern of pond presence with respect to velocity and gradient seems absent at Langtang Glacier.

I observe pond clustering on the main tongue just downstream of each confluence, primarily on the side of the glacier closest to the tributary, both on the RapidEye and on the UAV data. I therefore hypothesize that, in addition to factors of velocity and slope, transverse compression at confluences might promote supraglacial pond formation. Compression might result in the clo-

sure of conduits present on the main tongue and limit englacial drainage of ponds. Downglacier of the confluences the pond density reduces again as englacial drainage is no longer reduced by the confluence-induced compression. Unfortunately, the resolution and quality of the ASTER data in combination with the relatively low surface velocity at the confluences made it impossible to study the compressional flow accurately. In future research, I aim to derive accurate flow vectors using imagery from the new Sentinel 2 satellite and additional UAV surveys to further investigate the validity of the hypothesis. It is important to note that seasonality plays a strong role in pond presence (Miles et al., 2017c) and that further study of high-resolution imagery is also needed to determine if these effects at the confluences are observed during different times of the year.

Visual comparison of pond density on the RapidEye image with glacier elevation differences found for the periods 1974–2006 and 2006–2015 (Pellicciotti et al., 2015; Ragettli et al., 2016a) reveal interesting patterns. In the area where pond density is largest, downstream of the tributary at 12 km, mean surface elevation changes of  $-1 \text{ m a}^{-1}$  are observed between 2006 and 2015. However, the pond density here would suggest greater overall surface elevation losses, and ice emergence due to longitudinal compression caused by deceleration of the tongue (Figure 6.10) may play a role. Upstream of the confluence at 8 km, a reduced number and coverage of ponds was found and elevation losses for the recent period are minimal, as expected. Comparison with higher resolution geodetic mass balance studies of the glacier in the future might reveal new and improved correlations between pond presence and melt that may help to unravel these patterns.

The RapidEye classification performed in this study showed 267 ponds on Langtang Glacier, versus 53 found in a pre-monsoon Landsat classification (Miles et al., 2017c). The most likely cause of this difference is that the 5 m resolution of the RapidEye image reveals more small scale ponds than the 30 m pixels of Landsat. There may even be a greater number of ponds present, as the UAV data has revealed about 4 times more ponds than the RapidEye image. The effects of the presence of many small ponds on glacier melt have not been studied. It could be limited, but may also help to further unravel some of the spatial melt patterns observed.

## 6.5 Conclusions

In this study I have developed a method to delineate ice cliffs and supraglacial ponds on the debris-covered Langtang Glacier by using OBIA of high-resolution UAV imagery. Delineated surface features were analysed quantitatively on their geometrical characteristics and spatial distribution. Classification of RapidEye satellite imagery was performed to determine the pond distribution over the entire glacier.

Our study demonstrates that OBIA is a valuable tool for accurate delineation of surface features on debris-covered glaciers. With a combination of high-resolution UAV imagery and digital elevation models, the semi-automatic approach used here is able to objectively derive characteristics of ice cliffs and supraglacial ponds. OBIA of satellite imagery offers the potential

to delineate and analyse surface features for large areas, and results can be applied to improve glacio-hydrological models. Systematic analyses of UAV-derived point clouds are a promising method for the analysis of ice cliff (undercut) morphology and evolution.

Ice cliffs present on the glacier have a predominantly northern aspect and a mean slope between  $40^\circ$  and  $60^\circ$ . Most of the large cliffs have adjacent supraglacial ponds. South-facing ice cliffs are rare and ice cliffs with aspects that deviate from the north generally have relatively low slopes and are connected to large supraglacial ponds that sustain them. Our results largely confirm current hypotheses on the survival of north-facing ice cliffs. Spatially, the ice cliffs appear to form primarily at areas where high strain rates are expected in the ice. Longitudinal compression and related englacial processes are the probable cause. Further analysis should confirm these patterns for the entire glacier.

A distinct spatial distribution of ponds over Langtang Glacier is absent. High pond densities are related to low glacier velocities and low gradients, but high pond densities are also found near confluences. I hypothesize that the transverse compression at confluences may close englacial conduits, limit drainage, and promote pond formation.

### **Author contributions**

PK, WI, and SJ designed the study. WI and JS performed the UAV and dGPS surveys. PK processed the UAV imagery and performed all analyses. PK wrote the manuscript with suggestions by JS, FP, SJ and WI.



---

## The future of Asia's glaciers

Glaciers in High Mountain Asia (HMA) play a substantial role in the water supply of millions of people (Immerzeel et al., 2010; Lutz et al., 2014), and they are retreating and losing mass as a result of man-made climate change (Marzeion et al., 2014) at similar rates as elsewhere in the world (Bolch et al., 2012; Kääb et al., 2015). In the 'Paris Agreement' of 2015, 195 nations agreed on the aspiration to limit the level of global temperature rise to 1.5 °C above pre-industrial levels. However, it is not known what an increase of 1.5 °C would mean for the glaciers in HMA. Here I show that a global temperature rise of 1.5 °C leads to a warming in HMA of  $2.1 \pm 0.1$  °C, and that  $64 \pm 7\%$  of the present-day ice mass stored in the glaciers will remain by the end of the century. The 1.5 °C goal, however, is extremely ambitious and is only projected by a small number of climate models of the conservative RCP2.6 ensemble. Projections for RCP4.5, RCP6.0 and RCP8.5 reveal that much of the glacier ice is likely to disappear with projected mass losses of  $49 \pm 7\%$ ,  $51 \pm 6\%$  and  $65 \pm 6\%$ , respectively; these projections have potentially serious consequences for regional water management and mountain communities.

Chapter based on:

Kraaijenbrink, P. D. A., M. F. P. Bierkens, A. F. Lutz, and W. W. Immerzeel (2017). **Impact of a global temperature rise of 1.5 degrees Celsius on Asia's glaciers.** *Nature*, 549(7671), 257-260.

## 7.1 Future temperature rise

In high-altitude regions temperatures are rising faster than in the low-lying plains and this is also observed for HMA (Pepin et al., 2015). Possible mechanisms suggested to explain this elevation-dependent warming in mountains are snow albedo and surface-based feedbacks, water vapour changes and latent heat release, radiative flux changes, surface heat loss and temperature change, and aerosols. A global ensemble of 110 general circulation model (GCM) runs spanning the full range of radiative forcing defined in CMIP5 (Taylor et al., 2012) (RCP2.6 ( $n = 25$ ), RCP4.5 ( $n = 35$ ), RCP6.0 ( $n = 18$ ), RCP8.5 ( $n = 32$ )) (Table A.4) shows an evident relation between radiative forcing and projected temperature increase from pre-industrial conditions (1851–1880) to the end of century (2071–2100, EOC) (Figure 7.1). It also shows that the glacierised areas of HMA are consistently warming at much higher rates than the global average and the difference between global and HMA temperature rises is increasing with radiative forcing (Figure 7.1). Compared to the global warming of land masses only, the enhanced warming in HMA is less pronounced, but still evident.

From the GCM ensemble I have selected models that result in a 1.5 °C temperature rise globally relative to pre-industrial conditions ( $n = 6$ , see Section 7.6). All of the selected models originate from the conservative RCP2.6 model ensemble. The 1.5 °C global increase implies a warming of  $2.1 \pm 0.1$  °C for the glacierised areas in HMA (Figure 7.2). Although there is considerable regional variation, with the Hindu Kush warming the most (2.3 °C) and the Eastern Himalaya the least (1.9 °C), all regions warm by more than 1.5 °C. These spatial patterns persist for the actual RCP2.6, RCP4.5, RCP6.0 and RCP8.5 scenarios for which considerably higher warming is projected in the western parts of HMA (Figure A.9). A strong divergence is observed towards the EOC between the 1.5 °C scenario and RCP4.5 ( $3.5 \pm 0.2$  °C), RCP6.0 ( $4.1 \pm 0.2$  °C), and RCP8.5 ( $6.0 \pm 0.3$  °C) (Figure A.7).

## 7.2 Debris cover abundance

The Randolph Glacier Inventory (RGI) version 5.0 (Pfeffer et al., 2014) identifies 95 537 glaciers with a total glacier area of 97 605 km<sup>2</sup> in the RGI regions covering HMA (Figure 7.2, Table A.1). Considerable parts of these glaciers, in particular the low-lying glacier tongues, are covered by thick debris mantles caused by erosion from the generally steep headwalls and the subglacial material on which the glaciers reside. The debris is an important control on glacier ablation, and thus on its climate sensitivity. A thin layer of debris accelerates melt because of a lower albedo compared with debris-free ice, whereas a debris layer thicker than a few cm suppresses melt because of insulation of the underlying ice (Evatt et al., 2015; Lejeune et al., 2013; Østrem, 1959; Pellicciotti et al., 2015; Reid et al., 2012; Vincent et al., 2016). Except for a few small scale studies (Immerzeel et al., 2013; Ragetti et al., 2015), the role of debris is generally not taken into account in climate change impact studies over larger regions, mostly because a debris classifica-

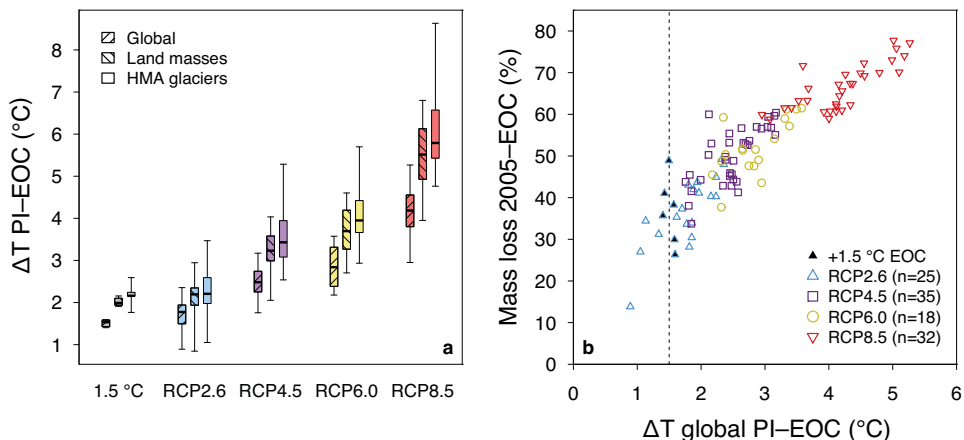


**Figure 7.1:** Relation between radiative forcing, temperature increase and ice mass loss. Temperature changes between pre-industrial (PI, 1851–1880) and the end of century (EOC, 2071–2100) for the 1.5°C models, RCP2.6, RCP4.5, RCP6.0 and RCP8.5 (a). Temperature changes are shown separately for the entire globe, land masses, and the glaciers of High Mountain Asia. The horizontal bars denote the median, the boxes the interquartile range, and the whiskers extend the full data range. Panel b shows projected ice mass loss against global temperature change for the EOC for each of the 110 model runs.

tion of HMA glaciers is not available. Here I have developed such a classification using Landsat 8 imagery. For all glaciers larger than  $0.4 \text{ km}^2$  (33 587, 91% of the total glacier area, 99.6% of the glacier ice volume), debris cover was identified by selecting pixels below a normalized difference snow index (NDSI) value and a slope threshold (see Section 7.6).

The results show that about 11% of the glacier area in HMA is debris covered (Figure 7.3), with the largest relative debris-cover in the Hindu Kush (19% of the regional glacier area). Ice volume stored in each glacier was subsequently calculated using the GlabTop2 model (Frey et al., 2014; Linsbauer et al., 2012), which was converted to mass using a  $900 \text{ kg m}^{-3}$  ice density (Frey et al., 2014; Kääb et al., 2012). It was estimated that the total HMA ice mass, excluding glaciers smaller than  $0.4 \text{ km}^2$ , is  $4754 \pm 350 \text{ Gt}$  (Figure 7.3), with over one-third of this volume stored in Karakoram glaciers. The relative ice mass under debris in the HMA is 18%, which is considerably larger than the relative ice area under debris. This is caused by the predominance of debris on gently sloping tongues with thick ice. If only the ablation area below the equilibrium line altitude (ELA) is considered, the ice mass contribution under debris even reaches values up to 30% in the entire region and up to 48% in the Hindu Kush.

### 7.3 Mass loss projections

To estimate the HMA glaciers' response to a global temperature increase of  $1.5^\circ\text{C}$  a model based on the mass balance gradient (Benn & Lehmkühl, 2000) was set up for all individual glaciers larger than  $0.4 \text{ km}^2$ . The mass balance gradient for each glacier was constrained by a maximum

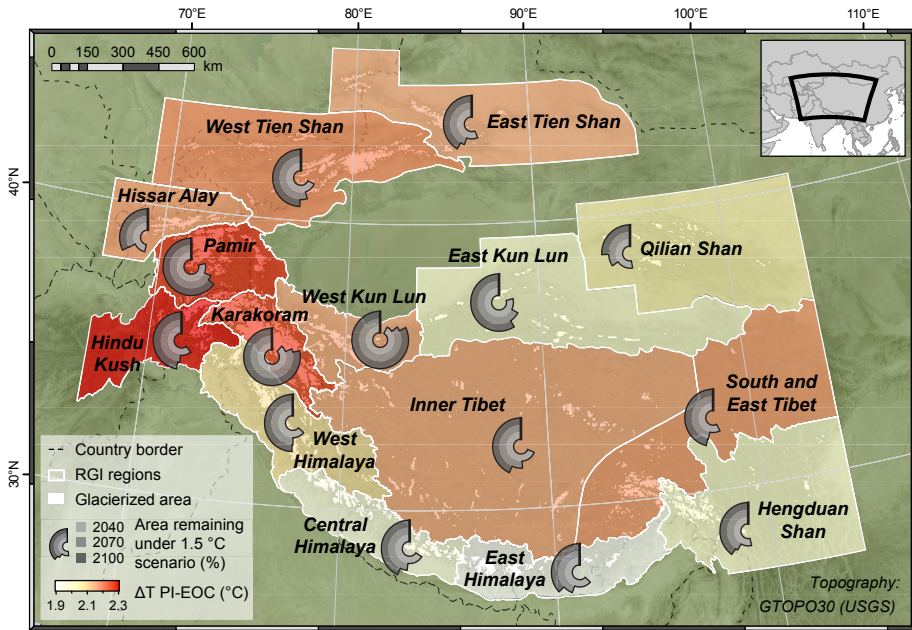


**Figure 7.2:** Regional temperatures and projected glacier area associated to a 1.5°C increase. The map shows the mean temperature increase at the glaciers between pre-industrial (PI, 1851–1880) and end of century (EOC, 2071–2100) for the global 1.5°C scenario, aggregated by Randolph Glacier Inventory sub-regions (Pfeffer et al., 2014) (Table A.1). The circular graphs depict the projected reduction in glacierized area within each region for the 1.5°C scenario for three points in time.

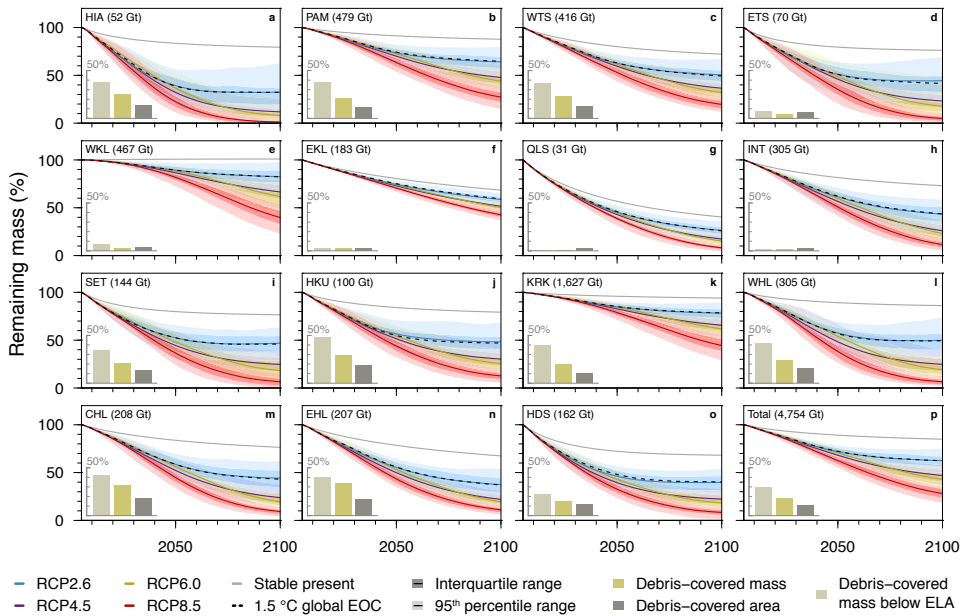


**Figure 7.3:** Future ice mass loss and prevalence of debris-covered glaciers. The panels show mass loss projections aggregated by RGI sub-region (a–o) and the entire HMA (p) for the RCP scenarios, a stable present day climate, and a selection of six models that have a temperature rise of 1.5 °C at the end of century. Error bands are shown for the RCP scenarios, based on the interquartile and 95th percentile range of the Monte Carlo ensemble for each RCP. This includes both the variability between climate models and glacier model parameter uncertainty. The bar charts show the relative presence of debris in each region.

ablation at the glacier terminus estimated using a degree-day climatology and by a maximum accumulation estimated from the maximum precipitation in the glacier accumulation zone (see Section 7.6). The approach takes into account the reduced melt under debris as function of debris thickness, the increased melt that is due to supraglacial ponds and the observed regional mass balance (Farinotti et al., 2015; Gardner et al., 2013; Kääb et al., 2015) (Table A.3). The results indicate that the glaciers are out of balance in all RGI sub-regions and, except for West Kun Lun, are losing mass under present day (1996–2015) climate (Table A.3). The results also show that, even if temperatures stabilise at their current level, mass loss will continue for decades to come until a new equilibrium is reached (Figure 7.3). For the whole of HMA, about 86% of the present ice mass and 85% of the present-day area would remain by the EOC.

To estimate the future mass balance, the present mass balance curve, of fixed gradient, was shifted using the sensitivity of the ELA to temperature change (Shea & Immerzeel, 2016) and the projected temperature rise between the present day climate and the EOC for each of the 110 GCMs (Table A.4). Additionally, the mass balance curve's height of maximum accumulation was modified based on projected precipitation change from the same 110 GCMs. To account for the uncertainty in model parameters, observed mass balance and climate projections, the analyses were performed in a Monte Carlo simulation framework, varying randomly the parameter values and mass balance for each GCM forcing for each of the 33,587 glaciers (see Section 7.6). Subsequent results are thus given as the mean  $\pm$  1 standard deviation from the Monte Carlo runs. Results reveal that if the 1.5 °C target is met, an estimated  $64 \pm 7\%$  of the ice mass and  $64 \pm 8\%$  of the glacier area in HMA will remain by the EOC (Figure 7.1, Figure 7.3, Figure A.11). In the most extreme case (RCP8.5), the ensemble shows that only  $36 \pm 5\%$  of the ice mass and  $32 \pm 5\%$  of the total area remains by the EOC. RCP2.6 ( $64 \pm 8\%$ ), RCP4.5 ( $51 \pm 7\%$ ) and RCP6.0 ( $49 \pm 6\%$ ) result in intermediate mass losses that fall between the 1.5 °C scenario and RCP8.5. A near-linear relation between temperature increase and projected mass loss is observed at the regional scale (Figure 7.1). There are only six models out of the entire model ensemble that result in a global 1.5 °C EOC, and the majority of projections result in a much higher warming and a stronger decrease of HMA ice mass (Figure 7.1).

The regional variation in mass loss is large, and there are several regions where for RCP8.5 the ice mass and glacier area drop below 10% of their present-day value (Figure 7.3). This will evidently impact the timing of downstream water supply and water access of mountain communities near the glaciers. In particular for RCP8.5 a strong increase in downstream melt water availability will, for example, prevail on the short to medium term with a peak around 2050 (Figure 7.4), which agrees well with previous findings (Bliss et al., 2014; Immerzeel et al., 2013). Melt water peaks for the remaining RCPs generally occur earlier at around 2030, although for many of the regions peak melt water has already occurred.

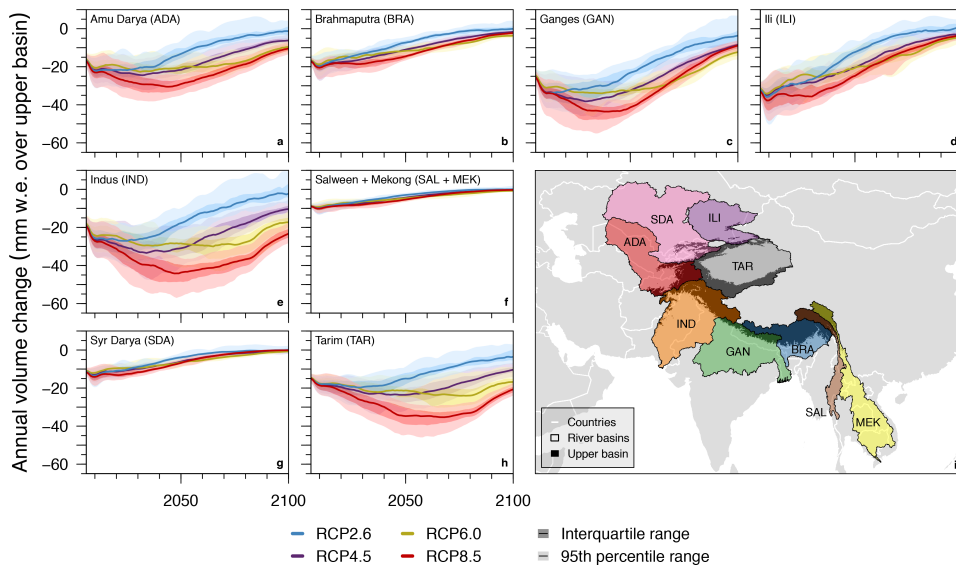


**Figure 7.4:** Annual glacier mass change for major river basins in HMA. The figure shows the transient annual glacier mass changes for the four RCP ensembles, aggregated over the major river basins in HMA that have substantial glacierized areas (a–h). The mass is expressed in mm w.e. over the upper basin area, i.e. the part of the basin with an elevation higher than its lowest glacier terminus, for better comparison with precipitation. A map of the basins and the upper basin area is shown in panel i.

## 7.4 Regional differences

Even under a global  $1.5^{\circ}\text{C}$  increase, there are considerable regional differences in glacier response within HMA that are caused by differences in regionally projected warming rates and precipitation trends, by specific regional glacier properties (e.g. glacier hypsometry and the presence of debris), and by the present-day imbalance of the glaciers (Table A.3). For example, Hissar Alay and the Qilian Shan are the regions that show the most extreme decline and by the EOC only  $32 \pm 14\%$  and  $30 \pm 5\%$  of the glacier mass remains (Figure 7.3), respectively. On the other hand, in the Karakoram, despite a higher regional warming rate,  $80 \pm 7\%$  of the ice mass remains by EOC. These differences are explained by the large ice masses stored in the debris-covered tongues in the Karakoram compared to Qilian Shan in particular (Figure 7.3), by the fact that Qilian Shan ( $-0.49 \pm 0.11 \text{ m w.e. a}^{-1}$ ) and Hissar Alay ( $-0.36 \pm 0.31 \text{ m w.e. a}^{-1}$ ) at present experience much more negative mass balances than the Karakoram ( $-0.13 \pm 0.34 \text{ m w.e. a}^{-1}$ ), and by differences in sensitivity of the ELA to climate perturbations.

Debris on the glacier ice plays an important role in regulating melt processes of HMA glaciers (Mihalcea et al., 2008b; Rounce et al., 2015). It buffers the impacts of climate change as the lower melt rates slow down glacier retreat and mass loss under rising temperatures. There is however great variability in the relative area covered by debris (Figure 7.5a), the relative ice mass stored under debris (Figure 7.5b) and the relative ice mass in the ablation zone stored under

debris (Figure 7.5c). Although the debris-covered area is relatively small, there are regions in the Karakoram and Himalaya where the ice mass under debris in the ablation zones exceeds 40% and this results in a strong buffering effect (Figure 7.5d-f). Since glacier thinning and a rise of the ELA can result in thickening of debris and an increase in debris extent (Rowan et al., 2015), its effects on glacier melt may even increase over the course of the century.

## 7.5 Conclusions

To conclude, HMA is consistently warming more rapidly than the global average. The differences in impact on the HMA's glaciers between the ambitious 1.5 °C target and the RCP4.5, RCP6.0 and RCP8.5 scenarios are large. It may well be the difference between sustaining the glaciers for generations to come and losing the majority of Asia's glacier ice mass by the EOC. The presence of debris may in some regions provide a considerable retention of glacier mass, but clearly policy decisions can make a difference and for the survival of the HMA glaciers it is essential to minimise the global temperature increase. To meet the 1.5 °C target will be a task of unprecedented difficulty and even then,  $36 \pm 7\%$  of the ice mass in HMA is projected to be lost by the EOC.

## 7.6 Methods

### 7.6.1 Debris classification

The extent of debris cover on HMA glaciers was mapped for the entire area within the glacier outlines defined in the Randolph Glacier Inventory 5.0 (RGI) (Pfeffer et al., 2014) for the RGI regions Central Asia, South Asia East and South Asia West. Debris-free ice was distinguished from debris-covered ice by using a normalised difference snow index (Hall et al., 1995) (NDSI). I calculated the NDSI from a Landsat 8 OLI composite that was produced by a pixel-wise selection of the scene with the highest brightness temperatures of thermal infrared (TIR) band 10 in the Landsat 8 top-of-atmosphere reflectance archive. The procedure, performed in Google Earth Engine (Google Earth Engine Team, 2017), ensures a composite image that has: (i) no cloud cover since clouds are colder than both snow and debris, (ii) the least amount of shadow since shadows are colder than sunlit terrain, and (iii) the least amount of snow-covered debris because debris is warmer than snow. Pixels were classified as debris for a NDSI below 0.25, a threshold determined by visual comparison of classification results with the imagery Figure A.2. A maximum slope constraint of 24° was set for debris-cover (Paul et al., 2004) on 1 arc second Shuttle Radar Topography Mission elevation data (Farr et al., 2007) (SRTM) to prevent misclassification of rock outcrop as debris, which set 23% of the pixels in the debris-covered class to debris-free.

Supraglacial ponds and lakes are often present on debris-covered tongues and are generally

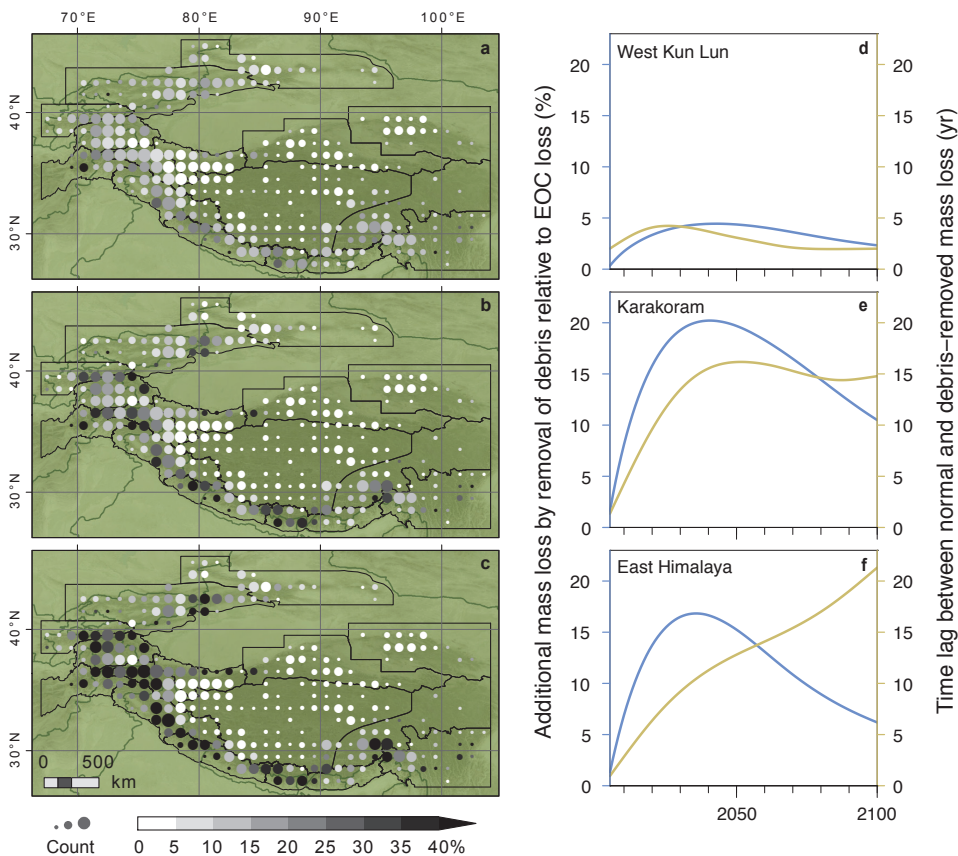


**Figure 7.5:** Spatial patterns in the occurrence of debris-covered glaciers and the impact of debris on delaying climate change impact. Panel a shows the relative glacier area that is debris covered, panel b shows the relative ice mass stored under debris, and panel c shows the relative ice mass stored under debris in the ablation zone (below the equilibrium line altitude). The points represent data aggregated over a 1 × 1 degree grid and the size of points indicate glacier abundance in a grid cell. The panels d–f show for three different sub-regions the increase in mass loss that results from a model experiment for which all debris cover was removed (blue line) and the lead in glacier response this yields (orange line).

associated with the presence of ice cliffs. Recent findings have revealed that ponds and cliffs may accelerate local melt considerably (Chapter 3), and are thus important to include in the analysis. Pond classification was performed by applying an upper threshold of  $-0.1$  to the normalized difference vegetation index (Lillesand et al., 2015) (NDVI) for pixels classified as debris. A maximum slope of  $20^\circ$  and minimum brightness temperature of  $10^\circ\text{C}$  were set as secondary constraints. Ponds misclassified as debris-free ice were identified by selecting connected groups of fifty or fewer debris-free pixels, and applying the same secondary constraints.

Classification accuracy was evaluated visually for a 1000-pixel sample. A total of 800 samples were equally distributed over the classes debris-covered ice and debris-free ice in a stratified random sampling procedure. A 200-pixel sample was taken for the less abundant supraglacial lake class. The overall classification accuracy is 91% (Table A.2).

### 7.6.2 Ice thickness modelling

To obtain region wide glacier thicknesses I have implemented the GlabTop2 model (Farinotti et al., 2017; Frey et al., 2014) using RGI glacier outlines and the SRTM dataset (Figure A.3). The model calculates ice thickness for each pixel within a glacier outline using a basal shear stress estimation and local slope. All calibrated input parameters of the model (Frey et al., 2014) were maintained, except the spatial density of random points for which the thickness is calculated in the GlabTop2 algorithm. This was reduced by a factor 9 to account for the difference in spatial resolution of the elevation datasets used in the original study by Frey et al. (2014) (3 arc seconds) and in this study (1 arc second). This results in approximately the same number of random points per glacier in both cases. In addition, I have improved the computational efficiency of the model by calculating the local slope using a circular neighbourhood filter. The radius of this circular filter is a function of the glacier size, but constrained between 30 and 300 m. The minimum slope that is used in the thickness calculations was set to  $2^\circ$  to prevent unrealistically thick ice for the mountain glaciers of HMA.

### 7.6.3 Mass balance gradient and mass redistribution model

#### Concept

To model each glacier in the study area I developed a mass balance gradient (MBG) model (Benn & Lehmkuhl, 2000) in combination with a mass redistribution component. The model concept is illustrated in Figure 7.6. I constructed the MBG model, in which mass balance is expressed as a function of elevation, based on 6 to 25 equal elevation bands, depending on a glacier's area. Glaciers that have an area of less than  $0.4\text{ km}^2$  were discarded from analysis, as a minimum number of pixels is required per elevation band to enable model simulations. In total, only 9.8% of the area and 0.7% of the volume were excluded from the analysis (Table A.1, Figure A.1).

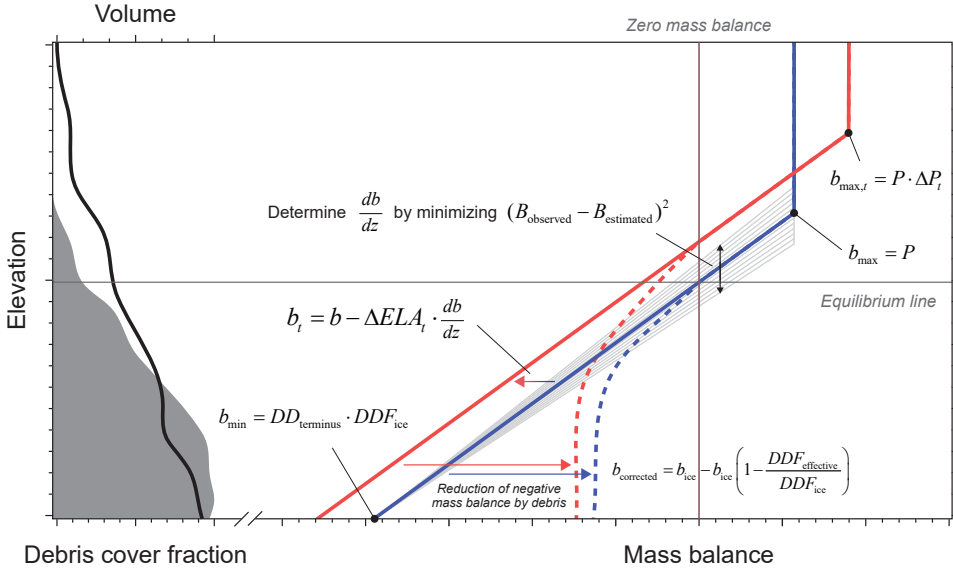


**Figure 7.6:** Concept of the mass balance gradient model. The schematic figure shows the MBG approach used in this study with idealized mass balance curves for the current (blue) and future (red), debris-cover fraction (grey), and debris-corrected mass balances (dashed lines).

The annual ablation at the terminus (m w.e. a<sup>-1</sup>) is calculated by:

$$b_1 = DD \cdot DDF^C \tag{7.1}$$

where DD is the mean annual positive degree-day sum obtained from WATCH-Forcing-Data-ERA-Interim dataset (Weedon et al., 2014) (WFDEI) over the period 1996–2014, downscaled using SRTM and a temperature lapse rate of 0.0065 °C m<sup>-1</sup>. DDF<sup>C</sup> is the degree-day factor for debris-free (clean) ice (Immerzeel et al., 2015). Mass balance for the remaining elevation bands is determined by applying a linear MBG with respect to elevation:

$$b_i = b_1 + (z_i - z_1) \frac{db}{dz} \tag{7.2}$$

where  $z_i$  is the surface elevation of elevation band  $i$ .

The annual maximum accumulation is constrained by the mean annual precipitation at each glacier ( $b_{\max} = P$ ). Here the ERA-Interim reanalysis data (Dee et al., 2011) for the period 1996–2015 was used, since it was pointed out that high-elevation precipitation is represented better in ERA-Interim than in other large-scale reanalysis products (Dahri et al., 2016; Immerzeel et al., 2015; Palazzi et al., 2013).

Debris on glaciers is generally thin at higher elevations and thickens towards the terminus. To incorporate a spatially variable melt reduction that corresponds to these different debris thick-

nesses (Østrem, 1959), I have applied a simplified surface temperature inversion method (Foster et al., 2012; Mihalcea et al., 2008b; Rounce & McKinney, 2014). Surface temperatures were derived from TIR band 10 of the Landsat 8 composite by correcting for emissivity using the ASTER global emissivity product. For the debris-covered area of a glacier, I assumed that the lowest surface temperature corresponds to a debris thickness of 1 cm, and that the 95th percentile corresponds to thick debris (Juen et al., 2014; Nicholson & Benn, 2013; Rounce & McKinney, 2014; Rounce et al., 2015) (Table 7.1). Following from the non-linear relation between thickness and temperature reported in literature (Foster et al., 2012; Mihalcea et al., 2008b; Rounce & McKinney, 2014), I estimated debris thickness using exponential scaling:

$$h = e^{\frac{(T - T_{\min}) \ln h_{\max}}{T_{p95} - T_{\min}}} \quad (7.3)$$

where  $h$  is debris thickness in cm,  $T$  is the surface temperature,  $T_{\min}$  the minimum surface temperature of the debris,  $h_{\max}$  is the thickness that corresponds to the 95th percentile surface temperature, and  $T_{p95}$  the 95th percentile surface temperature. A map of melt reduction was subsequently produced using a relative relation between debris thickness and ablation, which was constructed using data from the literature (Collier & Immerzeel, 2015; Juen et al., 2014; Kayastha et al., 2000; Mihalcea et al., 2006; Nicholson & Benn, 2006; Østrem, 1959) (Figure A.4). To account for the high melt observed for surface features on debris-covered glaciers I have attributed a melt enhancement factor to supraglacial ponds that is 10 times as high as the melt of thick debris, based on detailed research on a debris-covered glacier in the Himalaya (Chapter 3).

For each elevation band, I calculate an effective degree-day factor  $DDF_i$  from the fractional class coverages of each band and their respective melt factors. This is used to calculate a corrected negative mass balance using:

$$b_i^{\text{Corrected}} = b_i - b_i \left( 1 - \frac{DDF_i}{DDFC} \right) \quad (7.4)$$

Given a terminus ablation defined by the degree-day sum, maximum accumulation defined by precipitation and the mass-balance debris correction (Equation (4)), the slope of the mass balance gradient  $db/dz$  (m w.e.  $a^{-1} m^{-1}$ ) is determined by minimisation (Figure 7.6) of:

$$\left( \sum_{i=1}^n (b_i a_i) - B_{\text{obs}} \right)^2 \quad (7.5)$$

with  $B_{\text{obs}}$  being the observed glacier mass balance, which is discussed in the next section, and  $a_i$  the surface area of elevation band  $i$ .

The determination of  $db/dz$  by minimisation of Equation (5) resulted occasionally in unrealistically low equilibrium line altitudes (ELAs), especially for large glaciers in low-precipitation regions. This is largely due to an underestimation of the high-altitude precipitation for such glaciers, which is a known issue of the gridded climate products (Immerzeel et al., 2015). To

correct for this issue, I increased the maximum accumulation of a glacier iteratively (up to a maximum of 3000 mm) until the modelled ELA is at least greater than the 25th percentile of its SRTM elevation.

### Regional observed mass balance

Data on recent glacier mass balances in HMA are relatively sparse. To obtain a region-covering dataset I have therefore compiled recent regional mean mass balances and inter-glacier mass balance variability from multiple remote sensing and in situ studies (Farinotti et al., 2015; Gardelle et al., 2013; Gardner et al., 2013; Kääb et al., 2015; Ke et al., 2015; Sorg et al., 2012; Yao et al., 2012a; Zhang et al., 2016) (Table A.3). The regional mass balance data were converted to a grid of points at an equidistance of approximately one degree, covering only the regions for which data was available. Kriging interpolation of the points was performed subsequently to obtain coverage for the entire HMA. The final regional data were acquired by aggregating the interpolated product. A comparison with regional mass balance datasets that are less complete (Cogley, 2009; Gardelle et al., 2013) shows there is overall agreement, but also that there are some clear differences (Figure A.12). This indicates that there is still a need for a more consistent and comprehensive mass balance dataset for the entire HMA.

### Future climate implementation

To simulate future changes, I shifted the calibrated present-day mass balance curve using the temperature sensitivity of the ELA (Shea & Immerzeel, 2016), which can range from about 55 to 200  $\text{m}^{\circ}\text{C}^{-1}$  depending on local climate, and a projected temperature trajectory between the present and the end of century (Figure A.7). The maximum accumulation of a glacier was changed according to projected changes in precipitation for the same period (Figure A.8). The ensemble of temperature and precipitation projections that was used was compiled from all general circulation models (GCMs) for all representative concentration pathways (RCPs) within the Coupled Model Intercomparison Project Phase 5 (CMIP5) multi-model ensemble (Taylor et al., 2012) ( $n = 110$ , Table A.4). From the ensemble, I have selected models for the 1.5  $^{\circ}\text{C}$  scenario that have a global temperature change between pre-industrial (1851–1880) and the end of century (2071–2100) of 1.4 to 1.6  $^{\circ}\text{C}$  ( $n = 6$ ).

For the GCM runs, I extract grids of the projected changes in average air temperature and precipitation between present (1996–2015) and multiple future time slices of five years (2006–2010, 2011–2015, ..., 2096–2100). The GCM grids of varying spatial resolution were all interpolated to 0.05° resolution. The changes for temperature and precipitation were superimposed on the reference climatology, i.e. mean WFDEI temperature (1996–2014) and mean ERA-Interim precipitation (1996–2015), to generate the relative changes with respect to the present day. To obtain the final forcing input for the MBG model a moving window average was determined for each of the 5-year slices to obtain moving 30-year climatological changes, which were subsequently

interpolated to a yearly time series.

### Dynamic mass redistribution

Ice mass redistribution within individual glaciers is performed using a lumped parametrisation of ice flow (Marshall et al., 2011) to each elevation band  $i$ :

$$Q_i = \chi a_i H_i^5 \nabla z_i^3 \quad (7.6)$$

where  $Q_i$  is the volume that flows to the elevation band below,  $a_i$  the surface area,  $H_i$  the mean ice thickness, and  $\nabla z_i$  the gradient of the glacier surface at elevation band  $i$ . Parameter  $\chi$  describes ice rheology and governs the flow rate. It was determined separately for each glacier at the first time step by optimisation of the unknown  $\nabla z_i$ . This can be performed by constraining the optimisation by (i) the glacier length defined in the RGI database, (ii) a stagnant glacier terminus ( $Q_1 = 0$ ), (iii) the observed mass balance and (iv) the degree-day sum and precipitation. Using this procedure, an optimal combination of the unknown  $\nabla z_i$  and  $\chi$  is found that satisfies the glacier hypsometry, mass balance and the external forcing. Based on mass balance  $b_i$  of an elevation band that follows from the mass balance curve, and the computed ice flux, the ice thickness is updated each time step for each elevation band.

The model runs were performed transiently for the period 2005 to 2100 with a yearly time step. At each time step  $b_i$  is updated according to the translated mass balance curve and mass is redistributed. After calculating new volumes for each elevation band,  $a_i$  is updated using the exact volume–area relation for each band  $i$ , which is determined separately for each band from the modelled glacier bed shape, i.e. the ice thickness, by fitting a predictive spline model at the first time step. Cross sections and maps that show examples of modelled ice thickness over time are presented in Figure A.6 and Figure A.10, respectively.

Glaciers can have elevation bands that have much lower volumes than the rest of the glacier, e.g. at ice falls. Consequently, the ice flux through these bands can be a multiple of the ice volume present in the band itself, which cannot be resolved properly within the model time step and results in numerical instability. To counteract this, I have constrained the net flux of an elevation band to 20% of its initial ice volume; however, mass is conserved by iteratively transferring excess to adjacent lower elevation bands. The value of 20% is the largest threshold that resulted in numerically stable simulation.

The model concept does not allow ice to advance beyond the initial glacier extent. To account for glacier advance, all excess ice volume is captured in the lowest elevation band. Surface area and ablation rate for the band are adapted proportionally to the excess volume. In absence of any knowledge about the bed shape of lower elevation bands, I have chosen to calculate the increase in area caused by excess mass using a linear relation between the volume and area of a glacier. The extent to which an advance reaches lower elevation bands that are outside the glacier's initial extent is governed by the ratio between the advancing volume and the mean

**Table 7.1:** Model parameters that were used in the Monte Carlo sampling. The table shows the parameters for which Monte Carlo sampling was used. For each parameter, the type of statistical distribution, the mean, the standard deviation, and the range is given. The values and ranges for the degree-day factor (Immerzeel et al., 2015) and debris thickness (Juen et al., 2014; Nicholson & Benn, 2013; Rounce & McKinney, 2014; Rounce et al., 2015) were estimated from literature.

Parameter	Distribution	$\mu$	$\sigma$	min	max
Degree-day sum ( $^{\circ}\text{C d}^{-1}$ )	Gaussian	WFDEI climatology	$\sigma/\sqrt{n_{\text{years}}}$	-	-
DDF debris-free ice (mm w.e. $^{\circ}\text{C}^{-1} \text{d}^{-1}$ )	Truncated Gaussian	7	2	0	Inf
Debris thickness (cm)	Truncated Gaussian	50	20	0	Inf
Precipitation changes (-)	Truncated Gaussian	1	0.33	0.5	2
Obs. mass balance (m)	Gaussian	Table A.3	Table A.3	-	-

volume of all elevation bands, i.e. the advance reaches exactly one elevation band lower if the volumes are equal. Finally, the ablation of the lowest elevation band is scaled using the mass balance gradient to incorporate the advance.

## Uncertainty

To express the uncertainty in the model parameters I have applied a Monte Carlo approach to the MBG model (Figure A.5) in which I sampled five different model input variables: (1) degree-day sum, (2) maximum precipitation, (3) degree-day factor for debris-free ice, (4) debris thickness and (5) the observed regional mass balance. Sampling means, standard deviations, ranges and distributions are presented in Table 7.1. Following deterministic runs for each climate model projection that use the mean parameter values as input, I drew ten random combinations of input parameters for each of the 110 climate model projections of each modelled glacier. This yielded a total of 1210 different model realisations per glacier.

## Model validation

The accuracy of the model dynamics was evaluated using two independent datasets. I first used a geodetic dataset of elevation changes (Gardelle et al., 2013) ( $dH$ ) for the period 1999–2011 to compare observed and modelled  $dH$  of the ablation zone for eight separate regions. The model was forced with current climate conditions and run for ten years. Regional mass balances for the validation run were taken from the validation dataset itself (Figure A.12) to enable optimal evaluation of the model dynamics. There is generally good agreement between modelled and observed  $dH$  on a regional level (Figure A.13a), for both debris-free and debris-covered glaciers. Apart from compensating effects that can never be ruled out if individual processes are not monitored separately at individual glaciers, this indicates that accumulation, ablation, debris effect, and mass redistribution are well represented in the model at the regional scale. There is, however, large variability within the regions (Figure A.13a), and at the glacier scale there can be differences between observed and modelled  $dH$ . This is inevitable, however, since the large

differences in glacier-specific boundary conditions caused by complex local topography and climate are impossible to model with the data that is currently available. For interpretation of the model results regional aggregation is therefore important.

For a second validation of the model dynamics, a dataset of satellite-derived frontal changes of 255 glaciers (Scherler et al., 2011) distributed over six regions in the HMA was compared with the model results. The model, being based on a lumped approach, cannot provide frontal changes directly. I have therefore estimated the changes in the terminus position by linear scaling of the length of the lowermost elevation band (or multiple bands in the case of disappearance of the lowermost band) by its relative volume loss. Again, a ten-year model run forced by current climate conditions was used, but now with the original mass balances (Table A.3). Figure A.14a shows that the observed and modelled frontal changes are generally in agreement. There is disagreement for the Karakoram and West Kun Lun, which is most likely caused by the abundance of surging glaciers in the Karakoram, a process not incorporated in the model, and the very minimal mass balance forcing used for the entire West Kun Lun.

To determine whether the glaciers' ablation and accumulation is well represented in the MBG model procedure, I have also compared the ELAs that follow from the MBG fit with reported regional ELA (Gardelle et al., 2013) and snowline elevation (Scherler et al., 2011) estimates. For both datasets, the modelled ELAs agree well (Figure A.13b; Figure A.14b), indicating that boundary conditions and model processes that are part of the MBG fit, e.g. degree days, precipitation and debris melt reduction, are of the correct magnitude.

### **Code and data availability**

The Google Earth Engine classification code (*JavaScript*) and the model code (*R*) are available at <http://github.com/kraaijenbrink/nature-2017>. Supplementary data can be downloaded from <http://www.mountainhydrology.org/data-nature-2017>. This includes grids per glacier of the debris classification and ice thickness, model forcing data, and region-aggregated data in vector format. Other relevant data is available from the author upon request.

### **Author contributions**

PK, WI and MB conceived the study. PK performed all analyses and wrote the model code. AL contributed the climate change scenarios. PK and WI wrote the manuscript with suggestions by MB and AL.

---

## Synthesis

Since the industrial revolution climate on earth has been changing rapidly (IPCC, 2014). Global temperature has increased considerably (WMO, 2018) and in recent decades there are clear indications of changing weather patterns (Coumou & Rahmstorf, 2012). The combination of global population growth and climate change has resulted in increased stress on water resources, which are of paramount environmental and societal importance.

Climate warming has resulted in retreat and thinning of earth's ice caps, ice sheets and mountain glaciers (Kaser et al., 2006). This has implications for coastal regions because of sea level rise (Larour et al., 2017) and for water availability in river basins that have considerable glacierized areas in their headwaters, such as High Mountain Asia (HMA). Glaciers in HMA provide an important gradual release of water that is used by many people locally and downstream for irrigation, drinking water and hydropower. Climate change in this densely populated region may have serious consequences for glacier melt water supply to the rivers (Immerzeel et al., 2010).

A considerable fraction of the glaciers in HMA are covered by debris and thus they are important for the long-term evolution of glacier melt water contribution to stream flow (Bolch et al., 2012). However, the surface dynamics of these glaciers are not fully understood. More detailed data and process-based studies are required, but research is complicated by inaccessibility of the glaciers and difficult fieldwork conditions. Recent advances in UAV technology provide the opportunity to collect high-resolution data on surface changes of debris-covered glaciers. The main objective of the thesis therefore was *to increase understanding of small scale dynamics of debris-covered glaciers in order to improve projections of climate-induced glacier change*, with a specific focus on the potential application of UAVs. This has been achieved by focusing on the following five specific research questions:

1. What are the detailed spatial patterns in elevation change of a debris-covered glacier?
2. Are there spatio-temporal differences in debris-covered glacier surface velocity?
3. Can UAV thermal imaging provide new insights into debris surface properties?
4. How can ice cliffs and supraglacial ponds be analysed systematically?
5. What will be the response of HMA glaciers to future climate change and are there differences between debris-free and debris-covered glaciers?

In this chapter, I synthesize the research presented in this thesis. I discuss the main findings, integrate them in a broader perspective, and provide recommendations and a future outlook.

## 8.1 Spatially variable surface response

The surface dynamics of debris-covered glaciers are not fully understood. Thick debris insulates the ice and thin debris enhances melt (Østrem, 1959), but spatio-temporal variability in debris thickness, surface roughness, turbulent fluxes, and energy transport through the (moist) debris makes melt patterns complex and spatially heterogeneous (e.g. Benn et al., 2012; Collier et al., 2014; Nicholson & Benn, 2006; Ragetti et al., 2016a; Rounce & McKinney, 2014). Clear knowledge gaps exist with respect to the intricate dynamics of small scale surface processes, i.e. the exact interplay between the ice, debris and atmosphere. Spatial variability of many important debris properties, such as debris moisture content (Collier et al., 2014), debris thickness (Rounce & McKinney, 2014), grain size and pore space (Evatt et al., 2015), surface roughness (Miles et al., 2017b), and the atmospheric boundary layer over debris-covered glaciers (Brock et al., 2010) are largely unknown. To better understand melt processes of debris-covered glaciers and how these may be affected by a changing climate, detailed observations and improved models of debris-covered glacier change are required.

In Chapter 3, I use multi-temporal high-resolution imagery and DEMs obtained using a UAV and SfM-MVS processing (Carrivick et al., 2016) to detail surface thinning patterns on the debris-covered tongue of Lirung Glacier, and show for the first time that thinning of the tongue is highly heterogeneous. The UAV-derived DEMs enabled accurate geodetic monitoring method at centimetre resolution, which cannot be met by current satellite products, including high-resolution commercial satellites (Berthier et al., 2014; Brun et al., 2018; Ragetti et al., 2016a). On average thinning was limited, but in the vicinity of ice cliffs and supraglacial ponds surface thinning rates were much higher than the glacier average. Ice cliffs and ponds appear to contribute considerably to the total melt of the glacier, despite their relatively small surface area, and are responsible for a large part of the spatial heterogeneity at the glacier surface.

Although Lirung Glacier was shown to have relatively low surface velocity (Chapter 3) and the effects of glacier flow dynamics and ice emergence are potentially limited, they are important to consider. Knowledge of ice dynamics and emergence are crucial for the interpretation of glacier thinning rates derived from geodetic measurements from satellite or UAV platforms, because the ice influx of the tongue constrains the emergence velocity and together with the surface thinning determines the mass balance (Banerjee, 2017; Brun et al., 2018; Vincent et al., 2016). Estimating ice dynamics of a debris-covered glacier tongue is not straightforward, however, and requires knowledge of the ice flow velocity and thickness (Vincent et al., 2016). In Chapter 4, I demonstrate the application of a frequency cross-correlation algorithm to multi-temporal optical UAV data to derive high-resolution spatially-continuous surface velocity fields. These fields provide a valuable addition to the analysis and modelling of glacier flow dynamics and emergence. Two velocity maps revealed differences in glacier surface velocities between the summer and the winter, and between the upper and lower tongue. The high spatial resolution of the UAV data allowed for detection of subtle patterns in flow, despite the relatively low surface

velocity and the short periods between the surveys. This evidences that UAVs are particularly useful for surveys of slow processes, such as debris-covered glacier flow.

The high-resolution elevation difference maps (Chapter 3) and velocity fields (Chapter 4) show the dynamic and heterogeneous response of debris-covered glaciers in high resolution, but shed little light on the causes of the spatial variation. This requires more data on surface properties and near-surface atmosphere that help to reveal energy storage of the debris and energy exchange with the ice and atmosphere. In Chapter 5, I outline the first spatially distributed surface temperature measurements of a high-altitude debris-covered glacier made with a UAV. In conjunction with *in situ* measurements and modelling, these surface temperature data can help estimate spatial variability in debris thickness (Rounce & McKinney, 2014), longwave radiation (Steiner & Pellicciotti, 2016), sensible heat flux, and may reveal the complex supra- and englacial hydrology network (Miles et al., 2017a). The temperature of the supraglacial debris layer was remarkably variable in space and time. Statistical analysis revealed that the variability was largely independent of incoming radiation and topography, and that much of the signal in surface temperature originates from variation in properties of the debris and is useful for further research.

## 8.2 Ice cliffs and supraglacial ponds

Ground-based and modelling efforts have revealed high ablation rates of ice cliffs in great detail (e.g Buri et al., 2016a,b; Han et al., 2010; Sakai et al., 2002; Steiner et al., 2015; Watson et al., 2016a, 2017), and showed increased ablation near supraglacial ponds (Miles et al., 2016, 2017a). The UAV datasets presented in Chapter 3 and Chapter 4 further support these studies. However, it is poorly understood to what extent the surface features affect total glacier melt and whether they are responsible for the equal thinning rates observed for debris-covered and debris-free glaciers (Gardelle et al., 2013; Kääh et al., 2012). Ice cliff ablation is strong and might be of importance (Chapter 3; Pellicciotti et al., 2015), but only a very limited fraction of the surface is covered by these features, and ice cliff melt rates would have to be extremely high relative to debris-covered ice (Brun et al., 2018). Differences and potential climate-induced changes in ice flow dynamics and emergence in the ablation zone may therefore be a more logical explanation (Anderson & Anderson, 2016; Banerjee, 2017; Brun et al., 2018; Vincent et al., 2016). Besides knowledge on ice velocity (Chapter 4) and ice depth, detailed information of the spatial distribution of surface features, their morphology, temporal dynamics, and specifics of the surrounding glacier are required to improve our understanding on this topic.

To quantify this systematically, I present a method to delineate and characterise ice cliffs and supraglacial ponds on a debris-covered glacier in Chapter 6. The semi-automatic approach was able to objectively delineate the surface features from a UAV orthomosaic and DEM, and provided the opportunity to extract detailed morphological characteristics of ice cliffs. Consequently, it has provided insights into the characteristics and spatial distribution of the surface

features, which is valuable information for ice cliff evolution studies (e.g. Buri & Pellicciotti, 2018; Sakai et al., 2002) and their contribution to total glacier melt (Pellicciotti et al., 2015; Ragetti et al., 2016a). Because of the relatively low flight height of the UAV above the ground level the full three-dimensional morphology of ice cliffs could be derived automatically, and this has great potential for a systematic calibration and validation of melt models and provides advantages compared to terrestrial approaches (Brun et al., 2016; Watson et al., 2017).

### 8.3 Future of the glaciers

Glaciers in HMA provide an important seasonal contribution to stream flow (Marzeion et al., 2014), as they gradually release precipitation and act as a reservoir (Jansson et al., 2003). In arid regions in the west their melt water is particularly important for irrigation and hydropower (Lutz et al., 2014), and hence of importance for future power and food security (Immerzeel et al., 2010). Past and ongoing glacier mass loss of the glaciers in HMA (Brun et al., 2017) has increased the glacier melt water component in the rivers, but continued reduction of glacier area will result in reduced release of glacier melt water eventually (Huss & Hock, 2018; Immerzeel et al., 2013). It is a key scientific challenge to translate results from local scale, i.e. single glacier studies, to reliable projections of regional response of glaciers to climate change. In Chapter 7, I use the knowledge about the response of debris covered glaciers to develop a large scale model for the entire HMA to understand how climate change will impact (debris-covered) glaciers and what the potential impacts are on water resources.

I show that the HMA is subject to elevation dependent warming and that the mountains are warming more rapidly than the global average. Hence, there is an increased sensitivity of HMA glaciers to climate change and a large volume of ice will be lost this century, even under an optimistic climate change scenarios such as the 1.5 °C target of the 2015 Paris climate agreement. More realistic climate change projections (Raftery et al., 2017) are detrimental for the ice reserves in many regions of HMA, with potentially strong consequences for regional water management in the second half of this century. My results also revealed that regions with many debris-covered glaciers have a delayed response to warming as a result of the insulation of a thick debris layer and that debris thus provides a buffer to climate change. Water availability issues related to future glacier loss are thus less urgent in basins with a greater proportion of debris-covered glaciers.

### 8.4 Challenges, recommendations and research outlook

The studies presented in this thesis provide insights into the surface evolution of debris-covered glaciers. There are, however, still various research gaps to overcome before the role of debris-covered glaciers is well understood. In this section, I indicate important remaining scientific challenges, and provide recommendations and an outlook for future research.

### Thinning of debris-covered glaciers

This thesis reveals the high spatial variability of thinning rates and surface temperatures on debris-covered glaciers and shows that surface temperature varies because of surface properties and processes. However, the exact processes and their influence on melt have not yet been quantified. Future studies should focus on combining UAV-based data with field observations of debris properties to improve empirical and process-based models of debris-covered glacier melt. Linking UAV-derived surface warming and thinning with *in situ* measurements will provide important clues on the surface energy balance and can help to quantify ablation and emergence.

Supraglacial features and ice flow dynamics are identified as potential causes of the largely equal thinning rates of debris-covered and debris-free glaciers, but specifics are unknown and a clear attribution cannot be made yet. This limits our understanding of future changes to the melt of these glaciers. Ice cliff ablation has been studied in detail, but important information of ice flow and the emergence component of thinning are largely lacking at present and should be expanded in future research. Glacier velocity measurements from UAV or high-resolution satellite data can be useful, but to obtain the ice mass fluxes that are required to estimate emergence it is important to perform those in conjunction with measurements of ice depths. As these are currently difficult to perform, developments in (airborne) GPR systems (Eisenburger et al., 2008) are very promising and key to collecting detailed ice depth information for a large sample of glaciers in order to fully understand the dynamics of thinning.

### Advances in UAV technology and sensors

Recent advances in UAV technology are expected to continue in the future with potentially exciting opportunities in the research of debris-covered glaciers. For instance, improvements in battery power, flight software and communication devices will lead to autonomous UAV systems operating from a base station that can survey regularly for longer periods of time without human interference (Blockley et al., 2017; Teixeira et al., 2018). Combined with other developments such as better location accuracy and endurance, this may provide powerful automatic monitoring systems that acquire data on high spatial and temporal resolution for relatively large extents.

With increased UAV endurance it may also be possible to survey both the accumulation and ablation area of a glacier in detail, which would allow glacier mass balance to be determined more accurately and could provide information on glacier flow dynamics. However, for most glaciers in HMA this would require additional improvements in the stability, navigation and sensor capabilities of UAVs, because the accumulation zone is characterized by high wind and low air pressure, complex steep topography, and limited surface contrast. Moreover, this would require good estimates of the density of snow and ice.

Improvements in UAV-mounted sensors may also significantly change the analysis of debris-covered glaciers. Multi- or hyperspectral sensors will enable better systematic classification of

ice cliffs and ponds on debris-covered glaciers. They could also be used to gather detailed spectral and particle size information for snow and firn in the accumulation area (Nolin & Dozier, 2000), or determine the lithological composition and potentially the source of the debris (Gibson et al., 2017). Sensing in shortwave infrared will provide better capabilities to detect moist debris (Sadeghi et al., 2015), which could provide additional information for energy balance models, especially valuable when deployed together with thermal infrared sensors. Future advances in the weight and power consumption of LiDAR and GPR systems may allow them to be used as UAV payload at high-altitude, allowing for the mapping of glacier surface elevation without ground control and SfM, and mapping of ice thickness (Fasano et al., 2017; Sankey et al., 2018).

Besides imaging sensors, UAVs can also be equipped with sensors that measure meteorological variables such as wind speed, wind direction, pressure, air temperature and humidity (Knuth & Cassano, 2014), and have the potential to measure turbulent fluxes (Reineman et al., 2013). Surveying these variables in longitudinal, transverse and vertical profiles over (debris-covered glaciers) will provide high-resolution three-dimensional measurements of the atmospheric boundary layer. Together with synchronous surface temperature measurements and *in situ* meteorological measurements, this has great potential to further research the glacier surface energy balance.

### **Combining UAVs, satellites, in situ and modelling**

UAVs are particularly valuable for studies of small scale processes, due to their capability to deliver distributed data at high resolution. These abilities allow researchers to develop methods and insights that can be extrapolated to the glacier or catchment scale through modelling and satellite remote sensing, as this thesis exemplifies. Future possibilities of such integration are valuable and should be pursued to understand variability from site to site and scale to scale. A integrated system that would combine advances in computational capabilities, analytical methods, and *in situ*, satellite and UAV data would be of particular value for the research of debris-covered glaciers and the environment in general.

The cloud-computing power and data availability of Google Earth Engine (GEE) (Google Earth Engine Team, 2017) could be a central component of such a system. The platform allows for complex high-resolution spatial analyses for large areas and easy access to a wide range of different satellite, landcover, climate, weather and other data (Gorelick et al., 2017). Consequently, it has the potential to perform and combine different large scale analyses easily in unprecedented ways, which would allow better interpretation of changes and feedbacks in the entire system, e.g. analysis of climate and weather data, changes in glacier mass (Brun et al., 2017), changes in debris-cover (Chapter 7), changes in surface water (Pekel et al., 2016), and changes in vegetation (Hansen et al., 2013). GEE's database is also constantly updated with recent data, which enables near real-time change detection and model data assimilation.

UAV data in integrated observational-statistical-model systems can be utilized by assimilation,

validation or calibration and can greatly improve large scale measurements and model predictions. Sub-grid variability of a model can for instance be parametrized using UAV data and be used to upscale its findings to large regions. On the other hand, UAV data can be used for statistical downscaling and calibration of satellite data or derivative products, e.g. thermal infrared imagery (Chapter 5) or land cover classifications (Chapter 6). It is important to improve the satellite observations to enable better large scale analyses, particularly because the UAV approach is limited to relatively small extents and accessible locations. For all these applications a substantial amount of UAV data is required and hence it is important to perform more UAV surveys in varied locations to capture and compare spatial variability.

The large amount of data that is available nowadays requires and enables a new data processing approaches. Past and future developments in artificial intelligence and machine learning algorithms, e.g. deep neural networks, random forests and support vector machines (Lary et al., 2016), are able to extract meaningful information from large amounts of data and are therefore crucial in future research of glaciers and the water cycle. Integration of such empirical predictor-based approaches in process-based models will yield new possibilities in glacier research. For instance, they could statistically combine data at many scales on spatial variability in glacier melt, climate and weather, complex topographical descriptors, and process-based responses to provide details on the cause and effects of local and regional variability in glacier response. Moreover, the algorithms are valuable for down- and upscaling of spatial data (Dong et al., 2016; He et al., 2016), and combining distributed and point data.

For large scale integrated analyses continued advances in quality and quantity of satellite data are valuable. For example, the recently launched satellite of the Gravity Recovery and Climate Experiment Follow-On mission (GRACE-FO) (Flechtner et al., 2014) provides continued and improved monitoring of the large scale distribution of earth's water, which helps to identify changes to glaciers, permafrost and ground water. On smaller scale, the ongoing development of a constellation of high-resolution CubeSat miniature satellites (Planet Team, 2017) allows for determination of high-resolution spatio-temporal dynamics of glaciers in unprecedented ways (e.g. Steiner et al., 2018), and provides valuable data for statistical downscaling.

### **Integration into the larger system**

In this thesis I focus strongly on debris-covered glaciers and the implementation of UAVs in their research. Although this type of glacier is present in many of the high-altitude mountainous catchments of HMA, its melt and water storage comprises only a single component of the water balance. To understand the mountain water cycle and determine the full impact of climate change on the mountains it is required to understand the dynamics and future changes of all components and processes. However, various knowledge gaps still exist at present.

Valley scale atmospheric dynamics are yet uncertain and we know relatively little about the spatio-temporal variability of temperature and precipitation at high altitude (Collier et al., 2015;

Immerzeel et al., 2015). This information is crucial to understand patterns in high-altitude precipitation, snow fall and melt, glacier accumulation and ablation, and their effect on seasonal variability in discharge. Specific snow dynamics complicate the balance. The largely unknown and variable turbulent fluxes and wind redistribution of snow strongly affect sublimation rates (Stigter et al., 2017), which regulate for a large part the amount of precipitation released as runoff and glacier accumulation. Glacier and snow melt models are generally simplified by using temperature index approaches and these work well for regional and catchment scale approaches, but can be incompetent for estimation of high-altitude melt. This requires more physics-based approaches and better estimation of spatio-temporal dynamics of meteorological variables (Hock et al., 2017). Groundwater provides an important base flow for mountain rivers and downstream areas (Andermann et al., 2012; Bookhagen, 2012), but it is difficult to measure and as such yet poorly understood. Finally, the components of the water balance cannot be studied properly if river discharge is unknown, but accurate measurements of discharge in remote mountainous catchments are also challenging and lacking.

UAVs have potential to contribute to advancements in the research challenges above. For example, UAV surveys can (1) provide data on spatial variability of meteorological variables; (2) produce high-resolution DEMs to determine snow depth and provide surface temperature to support snow energy balance studies; (3) identify and quantify the inflow of ground water in river streams by thermal imaging, and help to detect soil moisture and mountain springs; and (4) produce high-resolution maps of the topography of the river bed to support river discharge measurements. Nevertheless, understanding the mountain water cycle requires a multi-faceted systems approach that consists of field measurements, aerial and spaceborne remote sensing, and modelling of all the components to acquire the in-depth knowledge of mountain river catchments required to understand their impact on downstream areas.

From a downstream water resource perspective, there are also many factors to consider besides the glaciers. This comprises direct effects on stream flow, such as changes in precipitation and evaporation, and indirect effects, such as ground water depletion by unsustainable irrigation practices. Moreover, the large population growth and rapid socio-economic developments in HMA have the potential to put stress on the water balance and changes in water demand are conceivably very important in the short term future.

Unravelling small scale processes lies at the basis of understanding our environment. To understand water supply and demand and possible implications of future climate change in full, it is key to understand each component completely and utilize specific knowledge, such as gained in this thesis, in multidisciplinary studies and system approaches. Integration of details into the larger picture will help to improve concepts and contribute to a larger understanding of our environment, and ultimately will help us to improve our insights into climate change, its impacts and required measures, now and in the future.



## Supplementary information to Chapter 7

### A.1 Supplementary figures

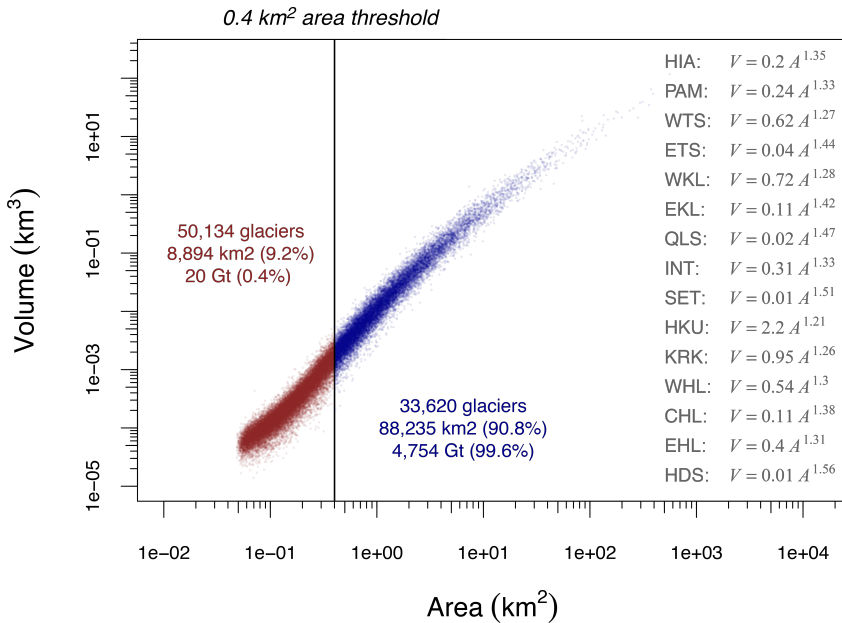


**Figure A.1:** Relation between area and volume for the entire HMA. The graph shows volume versus area for all glaciers that are larger than 25 Landsat pixels, i.e. 0.0225 km<sup>2</sup> ( $n = 83754$ ), based on modelled ice thickness. The glaciers below the 0.4 km<sup>2</sup> threshold were discarded for further analysis. Volume-area scaling relations for each RGI sub-region were determined using regression and are shown in the plot as grey annotation. Note that these volume-area scaling relationships are shown as additional information for the reader, they were not used in our modelling.

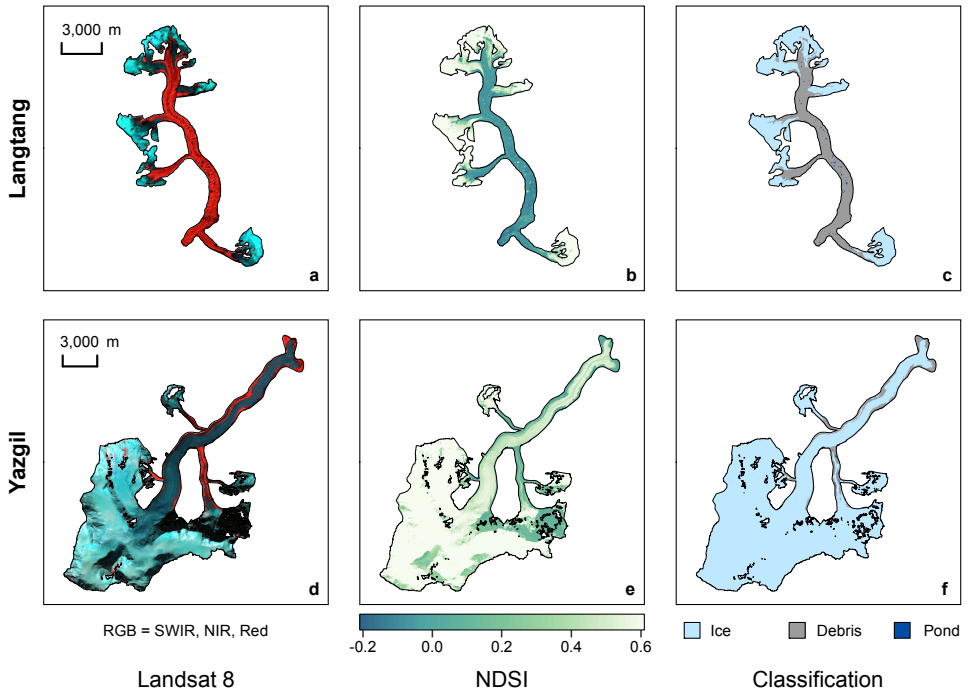


**Figure A.2:** Example maps of the debris classification. Landsat 8 imagery (a, d), Normalised Difference Snow Index (NDSI) (b, e) and final debris classification (c, f) for the 38 km<sup>2</sup> Langtang Glacier (a–c) and the 134 km<sup>2</sup> Yazghil Glacier (d–f). The RGI glacier outline is depicted as a black line.

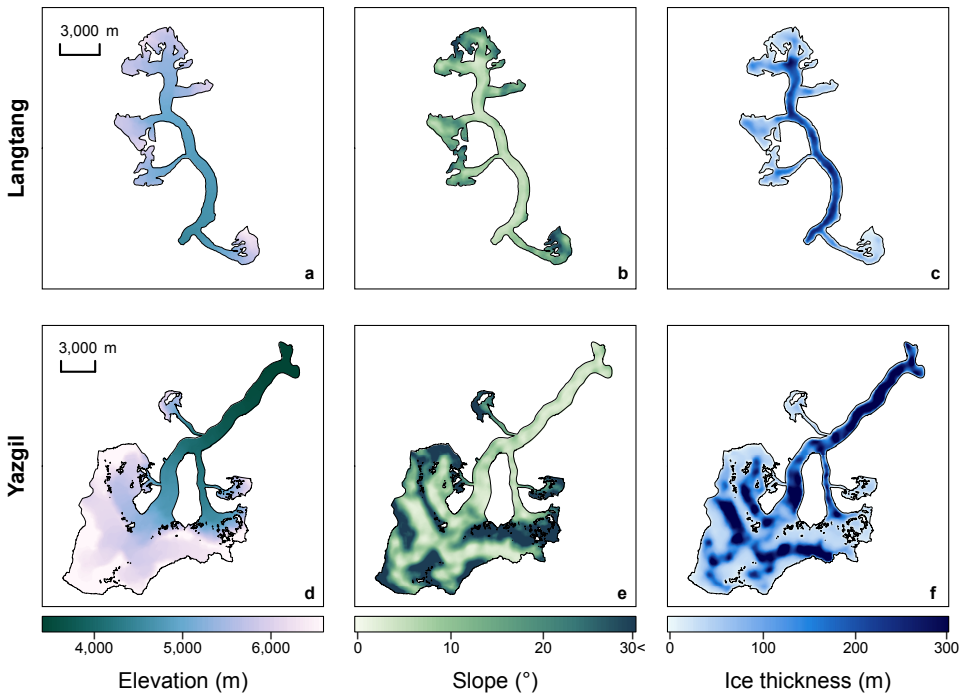


**Figure A.3:** Example maps of the ice thickness modelling. SRTM elevation (a, d), SRTM slope (b, e) and GlabTop2 ice thickness (c, f) for Langtang Glacier (a–c) and Yazghil Glacier (d–f). The RGI glacier outline is depicted as a black line.

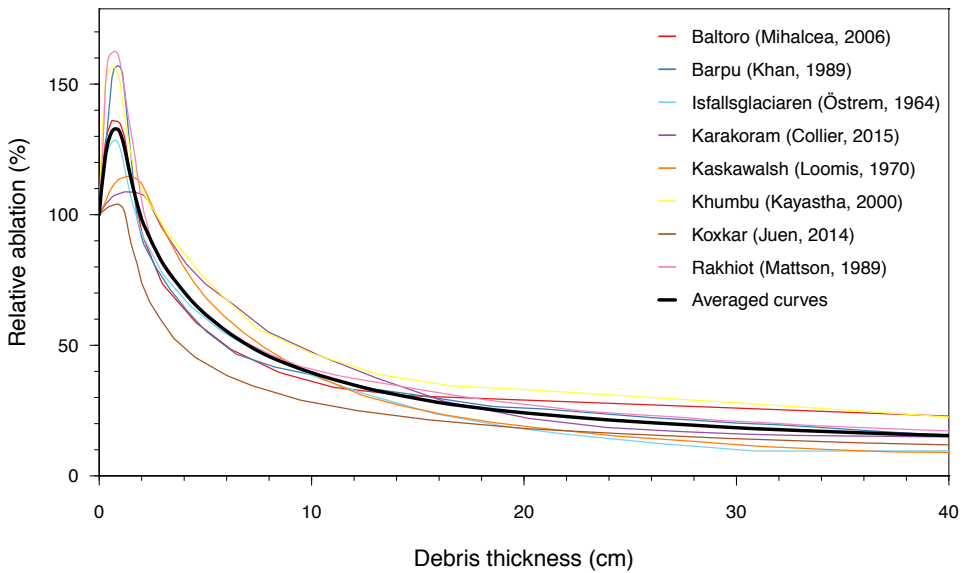


**Figure A.4:** Ice ablation versus debris thickness. The figure shows ablation under debris cover relative to debris-free ice ablation determined for different glaciers (Collier & Immerzeel, 2015; Juen et al., 2014; Kayastha et al., 2000; Mihalcea et al., 2006; Nicholson & Benn, 2006; Østrem, 1959). The average of the curves is used in the mass balance gradient model to calculate reduction of ice ablation by debris.

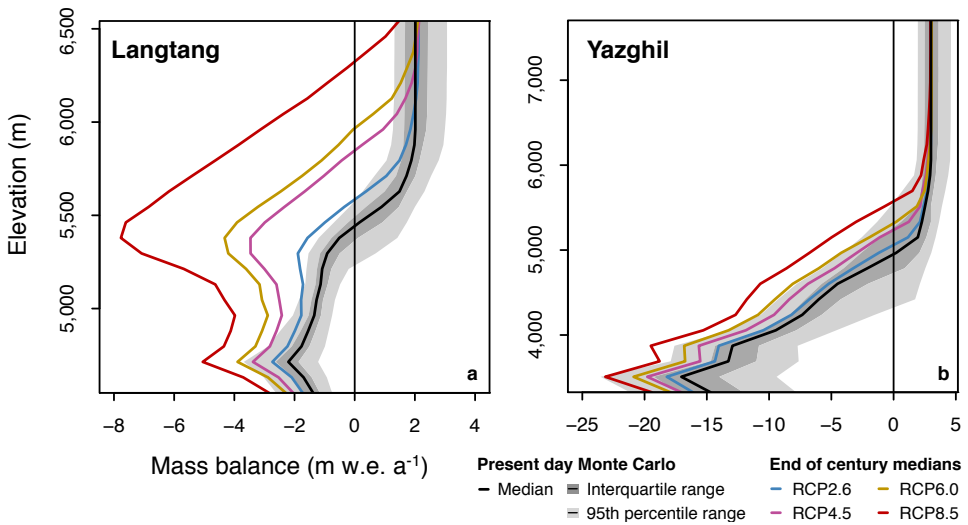


**Figure A.5:** Examples of mass balance curves fitted using the MBG model. The panels show the median and the spread of mass balance curves for the present day that follow from the Monte Carlo parameter ensemble for both Langtang (a) and Yazghil (b). Additionally, median mass balance curves are plotted for each RCP ensemble in the end of century (2071–2100).

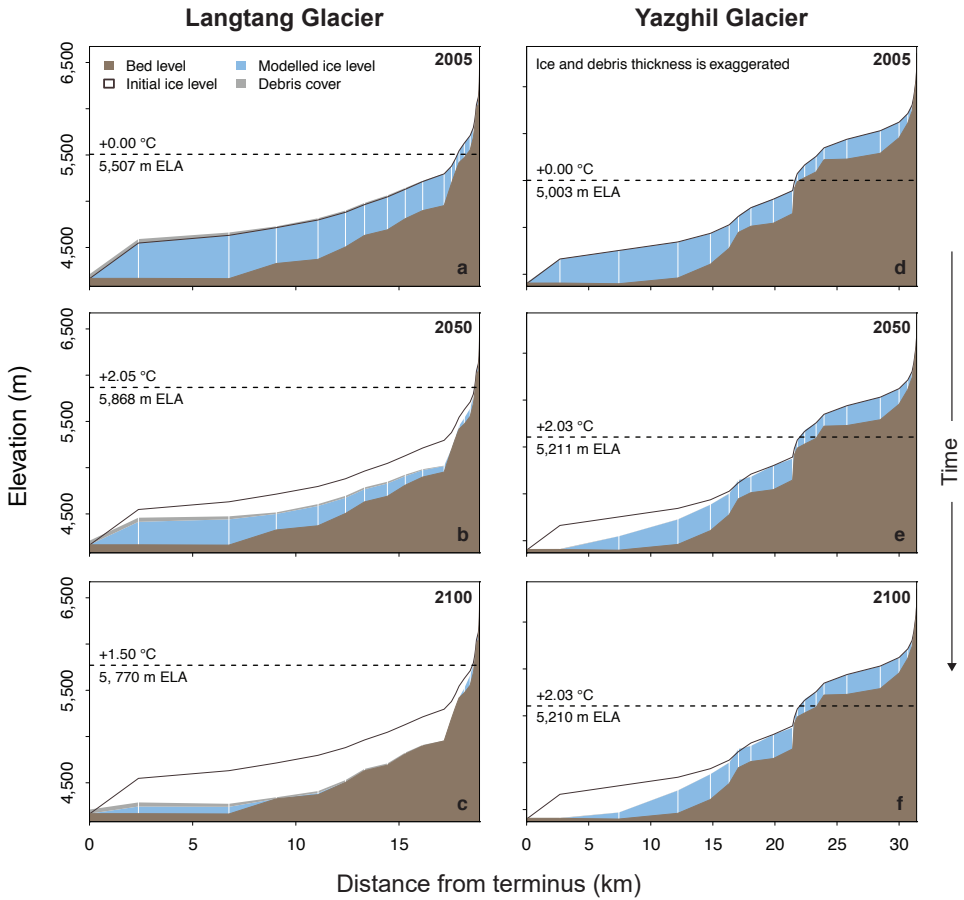


**Figure A.6:** Schematic cross profiles of modelled ice thicknesses. The panels show examples of modelled reduction in ice thickness at different time steps for Langtang Glacier (a–c) and Yazghil Glacier (d–f). The separation between the different elevation bands is indicated by the vertical white lines. The forcing used in the figure for both glaciers is MIROC5 RCP2.6 (Table A.4).

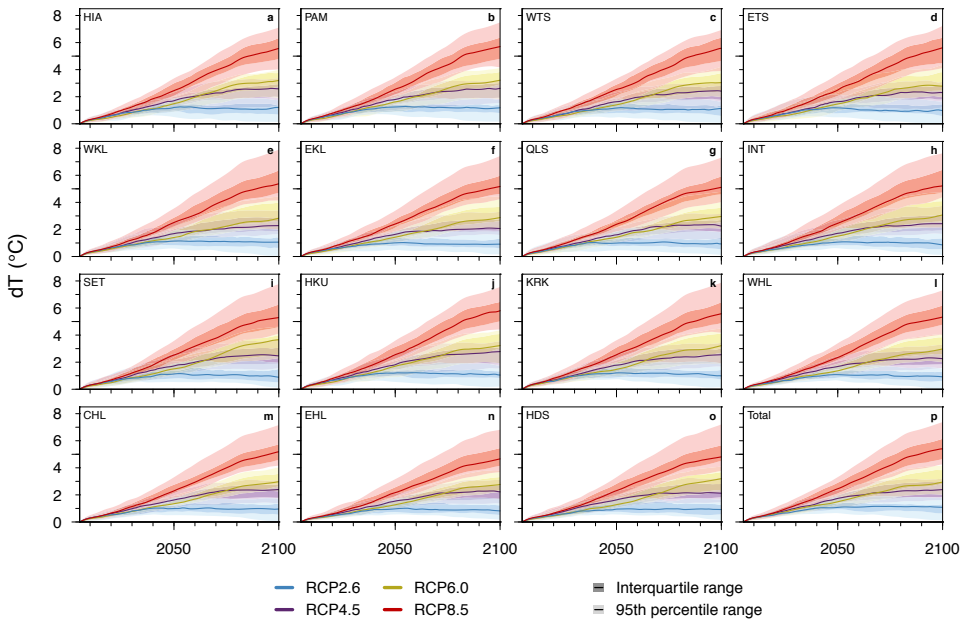


**Figure A.7:** Temperature forcing over the period 2005–2100. The panels show the transient temperatures that were used to force the mass balance gradient model for the entire model period for all RCPs. Each panel shows a line with the mean temperature and a shading with the RCP ensemble spread for a specific RGI sub-region (a–o) or the total HMA (p).

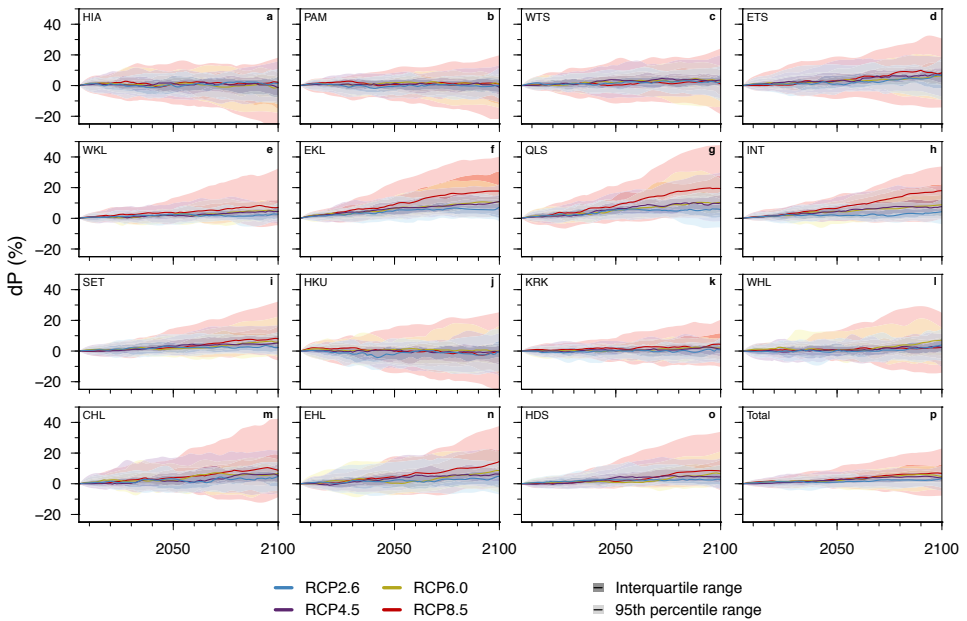


**Figure A.8:** Precipitation forcing over the period 2005–2100. The panels show the transient precipitation changes that were used to force the mass balance gradient model for the entire model period for all RCPs. Each panel shows a line with the mean precipitation changes and a shading with the RCP ensemble spread for a specific RGI sub-region (a–o) or the total HMA (p).

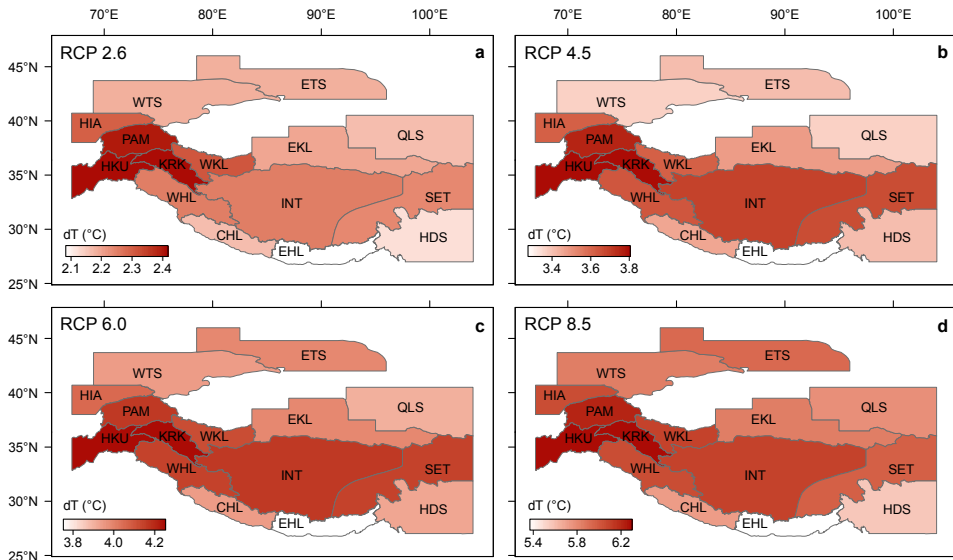


**Figure A.9:** Mean temperature increases for all four RCPs. Maps with the mean temperature increase at the glaciers of an RGI sub-region between pre-industrial (1851–1880) and end of century (2071–2100) for RCP2.6 (a), RCP4.5 (b), RCP6.0 (c) and RCP8.5 (d).

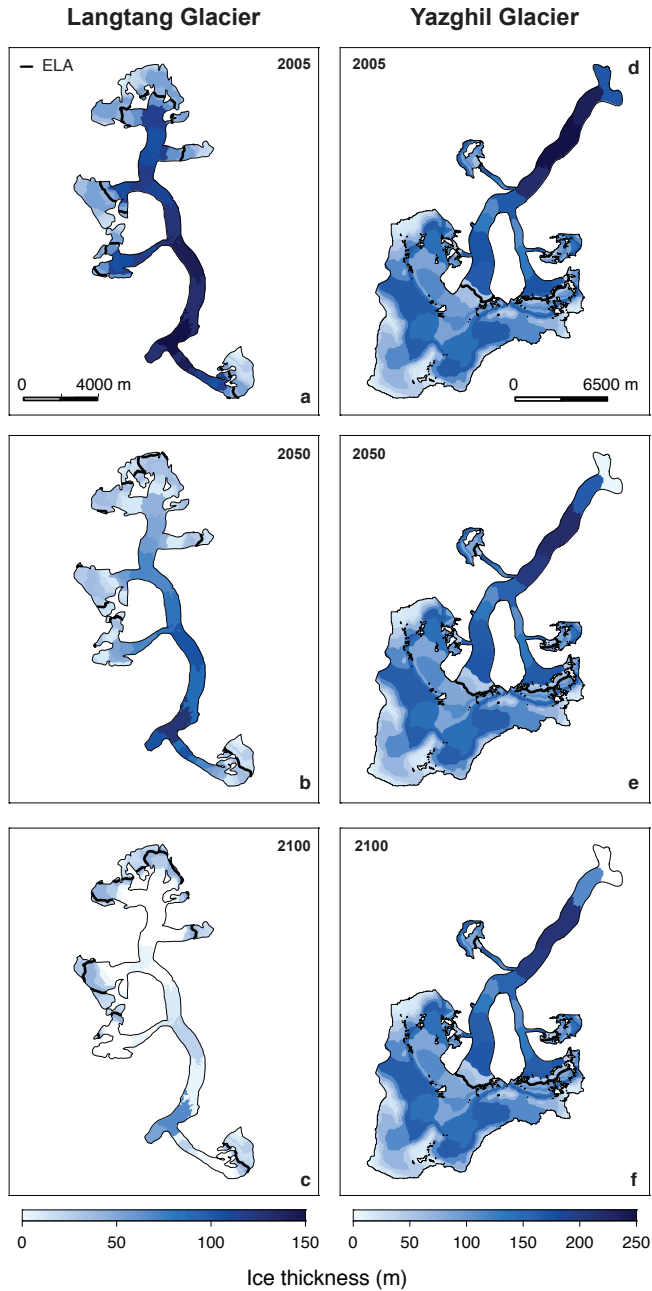


**Figure A.10:** Example maps of future ice thickness for elevation bands of a glacier. The maps show for Langtang Glacier (a-c) and Yazghil Glacier (d-f) examples of modelled reduction in average ice thickness per elevation band for three different time steps, which are annotated in each panel. The forcing used in the figure for both glaciers is MIROC5 RCP2.6 (Table A.4).

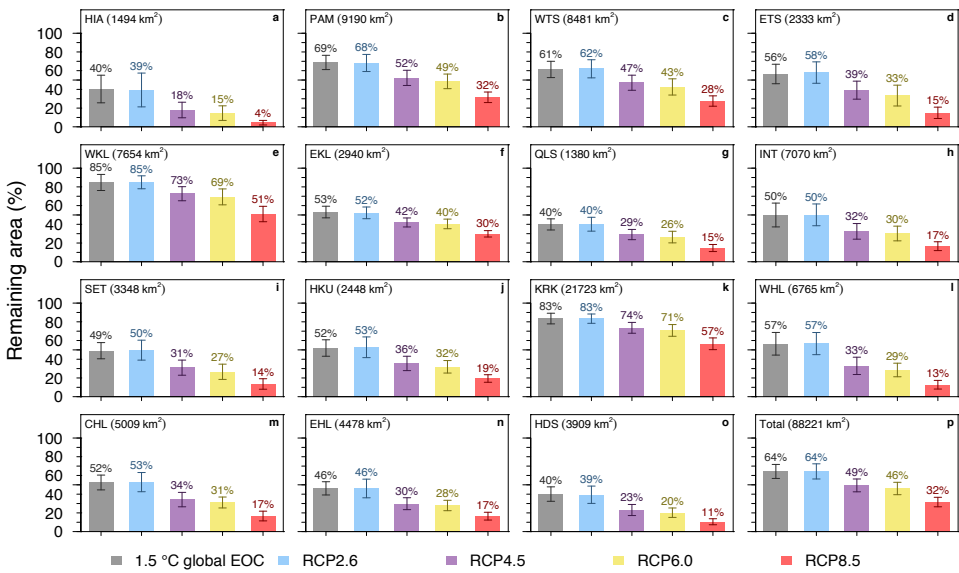


**Figure A.11:** Remaining glacier area by the end of century. For every RGI sub-region (a–o) bar plots show the glacierized area that will remain in the end of century (EOC, 2071–2100) for all RCP ensembles and the models selected for the 1.5 °C scenario (Table A.4). The error bars indicate the standard deviation of the ensembles. Remaining areas for the entire HMA are shown in panel p.

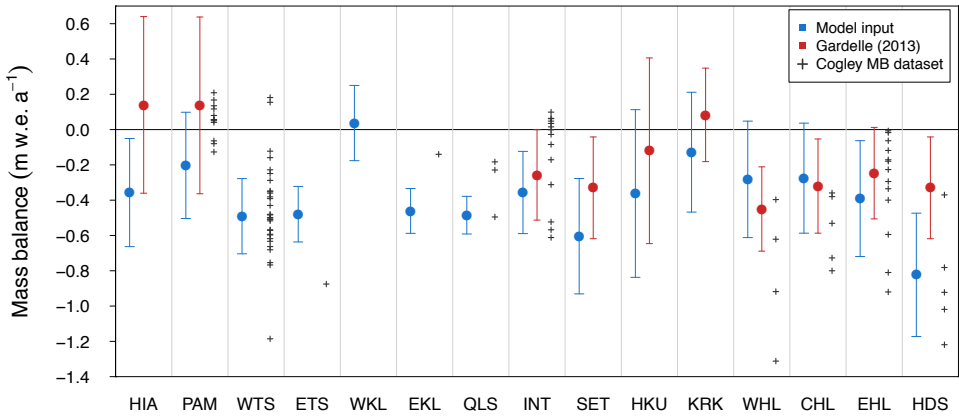


**Figure A.12:** Comparison of mass balance data. A comparison of the regional mass balance means and inter-glacier standard deviations that were used to force the model (blue) with those determined from data of a large-scale geodetic study (Gardelle et al., 2013) (red). Mass balances of the Cogley GMBAL dataset (release 1501) (Cogley, 2009) available for glaciers in the RGI sub-regions that fall in the period 2000–2010 ( $n = 91$ ) are plotted as grey crosses.

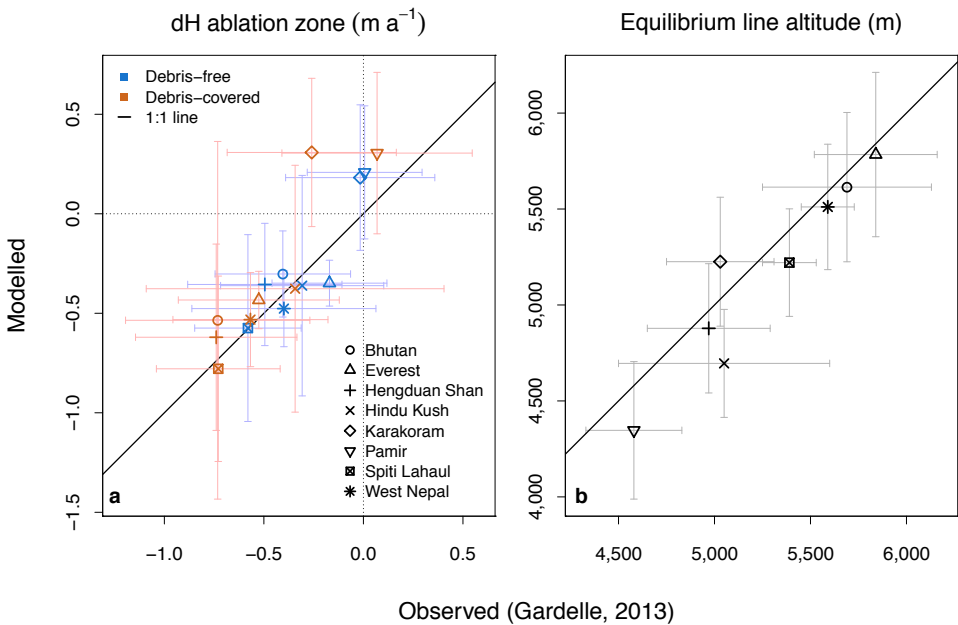


**Figure A.13:** Validation of modelled elevation change and ELA. Modelled versus observed (Gardelle et al., 2013) elevation changes of the ablation zone, shown separately for debris-free and debris-covered tongues (a). Modelled ELAs versus reported ELAs (Gardelle et al., 2013) for the same regions (b). The points denote the regional mean and the whiskers the standard deviation.

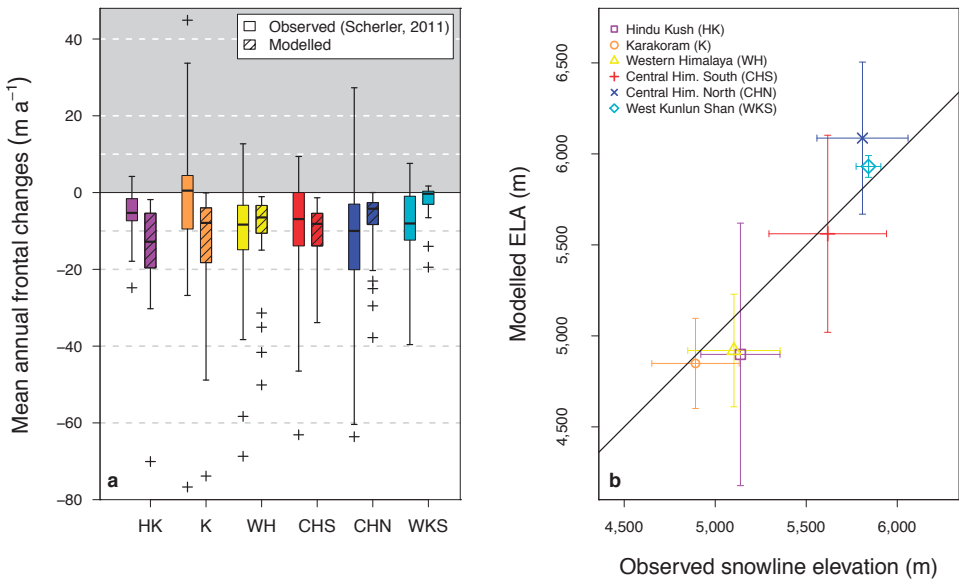


**Figure A.14:** Validation of frontal changes and ELA. Modelled versus observed (Scherler et al., 2011) frontal changes of glacier tongues (a). The horizontal bars denote the median, the boxes the interquartile range, and the crosses denote outliers that are outside 2.5 times the interquartile range. Panel b shows modelled ELAs versus estimated snow line elevations (Scherler et al., 2011) for the same regions. The points denote the regional mean and the whiskers the standard deviation.

## A.2 Supplementary tables

**Table A.1:** Glacier statistics for every RGI sub-region. Processed glaciers are those on which the analysis was performed, i.e. glaciers larger 0.4 km<sup>2</sup>. Processed area was determined from RGI metadata. Processed volume was determined using the GlabTop2 model results, which was limited to glaciers that are larger than 25 Landsat pixels ( $n = 83,754$ ).

RGI sub-region	Glaciers	Processed glaciers	Processed glaciers (%)	Processed area (%)	Processed volume (%)
Hissar Alay	3,151	942	29.9	80.9	98.5
Pamir	10,234	3,737	36.5	88	99.5
West Tien Shan	9,739	3,388	34.8	89	99.4
East Tien Shan	5,227	1,461	28	81.7	98.4
West Kun Lun	5,396	2,281	42.3	94.1	99.8
East Kun Lun	3,519	1,275	36.2	90.5	99.7
Qilian Shan	2,730	850	31.1	84.3	98.4
Inner Tibet	9,365	3,093	33	89.2	99.4
South Tibet	5,066	1,582	31.2	86.2	99.1
Hindu Kush	4,401	1,298	29.5	83.3	99
Karakoram	13,759	4,963	36.1	94.9	99.9
West Himalaya	9,832	3,194	32.5	87	99.3
Central Himalaya	4,529	2,015	44.5	92	99.5
East Himalaya	4,237	1,750	41.3	91.4	99.6
Hengduan Shan	4,352	1,758	40.4	89.3	99.4
Total	95,537	33,587	35.2	90.2	99.3

**Table A.2:** Error matrix and statistics that show the accuracy of the debris classification. The error matrix is based on a stratified sample of 1000 random points for which ground truth was determined visually. For 15 of the random samples ground truth could not be determined accurately. Classification accuracy statistics (Lillesand et al., 2015) calculated from the error matrix are shown in the table as well as class abundances for the entire composite mosaic.

<b>Error matrix</b>	<i>Ground truth</i>		
<i>Classification</i>	Debris-free	Debris-covered	Lake
Debris-free	371	19	0
Debris-covered	21	373	4
Lake	21	22	154
<i>28% of debris samples on slope &gt;24°</i>			
<b>Error statistics</b>			
Producer's accuracy	90%	90%	97%
User's accuracy	95%	94%	78%
Overall accuracy	91%		
Kappa value	0.86		
Class abundance	102,202,797 (85.9%)	16,501,140 (13.9%)	237,475 (0.2%)

**Table A.3:** Observed regional mass balances. The table shows the regional mass balances and mass balance standard deviations that were used to run the MBG model. The values were taken from various remote sensing and *in situ* studies (Farinotti et al., 2015; Gardelle et al., 2013; Gardner et al., 2013; Kääb et al., 2015; Ke et al., 2015; Sorg et al., 2012; Yao et al., 2012a; Zhang et al., 2016).

Region	Observed MB (m)	MB source	Area-weighted SD(m)	SD source
Hissar Alay	-0.36	Kääb 2015	0.31	-
Pamir	-0.20	Kääb 2015	0.30	Zhang 2016
West Tien Shan	-0.49	Farinotti 2015	0.21	Sorg 2015
East Tien Shan	-0.48	Farinotti 2015	0.16	Sorg 2015
West Kun Lun	0.04	Kääb 2015	0.21	Ke 2015
East Kun Lun	-0.46	Kääb 2015	0.13	Ke 2015
Qilian Shan	-0.49	Kääb 2015	0.11	-
Inner Tibet	-0.36	Kääb 2015	0.23	Yao 2012
South Tibet	-0.60	Kääb 2015	0.33	Yao 2012
Hindu Kush	-0.36	Kääb 2015, Gardner 2013	0.48	Gardelle 2013
Karakoram	-0.13	Kääb 2015	0.34	Gardelle 2013
West Himalaya	-0.28	Kääb 2015	0.33	Gardelle 2013
Central Himalaya	-0.28	Kääb 2015	0.31	Gardelle 2013
East Himalaya	-0.40	Kääb 2015	0.33	Gardelle 2013
Hengduan Shan	-0.82	Kääb 2015, Gardner 2013	0.35	Gardelle 2013, Yao 2012

**Table A.4:** CMIP5 climate models used for climate forcing. The table shows the models part of each RCP ensemble of CMIP5 GCMs that are used to force the mass balance gradient model. For each model the global and HMA dT (°C) and dP (%) are shown for both pre-industrial to end of century and present to end of century. Models part of the 1.5 °C EOC ensemble are flagged with an asterisk.

RCP	Model run	Global dT 1851-1880 – 2071-2100	Regional dT 1851-1880 – 2071-2100	Regional dP 1851-1880 – 2071-2100	Regional dT 1996-2015 – 2071-2100	Regional dP 1996-2015 – 2071-2100
RCP2.6	bcc-csm1-1-m_r1i1p1	1.86	2.36	6.40	0.83	2.90
RCP2.6	bcc-csm1-1_r1i1p1	1.77	2.20	3.50	0.80	2.80
RCP2.6	BNU-ESM_r1i1p1	2.15	2.65	7.20	1.16	3.40
RCP2.6	CanESM2_r1i1p1	2.24	2.91	19.40	1.39	8.30
RCP2.6	CCSM4_r1i1p1	1.82	2.09	5.10	0.53	2.00
RCP2.6	CESM1-CAM5_r1i1p1	1.97	2.01	16.00	1.29	1.40
RCP2.6	CNRM-CM5_r1i1p1	1.70	1.92	11.70	1.12	2.40
RCP2.6	CSIRO-Mk3-6-0_r1i1p1	1.88	2.45	10.60	1.44	4.20
RCP2.6	EC-EARTH_r8i1p1	1.85	2.45	9.60	0.72	1.30
RCP2.6	FGOALS_g2_r1i1p1	1.13	1.98	2.30	0.84	-1.90
RCP2.6	FIO-ESM_r1i1p1	0.89	1.06	-6.30	-0.58	-7.20
RCP2.6	GISS-E2-H_r1i1p1	1.62	2.36	5.80	0.90	2.30
RCP2.6	GISS-E2-R_r1i1p1	1.05	1.52	9.30	0.27	1.50
RCP2.6	HadGEM2-AO_r1i1p1*	1.57	1.75	5.90	1.15	5.20
RCP2.6	HadGEM2-ES_r2i1p1	1.80	1.87	0.50	1.29	3.30
RCP2.6	IPSL-CM5A-LR_r1i1p1	2.23	3.46	-1.60	1.34	3.60
RCP2.6	IPSL-CM5A-MR_r1i1p1	1.94	3.23	-5.40	1.24	-3.20
RCP2.6	MIROC-ESM-CHEM_r1i1p1	2.35	3.05	3.50	1.82	1.50
RCP2.6	MIROC-ESM_r1i1p1	2.33	3.21	4.90	2.00	2.80
RCP2.6	MIROC5_r1i1p1*	1.49	2.58	14.20	1.84	6.00
RCP2.6	MPI-ESM-LR_r1i1p1*	1.58	2.16	0.70	0.41	2.70
RCP2.6	MPI-ESM-MR_r1i1p1*	1.59	2.14	3.40	0.42	1.00
RCP2.6	MRI-CGCM3_r1i1p1	1.34	1.57	13.30	0.86	3.10
RCP2.6	NorESM1-M_r1i1p1*	1.40	2.24	3.40	1.10	0.60
RCP2.6	NorESM1-ME_r1i1p1*	1.43	2.15	5.10	1.32	-1.90

<i>Continuation of Table A.4</i>						
RCP4.5	ACCESS1-0_r1i1p1	2.63	4.01	4.40	2.92	3.40
RCP4.5	ACCESS1-3_r1i1p1	2.44	2.96	4.80	2.61	2.80
RCP4.5	bcc-csm1-1-m_r1i1p1	2.50	3.31	9.10	1.67	8.00
RCP4.5	bcc-csm1-1_r1i1p1	2.48	3.27	6.50	1.83	2.60
RCP4.5	BNU-ESM_r1i1p1	3.16	3.90	3.30	2.50	-3.90
RCP4.5	CanESM2_r1i1p1	3.04	4.46	18.20	2.99	10.80
RCP4.5	CCSM4_r1i1p1	2.56	3.29	7.30	1.72	4.00
RCP4.5	CESM1-BGC_r1i1p1	2.45	3.43	6.50	1.86	3.80
RCP4.5	CESM1-CAM5_r1i1p1	2.76	3.41	18.70	2.62	9.40
RCP4.5	CMCC-CM_r1i1p1	2.73	3.72	9.40	2.71	6.30
RCP4.5	CMCC-CMS_r1i1p1	2.70	3.97	1.60	2.73	-0.40
RCP4.5	CNRM-CM5_r1i1p1	2.51	2.91	14.80	2.23	4.90
RCP4.5	CSIRO-Mk3-6-0_r1i1p1	2.66	3.74	9.90	2.63	7.40
RCP4.5	EC-EARTH_r8i1p1	2.58	3.33	13.60	1.71	11.30
RCP4.5	FGOALS_g2_r1i1p1	1.82	3.02	2.90	1.68	0.40
RCP4.5	FIO-ESM_r1i1p1	1.85	2.54	-5.20	0.89	-3.80
RCP4.5	GISS-E2-H-CC_r1i1p1	2.34	3.94	10.10	1.87	6.50
RCP4.5	GISS-E2-H_r1i1p1	2.38	3.60	12.00	2.17	7.70
RCP4.5	GISS-E2-R-CC_r1i1p1	1.85	3.11	12.70	1.54	6.40
RCP4.5	GISS-E2-R_r1i1p1	1.76	2.89	1.10	1.58	0.60
RCP4.5	HadGEM2-AO_r1i1p1	2.87	3.86	3.70	3.02	4.60
RCP4.5	HadGEM2-CC_r1i1p1	2.44	2.87	2.10	2.86	7.70
RCP4.5	HadGEM2-ES_r2i1p1	2.95	3.55	3.40	2.98	6.00
RCP4.5	inmcm4_r1i1p1	1.81	2.95	-0.10	1.51	1.30
RCP4.5	IPSL-CM5A-LR_r1i1p1	3.10	5.08	-5.20	2.93	0.30
RCP4.5	IPSL-CM5A-MR_r1i1p1	3.05	5.25	-4.60	3.12	2.40
RCP4.5	IPSL-CM5B-LR_r1i1p1	2.47	2.90	8.80	1.80	5.00
RCP4.5	MIROC-ESM-CHEM_r1i1p1	3.17	4.37	9.30	3.36	6.90
RCP4.5	MIROC-ESM_r1i1p1	3.15	4.50	6.70	3.24	5.20
RCP4.5	MIROC5_r1i1p1	2.12	4.08	15.50	3.17	4.50
RCP4.5	MPI-ESM-LR_r1i1p1	2.39	3.86	-4.40	2.17	-2.30
RCP4.5	MPI-ESM-MR_r1i1p1	2.45	3.74	3.90	2.02	4.10
RCP4.5	MRI-CGCM3_r1i1p1	1.99	2.64	19.80	1.90	8.90
RCP4.5	NorESM1-M_r1i1p1	2.12	3.33	3.10	2.33	1.40
RCP4.5	NorESM1-ME_r1i1p1	2.16	3.42	5.60	2.52	-1.60

<i>Continuation of Table A.4</i>						
RCP6.0	bcc-csm1-1-m_r1i1p1	2.90	4.09	4.80	2.52	1.30
RCP6.0	bcc-csm1-1_r1i1p1	2.83	3.84	3.80	2.25	0.00
RCP6.0	CCSM4_r1i1p1	2.94	3.70	6.90	2.05	2.20
RCP6.0	CESM1-CAM5_r1i1p1	3.15	4.05	20.80	3.31	9.90
RCP6.0	CSIRO-Mk3-6-0_r1i1p1	2.74	3.57	16.10	2.52	13.60
RCP6.0	FIO-ESM_r1i1p1	2.32	3.07	-5.00	1.33	-4.60
RCP6.0	GISS-E2-H_r1i1p1	2.64	3.94	12.40	2.59	7.50
RCP6.0	GISS-E2-R_r1i1p1	2.64	3.94	1.30	2.59	0.80
RCP6.0	HadGEM2-AO_r1i1p1	2.85	3.69	7.10	3.02	5.70
RCP6.0	HadGEM2-ES_r2i1p1	3.31	3.91	1.40	3.50	6.20
RCP6.0	IPSL-CM5A-LR_r1i1p1	3.39	5.61	-9.30	3.41	-5.60
RCP6.0	IPSL-CM5A-MR_r1i1p1	3.34	5.65	-6.40	3.67	-3.00
RCP6.0	MIROC-ESM-CHEM_r1i1p1	3.57	5.26	7.50	3.98	5.90
RCP6.0	MIROC-ESM_r1i1p1	3.49	5.18	8.80	3.90	7.90
RCP6.0	MIROC5_r1i1p1	2.35	4.40	20.00	3.70	9.00
RCP6.0	MRI-CGCM3_r1i1p1	2.18	2.93	23.90	2.26	10.70
RCP6.0	NorESM1-M_r1i1p1	2.32	3.66	8.20	2.66	5.30
RCP6.0	NorESM1-ME_r1i1p1	2.38	3.56	9.60	2.72	3.70

<i>Continuation of Table A.4</i>						
RCP8.5	ACCESS1-0_r1i1p1	4.26	6.34	4.90	5.25	5.10
RCP8.5	ACCESS1-3_r1i1p1	4.17	4.88	8.60	4.44	5.70
RCP8.5	bcc-csm1-1_r1i1p1	4.12	5.64	8.80	4.14	7.20
RCP8.5	BNU-ESM_r1i1p1	5.10	6.54	-2.90	5.08	-6.90
RCP8.5	CanESM2_r1i1p1	4.99	7.41	33.10	5.94	22.20
RCP8.5	CCSM4_r1i1p1	4.34	5.76	9.00	4.20	7.20
RCP8.5	CESM1-BGC_r1i1p1	4.20	5.71	8.60	4.09	6.00
RCP8.5	CESM1-CAM5_r1i1p1	4.37	5.96	26.00	5.05	14.70
RCP8.5	CMCC-CM_r1i1p1	4.50	6.63	11.70	5.75	7.90
RCP8.5	CMCC-CMS_r1i1p1	4.56	6.76	2.90	5.50	2.00
RCP8.5	CNRM-CM5_r1i1p1	3.92	4.90	24.40	4.12	15.60
RCP8.5	CSIRO-Mk3-6-0_r1i1p1	4.21	5.80	21.40	4.81	13.20
RCP8.5	EC-EARTH_r8i1p1	4.11	5.65	22.20	4.05	17.90
RCP8.5	FGOALS_g2_r1i1p1	3.30	5.03	11.50	3.73	8.00
RCP8.5	FIO-ESM_r1i1p1	4.00	5.33	-11.50	3.75	-9.90
RCP8.5	GISS-E2-H_r1i1p1	3.66	5.73	15.30	4.23	12.90
RCP8.5	GISS-E2-R_r1i1p1	2.95	4.73	1.80	3.55	1.30
RCP8.5	HadGEM2-AO_r1i1p1	4.34	5.79	7.90	5.13	6.70
RCP8.5	HadGEM2-CC_r1i1p1	4.55	5.78	1.20	5.71	5.10
RCP8.5	HadGEM2-ES_r2i1p1	4.79	6.00	2.30	5.41	5.30
RCP8.5	inmcm4_r1i1p1	3.08	5.22	2.30	3.87	1.60
RCP8.5	IPSL-CM5A-LR_r1i1p1	5.18	8.33	-10.80	6.14	-6.00
RCP8.5	IPSL-CM5A-MR_r1i1p1	5.01	8.57	-7.40	6.48	-4.10
RCP8.5	IPSL-CM5B-LR_r1i1p1	4.02	5.20	16.40	4.13	11.30
RCP8.5	MIROC-ESM-CHEM_r1i1p1	5.27	8.10	10.20	6.89	7.20
RCP8.5	MIROC-ESM_r1i1p1	5.06	7.87	8.00	6.60	5.90
RCP8.5	MIROC5_r1i1p1	3.59	6.20	32.70	5.44	20.70
RCP8.5	MPI-ESM-LR_r1i1p1	4.15	6.58	-3.30	5.02	-2.90
RCP8.5	MPI-ESM-MR_r1i1p1	4.11	6.04	5.50	4.37	4.60
RCP8.5	MRI-CGCM3_r1i1p1	3.41	5.03	31.20	4.31	17.90
RCP8.5	NorESM1-M_r1i1p1	3.53	5.51	6.00	4.44	3.10
RCP8.5	NorESM1-ME_r1i1p1	3.68	5.62	7.80	4.73	1.90



---

## Bibliography

- Addink, E., Jong, S. D., & Pebesma, E. (2007). The importance of scale in object-based mapping of vegetation parameters with hyperspectral imagery. *Photogrammetric Engineering & Remote Sensing*, 73, 905–912.
- Agisoft LLC (2013). *Agisoft PhotoScan Professional Edition User Manual, Version 0.9.1*. St. Petersburg: Agisoft LLC. URL: <http://www.agisoft.com/features/professional-edition/>.
- Agisoft LLC (2014). *Agisoft PhotoScan Professional Edition User Manual, Version 1.1*. St. Petersburg, Russia: Agisoft LLC. URL: <http://www.agisoft.com/features/professional-edition/>.
- Agisoft LLC (2016). *Agisoft PhotoScan Professional Edition User Manual, Version 1.2*. St. Petersburg, Russia: Agisoft LLC. URL: <http://www.agisoft.com/features/professional-edition/>.
- Aitchison, J. C., Ali, J. R., & Davis, A. M. (2008). When and where did India and Asia collide? *Geological Bulletin of China*, 27, 1351–1370. doi:10.1029/2006JB004706.
- Andermann, C., Longuevergne, L., Bonnet, S., Crave, A., Davy, P., & Gloaguen, R. (2012). Impact of transient groundwater storage on the discharge of Himalayan rivers. *Nature Geoscience*, 5, 127–132. doi:10.1038/ngeo1356.
- Anderson, L. S., & Anderson, R. S. (2016). Modeling debris-covered glaciers: response to steady debris deposition. *The Cryosphere*, 10, 1105–1124. doi:10.5194/tc-10-1105-2016.
- Ardelean, F., Török-Oance, M., Urdea, P., & Onaca, A. (2011). Application of Object Based Image Analysis for Glacial Cirques Detection. Case Study: The arcu Mountains (Southern Carpathians). *Forum geografic*, X, 20–26. doi:10.5775/fg.2067-4635.2011.007.i.
- Arnold, N. S., Rees, W. G., Devereux, B. J., & Amable, G. S. (2006). Evaluating the potential of high-resolution airborne LiDAR data in glaciology. *International Journal of Remote Sensing*, 27, 1233–1251. doi:10.1080/01431160500353817.
- Atkinson, P. M. (2013). Downscaling in remote sensing. *International Journal of Applied Earth Observation and Geoinformation*, 22, 106–114. doi:10.1016/j.jag.2012.04.012.
- Aubry-Wake, C., Baraer, M., McKenzie, J. M., Mark, B. G., Wigmore, O., Hellström, R. Å., Lutz, L., & Somers, L. (2015). Measuring glacier surface temperatures with ground-based thermal infrared imaging. *Geophysical Research Letters*, 42, 8489–8497. doi:10.1002/2015GL065321.
- Aubry-Wake, C., Zéphir, D., Baraer, M., McKenzie, J. M., & Mark, B. G. (2017). Importance of longwave emissions from adjacent terrain on patterns of tropical glacier melt and recession. *Journal of Glaciology*, (pp. 1–12). doi:10.1017/jog.2017.85.
- Ayoub, F., Leprince, S., & Keene, L. (2009). *User's Guide to COSI-CORR Co-registration of Optically Sensed Images and Correlation*. Pasadena: California Institute of Technology.
- Azam, M. F., Wagnon, P., Berthier, E., Vincent, C., Fujita, K., & Kargel, J. S. (2018). Review of the status and mass changes of Himalayan-Karakoram glaciers. *Journal of Glaciology*, 64, 61–74. doi:10.1017/jog.2017.86.
- Baatz, M., & Schäpe, A. (2000). Multiresolution segmentation: an optimization approach for high quality multi-scale image segmentation. *ISPRS Journal of Photogrammetry and Remote Sensing*, 58.
- Bajracharya, S. R., Maharjan, S. B., Shrestha, F., Guo, W., Liu, S., Immerzeel, W., & Shrestha, B. (2015). The glaciers of the Hindu Kush Himalayas: current status and observed changes from the 1980s to 2010. *International Journal of Water Resources Development*, 31, 161–173. doi:10.1080/07900627.2015.1005731.
- Bamber, J. L., & Rivera, A. (2007). A review of remote sensing methods for glacier mass balance determination. *Global and Planetary Change*, 59, 138–148. doi:10.1016/j.gloplacha.2006.11.031.
- Banerjee, A. (2017). Brief communication: Thinning of debris-covered and debris-free glaciers in a warming climate. *Cryosphere*, 11, 133–138. doi:10.5194/tc-11-133-2017.
- Baral, P., Kayastha, R. B., Immerzeel, W. W., Pradhananga, N. S., Bhattarai, B. C., Shahi, S., Galos, S., Springer, C., Joshi, S. P., & Mool, P. K. (2014). Preliminary results of mass-balance observations of Yala Glacier and analysis of temperature and precipitation gradients in Langtang Valley, Nepal. *Annals of Glaciology*, 55, 9–14. doi:10.3189/2014AoG66A106.
- Barnard, P. L., Owen, L. A., Finkel, R. C., & Asahi, K. (2006). Landscape response to deglaciation in a high relief, monsoon-influenced alpine environment, Langtang Himal, Nepal. *Quaternary Science Reviews*, 25, 2162–2176. doi:10.1016/j.quascirev.2006.02.002.
- Becker, F., & Li, Z.-L. (1995). Surface temperature and emissivity at various scales: Definition, measurement and related problems. *Remote Sensing Reviews*, 12, 225–253. doi:10.1080/02757259509532286.
- Benn, D., Bolch, T., Hands, K., Gullej, J., Luckman, A., Nicholson, L. I., Quincey, D. J., Thompson, S., Toumi, R., & Wiseman, S. (2012). Response of debris-covered glaciers in the Mount Everest region to recent warming, and implications for outburst flood hazards. *Earth-Science Reviews*, 114, 156–174. doi:10.1016/j.earscirev.2012.03.008.
- Benn, D., Gullej, J., Luckman, A., Adamek, A., & Glowacki, P. S. (2009). Englacial drainage systems formed by hydrologically driven crevasse propagation. *Journal of Glaciology*, 55, 513–523. doi:10.3189/00214309788816669.
- Benn, D. I., & Evans, D. (2010). *Glaciers and Glaciation*. (2nd ed.). London: Routledge.
- Benn, D. I., & Lehmkuhl, F. (2000). Mass balance and equilibrium-line altitudes of glaciers in high-mountain environments. *Quaternary International*, 66, 15–29.
- Benn, D. I., & Owen, L. A. (2002). Himalayan glacial sedimentary environments: A framework for reconstructing and dating the former extent of glaciers in high mountains. *Quaternary International*, 97–98, 3–25. doi:10.1016/S1040-6182(02)00048-4.

- Benn, D. I., Wiseman, S., & Warren, C. R. (2000). Rapid growth of a supraglacial lake, Ngozumpa Glacier, Khumbu Himal, Nepal. *IAHS Publication*, 264, 177–185.
- Benz, U. C., Hofmann, P., Willhauck, G., Lingenfelder, I., & Heynen, M. (2004). Multi-resolution, object-oriented fuzzy analysis of remote sensing data for GIS-ready information. *ISPRS Journal of Photogrammetry and Remote Sensing*, 58, 239–258. doi:10.1016/j.isprsjprs.2003.10.002.
- Bernard, É., Friedt, J. M., Saintenoy, A., Tolle, F., Griselin, M., & Marlin, C. (2014). Where does a glacier end? GPR measurements to identify the limits between valley slopes and actual glacier body. Application to the Austre Lovénbreen, Spitsbergen. *International Journal of Applied Earth Observation and Geoinformation*, 27, 100–108. doi:10.1016/j.jag.2013.07.006.
- Berthier, E., Arnaud, Y., Kumar, R., Ahmad, S., Wagnon, P., & Chevallier, P. (2007). Remote sensing estimates of glacier mass balances in the Himachal Pradesh (Western Himalaya, India). *Remote Sensing of Environment*, 108, 327–338. doi:10.1016/j.rse.2006.11.017.
- Berthier, E., Vincent, C., Magnússon, E., Gunnlaugsson, Á., Pitte, P., Le Meur, E., Masiokas, M., Ruiz, L., Pálsson, F., Belart, J. M. C., & Wagnon, P. (2014). Glacier topography and elevation changes derived from Pléiades sub-meter stereo images. *The Cryosphere*, 8, 2275–2291. doi:10.5194/tc-8-2275-2014.
- Bhambri, R., Bolch, T., Chaujar, R. K., & Kulshreshtha, S. C. (2011). Glacier changes in the Garhwal Himalaya, India, from 1968 to 2006 based on remote sensing. *Journal of Glaciology*, 57, 543–556. doi:10.3189/002214311796905604.
- Bhardwaj, A., Sam, L., Martín-torres, F. J., & Kumar, R. (2016). Remote Sensing of Environment UAVs as remote sensing platform in glaciology : Present applications and future prospects. *Remote Sensing of Environment*, 175, 196–204. doi:10.1016/j.rse.2015.12.029.
- Björnsson, H. (1998). Hydrological characteristics of the drainage system beneath a surging glacier. *Nature*, 395, 771–774. doi:10.1038/27384.
- Blaschke, T. (2010). Object based image analysis for remote sensing. *ISPRS Journal of Photogrammetry and Remote Sensing*, 65, 2–16. doi:10.1016/j.isprsjprs.2009.06.004.
- Blaschke, T., Hay, G. J., Kelly, M., Lang, S., Hofmann, P., Addink, E., Queiroz Feitosa, R., van der Meer, F., van der Werff, H., van Coillie, F., & Tiede, D. (2014). Geographic Object-Based Image Analysis - Towards a new paradigm. *ISPRS Journal of Photogrammetry and Remote Sensing*, 87, 180–191. doi:10.1016/j.isprsjprs.2013.09.014.
- Blaschke, T., Lang, S., & Hay, G. J. (2008). *Object-based image analysis: spatial concepts for knowledge-driven remote sensing applications*. Berlin: Springer.
- Bliss, A., Hock, R., & Radić, V. (2014). Global response of glacier runoff to twenty-first century climate change. *Journal of Geophysical Research*, 119, 1–14. doi:10.1002/2013JF002931.Received.
- Blockley, R., Shyy, W., Atkins, E., Ollero, A., & Tsourdos, A. (2017). *Unmanned Aircraft Systems*. New York: John Wiley & Sons.
- Bolch, T. (2007). Climate change and glacier retreat in northern Tien Shan (Kazakhstan/Kyrgyzstan) using remote sensing data. *Global and Planetary Change*, 56, 1–12. doi:10.1016/j.gloplacha.2006.07.009.
- Bolch, T., Kulkarni, A., Kääh, A., Huggel, C., Paul, F., Cogley, J. G., Frey, H., Kargel, J. S., Fujita, K., Scheel, M., Bajracharya, S., & Stoffel, M. (2012). The state and fate of Himalayan Glaciers. *Science*, 336, 310–314. doi:10.1126/science.1215828.
- Bolch, T., Pieczonka, T., & Benn, D. (2011). Multi-decadal mass loss of glaciers in the Everest area (Nepal Himalaya) derived from stereo imagery. *Cryosphere*, 5, 349–358. doi:10.5194/tc-5-349-2011.
- Bookhagen, B. (2012). Hydrology: Himalayan groundwater. *Nature Geoscience*, 5, 96–97. doi:10.1038/ngeo1366.
- Bookhagen, B., & Burbank, D. W. (2010). Toward a complete Himalayan hydrological budget: Spatiotemporal distribution of snowmelt and rainfall and their impact on river discharge. *Journal of Geophysical Research: Earth Surface*, 115, 1–25. doi:10.1029/2009JF001426.
- Bothe, O., Fraedrich, K., & Zhu, X. (2012). Precipitation climate of Central Asia and the large-scale atmospheric circulation. *Theoretical and Applied Climatology*, 108, 345–354. doi:10.1007/s00704-011-0537-2.
- Breiman, L. (2001). Random forests. *Machine learning*, (pp. 5–32). doi:10.1023/A:1010933404324.
- Brock, B. W., Mihalcea, C., Kirkbride, M. P., Diolaiuti, G., Cutler, M. E. J., & Smiraglia, C. (2010). Meteorology and surface energy fluxes in the 2005–2007 ablation seasons at the Miage debris-covered glacier, Mont Blanc Massif, Italian Alps. *Journal of Geophysical Research Atmospheres*, 115, 1–16. doi:10.1029/2009JD013224.
- Brock, B. W., Willis, I. C., & Sharp, M. J. (2000). Measurement and parameterisation of albedo variations at Haut Glacier d'Arolla, Switzerland. *Journal of Glaciology*, 46, 675–688. doi:10.3189/172756506781828746.
- Brun, F., Berthier, E., Wagnon, P., Kääh, A., & Treichler, D. (2017). A spatially resolved estimate of High Mountain Asia glacier mass balances, 2000–2016. *Nature Geoscience*, 10, 668–673. doi:10.1038/ngeo2999.
- Brun, F., Buri, P., Miles, E. S., Wagnon, P., Steiner, J., Berthier, E., Ragetli, S., Kraaijenbrink, P., Immerzeel, W. W., & Pellicciotti, F. (2016). Quantifying volume loss from ice cliffs on debris-covered glaciers using high-resolution terrestrial and aerial photogrammetry. *Journal of Glaciology*, 62, 684–695. doi:10.1017/jog.2016.54.
- Brun, F., Wagnon, P., Berthier, E., Shea, J., Immerzeel, W., Kraaijenbrink, P. D., Vincent, C., Reverchon, C., Shrestha, D., & Arnaud, Y. (2018). Ice cliffs cannot explain the "debris-cover anomaly": a case study on Changri Nup Glacier, Nepal, Central Himalaya. *The Cryosphere Discussions*, (pp. 1–32).
- Buades, A., & Coll, B. (2005). A non-local algorithm for image denoising. *Computer Vision and Pattern*, 2, 60–65. doi:10.1109/CVPR.2005.38.

- Buri, P., Miles, E. S., Steiner, J. F., Immerzeel, W. W., Wagnon, P., & Pellicciotti, F. (2016a). A physically based 3-D model of ice cliff evolution over debris-covered glaciers. *Journal of Geophysical Research: Earth Surface*, *121*, 2471–2493. doi:10.1002/2016JF004039.
- Buri, P., & Pellicciotti, F. (2018). Aspect controls the survival of ice cliffs on debris-covered glaciers. *Proceedings of the National Academy of Sciences*, *115*, 201713892. doi:10.1073/pnas.1713892115.
- Buri, P., Pellicciotti, F., Steiner, J. F., Miles, E., & Immerzeel, W. W. (2016b). A grid-based model of backwasting of supraglacial ice cliffs over debris-covered glaciers. *Annals of Glaciology*, *57*, 199–211. doi:10.3189/2016AoG71A059.
- Cannon, F., Carvalho, L. M., Jones, C., & Norris, J. (2016). Winter westerly disturbance dynamics and precipitation in the western Himalaya and Karakoram: a wave-tracking approach. *Theoretical and Applied Climatology*, *125*, 27–44. doi:10.1007/s00704-015-1489-8.
- Carrivick, J. L., Smith, M. W., & Quincey, D. J. (2016). *Structure from Motion in the Geosciences*. Analytical Methods in Earth and Environmental Science. New York: John Wiley & Sons.
- Chen, W., Fukui, H., Doko, T., & Gu, X. (2013). Improvement of glacial lakes detection under shadow environment using ASTER data in Himalayas, Nepal. *Chinese Geographical Science*, *23*, 216–226. doi:10.1007/s11769-012-0584-3.
- Cogley, J. G. (2009). Geodetic and direct mass-balance measurements: comparison and joint analysis. *Annals of Glaciology*, *50*, 96–100.
- Cogley, J. G. (2011). Present and future states of Himalaya and Karakorum glaciers. *Annals of Glaciology*, *52*, 69–73. doi:10.3189/172756411799096277.
- Cogley, J. G. (2016). Glacier shrinkage across High Mountain Asia. *Annals of Glaciology*, *57*, 41–49. doi:10.3189/2016AoG71A040.
- Collier, E., & Immerzeel, W. W. (2015). High-resolution modeling of atmospheric dynamics in the Nepalese Himalaya. *Journal of Geophysical Research: Atmospheres*, *120*, 1–15. doi:10.1002/2015JD023266.
- Collier, E., Maussion, F., Nicholson, L. I., Mölg, T., Immerzeel, W. W., & Bush, a. B. G. (2015). Impact of debris cover on glacier ablation and atmosphere-glacier feedbacks in the Karakoram. *The Cryosphere*, *9*, 1617–1632. doi:10.5194/tc-9-1617-2015.
- Collier, E., Nicholson, L. I., Brock, B. W., Maussion, F., Essery, R., & Bush, a. B. G. (2014). Representing moisture fluxes and phase changes in glacier debris cover using a reservoir approach. *The Cryosphere*, *8*, 1429–1444. doi:10.5194/tc-8-1429-2014.
- Colomina, I., & Molina, P. (2014). Unmanned aerial systems for photogrammetry and remote sensing: A review. *ISPRS Journal of Photogrammetry and Remote Sensing*, *92*, 79–97. doi:10.1016/j.isprsjprs.2014.02.013.
- Copland, L., Pope, S., Bishop, M., Shroder Jr, J. F., Clendon, P., Bush, A., Kamp, U., Seong, Y. B., & Owen, L. A. (2009). Glacier velocities across the central Karakoram. *Annals of Glaciology*, *50*, 41. doi:10.3189/172756409789624229.
- Coumou, D., & Rahmstorf, S. (2012). A decade of weather extremes. *Nature Climate Change*, *2*, 491–496. doi:10.1038/nclimate1452.
- Cuffey, K., & Paterson, W. (2010). *The physics of glaciers*. (4th ed.). Burlington, MA: Academic Press.
- Dahri, Z. H., Ludwig, F., Moors, E., Ahmad, B., Khan, A., & Kabat, P. (2016). An appraisal of precipitation distribution in the high-altitude catchments of the Indus basin. *Science of the Total Environment*, *548–549*, 289–306. doi:10.1016/j.scitotenv.2016.01.001.
- Davis, J. C. (2002). *Statistics and data analysis in geology*. New York City: John Wiley.
- Dee, D. P., Uppala, S. M., Simmons, A. J., Berrisford, P., Poli, P., Kobayashi, S., Andrae, U., Balmaseda, M. a., Balsamo, G., Bauer, P., Bechtold, P., Beljaars, a. C. M., van de Berg, L., Bidlot, J., Bormann, N., Delsol, C., Dragani, R., Fuentes, M., Geer, a. J., Haimberger, L., Healy, S. B., Hersbach, H., Hólm, E. V., Isaksen, I., Kållberg, P., Köhler, M., Matricardi, M., McNally, a. P., Monge-Sanz, B. M., Morcrette, J.-J., Park, B.-K., Peubey, C., de Rosnay, P., Tavolato, C., Thépaut, J.-N., & Vitart, F. (2011). The ERA-Interim reanalysis: configuration and performance of the data assimilation system. *Quarterly Journal of the Royal Meteorological Society*, *137*, 553–597. doi:10.1002/qj.828.
- Dobrev, I. D., Bishop, M. P., & Bush, A. B. (2017). Climate-glacier dynamics and topographic forcing in the Karakoram Himalaya: Concepts, issues and research directions. *Water*, *9*, 20–26. doi:10.3390/w9060405.
- Dong, C., Loy, C. C., & Tang, X. (2016). Accelerating the Super-Resolution Convolutional Neural Network. In B. Leibe, J. Matas, N. Sebe, & M. Welling (Eds.), *Computer Vision – ECCV 2016* (pp. 391–407). Cham: Springer International Publishing.
- Drgu, L., Csillik, O., Eisank, C., & Tiede, D. (2014). Automated parameterisation for multi-scale image segmentation on multiple layers. *ISPRS Journal of Photogrammetry and Remote Sensing*, *88*, 119–127. doi:10.1016/j.isprsjprs.2013.11.018.
- Dyurgerov, M. B., & Meier, M. F. (2005). Glaciers and the Changing Earth System: A 2004 Snapshot. *INSTAAR Occasional Paper*, (p. 117).
- Eisank, C., Drgu, L. D., & Blaschke, T. (2011). A generic procedure for semantics-oriented landform classification using object-based image analysis. *Geomorphometry 2011, 8 Sept. 2011, Redlands, USA*, (pp. 125–128).
- Eisenburger, D., Lentz, H., & Jenett, M. (2008). Helicopter-borne GPR systems: A way from ice thickness measurements to geological applications. In *IEEE International Conference on Ultra-Wideband 2008* (pp. 161–165). IEEE Hannover: IEEE volume 3. doi:10.1109/ICUWB.2008.4653441.
- Evatt, G. W., Abrahams, I. D., Heil, M., Mayer, C., Kingslake, J., Mitchell, S. L., Fowler, A. C., & Clark, C. D. (2015). Glacial melt under a porous debris layer. *Journal of Glaciology*, *61*, 825–836. doi:10.3189/2015JG14J235.
- Exelis (2014). *ENVI 5.2 user manual*. Boulder, CO, USA: Exelis. URL: <http://www.exelisvis.com/ProductsServices/ENVIProducts/ENVI.aspx>.

- Farinotti, D., Brinkerhoff, D. J., Clarke, G. K., Fürst, J. J., Frey, H., Gantayat, P., Giller-Chaulet, F., Girard, C., Huss, M., Leclercq, P. W., Linsbauer, A., Machguth, H., Martin, C., Maussion, F., Morlighem, M., Mosbeux, C., Pandit, A., Portmann, A., Rabatel, A., Ramsankaran, R., Reerink, T. J., Sanchez, O., Stentoft, P. A., Singh Kumari, S., Van Pelt, W. J., Anderson, B., Benham, T., Binder, D., Dowdeswell, J. A., Fischer, A., Helfricht, K., Kutuzov, S., Lavrentiev, I., McNabb, R., Hilmar Gudmundsson, G., Li, H., & Andreassen, L. M. (2017). How accurate are estimates of glacier ice thickness? Results from ITMIX, the Ice Thickness Models Intercomparison eXperiment. *Cryosphere*, *11*, 949–970. doi:10.5194/tc-11-949-2017.
- Farinotti, D., Longueuevegne, L., Moholdt, G., Duethmann, D., Mölg, T., Bolch, T., Vorogushyn, S., & Güntner, A. (2015). Substantial glacier mass loss in the Tien Shan over the past 50 years. *Nature Geoscience*, *8*, 716–722. doi:10.1038/ngeo2513.
- Farr, T., Rosen, P., Caro, E., Crippen, R., Duren, R., Hensley, S., Kobrick, M., Paller, M., Rodriguez, E., Roth, L., Seal, D., Shaffer, S., Shimada, J., Umland, J., Werner, M., Oskin, M., Burbank, D., & Alsdorf, D. (2007). The shuttle radar topography mission. *Reviews of Geophysics*, *45*, 1–33. doi:10.1029/2005RG000183.1.INTRODUCTION.
- Fasano, G., Renga, A., Vetrella, A. R., Ludeno, G., Catapano, I., & Soldovieri, F. (2017). Proof of concept of micro-UAV-based radar imaging. In *2017 International Conference on Unmanned Aircraft Systems (ICUAS 2017)* June (pp. 1316–1323). Miami. doi:10.1109/ICUAS.2017.7991432.
- Fischer, A. (2011). Comparison of direct and geodetic mass balances on a multi-annual time scale. *The Cryosphere*, *5*, 107–124. doi:10.5194/tc-5-107-2011.
- Flechtner, F., Morton, P., Watkins, M., & Webb, F. (2014). Status of the GRACE Follow-On Mission. In U. Marti (Ed.), *Gravity, Geoid and Height Systems* (pp. 117–121). Cham: Springer International Publishing.
- FLIR Systems (2017). *User's manual FLIR Cx series*. Wilsonville, OR: FLIR Systems.
- Foga, S., Stearns, L. A., & van der Veen, C. J. (2014). Application of Satellite Remote Sensing Techniques to Quantify Terminus and Ice Mélange Behavior at Helheim Glacier, East Greenland. *Marine Technology Society Journal*, *48*, 81–91. doi:10.4031/MTSJ.48.5.3.
- Fonstad, M., Dietrich, J., Courville, B., Jensen, J., & Carbonneau, P. (2013). Topographic structure from motion: a new development in photogrammetric measurement. *Earth Surface Processes and Landforms*, *38*, 421–430.
- Forsythe, N., Fowler, H. J., Li, X.-F., Blenkinsop, S., & Pritchard, D. (2017). Karakoram temperature and glacial melt driven by regional atmospheric circulation variability. *Nature Climate Change*, . doi:10.1038/nclimate3361.
- Foster, L. A., Brock, B. W., Cutler, M. E. J., & Diotri, F. (2012). A physically based method for estimating supraglacial debris thickness from thermal band remote-sensing data. *Journal of Glaciology*, *58*, 677–691. doi:10.3189/2012jogG11j194.
- Francou, B., & Coudrain, A. (2005). Glacier shrinkage and water resources in the Andes. *Eos, Transactions American Geophysical Union*, *86*, 415. doi:10.1029/2005EO430005.
- Frey, H., Machguth, H., Huss, M., Huggel, C., Bajracharya, S., Bolch, T., Kulkarni, A., Linsbauer, A., Salzmann, N., & Stoffel, M. (2014). Estimating the volume of glaciers in the Himalayan & Karakoram region using different methods. *The Cryosphere*, *8*, 2313–2333. doi:10.5194/tc-8-2313-2014.
- Fu, P., & Rich, P. M. (1999). Design and Implementation of the Solar Analyst: an ArcView Extension for Modeling Solar Radiation at Landscape Scales. In *19th Annual ESRI User Conference* February (pp. 1–24). San Diego, CA.
- Fujita, K., & Nuimura, T. (2011). Spatially heterogeneous wastage of Himalayan glaciers. *Proceedings of the National Academy of Sciences of the United States of America*, *108* 34, 14011–14014.
- Fujita, K., Suzuki, R., Nuimura, T., & Sakai, A. (2008). Performance of ASTER and SRTM DEMs, and their potential for assessing glacial lakes in the Lunana region, Bhutan Himalaya. *Journal of Glaciology*, *54*, 220–228. doi:10.3189/002214308784886162.
- Furukawa, Y., & Ponce, J. (2009). Accurate camera calibration from multi-view stereo and bundle adjustment. *International Journal of Computer Vision*, *84*, 257–268. doi:10.1007/s11263-009-0232-2.
- Furukawa, Y., & Ponce, J. (2010). Accurate, Dense, and Robust Multiview Stereopsis. *IEEE Transactions on Pattern Analysis and Machine Intelligence*, *32*, 1362–1376.
- Gades, A., Conway, H., Nereson, N., Naito, N., & Kadota, T. (2000). Radio echo-sounding through supraglacial debris on Lirung and Khumbu Glaciers, Nepal Himalayas. In *Debris-covered Glaciers (IAHS Publ. no. 264)* (pp. 13–22). International Association of Hydrological Sciences volume 264.
- Galewsky, J. (2009). Rain shadow development during the growth of mountain ranges: An atmospheric dynamics perspective. *Journal of Geophysical Research: Earth Surface*, *114*, 1–17. doi:10.1029/2008JF001085.
- Gao, Y. A. N., Mas, J. F., Kerle, N., & Navarrete Pacheco, J. A. (2011). Optimal region growing segmentation and its effect on classification accuracy. *International Journal of Remote Sensing*, *32*, 3747–3763. doi:10.1080/01431161003777189.
- Gardelle, J., Arnaud, Y., & Berthier, E. (2011). Contrasted evolution of glacial lakes along the Hindu Kush Himalaya mountain range between 1990 and 2009. *Global and Planetary Change*, *75*, 47–55. doi:10.1016/j.gloplacha.2010.10.003.
- Gardelle, J., Berthier, E., & Arnaud, Y. (2012). Slight mass gain of Karakoram glaciers in the early twenty-first century. *Nature Geoscience*, *5*, 322–325. doi:10.1038/ngeo1450.
- Gardelle, J., Berthier, E., Arnaud, Y., & Käab, A. (2013). Region-wide glacier mass balances over the Pamir-Karakoram-Himalaya during 1999–2011. *The Cryosphere*, *7*, 1263–1286. doi:10.5194/tc-7-1263-2013.
- Gardner, A. S., Moholdt, G., Cogley, J. G., Wouters, B., Arendt, A. A., Wahr, J., Berthier, E., Hock, R., Pfeffer, W. T., Kaser, G., Ligtenberg, S. R. M., Bolch, T., Sharp, M. J., Hagen, J. O., van den Broeke, M. R., & Paul, F. (2013). A reconciled estimate of glacier contributions to sea level rise: 2003 to 2009. *Science*, *340*, 852–7. doi:10.1126/science.1234532.
- Garrett, B., & Anderson, K. (2018). Drone methodologies: Taking flight in human and physical geography. *Transactions of the Institute of British Geographers*, (pp. 1–19). doi:10.1111/tran.12232.

- Genuer, R., Poggi, J.-m., Tuleau-malot, C., Genuer, R., Poggi, J.-m., Variable, C. T.-m., Genuer, R., Poggi, J.-m., & Tuleau-malot, C. (2010). Variable selection using Random Forests. *Pattern Recognition Letters*, 31, 2225–2236.
- Gibson, M. J., Glasser, N. F., Quincey, D. J., Mayer, C., Rowan, A. V., & Irvine-Fynn, T. D. (2017). Temporal variations in supraglacial debris distribution on Baltoro Glacier, Karakoram between 2001 and 2012. *Geomorphology*, 295, 572–585. doi:10.1016/j.geomorph.2017.08.012.
- Girardeau-Montaut, D. (2015). *CloudCompare version 2.6.1. user manual*. CloudCompare. URL: <http://www.danielgm.net/cc/>.
- Google Earth Engine Team (2017). Google Earth Engine: A planetary-scale geo-spatial analysis platform. <https://earthengine.google.com>.
- Gorelick, N., Hancher, M., Dixon, M., Ilyushchenko, S., Thau, D., & Moore, R. (2017). Google Earth Engine: Planetary-scale geospatial analysis for everyone. *Remote Sensing of Environment*, 202, 18–27. doi:10.1016/j.rse.2017.06.031.
- Gudmundsson, G. H. (1997). Ice deformation at the confluence of two glaciers investigated with conceptual map-plane and flowline models. *J. Glaciol.*, 43, 537–547.
- Gulley, J. (2009). Structural control of englacial conduits in the temperate Matanuska Glacier, Alaska, USA. *Journal of Glaciology*, 55, 681–690. doi:10.3189/002214309789470860.
- Gulley, J., & Benn, D. I. (2007). Structural control of englacial drainage systems in Himalayan debris-covered glaciers. *Journal of Glaciology*, 53, 399–412. doi:10.3189/002214307783258378.
- Haeblerli, W., Frauenfelder, R., Hoelzle, M., & Maisch, M. (1999). On Rates and Acceleration Trends of Global Glacier Mass Changes. *Geografiska Annaler, Series A: Physical Geography*, 81, 585–591. doi:10.1111/1468-0459.00086.
- Hagg, W., Mayer, C., Lambrecht, A., & Helm, A. (2008). Sub-debris melt rates on southern Inylchek Glacier, central Tian Shan. *Geografiska Annaler, Series A: Physical Geography*, 90 A, 55–63. doi:10.1111/j.1468-0459.2008.00333.x.
- Hagg, W. J., Braun, L. N., Uvarov, V. N., & Makarevich, K. G. (2004). A comparison of three methods of mass-balance determination in the Tuyuksu glacier region, Tien Shan, Central Asia. *Journal of Glaciology*, 50, 505–510. doi:10.3189/172756504781829783.
- Haidou, H. A. N., Jian, W., Junfeng, W. E. I., & Shiyin, L. I. U. (2010). Backwasting rate on debris-covered Kokkar glacier , Tuomuier mountain , China. *Journal of Glaciology*, 56, 287–296.
- Hall, D. K., Riggs, G. A., & Salomonson, V. V. (1995). Development of Methods for Mapping Global Snow Cover Using Moderate Resolution Imaging Spectroradiometer Data. *Remote Sensing of Environment*, 54, 127–140.
- Hambrey, M. J., Quincey, D. J., Glasser, N. F., Reynolds, J. M., Richardson, S. J., & Clemmens, S. (2009). Sedimentological, geomorphological and dynamic context of debris-mantled glaciers, Mount Everest (Sagarmatha) region, Nepal. *Quaternary Science Reviews*, 28, 1084. doi:10.1016/j.quascirev.2009.04.009.
- Han, H., Wang, J., Wei, J., & Liu, S. (2010). Backwasting rate on debris-covered Kokkar glacier, Tuomuier mountain, China. *Journal of Glaciology*, 56, 287–296. doi:10.3189/002214310791968430.
- Hansen, M. C., Potapov, P. V., Moore, R., Hancher, M., Turubanova, S. a., Tyukavina, A., Thau, D., Stehman, S. V., Goetz, S. J., Loveland, T. R., Kommareddy, A., Egorov, A., Chini, L., Justice, C. O., Townshend, J. R. G., Patapov, P., Moore, R., Hancher, M., Turubanova, S. a., Tyukavina, A., Thau, D., Stehman, S. V., Goetz, S. J., Loveland, T. R., Kommareddy, A., Egorov, A., Chini, L., Justice, C. O., & Townshend, J. R. G. (2013). High-Resolution Global Maps of 21st-Century Forest Cover Change. *Science*, 342, 850–854. doi:10.1126/science.1244693.
- Haralick, R. M., Shanmugam, K., Dinstein, I. I., Haralick M., R., Shanmugam, K., Dinstein, I. I., Haralick, R. M., Shanmugam, K., & Dinstein, I. I. (1973). Textural features for image classification. *IEEE Transactions on Systems, Man, and Cybernetics SMC-3*, 6, 610–621. doi:10.1109/TSMC.1973.4309314.
- He, X., Chaney, N., Schleiss, M., & Sheffield, J. (2016). Spatial downscaling of precipitation using adaptable random forests. *Water Resources Research*, 52, 8217–8237. doi:10.1002/2016WR019034.
- Heid, T., & Käab, A. (2012). Repeat optical satellite images reveal widespread and long term decrease in land-terminating glacier speeds. *Cryosphere*, 6, 467–478. doi:10.5194/tc-6-467-2012.
- Herman, F., Anderson, B., & Leprince, S. (2011). Mountain glacier velocity variation during a retreat/advance cycle quantified using sub-pixel analysis of ASTER images. *Journal of Glaciology*, 57, 197–207. doi:10.3189/002214311796405942.
- Hewitt, I. J. (2011). Modelling distributed and channelized subglacial drainage: The spacing of channels. *Journal of Glaciology*, 57, 302–314. doi:10.3189/002214311796405951.
- Hewitt, K. (2005). The Karakoram Anomaly? Glacier Expansion and the Elevation Effect, Karakoram Himalaya. *Mountain Research and Development*, 25, 332–340. doi:10.1659/0276-4741(2005)025[0332:TKAGEA]2.0.CO;2.
- Hewitt, K. (2014). Glacier Mass Balance Regimes. In *Glaciers of the Karakoram Himalaya: Glacial Environments, Processes, Hazards and Resources* chapter 6. (pp. 143–162). Dordrecht: Springer Netherlands.
- Hock, R., Hutchings, J. K., & Lehning, M. (2017). Grand Challenges in Cryospheric Sciences: Toward Better Predictability of Glaciers, Snow and Sea Ice. *Frontiers in Earth Science*, 5, 1–14. doi:10.3389/feart.2017.00064.
- Huang, Y. B., Thomson, S. J., Hoffmann, W. C., Lan, Y. B., & Fritz, B. K. (2013). Development and prospect of unmanned aerial vehicle technologies for agricultural production management. *International Journal of Agricultural and Biological Engineering*, 6, 1–10. doi:10.3965/j.ijabe.20130603.001.
- Hubbard, A., Willis, I., & Sharp, M. (2000). Glacier mass-balance determination by remote sensing and high-resolution modelling. *Journal of Glaciology*, 46, 491–498.
- Huss, M., & Hock, R. (2018). Global-scale hydrological response to future glacier mass loss. *Nature Climate Change*, . doi:10.1038/s41558-017-0049-x.

- Immerzeel, W., Kraaijenbrink, P., Shea, J., Shrestha, A., Pellicciotti, F., Bierkens, M., & de Jong, S. (2014a). High-resolution monitoring of Himalayan glacier dynamics using unmanned aerial vehicles. *Remote Sensing of Environment*, *150*, 93–103. doi:10.1016/j.rse.2014.04.025.
- Immerzeel, W. W., Pellicciotti, F., & Bierkens, M. F. P. (2013). Rising river flows throughout the twenty-first century in two Himalayan glacierized watersheds. *Nature Geoscience*, *6*, 742–745. doi:10.1038/ngeo1896.
- Immerzeel, W. W., Petersen, L., Ragetti, S., & Pellicciotti, F. (2014b). The importance of observed gradients of air temperature and precipitation for modeling runoff from a glacierized watershed in the Nepalese Himalayas. *Water Resources Research*, *50*, 2212–2226. doi:10.1002/2013WR014506.Received.
- Immerzeel, W. W., Wanders, N., Lutz, A. F., Shea, J. M., & Bierkens, M. F. P. (2015). Reconciling high-altitude precipitation in the upper Indus basin with glacier mass balances and runoff. *Hydrology and Earth System Sciences*, *19*, 4673–4687. doi:10.5194/hess-19-4673-2015.
- Immerzeel, W. W. W. W., Van Beek, L. L. P. H., & Bierkens, M. F. P. M. F. P. M. M. F. P. (2010). Climate change will affect the Asian water towers. *Science*, *328*, 1382–5. doi:10.1126/science.1183188.
- IPCC (2014). *Climate Change 2014: Synthesis Report. Contribution of Working Groups I, II and III to the Fifth Assessment Report of the Intergovernmental Panel on Climate Change [Core Writing Team, R.K. Pachauri and L.A. Meyer (eds)]*. Geneva, Switzerland: IPCC.
- Jansson, P., Hock, R., & Schneider, T. (2003). The concept of glacier storage: A review. *Journal of Hydrology*, *282*, 116–129. doi:10.1016/S0022-1694(03)00258-0.
- Jin, S., Cardellach, E., & Xie, F. (2014). *GNSS Remote Sensing: Theory, Methods and Applications* volume 19. Dordrecht: Springer Netherlands. doi:10.1007/978-94-007-7482-7.
- Juen, M., Mayer, C., Lambrecht, A., Han, H., & Liu, S. (2014). Impact of varying debris cover thickness on ablation: A case study for Koxkar Glacier in the Tien Shan. *Cryosphere*, *8*, 377–386. doi:10.5194/tc-8-377-2014.
- Kääb, A. (2005). Combination of SRTM3 and repeat ASTER data for deriving alpine glacier flow velocities in the Bhutan Himalaya. *Remote Sensing of Environment*, *94*, 463–474. doi:10.1016/j.rse.2004.11.003.
- Kääb, A., Berthier, E., Nuth, C., Gardelle, J., & Arnaud, Y. (2012). Contrasting patterns of early twenty-first-century glacier mass change in the Himalayas. *Nature*, *488*, 495–498. doi:10.1038/nature11324.
- Kääb, A., Treichler, D., Nuth, C., & Berthier, E. (2015). Brief Communication: Contending estimates of 2003–2008 glacier mass balance over the Pamir-Karakoram-Himalaya. *Cryosphere*, *9*, 557–564. doi:10.5194/tc-9-557-2015.
- Kapnick, S. B., Delworth, T. L., Ashfaq, M., Malyshev, S., & Milly, P. C. (2014). Snowfall less sensitive to warming in Karakoram than in Himalayas due to a unique seasonal cycle. *Nature Geoscience*, *7*, 834–840. doi:10.1038/ngeo2269.
- Kargel, J. S., Leonard, G. J., Shugar, D. H., Haritashya, U. K., Bevington, A., Fielding, E. J., Fujita, K., Geertsema, M., Miles, E. S., Steiner, J., Anderson, E., Bajracharya, S., Bawden, G. W., Breashears, D. F., Byers, A., Collins, B., Dhital, M. R., Donnellan, A., Evans, T. L., Geai, M. L., Glasscoe, M. T., Green, D., Gurung, D. R., Heijnen, R., Hilborn, A., Hudnut, K., Huyck, C., Immerzeel, W. W., Jiang Liming, Jibson, R., Kaab, A., Khanal, N. R., Kirschbaum, D., Kraaijenbrink, P. D. A., Lamsal, D., Liu Shiyin, Lv Mingyang, McKinney, D., Nahirmick, N. K., Nan Zhuotong, Ojha, S., Olsenholler, J., Painter, T. H., Pleasants, M., KC, P., Yuan, Q., Raup, B. H., Regmi, D., Rounce, D. R., Sakai, A., Shangguan Donghui, Shea, J. M., Shrestha, A. B., Shukla, A., Stumm, D., van der Kooij, M., Voss, K., Wang Xin, Weihs, B., Wolfe, D., Wu Lizong, Yao Xiaojun, Yoder, M. R., & Young, N. (2015). Geomorphic and geologic controls of geohazards induced by Nepals 2015 Gorkha earthquake. *Science*, *335*, 140. doi:10.1126/science.aac8353.
- Karimi, N., Eftekhari, M., Farajzadeh, M., Namdari, S., Moridnejad, A., & Karimi, D. (2015). Use of multitemporal satellite images to find some evidence for glacier changes in the Haft-Khan glacier, Iran. *Arabian Journal of Geosciences*, *8*, 5879–5896. doi:10.1007/s12517-014-1578-5.
- Kaser, G., Cogley, J. G., Dyurgerov, M. B., Meier, M. F., & Ohmura, A. (2006). Mass balance of glaciers and ice caps: Consensus estimates for 1961–2004. *Geophysical Research Letters*, *33*, 1–5. doi:10.1029/2006GL027511.
- Kaser, G., Grosshauser, M., & Marzeion, B. (2010). Contribution potential of glaciers to water availability in different climate regimes. *Proceedings of the National Academy of Sciences of the United States of America*, *107*, 20223–20227. doi:10.1073/pnas.1008162107.
- Kayastha, R. B., Takeuchi, Y., Nakawo, M., & Ageta, Y. (2000). Practical prediction of ice melting beneath various thickness of debris cover on Khumbu Glacier, Nepal, using a positive degree-day factor. *Debris-Covered Glaciers*, (pp. 71–81).
- Ke, L., Ding, X., & Song, C. (2015). Heterogeneous changes of glaciers over the western Kunlun Mountains based on ICESat and Landsat-8 derived glacier inventory. *Remote Sensing of Environment*, *168*, 13–23. doi:10.1016/j.rse.2015.06.019.
- Kirkbride, M. P. (1993). The temporal significance of transitions from melting to calving termini at glaciers in the central Southern Alps of New Zealand. *The Holocene*, *3*, 232–240. doi:10.1177/095968369300300305.
- Kirkbride, M. P. (2011). Debris-covered glaciers. In *Encyclopedia of snow, ice and glaciers* (pp. 180–182). Springer.
- Knuth, S. L., & Cassano, J. J. (2014). Estimating sensible and latent heat fluxes using the integral method from in situ aircraft measurements. *Journal of Atmospheric and Oceanic Technology*, *31*, 1964–1981. doi:10.1175/JTECH-D-14-00008.1.
- Koh, L. P., & Wich, S. A. (2012). Dawn of drone ecology: Low-cost autonomous aerial vehicles for conservation. *Tropical Conservation Science*, *5*, 121–132. doi:10.1177/194008291200500202.
- Kohn, M. J., Wieland, M. S., Parkinson, C. D., & Upreti, B. N. (2005). Five generations of monazite in Langtang gneisses: Implications for chronology of the Himalayan metamorphic core. *Journal of Metamorphic Geology*, *23*, 399–406. doi:10.1111/j.1525-1314.2005.00584.x.
- de Kok, R. J., Tuinenburg, O. A., Bonekamp, P. N. J., & Immerzeel, W. W. (2018). Irrigation as a potential driver for anomalous glacier behaviour in High Mountain Asia. *Geophysical Research Letters*, (pp. 1–8). doi:10.1002/2017GL076158.

- Lang, T. J., & Barros, A. P. (2004). Winter Storms in the Central Himalayas. *Journal of the Meteorological Society of Japan*, 82, 829–844. doi:10.2151/jmsj.2004.829.
- Larour, E., Ivins, E. R., & Adhikari, S. (2017). Should coastal planners have concern over where land ice is melting? *Science Advances*, 3, 1–9. doi:10.1126/sciadv.1700537.
- Lary, D. J., Alavi, A. H., Gandomi, A. H., & Walker, A. L. (2016). Machine learning in geosciences and remote sensing. *Geoscience Frontiers*, 7, 3–10. doi:10.1016/j.gsf.2015.07.003.
- Lehner, B., Verdin, K., & Jarvis, A. (2008). New global hydrography derived from spaceborne elevation data. *Eos*, 89, 93–94. doi:10.1029/2008EO100001.
- Lejeune, Y., Bertrand, J.-M., Wagnon, P., & Morin, S. (2013). A physically based model of the year-round surface energy and mass balance of debris-covered glaciers. *J. Glaciol.*, 59, 327–344. doi:10.3189/2013jogG12J149.
- Leprince, S., Ayoub, F., & Avouac, J.-P. (2007). Automatic and Precise Orthorectification, Coregistration, and Subpixel Correlation of Satellite Images, Application to Ground Deformation Measurements. *IEEE Transactions on Geoscience and Remote Sensing*, 45, 1529–1558. doi:10.1109/TGRS.2006.888937.
- Leprince, S., Berthier, E., Ayoub, F., Delacourt, C., & Avouac, J. J. P. (2008). Monitoring Earth Surface Dynamics With Optical Imagery. *Eos, Transactions American Geophysical Union*, 89. doi:10.1029/2008EO010001.
- Li, Z. L., Tang, B. H., Wu, H., Ren, H., Yan, G., Wan, Z., Trigo, I. F., & Sobrino, J. A. (2013). Satellite-derived land surface temperature: Current status and perspectives. *Remote Sensing of Environment*, 131, 14–37. doi:10.1016/j.rse.2012.12.008.
- Lillesand, T., Kiefer, R. W., & Chipman, J. (2015). *Remote Sensing and Image Interpretation*. (6th ed.). New York: John Wiley & Sons.
- Lillesand, T. M., Kiefer, R. W., & Chipman, J. W. (2003). *Remote sensing and image interpretation*. John Wiley & Sons New York.
- Linsbauer, A., Paul, F., & Haerberli, W. (2012). Modeling glacier thickness distribution and bed topography over entire mountain ranges with GlabTop: Application of a fast and robust approach. *Journal of Geophysical Research: Earth Surface*, 117, 1–17. doi:10.1029/2011JF002313.
- Liu, D., & Xia, F. (2010). Assessing object-based classification: advantages and limitations. *Remote Sensing Letters*, 1, 187–194. doi:10.1080/01431161003743173.
- Loupe, G., Wehenkel, L., Suter, A., & Geurts, P. (2013). Understanding variable importances in forests of randomized trees. In *Advances in Neural Information Processing Systems* (pp. 1–9). Stateline, NV.
- Lowe, D. G. (2004). Distinctive Image Features from Scale-Invariant Keypoints. *International Journal of Computer Vision*, 60, 91–110. doi:10.1023/B:VISI.0000029664.99615.94.
- Lucieer, A., Jong, S., & Turner, D. (2013). Mapping landslide displacements using Structure from Motion (SfM) and image correlation of multi-temporal UAV photography. *Progress in Physical Geography*, 38, 97–116. doi:10.1177/0309133313515293.
- Luckman, A., Quincey, D. J., & Bevan, S. (2007). The potential of satellite radar interferometry and feature tracking for monitoring flow rates of Himalayan glaciers. *Remote Sensing of Environment*, 111, 172–181. doi:10.1016/j.rse.2007.05.019.
- Lutz, A. F., Immerzeel, W. W., Shrestha, A. B., & Bierkens, M. F. P. (2014). Consistent increase in High Asia's runoff due to increasing glacier melt and precipitation. *Nature Climate Change*, 4, 587–592. doi:10.1038/nclimate2237.
- Mair, D., Nienow, P., Sharp, M., Wohlleben, T., & Willis, I. (2010). Influence of subglacial drainage system evolution on glacier surface motion: Haut Glacier d'Arolla, Switzerland. *Journal of Geophysical Research*, 107, 1–13. doi:10.1029/2001JB000514.
- Mäkynen, J., Saari, H., Holmlund, C., Mannila, R., & Antila, T. (2012). Multi- and hyperspectral UAV imaging system for forest and agriculture applications. In *SPIE Proceedings 8374: Next-Generation Spectroscopic Technologies V* (pp. 8374–8374). doi:10.1117/12.918571.
- Mallalieu, J., Carrivick, J., Quincey, D., Smith, M., & James, W. (2017). An integrated Structure-from-Motion and time-lapse technique for quantifying ice-margin dynamics. *Journal of Glaciology*, (pp. 1–13). doi:10.1017/jog.2017.48.
- Marshall, S. J., White, E. C., Demuth, M. N., Bolch, T., Wheate, R., Menounos, B., Beedle, M. J., & Shea, J. M. (2011). Glacier Water Resources on the Eastern Slopes of the Canadian Rocky Mountains. *Canadian Water Resources Journal*, 36, 109–134. doi:10.4296/cwrj3602823.
- Marzeion, B., Cogley, J. G., Richter, K., & Parkes, D. (2014). Attribution of global glacier mass loss to anthropogenic and natural causes. *Science*, 345, 919–921. doi:10.1126/science.1254702.
- Mattson, L. E., Gardner, J. S., & Young, G. J. (1993). Ablation on debris covered glaciers: an example from the Rakhiot Glacier, Punjab, Himalaya. In *Snow and Glacier Hydrology (IAHS Publ. no. 218)* 218 (pp. 289–296). Kathmandu.
- Mausson, F., Scherer, D., Mölg, T., Collier, E., Curio, J., & Finkelnburg, R. (2014). Precipitation seasonality and variability over the Tibetan Plateau as resolved by the high Asia reanalysis. *Journal of Climate*, 27, 1910–1927. doi:10.1175/JCLI-D-13-00282.1.
- McCarthy, M., Pritchard, H., Willis, I., & King, E. (2017). Ground-penetrating radar measurements of debris thickness on Lirung Glacier, Nepal. *Journal of Glaciology*, 63, 543–555. doi:10.1017/jog.2017.18.
- Mihalcea, C., Brock, B. W., Diolaiuti, G., D'Agata, C., Citterio, M., Kirkbride, M. P., Cutler, M. E. J., & Smiraglia, C. (2008a). Using ASTER satellite and ground-based surface temperature measurements to derive supraglacial debris cover and thickness patterns on Miage Glacier (Mont Blanc Massif, Italy). *Cold Regions Science and Technology*, 52, 341–354. doi:10.1016/j.coldregions.2007.03.004.
- Mihalcea, C., Mayer, C., Diolaiuti, G., D'Agata, C., Smiraglia, C., Lambrecht, A., Vuillermoz, E., & Tartari, G. (2008b). Spatial distribution of debris thickness and melting from remote-sensing and meteorological data, at debris-covered Baltoro glacier, Karakoram, Pakistan. *Annals of Glaciology*, 48, 49–57. doi:10.3189/172756408784700680.

- Mihalcea, C., Mayer, C., Diolaiuti, G., Lambrecht, A., Smiraglia, C., & Tartari, G. (2006). Ice ablation and meteorological conditions on the debris-covered area of Baltoro glacier, Karakoram, Pakistan. *Annals of Glaciology*, 43, 292–300. doi:10.3189/172756406781812104.
- Miles, E. S., Pellicciotti, F., Willis, I. C., Steiner, J. F., Buri, P., & Arnold, N. S. (2016). Refined energy-balance modelling of a supraglacial pond, Langtang Khola, Nepal. *Annals of Glaciology*, 57, 29–40. doi:10.3189/2016AoG71A421.
- Miles, E. S., Steiner, J., Willis, I. C., Buri, P., Immerzeel, W. W., Chesnokova, A., & Pellicciotti, F. (2017a). Pond dynamics and supraglacial-englacial connectivity on debris-covered Lirung Glacier. *Frontiers in Earth Science*, 5, 1–19. doi:10.3389/FEART.2017.00069.
- Miles, E. S., Steiner, J. F., & Brun, F. (2017b). Highly variable aerodynamic roughness length ( $z_0$ ) for a hummocky debris-covered glacier. *Journal of Geophysical Research: Atmospheres*, 122, 1–20. doi:10.1002/2017JD026510.
- Miles, E. S., Willis, I. C., Arnold, N. S., Steiner, J., & Pellicciotti, F. (2017c). Spatial, seasonal and interannual variability of supraglacial ponds in the Langtang Valley of Nepal, 1999–2013. *Journal of Glaciology*, 63, 88–105. doi:10.1017/jog.2016.120.
- Minnis, P., & Khaiyer, M. M. (2000). Anisotropy of Land Surface Skin Temperature Derived from Satellite Data. *Journal of Applied Meteorology*, 39, 1117–1129. doi:10.1175/1520-0450(2000)039<1117:AOLSST>2.0.CO;2.
- Murillo-García, F. G., Alcántara-Ayala, I., Ardizzone, F., Cardinali, M., Fiourucci, F., & Guzzetti, F. (2014). Satellite stereoscopic pair images of very high resolution: a step forward for the development of landslide inventories. *Landslides*, 12, 277–291. doi:10.1007/s10346-014-0473-1.
- Naito, N., Nakawo, M., Aoki, T., Asahi, K., Fujita, K., Sakai, A., Kadota, T., Shiraiwa, T., & Seko, K. (1998). Surface flow on the ablation area of the Lirung Glacier in Langtang Valley, Nepal Himalayas. *Bulletin of Glacier Research*, 16, 67–73.
- Naito, N., Nakawo, M., Kadota, T., & Raymond, C. F. (2000). Numerical simulation of recent shrinkage of Khumbu Glacier, Nepal Himalayas. *International Association of Hydrological Sciences*, 264, 245–254.
- Nakawo, M., Iwata, S., & Yoshida, M. (1986). Processes which distribute supraglacial debris on the Khumbu Glacier, Nepal Himalaya. *Annals of Glaciology*, 8, 129–131. doi:10.1017/S0260305500001294.
- Nakawo, M., Yabuki, H., & Sakai, A. (1999). Characteristics of Khumbu Glacier, Nepal Himalaya: recent change in the debris-covered area. *Annals of Glaciology*, 1995, 3–7.
- Neckel, N., Loibl, D., & Rankl, M. (2017). Recent slowdown and thinning of debris-covered glaciers in south-eastern Tibet. *Earth and Planetary Science Letters*, 464, 95–102. doi:10.1016/j.epsl.2017.02.008.
- Nex, F., & Remondino, F. (2014). UAV for 3D mapping applications: A review. *Applied Geomatics*, 6, 1–15. doi:10.1007/s12518-013-0120-x.
- Nicholson, L., & Benn, D. I. (2006). Calculating ice melt beneath a debris layer using meteorological data. *Journal of Glaciology*, 52, 463–470. doi:10.3189/172756506781828584.
- Nicholson, L., & Benn, D. I. (2013). Properties of natural supraglacial debris in relation to modelling sub-debris ice ablation. *Earth Surface Processes and Landforms*, 38, 490–501. doi:10.1002/esp.3299.
- Nie, Y., Liu, Q., & Liu, S. (2013). Glacial lake expansion in the Central Himalayas by landsat images, 1990–2010. *PLoS ONE*, 8, 1–8. doi:10.1371/journal.pone.0083973.
- Nie, Y., Zhang, Y., Liu, L., & Zhang, J. (2010). Glacial change in the vicinity of Mt. Qomolangma (Everest), central high Himalayas since 1976. *Journal of Geographical Sciences*, 20, 667–686. doi:10.1007/s11442-010-0803-8.
- Nijhawan, R., Garg, P., & Thakur, P. (2016). A comparison of classification techniques for glacier change detection using multispectral images. *Perspectives in Science (in press)*, . doi:10.1016/j.pisc.2016.04.080.
- Nolin, A. W., & Dozier, J. (2000). A hyperspectral method for remotely sensing the grain size of snow. *Remote Sensing of Environment*, 74, 207–216. doi:10.1016/S0034-4257(00)00111-5.
- Nuimura, T., Fujita, K., & Sakai, A. (2017). Downwasting of the debris-covered area of Lirung Glacier in Langtang Valley, Nepal Himalaya, from 1974 to 2010. *Quaternary International*, 455, 93–101. doi:10.1016/j.quaint.2017.06.066.
- Nuimura, T., Fujita, K., Yamaguchi, S., & Sharma, R. R. (2012). Elevation changes of glaciers revealed by multitemporal digital elevation models calibrated by GPS survey in the Khumbu region, Nepal Himalaya, 1992–2008. *Journal of Glaciology*, 58, 648–656. doi:10.3189/2012JoG11J061.
- Nuimura, T., Sakai, A., Taniguchi, K., Nagai, H., Lamsal, D., Tsutaki, S., Kozawa, A., Hoshina, Y., Takenaka, S., Omiya, S., Tsunematsu, K., Tshering, P., & Fujita, K. (2015). The GAMDAM Glacier Inventory: a quality controlled inventory of Asian glaciers. *The Cryosphere*, 9, 849–864. doi:10.5194/tc-9-849-2015.
- Oerlemans, J. (1994). Quantifying global warming from the retreat of glaciers. *Science*, 264, 243–245.
- Østrem, G. (1959). Ice melting under a thin layer of moraine, and the existence of ice cores in moraine ridges. *Geografiska Annaler*, 41, 228–230.
- Palazzi, E., Von Hardenberg, J., & Provenzale, A. (2013). Precipitation in the Hindu-Kush Karakoram Himalaya: observations and future scenarios. *Journal of Geophysical Research Atmospheres*, 118, 85–100. doi:10.1029/2012JD018697.
- Paul, F., Bolch, T., Kääb, A., Nagler, T., Nuth, C., Scharrer, K., Shepherd, A., Strozzi, T., Ticconi, F., Bhambri, R., Berthier, E., Bevan, S., Gourmelen, N., Heid, T., Jeong, S., Kunz, M., Lauknes, T. R., Luckman, A., Merryman, J., Moholdt, G., Muir, A., Neelmeijer, J., Rankl, M., VanLooy, J., & Van Niel, T. (2013). The glaciers climate change initiative: Methods for creating glacier area, elevation change and velocity products. *Remote Sensing of Environment*, . doi:10.1016/j.rse.2013.07.043.
- Paul, F., Huggel, C., & Kääb, A. (2004). Combining satellite multispectral image data and a digital elevation model for mapping debris-covered glaciers. *Remote Sensing of Environment*, 89, 510–518. doi:10.1016/j.rse.2003.11.007.
- Pekel, J.-F., Cottam, A., Gorelick, N., & Belward, A. S. (2016). High-resolution mapping of global surface water and its long-term changes. *Nature*, 540, 418–422. doi:10.1038/nature20584.

- Pellicciotti, F., Petersen, L., Wicki, S., Carenzo, M., & Immerzeel, W. (2013). Air temperature distribution over a debris covered glacier in the Nepalese Himalayas. *Geophysical Research Abstracts*, 15, 11389.
- Pellicciotti, F., Stephan, C., Miles, E., Immerzeel, W. W., & Bolch, T. (2015). Mass-balance changes of the debris-covered glaciers in the Langtang Himal in Nepal between 1974 and 1999. *Journal of Glaciology*, 61, 373–386. doi:10.3189/2015JG13J237.
- Pepin, N., Bradley, R. S., Diaz, H. F., Baraer, M., Caceres, E. B., Forsythe, N., Fowler, H., Greenwood, G., Hashmi, M. Z., Liu, X. D., Miller, J. R., Ning, L., Ohmura, A., Palazzi, E., Rangwala, I., Schöner, W., Severskiy, I., Shahgedanov, M., Wang, M. B., Williamson, S. N., & Yang, D. Q. (2015). Elevation-dependent warming in mountain regions of the world. *Nature Climate Change*, 5, 424–430. doi:10.1038/nclimate2563.
- Perry, E. M., & Moran, M. S. (1994). An evaluation of atmospheric corrections of radiometric surface temperatures for a semiarid rangeland watershed. *Water Resources Research*, 30, 1261–1269. doi:10.1029/93WR03056.
- Petersen, L., & Schauwecker, S. (2013). Deriving supraglacial debris thickness using satellite data on the Lirung Glacier in the Nepalese Himalayas. *Geophysical Research Abstracts*, 15, 10244.
- Pfeffer, W. T., Arendt, A. A., Bliss, A., Bolch, T., Cogley, J. G., Gardner, A. S., Hagen, J.-O. O., Hock, R., Kaser, G., Kienholz, C., Miles, E. S., Moholdt, G., Mölg, N., Paul, F., Radic, V., Rastner, P., Raup, B. H., Rich, J., Sharp, M. J., Andreassen, L. M., Bajracharya, S., Barrand, N. E., Beedle, M. J., Berthier, E., Bhambri, R., Brown, I., Burgess, D. O., Burgess, E. W., Cawkwell, F., Chinn, T., Copland, L., Cullen, N. J., Davies, B., De Angelis, H., Fountain, A. G., Frey, H., Giffen, B. A., Glasser, N. F., Gurney, S. D., Hagg, W., Hall, D. K., Haritashya, U. K., Hartmann, G., Herreid, S., Howat, I., Jiskoot, H., Khromova, T. E., Klein, A., Kohler, J., König, M., Kriegl, D., Kutuzov, S., Lavrentiev, I., Le Bris, R., Li, X., Manley, W. F., Mayer, C., Menounos, B., Mercer, A., Mool, P., Negrete, A., Nosenko, G., Nuth, C., Osmonov, A., Pettersson, R., Racoviteanu, A., Ranzi, R., Sarikaya, M. A., Schneider, C., Sigurdsson, O., Sirguey, P., Stokes, C. R., Wheate, R., Wolken, G. J., Wu, L. Z., Wyatt, F. R., Radić, V., Rastner, P., Raup, B. H., Rich, J., Sharp, M. J., & The Randolph Consortium (2014). The Randolph Glacier Inventory: A globally complete inventory of glaciers. *Journal of Glaciology*, 60, 537–552. doi:10.3189/2014JG13J176.
- Pix4D SA (2017). Photogrammetry software for professional drone-based mapping, Version 4.0. URL: <https://pix4d.com/product/pix4dmapper-photogrammetry-software/>.
- Planet Team (2017). Planet application program interface: In Space for life on earth.
- Plets, G., Gheyle, W., Verhoeven, G., De Reu, J., Bourgeois, J., Verhegge, J., & Stichelbaut, B. (2012). Three-Dimensional Recording of Archaeological Remains in the Altai Mountains. *Antiquity*, 86, 884–897. doi:10.1017/S0003598X00047980.
- Qiao, L., Mayer, C., & Liu, S. (2015). Distribution and interannual variability of supraglacial lakes on debris-covered glaciers in the Khan Tengri-Tumor Mountains, Central Asia. *Environmental Research Letters*, 10, 4545–4584. doi:10.1088/1748-9326/10/1/014014.
- Quincey, D. J., Copland, L., Mayer, C., Bishop, M., Luckman, A., & Belò, M. (2009a). Ice velocity and climate variations for Baltoro Glacier, Pakistan. *Journal of Glaciology*, 55, 1061–1071. doi:10.3189/002214309790794913.
- Quincey, D. J., Luckman, A., & Benn, D. (2009b). Quantification of Everest region glacier velocities between 1992 and 2002, using satellite radar interferometry and feature tracking. *Journal of Glaciology*, 55, 596–606. doi:10.3189/002214309789470987.
- Quincey, D. J., Richardson, S. D., Luckman, A., Lucas, R. M., Reynolds, J. M., Hambrey, M. J., & Glasser, N. F. (2007). Early recognition of glacial lake hazards in the Himalaya using remote sensing datasets. *Global and Planetary Change*, 56, 137–152. doi:10.1016/j.gloplacha.2006.07.013.
- Radic, V., Bliss, A., Beedlow, A. C., Hock, R., Miles, E., & Cogley, J. G. (2014). Regional and global projections of twenty-first century glacier mass changes in response to climate scenarios from global climate models. *Climate Dynamics*, 42, 37–58.
- Radić, V., Menounos, B., Shea, J., Fitzpatrick, N., Tessema, M. A., & Déry, S. J. (2017). Evaluation of different methods to model near-surface turbulent fluxes for an alpine glacier in the Cariboo Mountains, BC, Canada. *The Cryosphere*, 11, 2897–2918. doi:10.5194/tc-11-2897-2017.
- Raftery, A. E., Zimmer, A., Frierson, D. M. W., Startz, R., & Liu, P. (2017). Less than 2 °C warming by 2100 unlikely. *Nature Climate Change*, (pp. 637–641). doi:10.1038/nclimate3352.
- Ragetli, S., Bolch, T., & Pellicciotti, F. (2016a). Heterogeneous glacier thinning patterns over the last 40 years in Langtang Himal, Nepal. *The Cryosphere*, 10, 2075–2097. doi:10.5194/tc-10-2075-2016.
- Ragetli, S., Immerzeel, W. W., & Pellicciotti, F. (2016b). Contrasting climate change impact on river flows from high-altitude catchments in the Himalayan and Andes Mountains. *PNAS*, 113, 9222–9227. doi:10.1073/pnas.1606526113.
- Ragetli, S., Pellicciotti, F., Immerzeel, W., Miles, E., Petersen, L., Heynen, M., Shea, J., Stumm, D., Joshi, S., & Shrestha, A. (2015). Unraveling the hydrology of a Himalayan catchment through integration of high resolution in situ data and remote sensing with an advanced simulation model. *Advances in Water Resources*, 78, 94–111. doi:10.1016/j.advwatres.2015.01.013.
- Rastner, P., Bolch, T., Notarnicola, C., & Paul, F. (2014). A comparison of pixel- and object-based glacier classification with optical satellite images. *IEEE Journal of Selected Topics in Applied Earth Observations and Remote Sensing*, 7, 984–993. doi:10.1109/JSTARS.2013.2274668.
- Reid, T., & Brock, B. W. (2014). Assessing ice-cliff backwasting and its contribution to total ablation of debris-covered Miage glacier, Mont Blanc massif, Italy. *Journal of Glaciology*, 60, 3–13. doi:10.3189/2014JG13J045.
- Reid, T. D., & Brock, B. W. (2010). An energy-balance model for debris-covered glaciers including heat conduction through the debris layer. *Journal of Glaciology*, 56, 903–916. doi:10.3189/002214310794457218.

- Reid, T. D., Carenzo, M., Pellicciotti, F., & Brock, B. W. (2012). Including debris cover effects in a distributed model of glacier ablation. *Journal of Geophysical Research*, *117*, 1–15. doi:10.1029/2012JD017795.
- Reineman, B. D., Lenain, L., Statom, N. M., & Melville, W. K. (2013). Development and Testing of Instrumentation for UAV-Based Flux Measurements within Terrestrial and Marine Atmospheric Boundary Layers. *Journal of Atmospheric and Oceanic Technology*, *30*, 1295–1319. doi:10.1175/JTECH-D-12-00176.1.
- Reznichenko, N., Davies, T., Shulmeister, J., & McSaveney, M. (2010). Effects of debris on ice-surface melting rates: An experimental study. *Journal of Glaciology*, *56*, 384–394. doi:10.3189/002214310792447725.
- Ribeiro-Gomes, K., Hernández-López, D., Ortega, J. F., Ballesteros, R., Poblete, T., & Moreno, M. A. (2017). Uncooled thermal camera calibration and optimization of the photogrammetry process for UAV applications in agriculture. *Sensors*, *17*, 9–11. doi:10.3390/s17102173.
- Rinaudo, F., Chiabrand, F., Lingua, A. M., & Spanò, A. T. (2012). Archaeological site monitoring: UAV photogrammetry can be an answer. *International Archives of the Photogrammetry, Remote Sensing and Spatial Information Sciences*, *39*, 583–588.
- Robson, B. A., Höbbling, D., Nuth, C., Strozz, T., & Dahl, S. O. (2016). Decadal scale changes in Glacier area in the Hohe Tauern national park (Austria) determined by object-based image analysis. *Remote Sensing*, *8*. doi:10.3390/rs8010067.
- Robson, B. A., Nuth, C., Dahl, S. O., Höbbling, D., Strozz, T., & Nielsen, P. R. (2015). Automated classification of debris-covered glaciers combining optical, SAR and topographic data in an object-based environment. *Remote Sensing of Environment*, *170*, 372–387. doi:10.1016/j.rse.2015.10.001.
- Roe, G. H., Baker, M. B., & Herla, F. (2017). Centennial glacier retreat as categorical evidence of regional climate change. *Nature Geoscience*, *10*, 95–99. doi:10.1038/ngeo2863.
- Roehl, K., & Röhl, K. (2008). Characteristics and evolution of supraglacial ponds on debris-covered Tasman Glacier, New Zealand. *Journal of Glaciology*, *54*, 867–880. doi:10.3189/00221430878779861.
- Röhl, K. (2006). Thermo-erosional notch development at fresh-water-calving Tasman Glacier, New Zealand. *Journal of Glaciology*, *52*, 203–213. doi:10.3189/172756506781828773.
- Rounce, D. R., & McKinney, D. C. (2014). Debris thickness of glaciers in the Everest Area (Nepal Himalaya) derived from satellite imagery using a nonlinear energy balance model. *The Cryosphere*, *8*, 1317–1329. doi:10.5194/tc-8-1317-2014.
- Rounce, D. R., Quincey, D. J., & McKinney, D. C. (2015). Debris-covered glacier energy balance model for Imja-Lhotse Shar Glacier in the Everest region of Nepal. *Cryosphere*, *9*, 2295–2310. doi:10.5194/tc-9-2295-2015.
- Rowan, A. V. (2017). The Little Ice Age' in the Himalaya: A review of glacier advance driven by Northern Hemisphere temperature change. *Holocene*, *27*, 292–308. doi:10.1177/0959683616658530.
- Rowan, A. V., Egholm, D. L., Quincey, D. J., & Glasser, N. F. (2015). Modelling the feedbacks between mass balance, ice flow and debris transport to predict the response to climate change of debris-covered glaciers in the Himalaya. *Earth and Planetary Science Letters*, *430*, 427–438. doi:10.1016/j.epsl.2015.09.004.
- Rubio, E., Caselles, V., & Badenas, C. (1997). Emissivity measurements of several soils and vegetation types in the 8–14  $\mu\text{m}$  wave band: Analysis of two field methods. *Remote Sensing of Environment*, *59*, 490–521. doi:10.1016/S0034-4257(96)00123-X.
- Ruessink, B. G., Arens, S. M., Kuipers, M., & Donker, J. J. (2018). Coastal dune dynamics in response to excavated foredune notches. *Aeolian Research*, *31*, 3–17. doi:10.1016/j.aeolia.2017.07.002.
- Rufino, G., & Moccia, A. (2005). Integrated VIS-NIR Hyperspectral / Thermal-IR Electro-Optical Payload System for a Mini-UAV. In *Infotech@Aerospace* September (pp. 1–9). doi:10.2514/6.2005-7009.
- Ryan, J. C., Hubbard, A., Irvine-Fynn, T. D., Doyle, S. H., Cook, J. M., Stibal, M., & Box, J. E. (2017). How robust are in situ observations for validating satellite-derived albedo over the dark zone of the Greenland Ice Sheet? *Geophysical Research Letters*, *44*, 6218–6225. doi:10.1002/2017GL073661.
- Ryan, J. C., Hubbard, a. L., Box, J. E., Todd, J., Christoffersen, P., Carr, J. R., Holt, T. O., & Snooke, N. (2015). UAV photogrammetry and structure from motion to assess calving dynamics at Store Glacier, a large outlet draining the Greenland ice sheet. *The Cryosphere*, *9*, 1–11. doi:10.5194/tc-9-1-2015.
- Sadeghi, M., Jones, S. B., & Philpot, W. D. (2015). A linear physically-based model for remote sensing of soil moisture using short wave infrared bands. *Remote Sensing of Environment*, *164*, 66–76. doi:10.1016/j.rse.2015.04.007.
- Sakai, A., & Fujita, K. (2010). Formation conditions of supraglacial lakes on debris-covered glaciers in the Himalaya. *Journal of Glaciology*, *56*, 177–181. doi:10.3189/002214310791190785.
- Sakai, A., & Fujita, K. (2017). Contrasting glacier responses to recent climate change in high-mountain Asia. *Scientific Reports*, *7*, 1–8. doi:10.1038/s41598-017-14256-5.
- Sakai, A., Fujita, K., & Kubota, J. (2004). Evaporation and percolation effect on melting at debris-covered Lirung Glacier, Nepal Himalayas, 1996. *Bulletin of Glaciological Research*, *21*, 9–15.
- Sakai, A., Nakawo, M., & Fujita, K. (1998). Melt rate of ice cliffs on the Lirung Glacier, Nepal Himalayas, 1996. *Bulletin of Glacier Research*, *16*, 57–66.
- Sakai, A., Nakawo, M., & Fujita, K. (2002). Distribution characteristics and energy balance of ice cliffs on debris-covered glaciers, Nepal Himalaya. *Arctic, Antarctic, and Alpine Research*, *34*, 12–19.
- Sakai, A., Nishimura, K., Kadota, T., & Takeuchi, N. (2009). Onset of calving at supraglacial lakes on debris-covered glaciers of the Nepal Himalaya. *Journal of Glaciology*, *55*, 909–917. doi:10.3189/002214309790152555.
- Sakai, A., Takeuchi, N., Fujita, K., & Nakawo, M. (2000). Role of supraglacial ponds in the ablation process of a debris-covered glacier in the Nepal Himalayas. *Debris-covered Glaciers (IAHS Publ. no. 264)*, *265*, 119–132.

- Salerno, F., Thakuri, S., D'Agata, C., Smiraglia, C., Manfredi, E. C., Viviano, G., & Tartari, G. (2012). Glacial lake distribution in the Mount Everest region: Uncertainty of measurement and conditions of formation. *Global and Planetary Change*, 92–93, 30–39. doi:10.1016/j.gloplacha.2012.04.001.
- Salerno, F., Thakuri, S., Tartari, G., Nuimura, T., Sunako, S., Sakai, A., & Fujita, K. (2017). Debris-covered glacier anomaly? Morphological factors controlling changes in the mass balance, surface area, terminus position, and snow line altitude of Himalayan glaciers. *Earth and Planetary Science Letters*, 471, 19–31. doi:10.1016/j.epsl.2017.04.039.
- Salisbury, J., & D'Aria, D. (1992). Emissivity of Terrestrial Materials in the 8–14 micrometer Atmospheric Window. *Remote Sensing of Environment*, 42, 83–108.
- Sankey, T. T., McVay, J., Swetnam, T. L., McClaran, M. P., Heilman, P., & Nichols, M. (2018). UAV hyperspectral and lidar data and their fusion for arid and semi-arid land vegetation monitoring. *Remote Sensing in Ecology and Conservation*, 4, 20–33. doi:10.1002/rse2.44.
- Sasaki, O., Noguchi, O., Zhang, Y., Hirabayashi, Y., & Kanae, S. (2016). A global high-resolution map of debris on glaciers derived from multi-temporal ASTER images. *The Cryosphere Discussions*, (pp. 1–24). doi:10.5194/tc-2016-222.
- Scambos, T., Durkiewicz, M. J., Wilson, J. C., & Bindschadler, R. A. (1992). Application of image cross-correlation to the measurement of glacier velocity using satellite image data. *Remote Sensing of Environment*, 42, 177–186. doi:10.1016/0034-4257(92)90101-O.
- Schaner, N., Voisin, N., Nijssen, B., & Lettenmaier, D. P. (2012). The contribution of glacier melt to streamflow. *Environmental Research Letters*, 7, 1–8. doi:10.1088/1748-9326/7/3/034029.
- Schauwecker, S., Rohrer, M., Huggel, C., Kulkarni, A., Ramanathan, A. L., Salzmann, N., Stoffel, M., & Brock, B. (2015). Remotely sensed debris thickness mapping of Bara Shigri Glacier, Indian Himalaya. *Journal of Glaciology*, 61, 675–688. doi:10.3189/2015JogG14J102.
- Scherler, D., Bookhagen, B., & Strecker, M. R. (2011). Spatially variable response of Himalayan glaciers to climate change affected by debris cover. *Nature Geoscience*, 4, 156–159. doi:10.1038/ngeo1068.
- Scherler, D., Leprince, S., & Strecker, M. R. (2008). Glacier-surface velocities in alpine terrain from optical satellite imagery—Accuracy improvement and quality assessment. *Remote Sensing of Environment*, 112, 3806–3819. doi:10.1016/j.rse.2008.05.018.
- Seko, K. (1987). Seasonal variation of altitudinal dependence of precipitation in Langtang Valley, Nepal Himalayas. *Bulletin of Glaciological Research*, 5, 41–47.
- SenseFly (2015). Drones For Professionals, Mapping & Photogrammetry, Flight Planning & Control Software. URL: <https://www.sensefly.com/home.html>.
- SenseFly (2017a). Homepage of senseFly. URL: <https://www.sensefly.com/home.html>.
- SenseFly (2017b). SenseFly Drone Accessories. URL: <https://www.sensefly.com/drones/accessories.html>.
- Shaw, T. E., Brock, B. W., Fyffe, C. L., Pellicciotti, F., Rutter, N., & Diotri, F. (2016). Air temperature distribution and energy-balance modelling of a debris-covered glacier. *Journal of Glaciology*, 62, 185–198. doi:10.1017/jog.2016.31.
- Shea, J. M., & Immerzeel, W. W. (2016). An assessment of basin-scale glaciological and hydrological sensitivities in the Hindu Kush - Himalaya. *Annals of Glaciology*, 57, 308–318. doi:10.3189/2016AoG71A073.
- Shea, J. M., Immerzeel, W. W., Wagnon, P., Vincent, C., & Bajracharya, S. (2015). Modelling glacier change in the Everest region, Nepal Himalaya. *The Cryosphere*, 9, 1105–1128. doi:10.5194/tc-9-1105-2015.
- Shean, D. (2017). High Mountain Asia 8-meter DEM Mosaics Derived from Optical Imagery, Version 1. doi:10.5067/KXOVQ9L172S2.
- Shrestha, A. B. (2011). Climate Change and Glaciers. In *Encyclopedia of Snow, Ice and Glaciers* (pp. 145–152). Springer.
- Singh, V. P., Singh, P., Hariashya, U. K., & Haritashya, U. K. (2011). *Encyclopedia of snow, ice and glaciers*. Dordrecht: Springer.
- Smith, M. W., Carrivick, J. L., & Quincey, D. J. (2016). Structure from motion photogrammetry in physical geography. *Progress in Physical Geography*, 40, 247–275. doi:10.1177/0309133315615805.
- Smith, T., & Bookhagen, B. (2018). Changes in seasonal snow water equivalent distribution in High Mountain Asia (1987 to 2009). *Science Advances*, 4, e1701550. doi:10.1126/sciadv.1701550.
- Snavely, N. (2008). *Scene Reconstruction and Visualization from Internet Photo Collections: A Survey*. Doctoral Thesis. University of Washington.
- Snavely, N. (2011). Scene Reconstruction and Visualization from Internet Photo Collections: A Survey. *IJPS Transactions on Computer Vision and Applications*, 3, 44–66. doi:10.2197/ipsjtcva.3.44.
- Snavely, N., Seitz, S. M., & Szeliski, R. (2008). Modeling the world from Internet photo collections. *International Journal of Computer Vision*, 80, 189–210. doi:10.1007/s11263-007-0107-3.
- Sobrino, A., & Cuenca, J. (1999). Angular variation of thermal infrared emissivity for some natural surfaces from experimental measurements. *Applied Optics*, 38, 3931–3936.
- Sobrino, J. A., & Caselles, V. (1993). A field method for measuring the thermal infrared emissivity. *ISPRS Journal of Photogrammetry and Remote Sensing*, 48, 24–31. doi:10.1016/0924-2716(93)90061-Q.
- Sorg, A., Bolch, T., Stoffel, M., Solomina, O., & Beniston, M. (2012). Climate change impacts on glaciers and runoff in Tien Shan (Central Asia). *Nature Climate Change*, 2, 725–731. doi:10.1038/nclimate1592.
- Steiner, J. F., Kraaijenbrink, P. D., Jiduc, S. G., & Immerzeel, W. W. (2018). Brief Communication: The Khurdopin glacier surge revisited – extreme flow velocities and formation of a dammed lake in 2017. *The Cryosphere*, 12, 95–101. doi:10.5194/tc-12-95-2018.

- Steiner, J. F., & Pellicciotti, F. (2016). Variability of air temperature over a debris-covered glacier in the Nepalese Himalaya. *Annals of Glaciology*, 57, 295–307. doi:10.3189/2016AoG71A066.
- Steiner, J. F., Pellicciotti, F., Buri, P., Miles, E. S., Immerzeel, W. W., Reid, T. D., & Steiner, C. J. F. (2015). Modelling ice-cliff backwasting on a debris-covered glacier in the Nepalese Himalaya. *Journal of Glaciology*, (pp. 889–907). doi:10.3189/2015JogG14J194.
- Strigter, E. E., Wanders, N., Saloranta, T. M., Shea, J. M., & Bierkens, M. F. P. (2017). Assimilation of snow cover and snow depth into a snow model to estimate snow water equivalent and snowmelt runoff in a Himalayan catchment. *The Cryosphere*, 11, 1647–1664. doi:10.5194/tc-11-1647-2017.
- Stokes, C. R., Popovnin, V., Aleynikov, A., Gurney, S. D., & Shahgedanova, M. (2007). Recent glacier retreat in the Caucasus Mountains, Russia, and associated increase in supraglacial debris cover and supra-/proglacial lake development. *Annals of Glaciology*, 46, 195–203. doi:10.3189/172756407782871468.
- Strozzi, T., Kouraev, A., Wiesmann, A., Wegmüller, U., Sharov, A., & Werner, C. (2008). Estimation of Arctic glacier motion with satellite L-band SAR data. *Remote Sensing of Environment*, 112, 636–645. doi:10.1016/j.rse.2007.06.007.
- Sugiyama, S., Fukui, K., Fujita, K., Tone, K., & Yamaguchi, S. (2013). Changes in ice thickness and flow velocity of Yala Glacier, Langtang Himal, Nepal, from 1982 to 2009. *Annals of Glaciology*, 54, 157–162. doi:10.3189/2013AoG64A111.
- Sund, M., Lauknes, T. R., & Eiken, T. (2014). Surge dynamics in the nathorstbreen glacier system, Svalbard. *Cryosphere*, 8, 623–638. doi:10.5194/tc-8-623-2014.
- Szeliski, R. (2011). *Computer vision: algorithms and applications*. London: Springer.
- Takeuchi, N., & Kohshima, S. (2000). Effect of debris cover on species composition of living organisms in supraglacial lakes on a Himalayan glacier. In *Debris-covered Glaciers (IAHS Publ. no. 264)* (pp. 267–275).
- Taylor, K. E., Stouffer, R. J., & Meehl, G. A. (2012). An overview of CMIP5 and the experiment design. *Bulletin of the American Meteorological Society*, 93, 485–498. doi:10.1175/BAMS-D-11-00094.1.
- Teixeira, L., Alzugaray, I., & Chli, M. (2018). Autonomous Aerial Inspection Using Visual-Inertial Robust Localization and Mapping. In M. Hutter, & R. Siegwart (Eds.), *Field and Service Robotics* (pp. 191–204). Cham: Springer International Publishing.
- Thompson, S., Benn, D. I., Mertes, J., & Luckman, A. (2016). Stagnation and mass loss on a Himalayan debris-covered glacier: Processes, patterns and rates. *Journal of Glaciology*, 62, 467–485. doi:10.1017/jog.2016.37.
- Topcon Positioning Systems (2009). Topcon tools post-processing software. URL: <https://www.topconpositioning.com/software-solutions>.
- Torres-Rua, A. (2017). Vicarious calibration of sUAS microbolometer temperature imagery for estimation of radiometric land surface temperature. *Sensors*, 17, 5–9. doi:10.3390/s17071499.
- Toth, C., & Józkó, G. (2016). Remote sensing platforms and sensors: A survey. *ISPRS Journal of Photogrammetry and Remote Sensing*, 115, 22–36. doi:10.1016/j.isprsjprs.2015.10.004.
- Triggs, B., Zisserman, A., & Szeliski, R. (2007). *Vision Algorithms: Theory and Practice*. Berlin: Springer.
- Trimble (2015). *eCognition Developer User Guide, Version 9.1.2*. Munich, Germany: Trimble Documentation. URL: <http://www.ecognition.com/>.
- Trimble (2017). *eCognition Developer User Guide, Version 9.3.0*. Munich, Germany: Trimble Documentation. URL: <http://www.ecognition.com/>.
- Turner, D., Lucieer, A., Malenkovský, Z., King, D. H., & Robinson, S. A. (2014). Spatial co-registration of ultra-high resolution visible, multispectral and thermal images acquired with a micro-UAV over antarctic moss beds. *Remote Sensing*, 6, 4003–4024. doi:10.3390/rs6054003.
- USGS (2016). *Landsat 8 Data Users Handbook*. (2nd ed.). United States Geological Survey.
- van der Veen, C. (2013). *Fundamentals of glacier dynamics*. (2nd ed.). Boca Raton: CRC Press.
- Verhoeven, G. (2011). Taking Computer Vision Aloft – Archaeological Three-dimensional Reconstructions from Aerial Photographs with PhotoScan. *Archaeological Prospection*, 18, 67–73. doi:10.1002/arp.399.
- Vijay, S., & Braun, M. (2016). Elevation change rates of glaciers in the Lahaul-Spiti (Western Himalaya, India) during 2000–2012 and 2012–2013. *Remote Sensing*, 8, 1–16. doi:10.3390/rs8121038.
- Vincent, C., Wagnon, P., Shea, J. M., Immerzeel, W. W., Kraaijenbrink, P. D. A., Shrestha, D., Soruco, A., Arnaud, Y., Brun, F., Berthier, E., & Sherpa, S. F. (2016). Reduced melt on debris-covered glaciers: investigations from Changri Nup Glacier, Nepal. *The Cryosphere*, 10, 1845–1858. doi:10.5194/tc-10-1845-2016.
- Wagnon, P., Vincent, C., Arnaud, Y., Berthier, E., Vuillermoz, E., Gruber, S., Ménégoz, M., Gilbert, A., Dumont, M., Shea, J., Stumm, D., & Pokhrel, B. K. (2013). Seasonal and annual mass balances of Mera and Pokalde glaciers (Nepal Himalaya) since 2007. *The Cryosphere*, 7, 1769–1786. doi:10.5194/tc-7-1769-2013.
- Watson, C., Quincey, D., Carrivick, J., & Smith, M. (2016a). Ice cliff dynamics in the Everest region of the Central Himalaya. *Global and Planetary Change*, 142, 14–27. doi:10.1016/j.gloplacha.2016.04.008.
- Watson, C. S., & King, O. (2018). Everest's thinning glaciers: implications for tourism and mountaineering. *Geology Today*, 34, 18–25. doi:10.1111/gto.12215.
- Watson, C. S., Quincey, D. J., Carrivick, J. L., & Smith, M. W. (2016b). The dynamics of supraglacial ponds in the Everest region, central Himalaya. *Global and Planetary Change*, 142, 14–27. doi:10.1016/j.gloplacha.2016.04.008.
- Watson, C. S., Quincey, D. J., Smith, M., Carrivick, J., Rowan, A. V., & James, M. (2017). Quantifying ice cliff evolution with multi-temporal point clouds on the debris-covered Khumbu Glacier, Nepal. *Journal of Glaciology*, (pp. 1–15). doi:10.1017/jog.2017.47.





---

## Acknowledgements

More than five years ago I graduated as a physical geographer in Utrecht. I really enjoyed doing independent research during both my master thesis and internship at KNMI, so I looked at PhD opportunities. During this process, Steven approached me for a pilot project on drones, glaciers and the Himalaya. Although not yet a PhD project, it sounded like a boy's dream and I was quick to accept the offer. Thank you, Steven, for asking me for that project and introducing me to the world of drones, which I otherwise would not have ventured into. Also many thanks for your supervision during the follow-up PhD project, our joint field trips, and checking in on the progress despite your busy job as department head.

Walter, you were a very nice daily supervisor who was never too bothered to answer a question or provide insights, and generally just there when needed. You really learned me how to do independent research, helped me improve my writing, and upped my confidence as a scientist. Although not immediately clear to me in the beginning, being trained by you to be an academic has been a privilege and I am thankful for that. It has been an honour to be part of the first batch of PhDs in your career. Also thanks for taking me on several field trips to Nepal and Norway, which inspired me to live healthier and start working out regularly.

Joe, thanks for all your help in the field, your insights, and reading and correcting my non-native English time and time again. It is very much appreciated. It was very nice that you had me as a guest at the Coldwater Laboratory in Canmore and took me on several field trips in the Rockies. Although we weren't always successful in our field campaigns and it was sometimes tougher than Himalaya fieldwork, it was definitely a very nice experience.

Thanks to all of my colleagues, office mates and students with whom I worked during the past years. Particular thanks to all of the people of the Mountain Hydrology team for fruitful discussions and team meetings, which provided me insights into non-remote-sensing stuff I knew nothing about before. Thanks Marjolein, for agreeing to be my paranymph, for making the five-week summer school and our joint course assistances more interesting and joyous, and for the regular object-based chit-chat.

I thank the co-authors of all the publications featured in this thesis. Without their help and guidance I would not have been able to finish this project successfully. Special thanks to Marc and Arthur for constructive discussions on the *Nature* manuscript, which was a process that was not always easy and often stressful. Thanks to the reviewers of all my papers for their comments that helped me greatly in the learning process. I would also like to thank all other individuals who helped to facilitate this project by their contributions to fieldwork, provision of required equipment, and gathering of data.

Lastly, I would like to thank all my friends and family who supported me during the past years, believed in me and were proud, also when times were rough. Particularly you, Viola, thank you with whole my heart. Since we met my life has changed remarkably for the better. You not only provided me with love and faith, but also with structure and goals, and learned me to put things in perspective. Things I largely lacked before, and admittedly sometimes still do. I can safely say that I would never have been able to overcome my occasional *hattýúk halála* in good sanity and finish my thesis without your support, and I am very grateful for that.

16 July 2018, Utrecht

---

## About the author

Philip Kraaijenbrink (24 December 1987, Arnhem, The Netherlands) started a bachelor in Earth Sciences at Utrecht University in 2007. After his bachelor, he continued in Utrecht with a master in Physical Geography (Earth Observation and Natural Hazards track). In his master research, he focused on river morphodynamics through multi-temporal object-based analysis of Landsat imagery. His research, heart for computer analyses and eagerness to learn in this field made him an expert in advanced image classification techniques and highly skilled in GIS analyses. As an integral part of his graduate program, he also performed an eight-month internship at the Royal Netherlands Meteorological Institute (KNMI) in which he became knowledgeable on climate data analysis, statistical downscaling and R scripting.



Following his cum laude graduation, Philip took a junior researcher position at Utrecht University on a pilot project aimed at monitoring Himalayan glaciers using an unmanned aerial vehicles (UAV). After a temporary position at the consulting firm FutureWater in Wageningen, Philip started as a PhD Candidate at Utrecht University in 2014 and started working on the research presented in this thesis, which is a continuation of the pilot study. By linking analyses of UAV-derived elevation models, and optical and thermal UAV imagery to the larger scale through spaceborne data and large scale glacier modelling, he has increased knowledge on the dynamics of debris-covered glaciers and the impact of climate change on these systems. During his PhD, Philip has acquired fieldwork skills in the Himalaya, Norway and the Rocky Mountains, the latter as part of an exchange visit with the University of Saskatoon, Canada. Climate-KIC, the funder of the PhD project, provided Philip with the opportunity to experience a five-week summer school on climate innovation, where he learned extensively about valorisation, research placement and business opportunities. He assisted the bachelor and master remote sensing courses at Utrecht University for multiple years by giving (guest) lectures and guiding computer practicals, and he supervised various undergraduate and graduate students over the years.

## First author publications

- Kraaijenbrink, P.D.A., J. M. Shea, W. W. Immerzeel (2018), Five years of unmanned aerial vehicle surveys on two Himalayan debris-covered glaciers (in preparation).
- Kraaijenbrink, P.D.A., J. M. Shea, M. Litt, J. F. Steiner, D. Treichler, I. Koch, and W. W. Immerzeel (2018), Mapping surface temperatures on a debris-covered glacier with an unmanned aerial vehicle, *Frontiers in Earth Science*, 6(64), 1–19. doi:10.3389/feart.2018.00064
- Kraaijenbrink, P.D.A., M. F. P. Bierkens, A. F. Lutz, and W. W. Immerzeel (2017), Impact of a global temperature rise of 1.5 degrees Celsius on Asia's glaciers, *Nature*, 549(7671), 257–260, doi:10.1038/nature23878.
- Kraaijenbrink, P.D.A., J. M. Shea, F. Pellicciotti, S. M. De Jong, and W. W. Immerzeel (2016), Object-based analysis of unmanned aerial vehicle imagery to map and characterise surface features on a debris-covered glacier, *Remote Sensing of Environment*, 186, 581–595, doi:10.1016/j.rse.2016.09.013.
- Kraaijenbrink, P.D.A., S. W. Meijer, J. M. Shea, F. Pellicciotti, S. M. D. E. Jong, and W. W. Immerzeel (2016), Seasonal surface velocities of a Himalayan glacier derived by automated correlation of unmanned aerial vehicle imagery, *Annals of Glaciology*, 57(71), 103–113, doi:10.3189/2016AoG71A072.

## Co-authored publications

- Brun, F., P. Wagnon, E. Berthier, J. M. Shea, W. W. Immerzeel, P.D.A. Kraaijenbrink, C. Vincent, C. Reverchon, D. Shrestha, and Y. Arnaud (2018), Ice cliffs cannot explain the debris-cover anomaly: a case study on Changri Nup Glacier, Nepal, Central Himalaya, *Cryosph. Discuss.*, 1–32.
- Steiner, J. F., P.D.A. Kraaijenbrink, S. G. Jiduc, and W. W. Immerzeel (2018), Brief Communication: The Khurdopin glacier surge revisited - extreme flow velocities and formation of a dammed lake in 2017, *Cryosphere*, 12(August), 95–101, doi:10.5194/tc-12-95-2018.
- Vincent, C., P. Wagnon, J. M. Shea, W. W. Immerzeel, P.D.A. Kraaijenbrink, D. Shrestha, A. Soruco, Y. Arnaud, F. Brun, E. Berthier, and S.F. Sherpa (2016), Reduced melt on debris-covered glaciers: investigations from Changri Nup Glacier, Nepal, *Cryosph.*, 10, 1845–1858, doi:tc-10-1845-2016.
- Lutz, A. F., W. W. Immerzeel, P.D.A. Kraaijenbrink, and A. B. Shrestha (2016), Climate change impacts on the upper Indus hydrology: sources, shifts and extremes, *PLoS One*, 11(11), 1–33, doi:10.1371/journal.pone.0165630.
- Immerzeel, W. W., P.D.A. Kraaijenbrink, and L. M. Andreassen (2016), Use of an Unmanned Aerial Vehicle to assess recent surface elevation change of Storbreen in Norway, *Cryosph. Discuss.*, 1–31.
- Brun, F., P. Buri, E. S. Miles, P. Wagnon, J. Steiner, E. Berthier, S. Ragetti, P.D.A. Kraaijenbrink, W. W. Immerzeel, and F. Pellicciotti (2016), Quantifying volume loss from ice cliffs on debris-covered glaciers using high-resolution terrestrial and aerial photogrammetry, *J. Glaciol.*, 62(234), 684–695, doi:10.1017/jog.2016.54.
- Kargel, J.S., G. J. Leonard, D. H. Shugar, U. K. Haritashya, A. Bevington, E. J. Fielding, K. Fujita, M. Geertsema, E. S. Miles, J. Steiner, E. Anderson, S. Bajracharya, G. W. Bawden, D. F. Breashears, A. Byers, B. Collins, M. R. Dhital, A. Donnellan, T. L. Evans, M. L. Geai, M. T. Glasscoe, D. Green, D. R. Gurung, R. Heijnen, A. Hilborn, K. Hudnut, C. Huyck, W. W. Immerzeel, Jiang Liming, R. Jibson, A. Kääh, N. R. Khanal, D. Kirschbaum, P.D.A. Kraaijenbrink, D. Lamsal, Liu Shiyin, Lv Mingyang, D. McKinney, N. K. Nahirnick, Nan Zhuotong, S. Ojha, J. Olsenholler, T.H. Painter, M. Pleasants, K. C. Pratima, Q. I. Yuan, B. H. Raup, D. Regmi, D. R. Rounce, A. Sakai, Shangguan Donghui, J. M. Shea, A. B. Shrestha, A. Shukla, D. Stumm, M. van der Kooij, K. Voss, Wang Xin, B. Weihs, D. Wolfe, Wu Lizong, Yao Xiaojun, M. R. Yoder, N. Young. (2015), Geomorphic and geologic controls of geohazards induced by Nepal's 2015 Gorkha earthquake, *Science* (80), 8353, doi:10.1126/science.aac8353.

Immerzeel, W. W., P.D.A. Kraaijenbrink, J. M. Shea, A. B. Shrestha, F. Pellicciotti, M. F. P. Bierkens, and S. M. de Jong (2014), High-resolution monitoring of Himalayan glacier dynamics using unmanned aerial vehicles, *Remote Sens. Environ.*, 150, 93–103, doi:10.1016/j.rse.2014.04.025.

## **Awards**

*Outstanding Student Paper Award.* AGU Fall Meeting 2017, New Orleans, United States. Awarded by the American Geophysical Union.

*Outstanding Student Poster and PICO Award.* EGU General Assembly 2016, Vienna, Austria. Awarded by the European Geosciences Union.

*Best oral presentation by a student.* International Symposium on Glaciology in High-Mountain Asia 2015, Kathmandu, Nepal. Awarded by the International Association of Cryospheric Sciences.

